Vol. 293, No. 1–2, July 20, 1994

ISSN 0003-2670

ANALYTICA CHIMICA ACTA

An international journal devoted to all branches of analytical chemistry

ELSEVIER

ANALYTICA CHIMICA ACTA

Scope. *Analytica Chimica Acta* publishes original papers, rapid publication letters and reviews dealing with every aspect of modern analytical chemistry. Reviews are normally written by invitation of the editors, who welcome suggestions for subjects. Letters can be published within **four months** of submission. For information on the Letters section, see inside back cover.

Submission of Papers

Americas

Prof. Harry L. Pardue
Department of Chemistry
1393 BRWN Bldg, Purdue University
West Lafayette, IN 47907-1393
USA

Tel:(+1-317) 494 5320
Fax:(+1-317) 496 1200

Computer Techniques

Prof. J.T. Clerc
Universität Bern
Pharmazeutisches Institut
Baltzerstrasse 5, CH-3012 Bern
Switzerland

Tel:(+41-31) 6314191
Fax:(+41-31) 6314198

Prof. Sarah C. Rutan
Department of Chemistry
Virginia Commonwealth University
P.O. Box 2006
Richmond, VA 23284-2006
USA
Tel:(+1-804) 367 7517
Fax:(+1-804) 367 8599

Other Papers

Prof. Alan Townshend
Department of Chemistry
The University
Hull HU6 7RX
Great Britain

Tel:(+44-482) 465027
Fax:(+44-482) 466410

Prof. Willem E. van der Linden
Laboratory for Chemical Analysis
Department of Chemical Technology
Twente University of Technology
P.O. Box 217, 7500 AE Enschede
The Netherlands
Tel:(+31-53) 892629
Fax:(+31-53) 356024

Prof. Paul Worsfold
Dept. of Environmental Sciences
University of Plymouth
Plymouth PL4 8AA
Great Britain

Tel:(+44-752) 233006
Fax:(+44-752) 233009

Submission of an article is understood to imply that the article is original and unpublished and is not being considered for publication elsewhere. *Anal. Chim. Acta* accepts papers in English only. There are no page charges. Manuscripts should conform in layout and style to the papers published in this issue. See inside back cover for "Information for Authors".

Publication. *Analytica Chimica Acta* appears in 16 volumes in 1994 (Vols. 281-296). *Vibrational Spectroscopy* appears in 2 volumes in 1994 (Vols. 6 and 7). Subscriptions are accepted on a prepaid basis only, unless different terms have been previously agreed upon. It is possible to order a combined subscription (*Anal. Chim. Acta* **and** *Vib. Spectrosc.*).
Our p.p.h. (postage, packing and handling) charge includes surface delivery of all issues, except to subscribers in the U.S.A., Canada, Australia, New Zealand, China, India, Israel, South Africa, Malaysia, Thailand, Singapore, South Korea, Taiwan, Pakistan, Hong Kong, Brazil, Argentina and Mexico, who receive all issues by air delivery (S.A.L.-Surface Air Lifted) at no extra cost. For Japan, air delivery requires 25% additional charge of the normal postage and handling charge; for all other countries airmail and S.A.L. charges are available upon request.

Subscription orders. Subscription prices are available upon request from the publisher. Subscription orders can be entered only by calendar year and should be sent to: Elsevier Science B.V., Journals Department, P.O. Box 211, 1000 AE Amsterdam, The Netherlands. Tel: (+31-20) 5803 642, Telex: 18582, Telefax: (+31-20) 5803598, to which requests for sample copies can also be sent. Claims for issues not received should be made within six months of publication of the issues. If not they cannot be honoured free of charge. Readers in the U.S.A. and Canada can contact the following address: Elsevier Science Inc., Journal Information Center, 655 Avenue of the Americas, New York, NY 10010, U.S.A. Tel: (+1-212) 6333750, Telefax: (+1-212) 6333990, for further information, or a free sample copy of this or any other Elsevier Science journal.
Advertisements. Advertisement rates are available from the publisher on request.

US mailing notice - Analytica Chimica Acta (ISSN 0003-2670) is published 3 times a month (total 48 issues) by Elsevier Science B.V. (Molenwerf 1, Postbus 211, 1000 AE Amsterdam). Annual subscription price in the USA US$ 3035.75 (valid in North, Central and South America), including air speed delivery. Second class postage paid at Jamaica, NY 11431. *USA Postmasters*: Send address changes to Anal. Chim. Acta, Publications Expediting, Inc., 200 Meacham Av., Elmont, NY 11003. Airfreight and mailing in the USA by Publication Expediting.

ANALYTICA CHIMICA ACTA

An international journal devoted to all branches of analytical chemistry

(Full texts are incorporated in CJELSEVIER, a file in the Chemical Journals Online database available on STN International; Abstracted, indexed in: Aluminum Abstracts; Anal. Abstr.; Biol. Abstr.; BIOSIS; Chem. Abstr.; Curr. Contents Phys. Chem. Earth Sci.; Engineered Materials Abstracts; Excerpta Medica; Index Med.; Life Sci.; Mass Spectrom. Bull.; Material Business Alerts; Metals Abstracts; Sci. Citation Index)

VOL. 293 NO. 1–2 CONTENTS JULY 20, 1994

(Continued overleaf)

Contents (continued)

ANALYTICA CHIMICA ACTA
VOL. 293 (1994)

ANALYTICA CHIMICA ACTA

An international journal devoted to all branches of analytical chemistry
Revue internationale consacrée à tous les domaines de la chimie analytique
Internationale Zeitschrift für alle Gebiete der analytischen Chemie

Anal. Chim. Acta, Vol. 293 (1994)

ELSEVIER, Amsterdam–Lausanne–New York–Oxford–Shannon–Tokyo

0003-2670/94/$07.00

ELSEVIER

Analytica Chimica Acta 293 (1994) 1–17

ANALYTICA CHIMICA ACTA

A flexible instrument for voltammetry, amperometry and stripping potentiometry

Karsten N. Thomsen *,[1], Hans J. Skov [2], Maria E.R. Dam [3]

Environmental Engineering Laboratory, Department of Civil Engineering, Aalborg University, Sohngaardsholmvej 57, DK-9000 Aalborg, Denmark

(Received 1st November 1993)

Abstract

A computerized system capable of performing the techniques most commonly encountered in electroanalysis is described. The system consists of a personal computer with peripherals which controls several units, both commercially available and purpose-built, for data acquisition and experimental control. In addition, several optional devices such as pumps, valves, and a sample carousel may be controlled for automation of the analytical procedures. A main feature of the software is that it permits complex experiments and advanced data processing to be defined as a sequence of much simpler commands. Several of these may be gathered in a command macro which then is available as a single command. The data acquisition used for stripping potentiometry has been improved and now utilizes an A/D converter of the track and follow type, specially adapted for the purpose. The result is evident in terms of smoother stripping signals with high resolution on the potential axis, and the high sampling rate of maximum 800 kHz permits signals from analytes at the low μg/l level to be well-resolved even with moderate pre-electrolysis times. Precise timing of the pulsed amperometric and voltammetric techniques, independent of the execution speed of the program, is achieved by means of three counters in cascade counting clock pulses. The A/D converter is paced by one of those while another one times various delay periods. This facilitates high sampling rates to be combined with real-time display of the data. Three applications demonstrating the merits of the system are included. One of these compares the signal quality obtained with the improved data acquisition with that of an older apparatus for stripping potentiometry. Next the utility of comparing several sampling techniques when optimizing an analytical procedure is demonstrated for the determination of Pb in samples with very high salt content. Finally, the possibility of building highly automated analytical procedures by means of the command macros is shown for the amperometric detection of carbohydrates at a Cu electrode in a flow-injection set up.

Key words: Amperometry; Flow-injection; Stripping potentiometry; Voltammetry; Computerized system for electroanalysis

* Corresponding author.

[1] Present address: I/S Nordkraft, Østerbro 7, DK-9000 Aalborg, Denmark.

[2] Permanent address: Department of Chemistry, Aarhus University, DK-8000 Aarhus C, Denmark.

[3] Permanent address: University of Trondheim, Department of Chemistry, N-7055 Trondheim, Norway.

SSDI 0003-2670(94)00078-Z

1. Introduction

The use of computers for data acquisition and experimental control in the electroanalytical laboratory has, in general, widened the scope of the sampling techniques in terms of time resolution and scan rates available and certainly improved the possibilities for post-sampling manipulation and evaluation of the signals. However, the pulsed potential techniques of voltammetry and amperometry together with the potentiometric stripping techniques are sampling methods that have gained especially from this development. Computer-controlled instrumentation allows easy generation and precise timing of various excitation waveforms, and the parameters defining the size of potential steps and duration of delay and sampling periods are readily adjusted such that the technique may be optimized for a specific application. A technique like pulsed amperometric detection, PAD, developed by Johnson and LaCourse [1] for detection of carbohydrates, that repeats a sequence of potential steps for sampling, rinsing, and regeneration of the noble metal electrode, would hardly be realizable without the use of a computer.

In the potentiometric stripping techniques, trace metals accumulated in a mercury phase during an electrolysis step are re-oxidized at open potentiostatic circuit and the potential–time transient recorded. The metals may either be re-oxidized by means of an oxidant in solution (termed potentiometric stripping analysis, PSA) or by a constant current drawn through the working electrode (termed constant current chronopotentiometry, CCC, or constant current stripping analysis). In either case, re-oxidation of a trace metal will give rise to a plateau on the potential–time transient in such a way that the duration of the plateau reflects the bulk concentration, and the potential indicates the identity of the metal. With moderate electrolysis times and samples at the μg/l concentration level, the duration of the plateaus is typically in the millisecond order of magnitude. To obtain well-resolved signals at this level, the high sampling rates of computerized equipment are mandatory.

One particular data acquisition scheme for this purpose, described by Mortensen et al. [2] and Skov and Kryger [3], divides the potential range from the electrolysis potential to the cut-off potential in intervals of a few mV width and assigns a location in memory (a channel) to each one. During data acquisition, the computer samples the potential by means of an A/D converter at a constant rate and increments the count in the channel corresponding to the outcome of each conversion. The measured potential is compared to the pre-set cut-off potential, and the acquisition is stopped and potentiostatic control re-established when the final potential is reached. Following data acquisition, the count held in a channel specifies the number of times that a potential in the corresponding potential interval was registered. Alternatively, this may be formulated as the time (in units of the sampling period) that the potential spend in the specific potential interval while decaying toward the equilibrium potential. Mathematically, this corresponds to transforming the original potential–time (E,t) transient to the differential $\mathrm{d}t/\mathrm{d}E$ versus E. As a consequence, a plateau on the transient is transformed into a peak when $\mathrm{d}t/\mathrm{d}E$ versus E is plotted. The length of the plateau, which is proportional to the bulk concentration of the analyte, is obtained by integration of the differential across the peak. A particular advantage of the transformation is that it facilitates subtraction of the capacitative background which is part of any stripping potentiometric signal. Moreover, a certain degree of noise reduction is inherent to the scheme because random fluctuations imposed on the potential will cause the following conversions to be accumulated in channels not to far from the true channels, such that the fluctuations are averaged out in the final appearance of the signal. Finally, it allows efficient storage of large number of A/D conversions.

In the first implementations of this data acquisition scheme, the sampling rate was limited to around 5 kHz [3] by the execution time of the program loop responsible for reading the results from the A/D converter, addressing the memory for accumulation of data, and comparing the last potential reading with the cut-off potential. The PSA unit described by Høyer et al. [4] marked a

major advance because the acquisition scheme was implemented in hardware and took place without any action from the supervising computer which permitted the potential to be sampled at a rate of 667 kHz. With this equipment, signals recorded in samples with sub-μg/l concentrations of several trace metals were well-resolved, even with electrolysis times in the 30 to 60 s range [4].

Here, we present a flexible instrument capable of performing the voltammetric, amperometric, and potentiometric techniques most often encountered for electroanalytical work. The system consists of a personal computer (PC) equipped with commercially available cards for communication, data acquisition, and experimental control supervising an electrochemical module where tailor-made, modular units for fast data acquisition in potentiometric measurements, generation of voltage ramps in voltammetry, etc. are placed. The data acquisition used for the potentiometric techniques has been improved by utilizing that the potential–time transients by nature are continuous in time. This allows A/D conversion according to a different principle to be used, such that the systematic distortions introduced by the non-ideality of the converters applied sofar is avoided. In addition, even better noise reduction results from the use of the new type A/D converter. The timing of the pulsed voltammetric and amperometric techniques relies on a fast clock feeding three counters in cascade of which the second triggers the A/D converter and the third times delays. This configuration makes the data acquisition independent of the execution speed of the program and permits fast sampling rates to be combined with real-time display of the data.

The software controlling the system is mainly based on user-friendly menus and pop-up windows. However in one mode, the program accepts simple commands, each with a well-defined function. A main feature of the program is that sequences of commands may be gathered into macros. In this way maximum flexibility in experimental control and data processing is obtained, and the degree of automation of both is readily adjusted to suit the specific application.

Three examples illustrating the possibilities of the instrument are included. One of them compares the quality of PSA signals recorded by this instrument with those of an older implementation of the data acquisition scheme. The second example demonstrates that choosing the right sampling technique, when more are in principle applicable, may be a very important step for optimizing a new analytical procedure. More specifically, two voltammetric techniques are compared with a potentiometric for determination of Pb in samples containing very high concentrations of salt. Finally, the possibility of building fully automatic analytical procedures from the command macros is demonstrated for the determination of carbohydrates by the combination of flow-injection analysis (FIA) and amperometric detection.

2. Experimental

2.1. Hardware

The instrument consists of an IBM-compatible PC (80386SX processor, 16 MHz clock frequency, and 1 MB RAM) equipped with printer and plotter (Hewlett-Packard, Model HP7475A) and a laboratory-made electrochemical module (EM). A block diagram of the PC, EM, and several optional devices is shown in Fig. 1. The PC is interfaced with the outer world through four commercially available cards placed in expansion slots with access to the PC bus.

Parallel communication cards

The digital communication with the EM takes place through these two cards (PCIO Multi 24 bit I/O-port, Circuit Design, Karlslunde, Denmark) which are based on the Intel 8255 chip. Each card provides three 8 bit ports; two of which are used for sending and receiving data to and from the EM, respectively, while the third one addresses the functions available and reports on the communication status. The transfer rate is approx. 20 kByte/s which means that it takes around 0.25 s to read the 256 words in a potentiometric signal.

PCL-812

This card (PC LabCard series, Advantech) provides the A/D-converter (12 bit, successive approximation type, max. 30 kHz sampling rate, ±10 V analog input range) used for data acquisition in voltammetric and amperometric techniques. The speed and direction (reverse, stop, forward) of two peristaltic pumps (Alitea U1-XV and U4-XV) are controlled through sets of a D/A converter and three digital outputs (DOs). A 2 MHz clock on this card paces the A/D converter and is used for fast timing operations in general.

PCL-720

This digital I/O and counter card (PC LabCard series, Advantech) controls the functions (carousel forward, backward, or home; arm up, down, in from, or out to the wash position) of the sample carousel (Mikrolab A/S, Aarhus, Denmark) through 6 DOs and 1 digital input (DI). The busy signal from the sample carousel is sensed through the DI, so that the PC waits for one command to finish before sending the next when executing series of carousel operations. The carousel accommodates 20 samples in 20 ml polyethylene beakers which are intended for sin-

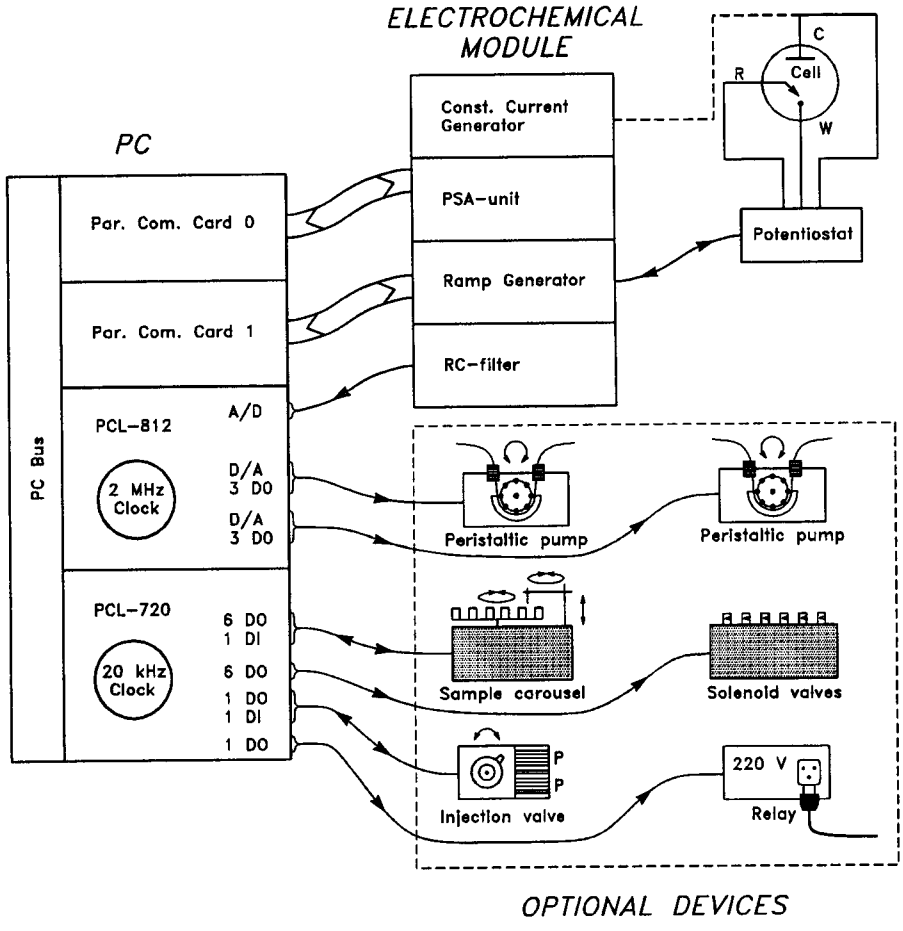

Fig. 1. Block diagram of the electrochemical instrument. The modules shown with the PC are placed in expansion slots. Broad connecting lines indicate digital communication while analog signals are shown with thin lines. The arrows illustrate the flow direction for information.

gle-use and are available from a number of sources. The relays determining the state of six pinch solenoid valves (Sirai S.r.I, type S104, 24 V DC, 2-way, normally closed) are controlled through the corresponding number of DOs. The valves function by pinching off a piece of silicone rubber (Dow-Corning Silastic) and are intended for flow experiments in which medium exchange is needed. The position (Inject or Load) of the pneumatic injection valve (Rheodyne 7126) is switched by a 100 ms pulse at a DO; the resulting position may be sensed through the DI connected to a microswitch set by the valve. Finally, the simplest possible experimental control is performed by a single DO controlling a 220 V AC power source by means of a relay. The clock present at the PCL-720 is configured to operate at 20 kHz and is used for timing of longer periods such as delays in various experiments.

The EM contains several independent units, all made as separate prints and assembled in a basis module (Hameg) with a built-in power source. This construction method ensures that new functionalities are easily added, and allows the units to be tested separately and thus promotes localization of bugs. Most of the units have several functions, all addressable through the parallel communication cards in the PC.

Current generator

This unit produces the constant current used for chronopotentiometric experiments by means of a 16 bit D/A converter. Thus, the current range is ± 500 μA with a resolution of 15 nA.

PSA-unit

The PSA unit acquires the potential–time transients of CCC or PSA. The potential interval between the initial and final potentials (typically the plating and cut-off potential, respectively) is divided into 256 intervals of equal width, and a location in the on-board memory is assigned to each interval. During data acquisition, the result of each A/D conversion is used as an address pointer to the memory, and the value at the addressed location is incremented. When the final potential is reached, the acquisition is stopped and potentiostatic control re-established. Two independent memory buffers are present in the unit so that main and background signals can be acquired in rapid succession. At a later time, the contents can be read by the PC; the buffers are nullified simultaneously and are thus ready for the next experiment.

Once the data acquisition is started, it takes place without any interaction with the PC. This is necessary because of the high sampling rates needed to resolve transients of a few ms total length. The maximum sampling frequency is 800 kHz, i.e. a minimum sampling period of 1.25 μs.

The resolution on the potential axis, i.e., the width of the potential intervals, is simply the difference between the final and initial potentials divided by 256. Accordingly, the resolution varies from one experiment to another. For a typical PSA experiment, the resolution will be between 2 to 3 mV which is considered adequate for most purposes.

The non-fixed potential resolution is one difference from earlier implementations of this scheme [2–5]; more importantly, the A/D conversion is based on a different principle giving smoother and less noisy signals. A more technical description of this is given below.

Ramp generator

The potential is generated by means of a 16 bit up/down counter; the value held by the counter is fed to a 16 bit D/A converter which generates the analog voltage for the potentiostat. This value can be set directly from the PC thereby setting the potential applied to the electrode. Linear ramps are formed by counting the value up or down at regular intervals and thus changing the output of the D/A converter in steps of 89 μV. This is effected by a pulse train on one input terminal, while the scan direction (count up or down) is determined by the state of another input terminal. These two input terminals are in turn controlled by a two 16 bit counters in cascade in a timer circuit (AM9513, Advanced Micro Devices). The first of these determines the scan rate by dividing down the 0.4 MHz clock frequency available and sending the resulting pulses to the up/down counter. The other one sets the scan range by toggling the scan direction when a certain

number of pulses have been sent to the up/down counter. In this way, ramps with scan rates from less than 1 mV/s to at least 8 V/s are generated reproducibly. Again, this is done independently of the PC which is free to acquire data while the scan is progressing. The design is based on principles described by He and Faulkner [6] who also found that with potential steps of 100 μV, the ramp was effectively linear due to the capacitance of the cell.

Potentiostat

The print constituting the potentiostat is placed separately in a small box ($3.5 \times 6 \times 11$ cm) with power and input voltage supplied from the ramp generator. This allows the potentiostat to be placed very near the cell and thus the high-impedance wires between cell and potentiostat to be short (approx. 15 cm) in order to minimize pick-up of electrical noise. The other wires in the system are all low-impedance and much less sensitive to noise. Four levels of amplification for the output voltage representing the cell current are available, either 0.1, 1, 10 or 100 μA/V.

RC filter

The output voltage from the potentiostat may be fed to a low-pass filter prior to A/D conversion. 17 logarithmically spaced cut-off frequencies between 50 kHz and 10 Hz can be selected or the current signal may be fed directly to the A/D converter at the PCL-812 card.

2.2. Data acquisition in chronopotentiometry

The data acquisition used for CCC and PSA measurements has been redesigned to give smoother and less noisy signals. The A/D conversion is now done by adapting the well-known track and follow-principle for this purpose.

Prior to data acquisition, a four quadrant multiplier is set such that the potential interval between the initial and final potentials is scaled to fit closely the input voltage range for the 8 bit A/D converter. During acquisition, the converter thus returns digital values between 0 and 255 which are in turn used as address pointers in one of the two 256 word memory buffers, and the count at the addressed location is incremented. When the voltage fed to the A/D converter overshoots the input range, it signals that the final potential has been reached, and data acquisition is stopped.

A block diagram of the A/D converter is shown in Fig. 2. Main components are an operational amplifier, a windows comparator, an 8 bit counter, and a 16 bit D/A converter. The operational amplifier adds the scaled input voltage and the output from the D/A converter which represents the negated result of the previous conversion; the output from the amplifier is fed to a windows comparator together with the voltage interval representing 1 bit – the window. Depending on the outcome of the comparison of the input values, one of three output terminals signalling larger than window, within window, and less than window will go high. The first and last of these terminals are connected to the input terminals of an 8 bit counter through AND gates. The clock pulses setting the sampling frequency are fed to the other legs of the AND gates such that a pulse comes through to the counter and changes its value when either the larger than window or the less than window condition is true. The value held in the counter is in turn fed to the most significant byte of the 16 bit D/A converter. The larger than window and the less than window conditions decrements and increments, respectively, the value in the counter. Since the polarity of the input potential and the output from the D/A converter is opposite, the circuit seeks to keep the added signals within the window. Thus, the value held in the counter reflects the digital value for the analog input potential. The value in the counter is available for addressing the memory blocks (Vref address) together with the clock pulses (Strobe) that effect counting up the content of the addressed word.

Since only the most significant byte of the 16 bit D/A converter is used, the digital values are accurate within 1/256 bit (instead of ± 1 bit for an 8 bit converter). One bit corresponds to the size of a single potential interval, that is typically 2 to 3 mV. Thus, the potential intervals giving rise to adjacent digital values are effectively of the same size, and the relation between input

voltage and digital value is *strictly* linear. This is one of the advantages of this circuit compared to the A/D converters of the successive approximation type that has been used in previous implementations where a 12 bit converter has covered the potential range −2047 to 2048 mV, with one bit corresponding to 1 mV [5,6]. For those, the relation between input voltage and digital value is monotonous and only linear *on average*, and a small and a large potential interval next to each other may give two adjacent digital values. When applied for the data acquisition scheme in which the results of many A/D conversions are accumulated, this situation will create a pair of spikes on the signal. The count corresponding to the small potential interval will be low whereas the count resulting from the large interval will be high compared to the values in the surrounding channels. Such spikes are often at first mistaken for random noise, but they occur systematically at the same positions in the signals. Usually, they have been averaged out either by simply merging 4 to 8 data points or by smoothing the signal, for instance by an N-point moving average routine; in both cases at the cost of resolution.

Another advantage of the track and follow principle is that it better suppresses high frequency random noise superimposed upon the input signal. Due to the way that the converter works, the result of a new conversion is at most changed by ± 1 relative to the previous one. If a noise pulse is present at the time where an A/D conversion takes place, the outcome will only be marginally offset relative to the undisturbed result, and the count will be accumulated in immediate vicinity of the true location. For an A/D converter of the successive approximation type, the outcome of an conversion is completely independent of the previous one, and the presence of a noise pulse at the moment of conversion may offset the location where the count is accumulated by several channels. Thus, inherently smoother signals are obtained by use of a track and follow type converter. The implicit disadvantage of the conversion method is that abrupt changes in the input signal are not handled very well because a number of conversions following a discontinuous change will be erroneous, before the converter catches up with the signal. In this application, problems of that kind are not actual because the potential–time transients are by nature continuous. The proper condition at start is ensured by always letting the converter sample the electrode potential. The data acquisition mode, in which the conversions are accumulated, is entered by enabling the clock pulses to get through to the memory module (Strobe, in Fig. 2).

2.3. Timing of data acquisition

Accurate timing of the voltammetric and amperometric methods is obtained by means of the 2 MHz clock and the timer circuit (Intel 8253) with three 16 bit counters available at the PCL-812 card. Two of the counters are cascaded and pre-defined for pacing the A/D converter whereas the third one is not reserved for any internal use. A block diagram of the configuration chosen for this application is shown in Fig. 3 together with an illustration of the transformation of pulses through the system. The clock pulses are fed to Counter 2 and the output pulses are used as input for Counter 1 which in turn triggers the A/D converter. Both counters operate in the Rate Generator mode [7], repeating a sequence in which the output goes low for one period of the input pulses when a preset number of pulses have been counted. Counter 0 has been setup to count the pulses that triggers the converter and its output is fed to a DI port such that the state can be sensed by the PC.

The sampling period, that is the time between output pulses from Counter 1, is a convenient time measure and in the pulsed voltammetric techniques, the duration of delay and sampling periods is specified in terms of this unit. The number of current samples accumulated thus equals the length of the sampling period. In these techniques, Counter 0 operates in the mode called Interrupt on Terminal Count [7] in which the output goes low when the count (N) is loaded and goes high after N input pulses have been counted. This is utilized for timing of delays and allows the PC to do other things in the meantime, such as process previously acquired data and display it in real-time. After fulfilling these tasks,

the PC waits for the state of Counter 0 to change and then proceeds.

In linear sweep voltammetry and the amperometric techniques, a certain number of evenly distributed data points has to be acquired. In these cases, Counter 0 functions as a rate generator and each output pulse marks the beginning of a new sampling period. This allows the A/D converter to operate at a higher rate such that each data point can be generated as the average of several conversions. Again, the time from the end of one sampling period to the beginning of the next is available for the PC to do other tasks without loosing track of time.

2.4. Software

The software is written in TurboPascal (version 5.0, Borland) which executes fast enough that even at the maximum A/D conversion rate (30 kHz) data can be transferred to memory under program control.

The program is organized with a main selection bar and several curtain submenus underneath. The items in the submenus represent separate functions which in most cases communicate through pop-up windows.

An exception from this is the Command Mode in which the program accepts commands from the keyboard in one of three independent windows; the others are used for display of signals and for reporting the results of various data processing routines, respectively. Each of the windows may be cleared or dumped to the printer separately. More than seventy different commands are recognized and the corresponding tasks executed in this mode. Some commands are device-related and communicate with the EM, perform data acquisition, time delays, or control the optional devices shown in Fig. 1; some process the signals and facilitate addition and subtraction of signals, search for peak positions, calculation of a linear backgrounds underneath peaks, integration within specified limits, accumulation of data for statistical treatment, and n-point moving average or

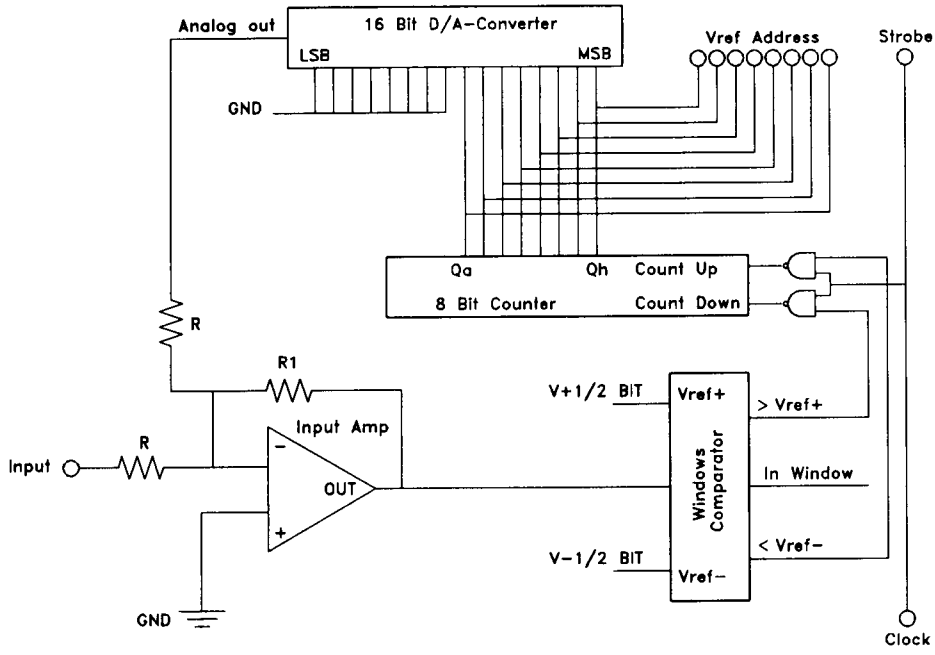

Fig. 2. Schematic diagram of the track and follow A/D converter used for data acquisition in the stripping potentiometric techniques.

Savitzky-Golay smoothing [8–10] of the signals. Other commands are graphics-related and control the display of signals on either screen or plotter and the cursor system implemented for signals displayed at the screen. A few commands control the program flow, for instance allowing the commands bracketed by two of them to be executed the number of times specified or the commands grouped in a macro to be carried out.

The main idea behind this system is to keep the commands and the tasks they perform simple and well-defined. The cost is that several commands have to be executed to perform more elaborate procedures but since a sequence of commands may be gathered in a command macro, the disadvantage is minimal. More complex experiments that, for instance, involve control of valves or the sample carousel and timing of various delays are defined as command macros which makes it easy to accommodate new experiments or to change existing ones. The data processing performed on the signals may be customized by means of a command macro such that the extend and the level of automation suit the circumstances. Because most of the commands allow arguments to be specified in terms of user-defined parameters, key parameters are readily changed without editing the command macro. A command structure based on the same principles has been described previously [5] (with examples of macros defining experiments and data processing) such that the merits in terms of flexibility and applicability for both research and routine work are well-proven.

Other facilities presented on the main menu include functions that maintain the command macros, define parameters for the techniques implemented, handle the storage or retrieval of signals from files, calculate various statistics for data accumulated during series of measurements, and customize the default parameters for graphic output, data buffer size, peak search, and smoothing. Finally, the program may be customized to work with different hardware such that it is portable.

The command macros are edited in a full screen editor and are saved as ordinary ASCII files. Once edited, they are interpreted to check for errors and to store them internally in a ready-for-use format. Ten different macros may be loaded at a time and each one is assigned to a function key for easy access in Command Mode.

Seven different techniques are currently implemented which include two potentiometric (constant current chronopotentiometry, CCC, and potentiometric stripping analysis, PSA), three voltammetric (linear sweep voltammetry, LSV, differential pulse voltammetry, DPV, and square-

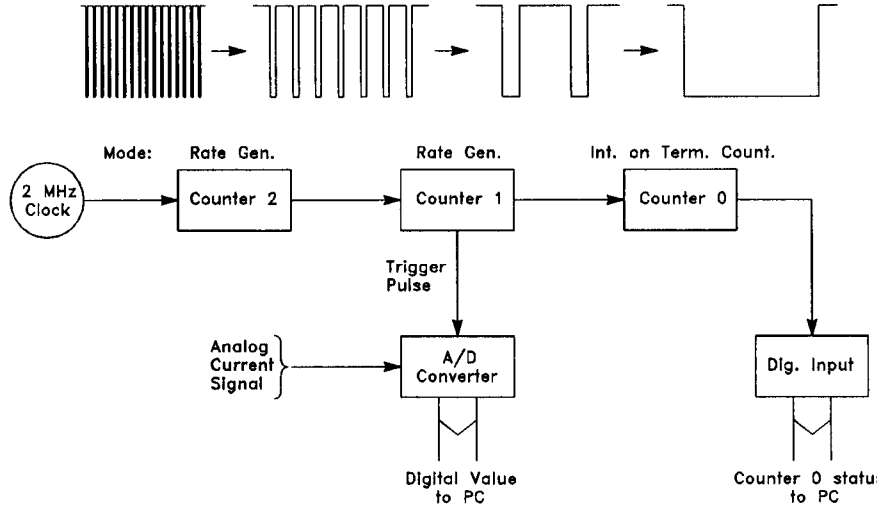

Fig. 3. Configuration of the clock and counters used for timing of voltammetric and amperometric techniques. The transformation of the clock pulses through the system is also indicated.

wave voltammetry, SWV), and two amperometric (standard amperometry, AMP, and pulsed amperometric detection, PAD). The parameters defining each technique exactly are adjusted in windows where all parameters are labelled and their present values shown. Furthermore, one set of parameters intended for reference by command macros are completely user-defined such that labels, minimum and maximum values accepted, and of course, the values may be edited.

Signals are stored on binary files together with a record containing information on type, date and time of acquisition, amplification, and minimum and maximum values. Signals may be stored sequentially as they are measured or individually from the memory buffers in which they are acquired. On the file, signals occupy the full size of the memory buffer even if it is only partly used. This permit signals to be retrieved non-sequentially such that the operator may browse the signals on a file and only transfer the ones of interest to the memory buffers. Finally, signals may be exported to or imported from ASCII files which allow easy data exchange with other programs.

Data reported as results of peak searches, integrations, etc., during series of measurements may be accumulated in a data buffer for later statistical treatment. At the time of processing, the raw data is read and a final report with the tabulated data and calculated statistics is generated for documentation of the experiment. The statistical treatment available include calculation of mean and standard deviation, linear regression assuming either constant errors or constant relative errors on the Y values, and determination of sample concentrations and the corresponding confidence intervals by the standard addition method [11,12] or by means of a calibration line.

2.5. Electrochemical experiments

Pb in water

Determination of Pb in samples of deionized and tap water by means of PSA were carried out using a rotating disc electrode (1500 rpm, Metrohm 628) with a glassy carbon tip, a saturated calomel reference (SCE, Radiometer K422), and a Pt-flag counter electrode (Radiometer P101). HCl (suprapure, Merck) and Hg(II) (1000 ppm Hg(II) in 2.5% HNO_3, Spectrascan) were added to the samples to a final concentrations of 7.5×10^{-2} M and 1×10^{-4} M, respectively, in order to adjust pH and provide mercury for the in situ generation of the film. The samples were not deaerated such that Pb was reoxidized during the stripping step by oxygen and mercury in combination.

The PSA experiments were initiated by a 60 s deposition step at -812 mV followed by acquisition of the main signal. Next, the potential was adjusted to -100 mV for 1 s and to -812 mV for 0.1 s after which the background signal was acquired and the potential adjusted to the rest potential, -100 mV. The sampling frequency during the stripping steps was 667 kHz and the cut-off potential was -300 mV, i.e., the signals were acquired with a resolution of 2 mV.

For comparison, PSA signals were also acquired by use of an older instrument described previously [4] utilizing a 12 bit A/D converter of the successive approximation type with 1 mV resolution of the potential transients. The signals recorded by this instrument were obtained using the parameters just described, but pairs of data points were merged such that the final resolution was 2 mV.

After stable PSA signals had been obtained with the old instrument, the electrodes were rapidly connected to the new instrument and the measurement repeated. Subsequently, the content of Pb in the sample was quantitated by adding small volumes of a 1 or 10 ppm Pb standard (prepared by diluting a 1000 ppm stock solution, Titrisol, Merck). For each addition, a series of four measurements were performed in which the background was subtracted from main signal and the net areas of the Pb stripping peaks used as analytical responses. Typically, the first of these was systematically less than the following and only the last three were accumulated for statistics.

Pb in salt

The concentration of Pb in two different samples of salt were determined in stripping mea-

surements using DPV, SWV and CCC for acquisition of the signals. The samples were sea salt produced from sea water at the Atlantic Coast in Brittany, France (imported by Dansk Helios AMBA, Fredericia, Denmark) and refined salt produced in Germany (imported by Dansk Salt I/S, Mariager, Denmark). The analytical procedure was based on a method for determination of trace elements in high purity materials recently described [13]. The samples were dissolved in high purity deionized water (Milli-Q water, Millipore). Since the sea salt contained some insoluble matter (presumably clay) and was rich in Pb, these samples contained 100 g/l salt whereas the refined salt was analyzed at a concentration of 150 g/l. The CCC experiments were performed at a concentration of 50 g/l for both samples. Ascorbic acid (L(+)-form, extra pure fine powder, Merck) was added to the samples to a final concentration of 2.8×10^{-2} M together with Hg(II) from a stock solution (1000 ppm in 2.5% HNO_3, Spectrascan) for in situ generation of the mercury film. The amount of Hg(II) varied according to the deposition time expected for the specific samples such that lower concentrations were used for samples requiring longer electrolysis times. Due to the ascorbic acid and the nitric acid added with the Hg(II), the pH was lowered to between 1.5 and 3 in the samples. The samples were deaerated by high purity argon prior to analysis.

The electrodes were similar to the ones described above except that the working electrode was rotated at 2000 rpm and the calomel electrode was a Radiometer K401.

A measurement cycle consisted of a deposition step at −900 mV for 10 to 300 s; then the electrode rotator was turned off and the solution allowed to equilibrate for a 15 s period. Next, the stripping signal was recorded by use of DPV, SWV or CCC followed by a 10 s rest period at the final potential of the applied technique. DPV was performed with a pulse height of 25 mV and a base potential increment (step height) of 2 mV. The delay and sampling periods were 30 and 20 ms, respectively, both at the base potential and with the pulse applied, i.e., the effective scan rate was 20 mV/s. The scan was stopped at −150 mV. The SWV operated with a pulse height of 25 mV, a step height of 5 mV, and delay and sampling periods of 5 ms which resulted in an effective scan rate of 250 mV/s. The final potential was −250 mV. CCC was performed with a sampling rate of 800 kHz, a 2 μA oxidation current, and a cut-off potential of −314 mV.

The concentration of Pb was determined by the standard addition method with three measurement cycles in series performed at each concentration. Two additions, each approximately corresponding to the initial Pb concentration in the cell, were added from standards (40 μg/l or 4 mg/l) prepared from the stock solution mentioned above. The stripping peaks were fitted with linear backgrounds underneath and the net areas taken as analytical responses.

Flow-injection analysis of carbohydrates

The carbohydrates were detected amperometrically at a Cu electrode in a simple FIA system. The flow system consisted of an Eldex AA100 HPLC pump equipped with a LiChroma pulse dampener (both Mikrolab, Aarhus, Denmark), the injection valve with a 20 μL sample loop, and a BAS flow cell (Bioanalytical Systems) to which a home-made Cu working electrode mounted in PTFE was fitted. The reference electrode (Radiometer, K422) was placed behind an extra salt bridge with saturated KCl to protect it from the mobile phase, which was 0.10 M NaOH prepared from a 50% stock solution (J.T. Baker) and thoroughly degassed, deionized water. A flow rate of 0.50 ml/min and a detection potential of +500 mV were applied throughout. The injection valve was automatically loaded from the sample carousel and flushed with deionized water between samples by means of a peristaltic pump. Three injections of each sample were carried out, and the net areas above fitted linear backgrounds were used as analytical responses. The samples tested were standards of D(+)-glucose (Merck), D(+)-galactose (Aldrich), D(+)-mannose (Aldrich), D(+)-glucuronic acid (Sigma), and D(+)-galacturonic acid (Aldrich), all made up in the mobile phase.

The voltammograms of the Cu electrode were recorded in a batch cell filled with the 0.10 M

NaOH solution. Cyclic LSV scans were initiated at 0 mV, switched at +700 mV, and progressed at a scan rate of 50 mV/s. After a stable voltammogram had been obtained in the pure base, spikes giving final concentrations of 3.0×10^{-4} and 5.6×10^{-4} M of glucose were added and new voltammograms recorded.

3. Results and discussion

3.1. Pb in water

In order to evaluate the performance of the data acquisition method for potentiometric signals, identical PSA experiments were performed by use of the instrument described here and an older apparatus [4] which utilized an A/D converter of the successive approximation type. Although the instrumental resolution of this was 1 mV, data points were merged to give a resolution of 2 mV comparable to the one obtained with the new instrument. The other parameters defining the data acquisition were identical and both converters operated at a sampling rate of 667 kHz. The procedure followed was such that the mercury film was generated in situ on the glassy carbon electrode by means of the old apparatus by running consecutive experiments until a stable reading was obtained. Then the electrodes were rapidly connected to the new instrument and the experiment repeated. Following that, the content of lead in the sample was determined by the standard addition method.

Two such comparisons were performed with samples of deionized and tap water. The stripping signals obtained are shown in Fig. 4. The signals A1 and A2 were recorded in the sample of deionized water using the old and the new instrument, respectively, whereas B1 and B2 signify the corresponding signals obtained in the tap water sample. The net areas of the peaks amounted to 1.15 ± 0.03 ms and 11.2 ± 0.2 ms (average and standard deviation for $N = 3$ consecutive measurements) for the deionized and tap water sample, respectively. The Pb contents of these two samples were found to be 1.85 ± 0.13 μg/l and 18.7 ± 1.4 μg/l (95% confidence intervals, $N = 9$); the sensitivities were identical within the standard deviations, 0.61 ± 0.02 ms $\times$ $(\mu g/l)^{-1}$ and 0.59 ± 0.03 ms $\times (\mu g/l)^{-1}$ respectively, and the correlation coefficients, $R^2 =$ 0.9997 and 0.9992, respectively, indicated a highly linear relationship between response and concentration.

It is evident that smoother signals are obtained if the potential–time transients are sampled by an A/D converter working according to the track and follow rather than the successive approximation method. Even though pairs of data points were merged, the spikes, that stemmed from uneven potential intervals leading to the different digital values, dominated the stripping signals recorded by means of the successive approximation type converter. That the spikes were not random noise was indicated by the fact that they appeared at the same positions in different signals. In a realistic application, the signal would either be smoothed or more data points merged in order to average out the spikes. Thus, the resulting resolution would be less than the 2 mV easily obtained by use of the track and follow converter. This is of importance in more fundamental studies, for instance where shape and position of the peaks are related to kinetics and equilibrium conditions, respectively, of reactions between the newly stripped metal ions and a complexing agent in the medium. If experimental signals are to be compared with those generated from a simulation model, smooth signals with high resolution on the potential axis are highly desirable. For analytical applications, where the signal typically is integrated across the peak to obtain the response, the importance of the spikes is limited and mostly is a matter of aesthetic.

3.2. Pb in salt

Determination of traces of heavy metals in samples containing high concentrations of salts is one type of analysis for which the electrochemical stripping methods are well-suited. Recently, Naumann et al. [13] published a procedure for determination of trace elements in high purity materials by means of anodic stripping voltammetry. The investigation focused on the analysis of trace

elements in suprapure salts and used a classical, slow scanning differential pulse waveform for recording the signals. This raised the question whether faster sampling techniques could be applied for this application without loss of precision and accuracy. Thus, two types of household salt, a sea salt and a refined salt, differing widely in Pb contents were analyzed by means of slow scanning DPV, fast scanning SWV, and CCC. The DPV used here was comparable to the technique applied in [13] and progressed at a scan rate of 20 mV/s while the SWV scans were performed at 250 mV/s. An oxidation current of 2 μA was used for effecting the stripping process in CCC and the potential–time transient was sampled at 800 kHz.

The specific conditions for analysis of the samples by the different techniques are shown in Table 1A. The concentrations of NaCl and Hg(II) together with the typical Pb content in the solutions analyzed are indicated. Furthermore, the deposition times are given. In preliminary CCC experiments conducted at the high salt concentrations used for the voltammetric methods, it was found that the equilibrium potential of the working electrode (determined by the Hg|Hg(II),Cl^- redox pair) was cathodic to the stripping potential of Pb. Consequently, determinations using CCC were performed at a lower concentration for both samples.

The final Pb concentrations found in the two samples as function of the detection technique

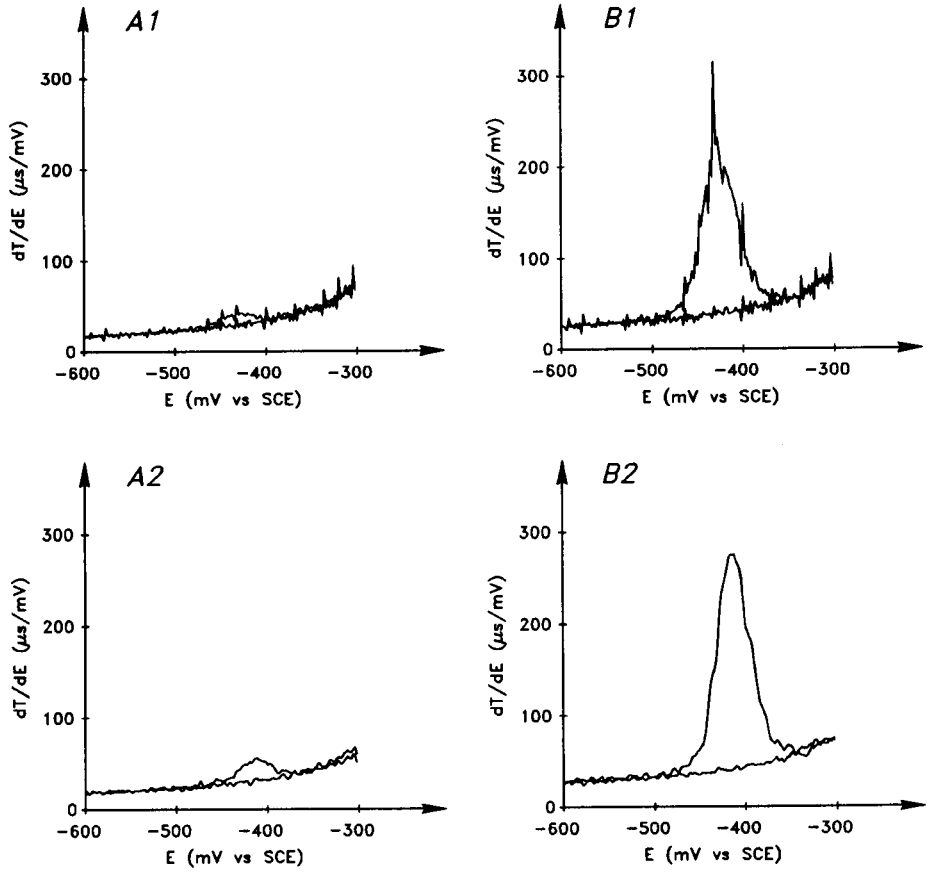

Fig. 4. PSA signals recorded in samples of deionized (A1 and A2) and tap (B1 and B2) water by use of an older apparatus (A1 and B1) and by the improved method (A2 and B2). Electrolysis at −900 mV for 60 s; sampling rate, 667 kHz.

are given in Table 1B as the average and standard deviation of several determinations. The relative standard deviation (R.S.D.) and the number of independent experiments are also displayed together with the total analysis time. The last figure is the time necessary to go through the 3×3 measurement cycles, that is the time used for adding the spikes is considered negligible. As expected the Pb contents of the two samples were very different; the amount found in the refined salt was actually at the level of suprapure chemicals (Merck guaranties maximum 10 μg/kg for the suprapure NaCl).

It is evident from the table that when precision of the results is addressed, SWV is superior to the other techniques giving a R.S.D. of less than 2% even for the very low concentrations of Pb found in the refined salt. With respect to accuracy, the SWV results are most trustworthy even though the results obtained with the two other techniques are in accordance. Three observations supports this conclusion. First, the reproducibility of the three signals measured on each concentration level of standard addition was best for SWV. Second, the sensitivity was observed to decrease slightly during the DPV experiments thus giving rise to a systematic overestimation of the Pb content. Third, even though the CCC experiments were performed at lower salt concentrations, the equilibrium potential of the working electrode was still fairly close to the stripping potential of Pb which meant that the stripping signals were situated on a large, curving background. Estimation the peak area by means of a fitted linear background, as done here, might not be feasible in that situation. If this was the case, as indicated by the systematic deviation from the SWV figures, or the CCC results simply reflected the inherent uncertainty of quantifying a small signal on a large background was not investigated further. To sum up, it seems that the data acquisition technique giving the shortest analysis time is also the one best suited for the particular application. Furthermore, this example demonstrates the utility of having several techniques, preferably both voltammetric and potentiometric, available when developing new analytical procedures.

Table 1
Determination of Pb in samples with high salt content

A: Conditions

Sample	Technique	NaCl conc. (M)	Hg(II) conc. (10^{-3} M)	Deposition time (s)	Pb conc. in sol. (μg/l)
Sea salt	DPV	1.71	0.0 [a]	10	35
	SWV	1.71	0.59	10	26
	CCC	0.86	0.67	20	18
Refined salt	DPV	2.57	0.13	300	0.3
	SWV	2.57	0.25	180	0.23
	CCC	0.86	0.27	240	0.14

B: Results

Sample	Technique	Pb conc. in salt (μg/kg)	R.S.D. (%)	No. of determ.	Analysis time (min)
Sea salt	DPV	352 ± 9	2.6	4	10.8
	SWV	294 ± 2	0.6	3	5.6
	CCC	338 ± 9	2.8	4	7.8
Refined salt	DPV	2.0 ± 0.2	9.5	3	54.3
	SWV	1.60 ± 0.03	1.8	3	31.1
	CCC	2.6 ± 0.3	12	4	39.9

[a] Mercury film prepared ex situ by 140 s electrolysis in 0.65×10^{-3} M Hg(II) solution.

3.3. Flow-injection analysis of carbohydrates

The possibility to build analytical procedures operating automatically by means of the command macros was demonstrated for the flow system shown in Fig. 5A, intended for FIA of carbohydrates. The carbohydrates are catalytically oxidized at the oxide-layer formed on Cu electrodes in strong base [14–16] which is demonstrated by the cyclic voltammograms displayed in Fig. 5B. Here, a Cu electrode was scanned in a batch cell filled with 0.10 M NaOH until a stable voltammogram was obtained (trace 1); next, spikes of glucose were added to final concentrations of 3.0×10^{-4} and 5.6×10^{-4} M and new voltammograms were recorded (traces 2 and 3, respectively). Glucose was oxidized over the potential range +300 to +700 mV with the highest net currents around +450 mV. Thus, a Cu electrode held at a potential close to +450 mV was well-suited for amperometric detection of carbohydrates in the FIA system.

The responses of several carbohydrates at the 5.0×10^{-5} M level relative to glucose was investigated at an operating potential of +500 mV. A series of standards were loaded from the sample

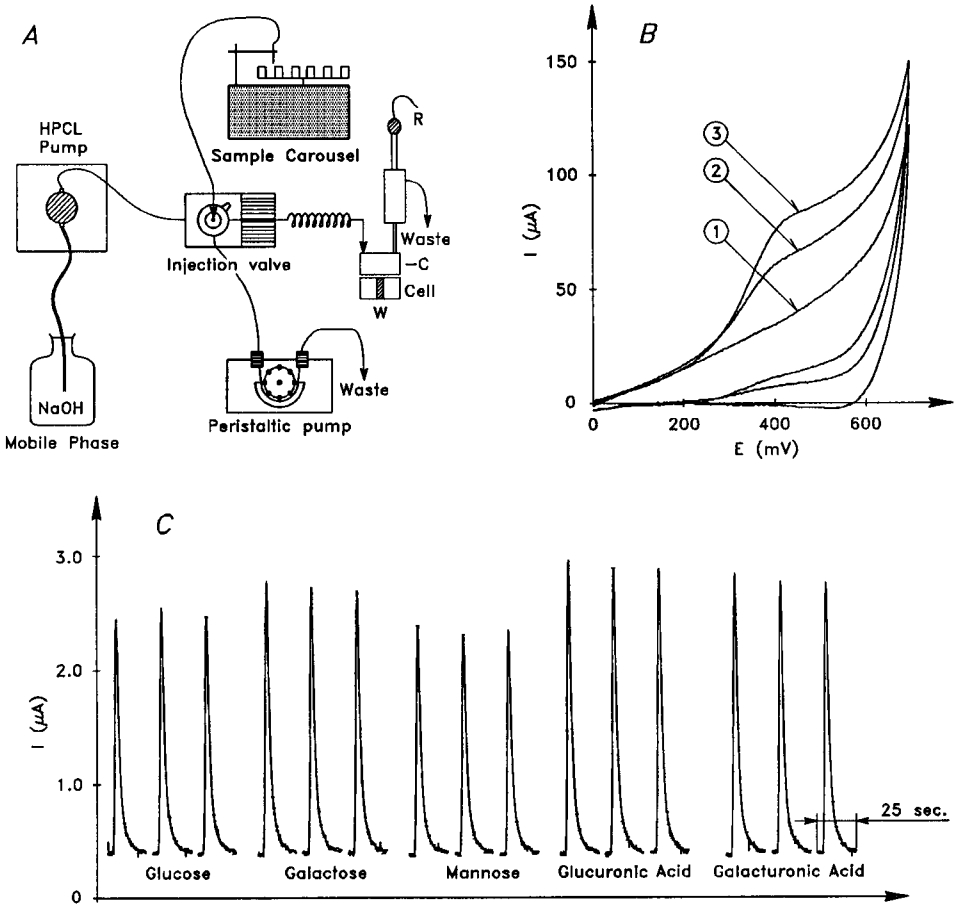

Fig. 5. (A) Flow injection system used for automated determination of carbohydrates. (B) Voltammograms of the Cu electrode in pure 0.10 M NaOH (trace 1) and following addition of 3.0×10^{-4} M (trace 2) and 5.6×10^{-4} M (trace 3) glucose. Scan rate, 50 mV/s. (C) FIA signals for a series of carbohydrates at the Cu electrode. Mobile phase, 0.10 M NaOH; concentration of standards, 5×10^{-5} M, potential, +500 mV.

Table 2
Relative responses for carbohydrates

Substance	FIA at Cu electrode			Anthrone
	Mean	S.D.	*N*	
Glucose	1.00			1.00
Galactose	1.14	0.07	4	0.06
Mannose	0.91	0.03	5	0.52
Glucuronic acid	1.10	0.13	5	0.06
Galacturonic acid	1.07	0.09	5	0.06

carousel and injected in triplicate. For each amperometric signal, a linear background was fitted underneath, and the net area accumulated for statistical analysis. One such series for glucose, galactose, mannose, glucuronic acid and galacturonic acid is shown in Fig. 5C and the relative responses as results of several independent measurements are listed in Table 2. The linearity of the responses was checked by running series of five calibration standards in the 2 to 40 mg/l range for the five carbohydrates, again with injections in triplicate, and accumulating the data for regression analysis. For thirty calibration runs measured unattended, the average R.S.D. of the sensitivity, estimated by linear regression, was 1.7%. The strict linearity was also indicated by the correlation coefficients: Only one value of R^2 was less than 0.99 while 25 were better than 0.996.

The significance of this method is clear when it is noted that the total saccharide content of activated sludge is a quality parameter for biological waste water treatment plants. The polysaccharides produced and excreted by bacteria are thought to be of essential importance for the flocking ability and thus the settling properties of the sludge. In turn, these factors influence both the final quality and the costs of the process because they determine how well and how fast the sludge can be separated from the purified waste water. Horan and Eccles [17] investigated the bacterial exopolysaccharides from five different treatment plants and found them to be composed of the five monosaccharides mentioned here, and that the content of uronic acids varied from 6 to 30%. They also noted that the total carbohydrate content was systematically in error when glucose was used for calibration of the phenol/sulphuric acid assay applied. Research conducted in this laboratory [18] has shown the same to be the case for the colorimetric anthrone method [19] used sofar. The relative responses to glucose for the other carbohydrates by use of this method are also shown in Table 2 and clearly indicate that the total carbohydrate content is grossly underestimated if glucose is used for calibration. On the other hand, the equimolar responses obtained at the Cu electrode vary at most 15% relative to glucose and thus this method provides a better means for determination of the total carbohydrate content of the samples.

Acknowledgements

Financial support from the Danish Technical Research Council (grant No. 16-4789K) is gratefully acknowledged. M.E.R.D. acknowledges support from the Norwegian Research Foundation.

References

[1] D.C. Johnson and W.R. LaCourse, Electroanalysis, 4 (1992) 367.
[2] J. Mortensen, E. Ouiziel, H.J. Skov and L. Kryger, Anal. Chim. Acta, 112 (1979) 297.
[3] H.J. Skov and L. Kryger, Anal. Chim. Acta, 122 (1980) 179.
[4] B. Høyer, H.J. Skov and L. Kryger, Anal. Chim. Acta, 188 (1986) 205.
[5] K.N. Thomsen, H.J. Skov and L. Kryger, Anal. Chim. Acta, 219 (1989) 105.
[6] P. He and L.R. Faulkner, J. Electroanal. Chem., 224 (1987) 277.
[7] PCL-812 Enhanced multi-lab card, Users Manual, Advantech Co., Ltd.
[8] A. Savitzky and M.J.E. Golay, Anal. Chem., 36 (1964) 1627.
[9] J. Steinier, Y. Termonia and J. Deltour, Anal. Chem., 44 (1972) 1906.
[10] P.A. Gorry, Anal. Chem., 63 (1990) 570.
[11] J.P. Franke, R.A. de Zeeuw and R. Hakkert, Anal. Chem., 50 (1978) 1374.
[12] M.J. Gardner and A.M. Gunn, Fresenius' Z. Anal. Chem., 325 (1986) 263.
[13] R. Naumann, W. Schmidt and G. Höhl, Fresenius' J. Anal. Chem., 343 (1992) 746.

[14] S.V. Prabhu and R.P. Baldwin, Anal. Chem., 61 (1989) 852.
[15] S.V. Prabhu and R.P. Baldwin, Anal. Chem., 61 (1989) 2258.
[16] P. Luo, S.V. Prabhu and R.P. Baldwin, Anal. Chem., 62 (1990) 752.
[17] N.J. Horan and C.K. Eccles, Water Res., 20 (1986) 1427.
[18] K. Keiding, Env. Eng. Lab., Aalborg University, personal communication.
[19] R. Dreywood, Ind. Eng. Chem., 19 (1946) 449.

ELSEVIER

Analytica Chimica Acta 293 (1994) 19–28

ANALYTICA CHIMICA ACTA

Determination of vanadium in sea water by catalytic adsorptive cathodic stripping voltammetry

Marisol Vega [1], Constant M.G. van den Berg *

Oceanography Laboratories, University of Liverpool, Liverpool L69 3BX, UK

(Received 17th December 1993; revised manuscript received 8th February 1994)

Abstract

The sensitivity of adsorptive cathodic stripping voltammetry (CSV) to vanadium is much improved by inclusion of a catalytic effect. The deposition step is based on the adsorptive accumulation of complex species with catechol on a hanging mercury drop electrode. The reduction current of the adsorbed complex is catalytically enhanced by addition of bromate. This effect is utilised to develop a sensitive method to determine vanadium in natural waters including sea water. Optimum response was obtained at pH 6.6 in the presence of 20 mM bromate and 0.1 mM catechol; the deposition potential was −0.1 V and the square-wave modulation (50 Hz) was used. The limit of detection was 0.07 nM vanadium using a deposition time of 120 s and 0.6 nM at a deposition time of 15 s.

Key words: Catalytic methods; Stripping voltammetry; Sea water; Vanadium; Waters

1. Introduction

Adsorptive cathodic stripping voltammetry (CSV) is a useful method to determine trace elements in natural waters combining excellent sensitivity, selectivity, accuracy and precision with low cost of instrumentation and maintenance. Applications of CSV and its potential for natural water analyses have recently been reviewed [1].

Vanadium occurs in sea water in a concentration range from 10 to 40 nM, with average levels of ~32 nM [2,3]. Several methods have been proposed for the determination of vanadium in natural waters, most of which require prior preconcentration steps (without a prior preconcentration step such as requiring the use of ion-exchange or co-precipitation) which prolong the analysis duration and increase the risk of sample contamination or loss of analyte. Adsorptive stripping procedures allow the determination of various trace elements directly in untreated sea water, leading to short analysis times and subnanomolar to picomolar detection limits. This method was therefore used to develop a sensitive procedure to determine vanadium in sea water.

The principle of adsorptive CSV is the measurement of the reduction current of either the element or the ligand preceded by adsorptive collection on the electrode surface of a complex of the element with an added specific ligand [1].

* Corresponding author.

[1] Permanent address: Department of Analytical Chemistry, University of Valladolid, 47006 Valladolid, Spain.

SSDI 0003-2670(94)00088-4

Several ligands including catechol [4], 5-Br-PADAP [5,6] and solochrome violet RS [7] have been used to accumulate vanadium as complexes by adsorption on the mercury electrode surface. It has been shown that vanadium can be determined successfully in sea water using one of these (catechol), but the sensitivity is not great and accurate analyses would require a deposition time of several minutes.

The CSV sensitivity can be increased greatly by the inclusion of a catalytic effect; this has been shown to work for several elements when the reduction step involved only one electron [1] and has been used with good advantage for the determination of titanium [8], iron [9], chromium [10,11] and platinum [12] in sea water. The reduction of vanadium in the presence of catechol involves a single electron reduction step from V(V) to V(IV) and its catechol complex is adsorbed on the mercury drop electrode [4]; it is therefore a good candidate for catalytic CSV.

It has been claimed that "ultra trace levels" of vanadium can be determined by catalytic CSV preceded by adsorptive collection of its complex with cupferron [13] giving a peak at ~ -0.1 V. The stated reduction potential is unexpectedly positive as the reduction potential for uncomplexed vanadium is situated at a more negative potential at ~ -0.3 V [4]. One would expect the complexed peak to be located at a more negative potential rather than at a more positive potential due to a combination of complex stabilisation and adsorption stabilisation. The potential of the peak would in any case preclude the application of this method to solutions containing chloride due to a negative shift of the mercury wave which causes a large background current at potentials > -0.05 V in sea water. During preliminary experiments using cupferron and vanadium using the published conditions [13] we were not able to reproduce the vanadium peak in either pure water or sea water; a peak which looks similar to that shown for vanadium could be produced by allowing a small amount of dissolved oxygen to diffuse into the deaerated solution, suggesting that the oxygen peak may have been erroneously identified as a reduction peak of vanadium. A vanadium peak could be obtained in the presence of cupferron at much enhanced vanadium levels (100 nM) at the more negative potential of -0.7 V without analytical usefulness as the sensitivity is poor.

We therefore set out to improve the voltammetric determination of vanadium in the presence of catechol by the inclusion of a catalytic effect which is reported in this paper. Several ligands (catechol, salicylaldoxime, tiron, 4-(2-pyridylazo)resorcinol (PAR), 1-(2-pyridylazo)-2-naphthol (PAN), *N*-benzoyl-*N*-phenylhydroxylamine and cupferron) and oxidants (bromate, chlorate and perchlorate) were tested, but only the successful results obtained in the presence of catechol and bromate are reported.

2. Experimental

2.1. Apparatus and reagents

The voltammetric experiments were carried out with an Autolab PSTAT10 voltammeter (Eco Chemie) connected to a Metrohm 663VA hanging mercury drop electrode (HMDE). The reference electrode was Ag/saturated AgCl/3 M KCl and the counter electrode was a Pt rod. Solutions in the voltammetric cell where stirred by a rotating PTFE rod. The potentiostat was controlled by an IBM-AT compatible computer (286 Intel processor) using a compiled BASIC programme (GPES31 from Eco Chemie). The mercury was triple-distilled and the drop size of the HMDE was 0.31 mm^2. pH values were determined with a Metrohm 605 pH meter and a Metrohm combined glass pH electrode.

A stock solution of 10^{-4} M vanadium(V) was prepared by dilution of BDH standard solution (1000 mg/l) for atomic absorption spectroscopy, and acidified with 10 μl of 11.4 M hydrochloric acid per 10 ml solution. An aqueous stock solution of 1 M PIPES (piperazine-*N*,*N*′-bis(2-ethanesulfonic) acid, from Sigma) was prepared by dissolution of its monosodium salt in 0.5 M ammonia hydroxide (BDH, AristaR grade). Addition of 200 μl of the PIPES solution to 10 ml sea water gave a pH of 6.6. Stock solutions of 0.2 M potassium bromate (BDH, AnalaR) and 0.1 M

catechol (BDH, AnalaR) were prepared by dissolving the respective compounds in water. Water used for dilution of the reagents and for rinsing of sample containers and the voltammetric cell was purified by reverse osmosis (Milli-Ro) and deionisation (Milli-Q). A mixed reagent solution containing 1 mM catechol and 0.2 M potassium bromate in 200 ml water was heated and boiled (180 s) in a microwave oven; the resultant solution was pink coloured due to oxidation of the catechol to orthobenzoquinone.

Sea water used for the optimisation experiments originated from the Menai Straits (Irish Sea). This sea water was UV-digested (3 h) using a 1000-W UV lamp in the presence of 9 mM hydrogen peroxide to remove potentially interfering surface active compounds. Vanadium and other metals present as traces in the sea water were removed by passing the UV-digested sea water through a column packed with ca. 3 ml Chelex-100 resin (in the ammonium form) at a flow rate of 1 ml/min to produce sea water with a low vanadium level; this sea water was used for the determination of the limit of detection of vanadium and for other experiments where indicated.

2.2. Procedure to determine vanadium in sea water

An aliquot of 10 ml of sea water was pipetted into the voltammetric cell and 1 ml of the mixed reagent solution was added giving final concentrations of 10^{-4} M catechol and 0.02 M bromate. The pH was adjusted to 6.6 by addition of 200 μl of the 1 M PIPES buffer, and the solution deaerated by purging with water-saturated nitrogen (3 min). A new mercury drop was extruded and the deposition potential was set to -0.1 V for a period of 15 s, whilst the solution was stirred at 2500 rpm. Then the stirrer was stopped and the potential was set to -0.4 V for a period of 10 s, whereafter the potential was scanned towards more negative potentials using the square-wave modulation. Scan parameters were: square-wave frequency: 50 Hz; square-wave amplitude: 25 mV; potential step: 2.4 mV (scan rate, 120 mV s^{-1}). A peak corresponding with the catalysed reduction of vanadium appeared at -0.74 V. The peak height (nA) was used as a measure of the reduction current. Each measurement was repeated at least twice; the measurements were repeated again after standard additions of vanadium to the sample to calibrate the CSV sensitivity and check for linearity of response.

3. Results and discussion

3.1. An investigation into the catalytic adsorptive stripping process

Preliminary experiments on CSV of vanadium in the presence of catechol in pH 6.6 sea water indicated the presence of a vanadium peak at ~ -0.7 V due to the reduction of vanadium(V) in the adsorbed complex of vanadium with catechol to vanadium(IV) [4]. The sensitivity was much improved by the addition of up to 20 mM bromate to the solution causing the peak current to increase and the peak potential to shift towards more negative potentials (details given below). Repeated measurements of the CSV peak height of vanadium in the presence of 20 mM bromate and 0.1 mM catechol preceded by 15 s deposition at -0.1 V revealed that the peak height was unstable in presence of the bromate, increasing gradually with time at a constant concentration of vanadium, reaching a further four-fold magnification over a period of 2 h. The effect could be accelerated and brought to completion by preparing a mixed reagent solution containing 1 mM catechol and 0.2 M bromate: heating of this stock solution in a microwave oven as described in the Methods section caused the catechol to become oxidised to orthobenzoquinone, imparting a pink colour to the solution typical of orthobenzoquinone [14] according to the following reaction:

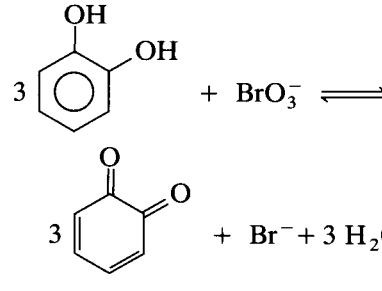

(1)

Addition of the oxidised catechol (orthobenzoquinone) and bromate produced stable CSV peak currents for vanadium. It is therefore likely that the initial unstable peaks were caused by the slow and gradual oxidation of the catechol by the bromate. The oxidised catechol (orthobenzoquinone) stock solution premixed with bromate was therefore used for further experiments.

Cyclic voltammetry of catechol in an aqueous solution of PIPES pH buffer (pH 6.8) without vanadium revealed the presence of an anodic peak at +0.16 V due to the oxidation of catechol to orthobenzoquinone. Cyclic voltammetry of catechol using the HMDE and a glassy carbon electrode (GCE) can be compared in Fig. 1A. The redox potential of the catechol/orthobenzoquinone couple at the HMDE (+0.16 V) is in good agreement with that (+0.18 V) reported for pH 7.0 [15]. The redox couple was not fully separated from the mercury oxidation wave and was situated on the shoulder of the mercury(II)/mercury(0) redox couple. An anodic and a cathodic peak could be identified, with peak potentials differing by ~ 80 mV, showing that the catechol/orthobenzoquinone redox reaction was reversible at the mercury electrode. This means that orthobenzoquinone (when added to the bulk solution instead of catechol) is reduced back to catechol (and available for complex formation) at the electrode surface at all times at potentials < +0.16 V during the deposition and scanning steps of the analytical procedure, as opposed to in the solution as in the previous work [4]. It is interesting that the sensitivity was much improved under these conditions.

Separate cyclic voltammetric experiments of catechol in PIPES buffer using a GCE produced a much larger potential difference between the anodic (+0.47 V) and cathodic (0.0 V) peak potentials showing that the redox couple was poorly reversible at this surface (Fig. 1A).

Cyclic voltammetry was used to evaluate the reaction mechanism. Cyclic voltammograms for 10 nM vanadium in pH 6.6 sea water in the presence of 10 mM PIPES, 10^{-4} M catechol and 20 mM bromate are shown in Fig. 1B. The first scan was carried out after 60 s adsorption at −0.1 V at a scan rate of 50 mV s^{-1}, and was immediately followed by a second scan without prior adsorption. A large reduction peak (300 nA at a vanadium concentration of 10 nM) was obtained at −0.84 V due the reduction of vanadium(V) to vanadium(IV) on the forward scan towards more negative potentials. The peak at −0.84 V was found to increase with the adsorption time in accordance with a process in which the current is predominantly derived from the reduction of an adsorbed compound. The peak was not present at this low level of vanadium (10 nM) in the absence of bromate but a reduction peak for the adsorbed complex of vanadium with catechol is known to appear at a more positive potential of ~ −0.7 V at a much higher concentration (mM level) of vanadium in otherwise similar conditions [4]. A cathodic peak apparent at ~ −0.45 V (Fig. 1B and C) was due to reduction of an adsorbed complex of molybdenum which is present at ~ 100 nM in sea water.

Interestingly a cathodic (reduction) peak appeared instead of an expected anodic (oxidation) peak in the reverse scans (towards more positive potentials) from −1.2 to −0.1 V (Fig. 1B). This observation is consistent with a reaction mechanism in which the peak current for the reduction of vanadium(V) to vanadium(IV) is catalytically enhanced and where the reduced (vanadium(IV)) complex with catechol does not adsorb on the mercury surface. Diffusion of the vanadium (IV)–catechol away from the electrode surface causes the peak current of the forward scans to drop steaply at potentials more negative than −0.84 V causing the peak-shape of the reduction wave (Fig. 1B) instead of the stepwise increase to be expected from a diffusion current. The diffusion of the vanadium(IV) from the electrode surface causes the main cathodic peak to decrease in the second and subsequent negative-going potential scans (Fig. 1B).

Cyclic voltammetry of the vanadium complex with catechol showed that the cathodic peak was asymmetric. The asymmetric peak shape illustrates that a diffusion component (that of the oxidant bromate) is important as a reversible reduction peak entirely due to the reduction of an adsorbed compound would be symmetric. Cyclic voltammograms at scan speeds of 5, 50 and

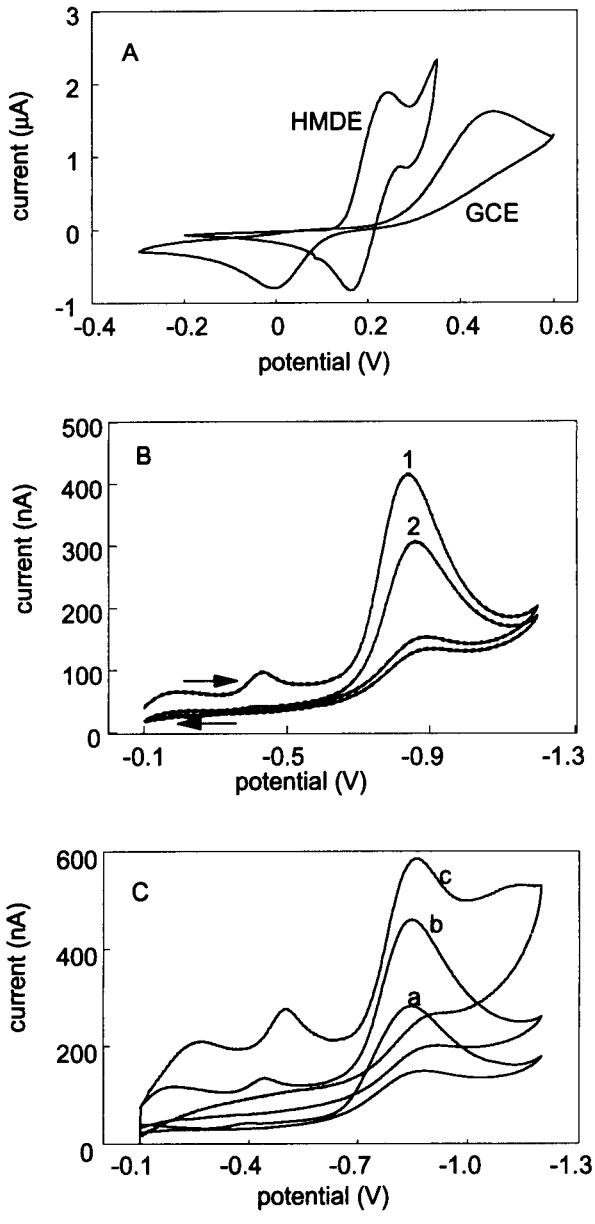

Fig. 1. Cyclic voltammetry of free catechol (A) and of catechol complexes with vanadium (B and C). (A) Cyclic voltammetry of free catechol in 0.02 M PIPES buffer using an HMDE (2 mM catechol) and a GCE (0.2 mM catechol). The scans were not preceded by deposition. The scan rate was 10 mV/s. (B) Consecutive cyclic voltammograms after 60 s of deposition from sea water containing 10 mM PIPES buffer (pH 6.6), 10 nM vanadium(V), 20 mM potassium bromate and 10^{-4} M catechol. Deposition potential, −0.1 V; scan speed, 50 mV/s. (C) Cyclic voltammograms of 10 nM vanadium at scan rates of 5 (a), 50 (b) and 500 (c) mV/s; solution composition as in (B).

500 mV s^{-1} showed that the asymmetry increased with increasing scan rate due to increasing diffusive and capacitive components (Fig. 1C). The reduction current of adsorbed species should increase linearly with the scan rate as the reducible charge is constant, whereas a linear relationship with the square root of the scan rate is valid for diffusion currents [16]. Interestingly a plot (Fig. 2A) of the peak height of the vanadium peak as a function of the square root of the scan rate is linear at scan rates < 50 mV s^{-1} indicating that the effect of the diffusion current (of the bromate) on the peak height is predominant at these scan rates. The linearity breaks down at greater scan rates giving less peak height than expected, presumably due to the slowness of the catalytic process (see below).

The catalytic nature of the vanadium(V)/(IV) redox reaction in the presence of bromate is illustrated by means of a diagnostic test [17] utilising a plot of $(i_{\text{cathodic}} \times v^{1/2})$ versus v (Fig. 2B), where i_{cathodic} is the peak current of the vanadium peak and v the scan rate. At low values of v a comparatively large amount of bromate diffuses towards the electrode surface reoxidising the vanadium(IV) and leading to current values higher than expected from the reduction of vanadium(V) alone, thus causing the shape of the plot shown in Fig. 2B which is typical for catalytic processes [17].

3.2. Reaction mechanism

The proposed mechanism is as follows.

Adsorption step at −0.1 V: Diffusion of orthobenzoquinone and vanadium to the electrode surface where the orthobenzoquinone is reduced to catechol, forming an adsorptive complex with vanadium:

$$\text{benzoquinone}_{\text{diffusion layer}} \xrightarrow{-0.8 < E_{\text{dep}} < -0.1\text{V}} \text{catechol}_{\text{diffusion layer}}$$

The catechol is retained in the reduced form at the electrode surface under the influence of the applied potential and furthermore the oxidation kinetics with the bromate were quite slow, requiring microwave boiling to reach completion within

minutes. The formed catechol is then available for complex formation with vanadium and adsorption on the electrode:

$$\text{catechol} + \text{vanadium(V)} \xrightarrow{-0.8 < E_{dep} < -0.1\,V} \text{vanadium(V)–catechol}_{adsorbed}$$

The vanadium in the adsorbed complex with catechol is reduced to vanadium(IV) at potentials < -0.84 V in the subsequent potential scan. The vanadium(IV) is chemically reoxidised to vanadium(V) by the bromate and is available again for repeated reduction, thus causing the catalytic increase in the reduction current:

$$\text{V(V)–catechol}_{adsorbed} + e^- \xrightarrow{-0.84\,V} \text{V(IV)–catechol}_{diffusion\ layer}$$

$$\uparrow \quad \text{CATALYTIC CYCLE} \quad \downarrow$$

$$\text{V(V)–catechol}_{adsorbed} \xleftarrow[bromate]{} \text{V(IV)–catechol}_{diffusion\ layer}$$

3.3. *Effects of varying the solution composition on the CSV of vanadium*

Preliminary experiments comparing linear sweep voltammetry with square-wave voltammetry showed that the peak shape and sensitivity were improved by using the square-wave modulation which was therefore used for analytical purposes.

The optimal concentration of bromate was determined by CSV after deposition at -0.1 V at two different deposition periods (20 and 60 s) at bromate concentrations increasing from 0 to 30 mM at a constant concentration of 0.1 mM of oxidised catechol (orthobenzoquinone). It was found (Fig. 3A) that the peak height increased with increasing concentration of bromate, the increase levelling off at 20 mM bromate, whereas the peak potential did not vary significantly with the bromate concentration. A similar effect of the bromate concentration was obtained when this experiment was carried out using catechol but the peak potential was found to shift from -0.67 V in the absence of bromate towards more negative potentials (-0.76 V at 20 mM bromate). This potential shift occurred apparently already at low bromate concentrations when the catechol was added as orthobenzoquinone to the solution.

A concentration of 20 mM bromate was selected for further analytical studies as it produced good sensitivity. It would be possible to increase the sensitivity further by using higher bromate concentrations but the additional increase is small compared to that reached already, and a disadvantage is that a large volume of bromate has to be added: a volume of 1 ml of 0.2 M bromate is

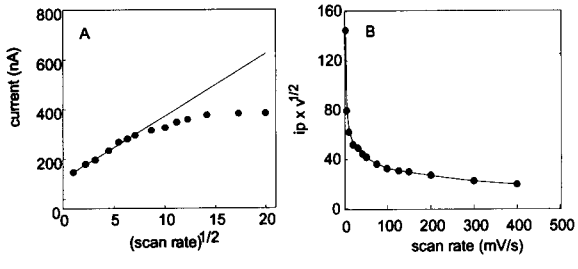

Fig. 2 Effect of varying the scan rate of cyclic voltammetry on the cathodic peak height of the vanadium complex of catechol. (A) The peak current versus the square root of the potential scan rate. (B) Diagnostic test for catalytic mechanisms (see text).

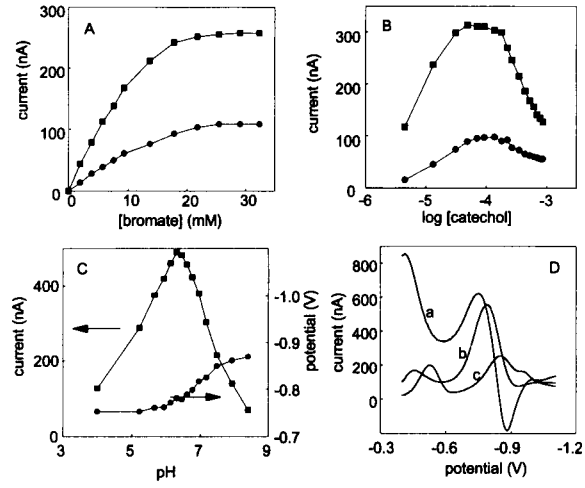

Fig. 3. Effect of varying the solution composition on the CSV sensivity for 10 nM vanadium in UV-digested purified sea water: (A) Variation of the concentration of bromate using a deposition period of 20 (●) and 60 (■) s. (B) Variation of the catechol concentration using a deposition period of 20 (●) and 60 s (■). (C) Variation of the pH using a deposition time of 60 s. (D) CSV scans after 60 s deposition at pH 5.2 (a), 6.6 (b) and 7.5 (c).

added to 10 ml sea water to obtain the concentration of 20 mM.

The influence of varying the catechol (added as oxidized catechol) concentration in the presence of 20 mM bromate on the CSV peak height is shown in Fig. 3B. The sensitivity for vanadium was found to increase with the catechol concentration reaching a maximum at 0.1 mM whilst decreasing at higher concentrations. The peak potential shifted gradually from −0.78 V (at 5 μM catechol) to −0.76 V (at 0.9 mM catechol).

The effect of varying the pH on the CSV sensitivity for vanadium in sea water is shown in Fig. 3C. Greatest sensitivity was obtained at pH values between 6.3 and 6.6, whereas the sensitivity was much less outside this pH range: an increase in the pH caused the peak height to decrease strongly probably due to hydrolysis of vanadium(V), whereas pH values below 6.0 caused a decrease in the peak height as well as a asymmetric peak shape possibly as a result of enhanced sensitivity for molybdenum which appears at a more positive potential. The effect of the pH on the peak shape is shown in Fig. 3D. The peak potential remained constant at pH values below 6, but was shifted towards more negative potentials when the pH was increased, at a rate of ~ 70 mV/pH unit, as a result of enhanced stability of the vanadium complex at higher pH values. A pH value of 6.6 (obtained by addition of 200 μl of 1 M PIPES buffer to sea water sample) was selected for the optimised analytical conditions to determine vanadium in sea water.

3.4. *Effect of varying voltammetric parameters: square-wave frequency, deposition potential and deposition time*

The sensitivity of CSV is affected by the deposition potential as it determines the charge on the electrode and therefore the Coulombic attraction or repulsion. The CSV sensitivity was recorded as a function of the deposition potential using a constant deposition period (15 s) and each scan was carried out from −0.4 V to −1.2 V using the square-wave modulation (50 Hz). The effect of the deposition potential on the peak height is shown in Fig. 4A. It was found that the peak

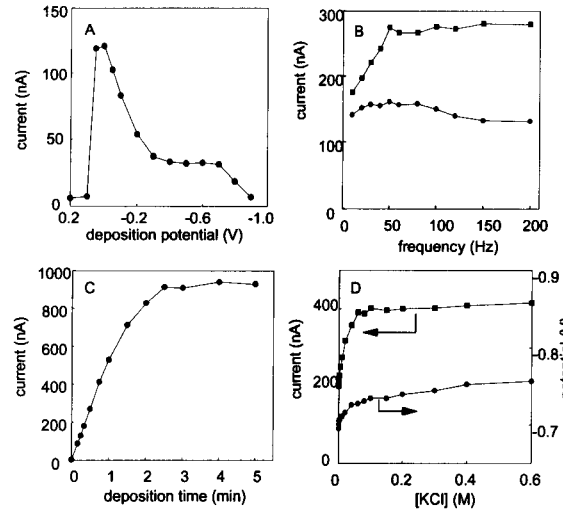

Fig. 4. Effect of varying voltammetric parameters and the concentration of chloride on the sensitivity for 20 nM vanadium in UV-digested purified sea water (A,B and C) and PIPES buffer solution (D). (A) Variation of the deposition potential using a deposition period of 15 s. (B) Variation of the square-wave frequency after a deposition period of 20 (●) and 60 s (■). (C) Variation of the deposition period. (D) Variation of the chloride concentration on the current (■) and potential (●) of the CSV peak after a deposition period of 60 s for 20 nM vanadium in 20 mM PIPES buffer.

current was almost zero at positive values of the deposition potential presumably due to oxidation of the mercury surface. Highest sensitivity was obtained at a deposition potential between 0.0 and −0.1 V, decreasing at more negative values and remaining constant at potentials more negative than −0.3 V. The apparently favourable adsorption conditions at potentials where the mercury electrode has a positive surface charge suggest that the catechol–vanadium complex has a negative charge.

The effect of varying the square-wave frequency on the CSV peak height for 20 nM vanadium in sea water is shown in Fig. 4B. Scans were performed after either 20 or 60 s deposition at −0.1 V. The peak current increased with increasing frequency levelling off at frequencies above 50 Hz. Higher frequencies led to faster scans, but without improvement of the signal/noise ratio probably due to slow kinetics of the catalytic

redox couple. A frequency of 50 Hz was used in subsequent experiments.

Variation of the deposition time showed that the peak height increased linearly with the deposition time, gradually levelling off at periods longer than 2 min (Fig. 4C) presumably due to saturation of the mercury surface with catechol complexes with vanadium and other elements. A deposition time of 15 s is adequate for the determination of vanadium in sea water because of the high sensitivity of the catalytic current. The data in Fig. 4C show that the sensitivity can be increased by a factor of eight by extending the adsorption period to 2 min.

Comparative determinations of the CSV sensitivity for vanadium in water (Milli-Q) and sea water showed that the sensitivity was greater in sea water. Variation of the concentration of chloride in water (Fig. 4D) showed that the CSV peak height approximately doubled when the chloride concentration was increased to 0.1 M, whilst the increase levelled off at higher chloride concentrations. A concomitant shift of the peak potential with increasing chloride concentration (Fig. 4D) suggests that the adsorbed complex is stabilised in this condition, possibly caused by the formation of a mixed (vanadium–catechol–chloride) complex with better adsorptive properties.

3.5. Interferences

Species such as Al(III), As(III), Cd(II), Co(II), Cr(VI), Cu(II), Fe(III), In(III), Mn(II), Mo(VI), Ni(II), Sb(III), Se(IV), Ti(IV), U(VI) and Zn(II) are able to form complexes with catechol [18,19] and are therefore potential interferences in the determination of vanadium. The selectivity of the optimised method was tested by addition of 100 nM of these metals to sea water containing 30 nM vanadium(V) in the presence of 20 mM potassium bromate and 0.2 mM catechol, using a deposition time of 15 s. In these conditions, small additional peaks were observed for Cu (−0.19 V, sensitivity (S) = 0.86 nA/nM), Fe(III) (−0.35 V, S = 0.61 nA/nM), Mo (VI) (−0.45 V, S = 0.10 nA/nM), Pb (−0.41 V, S = 0.34 nA/nM) and U(VI) (−0.53 V, S = 0.04 nA/nM) which were not found to interfere with the determination of vanadium (S = 9.6 nA/nM). High levels (100 nM, S = 1.36 nA/nM) of indium did interfere yielding a overlapping peak and decreasing the height of the vanadium peak. However, this interference does not occur in sea water as the indium concentration in sea water is very low (pM level).

Surface-active organic matter occurring in natural waters can interfere as a result of competitive adsorption on the mercury surface. Several surface-active substances, dodecylbenzenesulphonic acid (sodium salt, DBS, an anionic surfactant), Hyamine 1622 (a cationic surfactant) and Triton X-100 (a non-ionic surfactant) were used as model compounds for natural organic surfactants in sea water. These compounds were found to interfere less than usual in CSV, probably due to the short deposition time (15 s) used for the determination of vanadium in sea water. The peak of 30 nM vanadium in UV-digested sea water was diminished by ~ 50% in the presence of 2.6 ppm (μg ml^{-1}) Hyamine 1622, 5.2 ppm DBS and 3.2 ppm Triton X-100. The vanadium peak was completely masked in the presence of 5 ppm Hyamine, 10 ppm DBS or 5 ppm Triton X-100. It is likely that such substances affect the sensitivity when vanadium is determined in natural water samples. For instance the CSV sensitivity for vanadium in Mediterranean sea water was 8% less than that after UV digestion of the sample at pH 2. It is therefore advisable to calibrate the sensitivity for each sample separately by means of a vanadium standard addition to the sample. However, the same concentration is obtained before and after the UV digestion at pH 2, so this treatment is necessary only if the sensitivity is greatly diminished as in samples containing high levels of organic surface-active substances. Comparative measurements indicated that vanadium could be readily determined in sea water from estuarine or coastal origin.

3.6. UV digestion of sea water to remove interfering organic matter

UV digestion can be used to remove interfering organic matter with complexing or surface active properties. Preliminary experiments comparing UV digestion of acidified (to pH 2 with

hydrochloric acid) and unacidified sample aliquots (filtered Mediterranean sea water) and with and without addition of a known amount of vanadium standard indicated losses of 20–30% of vanadium from unacidified aliquots (Table 1). Furthermore, the vanadium concentration in the unacidified aliquots was found to decrease with increasing storage time suggesting that the vanadium adsorbed on the silica tube or on inorganic particles formed during the UV digestion at neutral pH.

Curiously, the CSV sensitivity for vanadium was not stable in acidified UV-digested samples, as the peak for vanadium increased with subsequent scans. Previously it has been shown that hypochlorite is formed upon UV digestion of acidified sea water interfering with the subsequent determination of copper [20]. Additions of hypochlorite confirmed that this has an interfering effect on the CSV peak for vanadium, confirming that the hypochlorite formation was the cause of the interference observed in UV-digested sample aliquots. This interference was eliminated by addition of 0.2 mM hydroxylammonium chloride to the sea water sample buffered at pH 6.6 to reduce the hypochlorite, and then bubbling nitrogen through the sample for 3 min prior the addition of bromate and catechol.

3.7. Linear range, sensitivity and limit of detection

The linear calibration range of the optimised method was evaluated from a calibration plot of vanadium in purified (by ion exchange to lower the vanadium concentration) and UV-digested sea water (to remove potentially interfering organic substances). Calibration graphs are shown for two deposition times in Fig. 5A, whilst low vanadium level (0.35 to 1.35 nM, much lower than normally occurring in sea water) scans are shown in Fig. 5B. The peak current was found to increase linearly with the vanadium concentration between 0.2 and 10 nM when a 120 s deposition period was used, whereas the linear range was from 2 to 60 nM using a 15 s deposition period.

The sensitivity of the method (calculated from the slope of a linear regression) was 60 nA nM^{-1} for the 120 s deposition period and 5.4 nA nM^{-1} for the 15 s deposition period.

The 3σ limit of detection was calculated from repeated CSV determinations of a low level (1 nM) of vanadium in purified sea water. The limit of detection was 0.07 nM (R.S.D. 2.2%) using a deposition time of 120 s, whereas it was 0.6 nM (R.S.D. 19%) using a deposition time of 15 s.

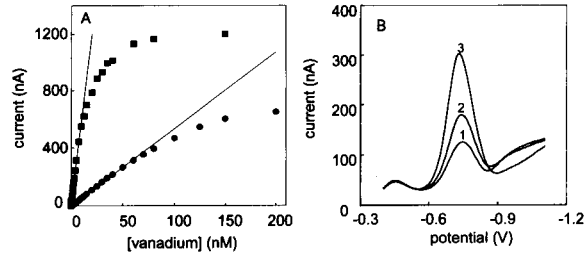

Fig. 5. CSV (square-wave modulation, 50 Hz) of vanadium in purified and UV-digested sea water. (A) Response as a function of the vanadium concentration after 15 (●) and 120 (■) s deposition at −0.1 V. (B) CSV scans of low levels of vanadium using a deposition time of 5 min; vanadium concentrations: 1, 0.35 nM; 2, 0.6 nM; 3, 1.35 nM.

Table 1
Influence of UV digestion on the concentrations of vanadium in sea water originating from the Mediterranean detected by CSV after a deposition time of 15 s (n indicates the number of repeats)

Sample pretreatment	Detected vanadium (nM)	R.S.D. (%)
Untreated	24.9 ± 1.5 (n = 5)	6.0
UV-digested at pH 8	20.2 ± 4.4 (n = 8)	21.8
UV-digested at pH 2	25.1 ± 1.3 (n = 5)	5.2
+20 nM vanadium		
Untreated	46.9 ± 2.0 (n = 5)	4.3
UV-irradiated at pH 8	33.5 ± 0.6 (n = 4)	1.8
UV-irradiated at pH 2	47.7 ± 3.7 (n = 4)	7.8

4. Conclusions

The reduction current of vanadium in an adsorbed complex with catechol (possibly a mixed complex with chloride when the analysis is carried out on sea water) is catalytically enhanced in the presence of bromate. The catechol is added in oxidised form (orthobenzoquinone) to the solution premixed with the bromate. The deposition step is complicated, involving the electrolytic re-

duction of the orthobenzoquinone back to catechol at −0.1 V with subsequent complex formation with vanadium(V) and adsorption on the mercury electrode. The vanadium in the adsorbed complex is reduced to vanadium(IV), and is reoxidised to vanadium(V) in the diffusion layer by the dissolved bromate, and is available for re-reduction thus catalytically enhancing the reduction current. The limit of detection is 0.6 nM using a deposition time of 15 s, so vanadium can be determined in sea water very quickly. Potential interference by surface-active organic compounds is comparatively minor because of the short deposition period used, so UV digestion is normally not required. However, if used, UV digestion has to be carried out after acidification of the sample, and any hypochlorite resulting from the UV digestion in saline waters has to be removed using hydroxylammonium chloride prior to the analysis.

Acknowledgements

M.V. is grateful for the hospitality of the Oceanographic Laboratories and financial assistance from the University of Valladolid which supported part of the travel costs to enable this collaboration.

References

[1] C.M.G. van den Berg, Anal. Chim. Acta, 250 (1991) 265.
[2] J. Jaendel, M. Caisso and J.F. Minster, Mar. Chem., 21 (1987) 51.
[3] K.W. Bruland, in J.P. Riley and R. Chester (Eds.), Chemical Oceanography, Vol. 8, Academic Press, London, 1983, p. 198.
[4] C.M.G. van den Berg and Z.Q. Huang, Anal. Chem., 56 (1984) 2383.
[5] S. Shi, J. Wang and J. Lu, Fenxi Huaxue, 17 (1989) 1085.
[6] J. Lu, W. Jin and S. Wang, Anal. Chim. Acta, 238 (1990) 375.
[7] A. Romanus, H. Müller and D. Kirsch, Fresenius' J. Anal. Chem., 340 (1991) 363.
[8] K. Yokoi and C.M.G. van den Berg, Anal. Chim. Acta, 245 (1991) 167.
[9] K. Yokoi and C.M.G. van den Berg, Electroanalysis, 4 (1992) 65.
[10] M. Boussemart, C.M.G. van den Berg and M. Ghaddaf, Anal. Chim. Acta, 262 (1992) 103.
[11] J. Golimowski, P. Valenta and H.W. Nürnberg, Fresenius' Z. Anal. Chem., 322 (1985) 315.
[12] C.M.G. van den Berg and G.S. Jacinto, Anal. Chim. Acta, 211 (1988) 129.
[13] J. Wang, B. Tian and J. Lu, Talanta, 39 (1992) 1273.
[14] S. Coffey (Ed.), Rodd's Chemistry of Carbon Compounds, Vol. IIIB, Elsevier, Amsterdam, 1974, p. 1.
[15] L. Meites and P. Zuman, Handbook Series in Organic Electrochemistry, Vol. I, CRC Press, Cleveland, OH, 1976, p. 222.
[16] A.J. Bard and L.R. Faulkner, Electrochemical Methods. Fundamentals and Applications, Wiley, New York, 1980, p. 520.
[17] R. Greef, R. Peat, L.M. Peter, D. Pletcher and J. Robinson, Instrumental Methods in Electrochemistry, Ellis Horwood, Chichester, 1990.
[18] IUPAC Chemical Data Series, Stability Constants of Metal–Ion complexes: Part B; Organic Ligands, Pergamon, Oxford, 1979, p. 346.
[19] A.E. Martell and R.M. Smith, Critical Stability Constants, Vol. 3, Plenum Press, New York, 1977, p. 200.
[20] E.P. Achterberg and C.M.G. van den Berg, Anal. Chim. Acta, 291 (1994) 213.

ELSEVIER

Analytica Chimica Acta 293 (1994) 29–34

ANALYTICA CHIMICA ACTA

Cathodic adsorptive stripping voltammetry of indium complexed with morin at a static mercury drop electrode

Pércio A.M. Farias [a,*], Caroline M.L. Martins [a], Aniy K. Ohara [a], Jon S. Gold [b]

[a] *Department of Chemistry, Pontifícia Universidade Católica, Rua Marquês de São Vicente, 225, CEP 22453-900, Rio de Janeiro, RJ, Brazil*

[b] *Department of Chemistry, Santa Clara University, Santa Clara, CA 95053, USA*

(Received 28th September 1993; revised manuscript received 23rd February 1994)

Abstract

A new method is described for the determination of indium based on the cathodic adsorptive stripping of In(III) complexed with 2',3,4',5,7-pentahydroxyflavone (morin) at a static mercury drop electrode. Optimal conditions were found to be: accumulation potential, −0.30 V (vs. Ag/AgCl); final potential, −1.00 V; accumulation time, 60 s; scan rate, 200 mV/s; linear scan mode; filter, 0.1 s; supporting electrolyte, acetic acid–acetate (0.1 M, pH 3.5); concentration of morin, 1×10^{-5} M. The response of the system was found to be linear in a range of In concentrations from 0 ppb to 40 ppb. The detection limit was found to be 0.4 nM (0.05 ppb) with 5 min of accumulation time. This is compared to a detection limit of 6.9 nM (0.8 ppb) for simple anodic stripping under the same conditions. The effect of various potential interferences (including a variety of cations, anions and organic surfactants) were also studied. At less than equimolar concentrations no significant interferences were observed. Al^{3+}, Ti^{4+}, Sc^{3+} and uranyl were found to interfere at concentrations larger than that of In, but may be masked by fluoride. The observed interference by V^{5+} may be masked by cyanide. The method was applied to a sample of jarosite (an industrial residue from the refinement of zinc ore) which is known to contain significant quantities of indium.

Key words: Stripping voltammetry; Indium; 2',3,4',5,7-Pentahydroxyflavone (Morin)

1. Introduction

The utility of indium has been described elsewhere [1]. Several methods have been described for the quantitative determination of indium including atomic absorption spectrometry [2], UV–visible spectroscopy [3], polarography [4] and anodic stripping voltammetry [5]. Each approach has its particular sensitivity and is subject to various interferences and limitations. In our laboratory we have been investigating various preadsorptive voltammetric techniques utilizing a variety of organic complexing agents for trace and ultratrace metal determinations which both maximize sensitivity and selectivity [6–9]. We report here the trace determination of In by cathodic stripping voltammetry using the complexing agent

* Corresponding author.

SSDI 0003-2670(94)00099-8

morin. We have found this technique to be both highly sensitive (detection limit of 0.05 ppb with 5 min of accumulation time) and relatively unaffected by a variety of commonly interfering substances. The effect of a number of experimental parameters is presented. The utility of the method is demonstrated by the determination of indium in a sample of jarosite.

2. Experimental

2.1. Apparatus and reagents

The voltammograms were obtained with a PAR 264-A voltammetric analyser interfaced with a PAR 303 static mercury drop electrode which have been described elsewhere [6,7]. A large-sized static mercury drop electrode (SMDE) with a surface area of 0.032 cm^2 was used. A Ag/AgCl (saturated KCl) reference electrode and platinum wire auxiliary electrode were used. All potentials reported are with respect to the Ag/AgCl electrode. Water purified in a Milli-Q water purification system (Millipore) was used for all dilutions and sample preparations. All chemicals were of analytical reagent grade. A 2000 ppm stock solution (Fluka, Buchs) was prepared by dissolving 0.2420 g In_2O_3 in a minimum of hot concentrated hydrochloric acid followed by dilution to 100 ml. A 2.0×10^{-3} M stock solution of morin was prepared in ethanol. A stock solution of the supporting electrolyte was prepared of 1 M acetate followed by addition of acetic acid to achieve pH 3.5. The sample of jarosite (a residue from the refinement of zinc) was obtained from an industrial source.

2.2. Procedure

10 ml of a supporting electrolyte solution (9.0 ml of water + 1.0 ml of the stock acetate buffer) containing 50 μl of the 2.0×10^{-3} M morin stock solution were pipetted into the cell and purged with nitrogen for 8 min. The preconcentration potential (−0.3 V vs. Ag/AgCl) was applied to a fresh mercury drop while the solution was stirred. Following the accumulation (typically 60 s) the stirring was stopped and allowed to equilibrate for 30 s. The voltammogram was recorded by a linear scan of negative-going voltage (scan rate = 200 mV/s) terminated at −1.0 V. After the background stripping voltammogram has been obtained, aliquots of the indium standard solution are introduced into the cell while maintaining a stream of nitrogen over the surface. All data were obtained at (23 ± 1)°C.

3. Results and discussion

3.1. Parameters affecting the adsorptive stripping behaviour

Fig. 1 shows repetitive cyclic voltammograms for 1×10^{-5} M morin recorded in the presence of 20 ppb In in an unstirred 0.1 M acetate buffer (pH 3.5) solution. The cathodic peak current of the In–morin complex (peak B) at −0.65 V gradually increases with repetitive scans while the current of the free ligand morin (peak A) at −0.39 V simultaneously decreases until almost returning to the baseline. A third small cathodic

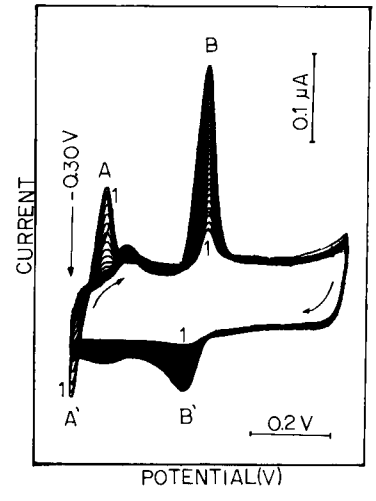

Fig. 1. Repetitive cyclic voltammograms for 1×10^{-5} M morin (A,A') with 20 μg l^{-1} of indium (B,B') in unstirred 0.1 M acetate buffer (pH 3.5) solution. Conditions: scan rate, 100 mV/s; equilibrium time, 30 s; large drop size; filter, 0.1 s. The first scan is indicated by the number one (1). Total time of the successive scans is 10 min.

peak at −0.44 V was observed to increase. A subsequent study of repetitive cyclic voltammetry of morin without In yielded an increasing peak at −0.44 V implying that this peak is of an electrochemically produced material. Three peaks are observed in the anodic branch. The peak A′ which has correspondence to the ligand peak A at −0.31 V was observed to decrease while the peak B′ at −0.59 V was observed to gradually increase. A third small peak at intermediate potential was observed to also gradually increase. It was observed that increasing the In concentration (while holding the concentration of ligand constant), resulted in an increase in the current of the complex's peaks with a smaller free ligand peak.

The effect of pH on the linear scan stripping peak current of the In–Morin complex was studied. When an accumulation potential of −0.3 V was used, the current is seen to increase from pH 3 until reaching a maximum at pH 3.5 and finally decrease at higher pH. Hence pH 3.5 was chosen for subsequent determinations. A similar behaviour was observed for an accumulation potential of 0.0 V but the currents were much lower. The potentials of the reduction of both morin and the indium–morin complex were both observed to shift to more negative potentials with increasing pH.

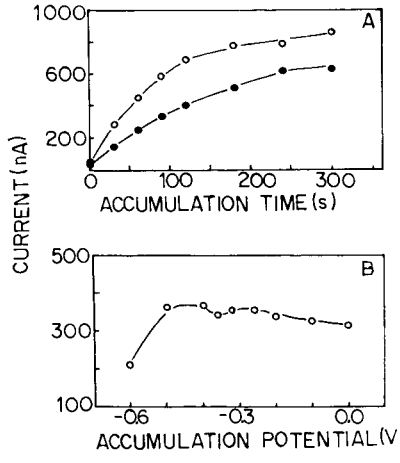

Fig. 2. The effect of accumulation time (A) and potential (B) on the current of the adsorptive stripping peak for the indium–morin complex. Conditions: electrolyte, 0.1 M acetate buffer (pH 3.5) containing 1×10^{-5} M morin with 8 (A, •), 16 (A, ○) and 20 $\mu g\ l^{-1}$ (B) of indium, accumulation time of 30 s (B only) at −0.30 V (A only); scan rate, 200 mV/s; equilibrium time, 30 s; filter, 0.1 s; large drop size.

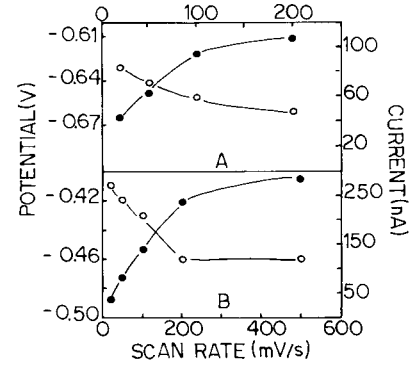

Fig. 3. Effect of scan rate on the potential (○) and current (•) of the indium–morin complex (A) and morin peak (B) as obtained by cyclic voltammetry. Conditions: electrolyte, 0.1 M acetate buffer (pH 3.5) containing 1×10^{-5} M morin and 80 $\mu g\ l^{-1}$ indium; equilibrium time, 30 s; large drop size; filter, 0.1 s; $E_{initial} = 0.00$ V and $E_{final} = -1.00$ V.

The stability of the complex was studied by performing repetitive measurements of a single sample over a period of 150 min. Within the noise level of the experiment, no appreciable variation in currents was observed (standard deviation = 3.6% for 22 measurements). The variation of current with acetate concentration was found to have a maximum (at pH 3.5) with an acetate concentration of 0.1 M. The effect on the current of the In–morin complex with concentration of ligand (20 ppb In) was also studied. The current is seen to sharply increase until 10 μM morin. At higher concentrations the current was observed to slowly fall.

The effect of current with accumulation time is shown in Fig. 2A for two different In concentrations (8 and 16 ppb). Both curves show initially linear behaviour, with the curve of higher concentration showing saturation more rapidly. Fig. 2B shows the effect of accumulation potential on the current of the In–morin complex's peak. The current is seen to increase at potentials more positive than that for the complex (±0.65 V) until levelling off at −0.5 V.

Fig. 3 shows the effect of scan rate on both the current and potential of morin (B) and the In–

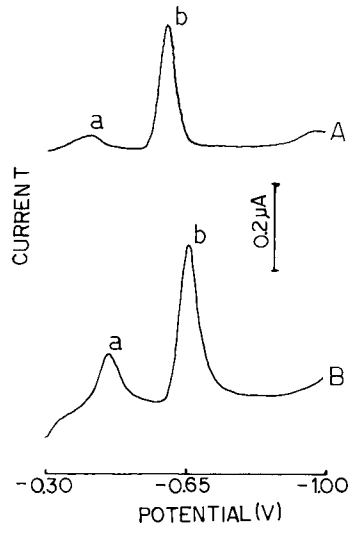

Fig. 4. Comparison between differential pulse (A) and linear scan (B) modes. For differential pulse scan pulse amplitude = 50 mV and scan rate = 10 mV/s. Linear scan experimental conditions as for Fig. 4B. Both modes were with an electrolyte solution of 0.1 M acetate buffer (pH 3.5) containing 1×10^{-5} M morin and 20 $\mu g\ l^{-1}$ indium, and with an accumulation time of 30 s at −0.30 V. For both curves peak a and b are of the ligand and complex, respectively.

morin complex (A) as obtained by cyclic voltammetry. For both cases, an increase in scan rate caused an increase in the current with a simultaneous decrease in potential. A separate study of the effect of scan rate for linear scan adsorptive stripping (20 ppb In, $t_{acc} = 30$ s at −0.30 V) yielded a linear increase in potential with scan rates from 5 to 100 mV/s with a subsequent levelling off of the current.

A comparison between a linear and differential pulse scan modes (Fig. 4) showed for the complex (peak b) a 27% increase in current for the linear scan mode and, as the linear scan mode is also faster, it was used for subsequent determinations. However, a differential pulse scan might prove useful under conditions of concentrations near the detection limit as it yields a better signal-to-noise ratio and a flatter baseline.

3.2. Quantitative utility

Fig. 5 shows the voltammograms obtained by varying the In concentration from 0 to 22 ppb (electrolyte, acetic acid–acetate, pH = 3.5; accumulation time, 30 s; accumulation potential, −0.30 V; final potential, −1.0 V; scan rate, 200 mV/s; large drop size; equilibrium time, 30 s). The resulting calibration curve, shown as the inset, is seen to be linear up to 40 ppb (correlation coefficient = 0.994 up to 36 ppb In). The detection limit was estimated to be 4.4×10^{-10} M after an accumulation time of 5 min of 1 ppb In ($S/N = 2$). A determination of In using simple anodic stripping yielded a detection limit 6.9×10^{-9} M under similar conditions (pH 3.5, $V_{init} = -0.9$ V, $V_{final} = +0.3$ V, scan rate = 200 mV/s). Beyond the improved sensitivity of the cathodic technique, is the increased selectivity in the presence of possibly interfering ions.

The major sources of interferences are likely to be coexisting ions and organic surfactants. These species could result in either new reduction peaks or the overlap with the In–morin peak

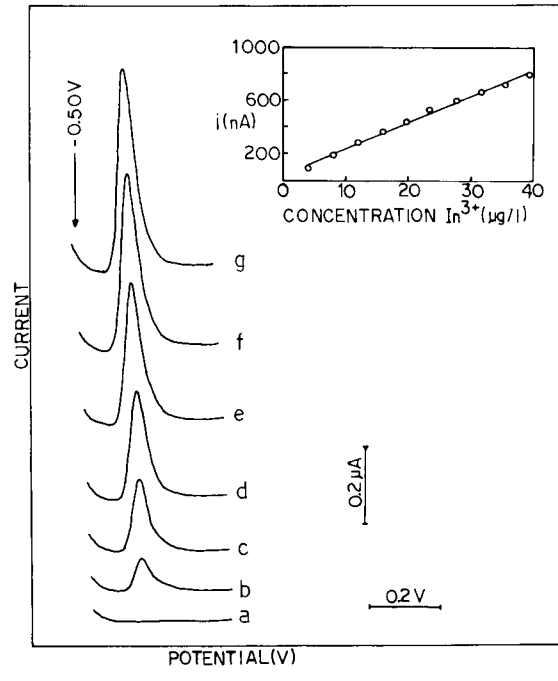

Fig. 5. Adsorptive stripping voltammograms obtained for solutions of increasing indium concentration from 0 (curve a) to 22 $\mu g\ l^{-1}$ (b–g). Conditions: electrolyte, 0.1 M acetate buffer (pH 3.5) containing 1×10^{-5} M morin; accumulation time, 30 s at −0.30 V; scan rate, 200 mV/s; equilibrium time, 30 s; filter, 0.1 s; large drop size. Also shown are the resulting calibration plots (4–40 $\mu g\ l^{-1}$).

thus obscuring the measurement. The effect of various ions that could yield interferences was studied. The determination of 5 ppb In was not affected by the addition of up to 5000 ppb of Cr^{3+}, Co^{2+}, Ca^{2+}, Ba^{2+}, Mg^{2+}, Zn^{2+}, Mn^{2+}, Fe^{3+}, Sr^{2+}, phosphate, chloride, fluoride, cyanide, carbonate, sulfate or thiosulfate. The determination of 5 ppb In was not affected by the addition of up to 500 ppb of Ni^{2+} or Cu^{2+}. No interference was noted for up to a thousand fold excess of Tl^{+}. The determination of 5 ppb In was not affected by the addition of up to 50 ppb of Al^{3+}, Th^{4+}, Cd^{2+}, Zr^{4+} or triton X-100. The determination of 5 ppb In was not affected by the presence of up to 5 ppb of Yb^{3+}, Sm^{3+}, Mo^{6+} or Pb^{2+}. The presence of 50 ppb of Sc^{3+}, uranyl or Ti^{4+} or 5000 ppb Al^{3+} interferes in a sample of 5 ppb In, but may be masked by 20 ppm fluoride. The interferences by Yb^{3+} (> 5 ppb) or Th^{4+} (> 50 ppb) were not masked by fluoride. The interference by V^{5+} (> 50 ppb) may be masked by 10 ppm cyanide. The interference by Cd^{2+} at 500 ppb was due to an overlapping peak (E = −0.59 V) with the In–morin complex which was not masked by EDTA.

The method was applied to a sample of jarosite (residue obtained in the refinement of zinc). The solid sample was first ground. The powder was then heated for 2 h at 120°C. 5 mg were then dissolved in 5 ml of 6 M HCl and 1 ml of concentrated sulfuric acid (to precipitate any lead which may be present). The sample was then centrifuged, filtered and the filtrate washed with 2% sulfuric acid. 1 ml of concentrated ammonia was then added to precipitate the hydroxides of indium, iron and aluminum. The precipitate was redissolved in a minimum of 1 M HCl and reprecipitated with ammonia. This precipitate was washed with ammonium chloride. The precipitate was dissolved in 50 ml of 1 M HCl. Finally, 100 μl was placed in the cell which contained 10 ml of supporting electrolyte (0.1 M acetic acid–acetate, pH 3.5) and 1 ppm of NaF (to mask the Al^{+3}). Fig. 6 shows the resulting voltammograms by the method of standard additions for a typical determination. The standard addition plot was linear (correlation coefficient of 0.995). The average of two determinations yielded an indium concentration of 644 ppm in the original solid sample. (Note that for the determination, the solution used was diluted to obtain a concentration in the linear range of the method.) This value falls within the ranges previously reported for samples of jarosite as determined by spectroscopic and plasma emission techniques [10]. The concentration of indium would be expected to vary significantly from one sample to another, as it is an industrial by-product.

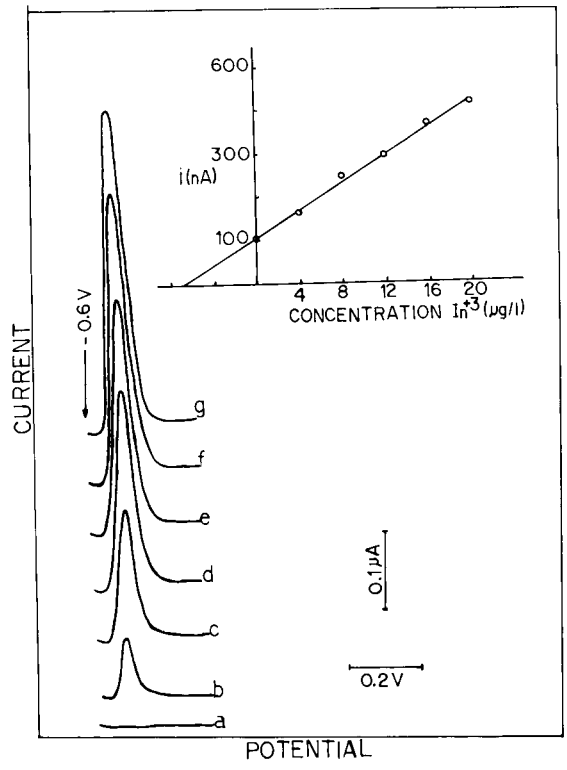

Fig. 6. Voltammograms from the determination of In in a sample of jarosite by the method of standard addition. Conditions as for Fig. 7. Curves a and b are of the blank and sample, respectively. Curves c–g result from the further addition of 4 ppb of a standard solution of In(III). Also shown is the resulting calibration curve for the sample.

4. Conclusions

The cathodic stripping of the In–morin complex has been shown to be an effective method for the determination of In. The approach is rapid and yields a high sensitivity and is largely

unaffected by a large number of commonly presented substances. In particular, this approach offers an advantage, in addition to greater sensitivity, over anodic stripping as the presence of up to ten-fold Cd and thousand-fold Tl do not interfere with the analysis of In [5]. Moreover, in contrast to previously reported techniques, in this case it is not necessary to first eliminate iron and aluminum from the sample [2].

Acknowledgements

The authors gratefully acknowledge the support of the CNPq and MCT of the Government of Brazil and PUC-Rio for support of this research. In addition, we thank Prof. João Alfredo Medeiros for helpful discussions and for generously supplying the sample of jarosite.

References

[1] A.I. Busev, V.G. Tiptsova and V.M. Ivanov, Analytical Chemistry of Rare Elements, MIRS Publishers, Moscow, 1981.
[2] T. Nakahara and S. Musha, Anal. Chim. Acta, 80 (1975) 47.
[3] K.L. Cheng and B.L. Goydish, Anal. Chim. Acta, 34 (1966) 154.
[4] T. Kurotu, Anal. Chim. Acta, 233 (1990) 325.
[5] J. Wang, Stripping Analysis – Principles, Instrumentation and Applications, VCH, Deerfield Beach, FL, 1985.
[6] P.A.M. Farias and A.K. Ohara, Electroanalysis, 3 (1991) 985.
[7] P.A.M. Farias and A.K. Ohara, Fresenius' J. Anal. Chem., 342 (1992) 87
[8] P.A.M. Farias, S.L.C. Ferreira, A.K. Ohara, M.B. Bastos and M.S. Goulart, Talanta, 39 (1992) 1245.
[9] P.A.M. Farias, A.K. Ohara, A.W. Nóbrega and J.S. Gold, Electroanalysis, in press.
[10] M.C.B. Quaresma, Master's Thesis, Department of Chemistry, PUC-Rio, 1990.

ELSEVIER

Analytica Chimica Acta 293 (1994) 35–41

ANALYTICA CHIMICA ACTA

Tubular detectors for flow-injection potentiometric determination of tetrafluoroborate in electroplating baths

A.N. Araújo [a], M.B. Etxebarria [b], J.L.F.C. Lima [a], M.C.B.S.M. Montenegro [a,*], R. Pérez Olmos [b]

[a] *Departamento de Química Física, Faculdade de Farmácia, 4000 Porto, Portugal*
[b] *Departamento de Química Analítica, Escuela Universitaria de Ingenieria Técnica Industrial, 48012 Bilbao, Spain*

(Received 11th November 1993; revised manuscript received 5th January 1994)

Abstract

PVC tetrafluoroborate tubular electrodes without an inner reference solution, based on tetraoctylammonium as the ion exchanger and 2-nitrophenyloctyl ether as the mediator solvent, were constructed. The general operating characteristics of the tubular detectors were evaluated by a single line flow-injection system with low sample dispersion and compared to those of corresponding conventionally-shaped electrodes, determined in batch conditions. In flow-injection analysis (FIA), the detector response was linear in the concentration range between 4×10^{-6} and 10^{-1} M, with a mean slope of 59.2 ± 0.9 mV/dec in the pH range between of 2.7 and 11.5. The reproducibility of the detector potentials was approximately 0.2 mV during a day of continuous operation. The membrane used showed a high degree of selectivity. The tubular detectors remained operational over a long period of time (approximately 36 months) and had a response time that enabled a sampling rate of 360 h^{-1}. The electrodes were later used in the determination of tetrafluoroborate in concentrated electrolytic baths for which a high dispersion FIA system was developed. The analyses of seven baths with different compositions presented results with mean recovery values of 98.8% with a coefficient variation of 1.9%.

Key words: Flow injection; Potentiometry; Electroplating baths; Fluoroborate; Tubular electrode

1. Introduction

In the plating industry, tetrafluoroborate is often used instead of cyanide as a stabilizer in electroplating baths due to its lesser toxicity [1]. Continuous analytical control during the coating processes is necessary as changes in the chemical composition cause the hydrolytic breakdown of this compound. Both on-line and off-line automation would improve the advantages of these procedures and reduce the cost of the analytical control.

Today, flow-injection analysis (FIA) is a well-established analytical method and can be regarded as a significant alternative in the automation of the analytical processes. FIA with potentiometric detection has proven to be highly advantageous over other detection processes in as much as it enables the user to perform analyses

* Corresponding author.

SSDI 0003-2670(94)00073-U

over a wide range of concentrations without having to subject the samples to prior treatment.

Although there are some references in the literature to electrodes sensitive to tetrafluoroborate [2–10], the characteristics of these are not appropriate for continuous flow determinations. The most noteworthy disadvantages are the instability of the values of the potentials, the reduced reproducibility of the results and, more specifically, the short lifetime of the devices, all of which can be attributed to the use of a liquid ion sensor and/or electrodes with an inner reference solution. The elimination of the inner reference solution from conventional electrodes [11,12] and the use of appropriate sensor systems have improved the aforementioned characteristics and furthermore, enabled the construction of tubular detectors that can be inserted in FIA manifolds for automatic analyses.

To prevent the problems described above, the authors constructed and evaluated tubular detectors without an inner reference solution, sensitive to tetrafluoroborate and based on tetraoctylammonium and 2-nitrophenyloctyl ether. The tubular detectors thus constructed were used for the quantitative tetrafluoroborate FIA determinations in metal fluorborate baths. The high concentrations of the analyte in the samples, required the development of a high-dispersion flow injection (FI) system that could be coupled on-line for the analytical control of this chemical parameter during electro-coating processes.

2. Experimental

2.1. Reagents and solutions

All chemicals were of analytical-reagent grade, or similar, and were used without further purification, except tetraoctylammonium bromide that was recrystallized in ethyl acetate. Deionized water (specific conductivity below 0.1 mS cm^{-1}) was used to prepare all solutions.

The stock sodium tetrafluoroborate (0.1 M) solution was prepared from the respective acid after a quantitative reaction with sodium hydroxide. The concentration of fluoroboric acid was initially determined by a potentiometric titration with sodium hydroxide (previously standardized with potassium hydrogenphthalate). The more dilute solutions used for electrodes evaluation within the low dispersion FIA system were obtained by diluting the previous one.

A 6 M sodium tetrafluoroborate solution for preparing the standards, used in the high dispersion FIA system, was obtained in a similar manner, whereby the preparation was made directly from the corresponding acid at 50% (w/w). The latter was previously titrated according to the British Standard 2657 [13]. The remaining sodium tetrafluoroborate standards with concentrations of 5, 4, 3, 2 and 1 M were prepared by diluting the more concentrated solution.

2.2. Equipment and electrodes

The potentiometric measurements were performed with a Crison micropH 2002 digital potentiometer (sensitivity of ± 0.1 mV), using an Orion 900200 double junction silver chloride/silver reference electrode with sodium sulphate 0.033 M in the outer compartment.

The fluoroboric acid potentiometric determinations were made with a Crison μTIT 802 automatic titrator and a 102023006 Ingold glass electrode as indicator.

A single channel Metrohm E586 Labograph recorder was used for recording the analytical signals obtained from the tubular electrodes inserted in the FIA manifolds.

Within the manifolds, the solutions were pumped by Gilson Miniplus 2 or Ismatec S-840 peristaltic pumps, and samples introduced into the manifold with a manual 4-way Rheodyne 5020 rotating injection valve. Omnifit PTFE tubing (internal diam. 0.8 mm) was used for connections. Some auxiliary laboratory-made devices, namely joints and grounding electrodes, were made from stainless steel tubing [14].

2.3. Construction of the electrodes

The tubular electrodes were constructed as previously described [12]. A sensor solution of tetraoctylammonium tetrafluoroborate in 2-

nitrophenyloctyl ether was used for preparing the membranes. The latter solution was obtained by dissolving approximately 0.04 g of tetraoctylammonium bromide in 1.2 g of 2-nitrophenyloctyl ether to which approximately 5 cm^3 of chloroform was added. The resulting solution was shaken with sodium tetrafluoroborate 0.1 M, in order to extract the tetrafluoroborate anion and the chloroform was later evaporated in a nitrogen stream.

The membranes were obtained by mixing 0.4 cm^3 of the sensor solution with 0.18 g of PVC previously dissolved in tetrahydrofuran.

Conventionally-shaped electrodes were also prepared with similar membranes and used for comparative studies of the characteristics of the tubular detectors.

After applying and drying the membranes, both the tubular and the conventionally-shaped detectors were conditioned in a sodium tetrafluoroborate 0.1 M solution. When not in use, these were kept in open air and conditioned for at least 15 min before they were next used.

2.4. Preparation of the plating baths

The different plating baths analyzed were prepared synthetically in accordance with the indications given in the literature [15] from concentrated solutions of different metal tetrafluoroborates, kindly supplied by Derivados del Flúor, S.A. (Spain). The resulting samples were introduced into the FIA manifold without any prior preparation.

3. Results and discussion

3.1. Evaluation of the tubular electrodes

A single channel FIA manifold (Fig. 1) was constructed for the evaluation of the intrinsic operating characteristics of the tubular electrodes. Where the dispersion of the injected solutions was less than 3 [16], this permits to compare their operational characteristics with the corresponding conventionally-shaped in batch conditions.

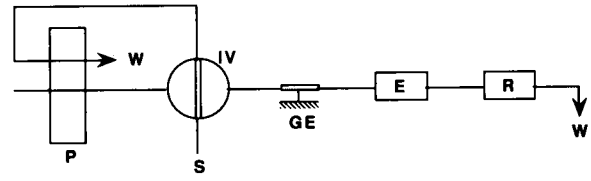

Fig. 1. Low dispersion FIA manifold for the evaluation of intrinsic response characteristics of the tubular electrode. (P) peristaltic pump; (IV) injection valve; (S) sample; (GE) grounding electrode; (E) tubular electrode, (R) Reference electrode; (W) waste; ($Q_1 = 8.2$ ml/min).

As an optimization criterion it was attempted to ensure that the intensity of the transient analytical signals resulting from the tubular electrodes as FIA detectors are, as far as possible, similar to those obtained with conventionally-shaped electrodes under batch conditions. Thus, the volume of the injected sample was increased until the peak height achieved corresponds to approximately 95% of the value related to the stationary state.

In order to obtain reproducible analytical signals and a high sampling rate, the length of the reaction coil, L_1, was diminished while the carrier flow, Q_1, was increased.

The above optimization led to the manifold illustrated in Fig. 1, in which the carrier ($Q_1 = 8.2$ ml/min) was a 0.033 M sodium sulphate solution with a fixed sodium tetrafluoroborate concentration (10^{-6} M) to stabilize the baseline potential of the detector, in which the sodium tetrafluoroborate standards (150 μl) with a 0.1 M ionic strength adjusted with sodium sulphate, were injected.

The above FIA manifold was used to determine the general performance of the tubular electrodes, namely the linear response range and the calibration slope. To do so, various successive calibrations of the tubular electrodes were performed in the concentration interval of between 5×10^{-8} and 10^{-1} M, by injecting into the manifold, solutions of sodium tetrafluoroborate with a set ionic strength of 0.1 M.

Table 1 gives the mean values for the calibration parameters obtained by two repeated determinations, respectively, with two tubular elec-

Table 1
General performances of the tubular detector and the conventionally-shaped electrode tested [a]

Characteristics	Conventionally-shaped electrodes	Tubular electrodes
LLLR (M) [b]	1.5×10^{-5}	3.7×10^{-6}
LLD (M) [c]	2.3×10^{-6}	1.1×10^{-6}
Slope (mV/dec)	58.2 ± 0.8	59.3 ± 0.9
Working pH range (10^{-2}–10^{-4} M) [d]	3.0–11.5	2.7–11.5
Reproducibility (mV/day)	± 0.5	± 0.5
Lifetime (years)	~3	~3
Sampling rate (h^{-1})	–	360

[a] Mean values of two assays performed with 3 conventionally-shaped electrodes and 2 tubular electrodes.
[b] Lower limit of linear response.
[c] Lower limit of detection.
[d] Concentration of sodium tetrafluoroborate in aquous solution.

trodes. Moreover the values for the same parameters as determined under batch conditions with the corresponding conventionally-shaped electrodes are given for comparison.

To evaluate the reproducibility of the analytical signals provided by the tubular electrodes, standard deviations of the potential readings obtained by twenty successive injections of sodium tetrafluoroborate standard solutions in the analytical range from 10^{-5} to 10^{-2} M, were determined. For all the concentrations tested, standard deviations lower than 1 mV were obtained.

The lifetime was evaluated by performing periodic evaluation calibrations of the tubular electrodes in the linear concentration range. The devices did function, with no changes in their response characteristics, for a continuous period of at least 3 years.

The studies of the influence of pH on the potential of the electrodes were carried out with an FIA manifold similar to the one previously described for a nitrate tubular electrode [17]. The experiments were performed with sodium tetrafluoroborate solutions with concentrations of 10^{-2}, 10^{-3} and 10^{-4} M. Under those conditions, no significant alterations in the tubular electrodes potential were observed in the pH range from about 2.7 to 11.5.

The potentiometric selectivity coefficients of the detectors towards different interferents were determined by a procedure similar to the separated solution method used for the evaluation of conventionally-shaped electrodes [18]. For this, 10^{-2}, 10^{-3}, 10^{-4} and 10^{-5} M solutions in the principal and interfering ion were successively injected into the flow-injection manifold.

Table 2
Potentiometric selectivity coefficients (log K^{pot}) for conventionally-shaped and tubular units

Interferents	Conventionally-shaped electrodes		Tubular electrodes	
	10^{-3} M	10^{-2} M	10^{-3} M	10^{-2} M
Fluoride	-2.8 ± 0.1	-3.6 ± 0.1	-2.7 ± 0.1	-3.6 ± 0.1
Borate	-1.9 ± 0.2	-2.7 ± 0.2	-1.7 ± 0.2	-2.6 ± 0.2
Phosphate	-3.9 ± 0.1	-4.3 ± 0.1	-4.10 ± 0.02	4.30 ± 0.02
Bromide	-2.07 ± 0.04	-2.47 ± 0.04	-1.6 ± 0.1	-2.1 ± 0.1
Nitrate	-1.56 ± 0.03	-1.87 ± 0.03	-0.81 ± 0.07	-1.0 ± 0.1
Perchlorate	$+0.7 \pm 0.1$	$+0.8 \pm 0.1$	$+0.60 \pm 0.07$	$+0.7 \pm 0.7$
Chloride	-2.7 ± 0.1	-3.26 ± 0.03	-2.4 ± 0.1	-2.9 ± 0.1

Table 2 gives the mean values of log K^{pot} for 10^{-2} and 10^{-3} M solutions of interferent when two of the detectors were evaluated in triplicate. In the same table the values determined with the conventionally-shaped electrodes under similar conditions were also included.

The results show that there is no interference from the majority of the ions tested, there only being a negligible interference from the perchlorate ion. The latter, however, is of no consequence given that the detectors are to be applied to electrolytic baths in which the perchlorate ion is not present.

3.2. Application of the tetrafluoroborate detectors in flow-injection systems for the analysis of plating baths.

Given the high content of the tetrafluoroborate anions in the baths to be analyzed (concentrations varying approximately from 1.5 to 5.6 M) and the difficulty in controlling the ionic strength of the samples, without resorting to a highly concentrated and consequently interfering electrolyte, a high dispersion FIA system was developed to perform, on-line, the required sample dilution [16]. Hence, a FIA manifold (Fig. 2) was developed whereby the sample, after injection, disperses into the carrier (water) throughout

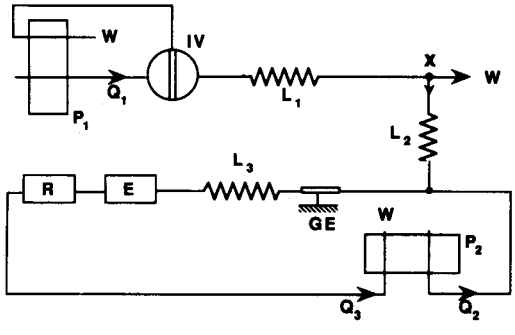

Fig. 2. Split zone flow-injection manifold for tetrafluorborate determination in plating baths: (P_1 and P_2) peristaltic pumps; (IV) injection valve; (S) sample; (GE) grounding electrode; (E) tubular electrode, (R) Reference electrode; (W) waste; ($Q_1 = 8.5$ ml/min; $Q_2 = 0.45$ ml/min; $Q_3 = 0.66$ ml/min), ($L_1 = 126$ cm; $L_2 = 3.6$ cm; $L_3 = 50$ cm); X = splitting point.

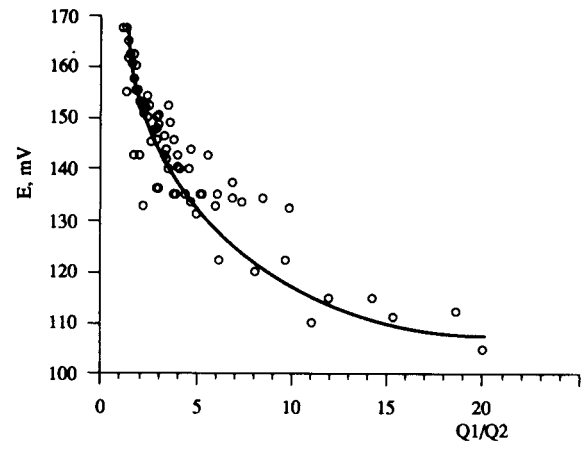

Fig. 3. Variation of the analytical signal (mV) as a function of the Q_1/Q_2 ratio for an injection volume of 7 μl in a 1 M sodium tetrafluorborate solution

the length (126 cm) of coil L_1. Meanwhile, as the sample passes split point X, a small amount is aspirated into coil L_2. The length of the latter was reduced to the minimum physically possible (3.6 cm) because it was noted that the sampling rate depended considerably on its length. The sample amount flowing through this coil, is determined by the difference between the actual flow Q_3 and the flow pertaining to the addition of the ionic strength adjuster, Q_2.

In order to simplify the optimization of the manifold, flow Q_3 was set at a reduced rate, 0.66 ml/min, so as to better control the separation flow at split point X. Thus, in a first stage, the optimization consisted of choosing that ratio of the flow rates of carrier (Q_1) and diluter (Q_2), which enables a high degree of dilution (Fig. 3). As shown in Fig. 3, the intensity of the analytical signal decreases significantly while the Q_1/Q_2 ratio increases. The experimental values chosen for both variables were 8.5 and 0.45 ml/min, respectively. Secondly, by lowering the volume of the sample plug, a minimum value that enables a reproducible analytical signal within the zone of the linear response of the electrode, was selected. An injection volume of 7 μl was selected.

In the final setup, shown in Fig. 2, the sample plug was injected into the carrier (water) flowing

Table 3
Tetrafluorborate determination of tetrafluorborate contents in plating baths by FIA

Type of bath	BF_4^- (mol dm^{-3})	Recovery (%)
$Cu(BF_4)_2$ for electroforming with low concentration	2.09 ± 0.09	98.0 ± 2.1
$Cu(BF_4)_2$ for electroforming with high concentration	4.02 ± 0.19	99.7 ± 3.4
$Pb(BF_4)_2$ for corrosion-protective deposits (up to 25 μm)	1.76 ± 0.11	96.0 ± 3.1
$Pb(BF_4)_2$ for corrosion-protective heavy deposits (to 1.25 mm)	4.08 ± 0.13	100.8 ± 3.9
$Pb(BF_4)_2$ and $Sn(BF_4)_2$, with 7% Sn, for bearings	3.44 ± 0.11	97.1 ± 1.7
$Pb(BF_4)_2$ and $Sn(BF_4)_2$, with 60% Sn for printed circuit	3.52 ± 0.15	98.9 ± 2.4
$Pb(BF_4)_2$ and $Sn(BF_4)_2$, for high throwing power soldering	5.66 ± 0.10	101.2 ± 3.9

at a rate of 8.5 ml/min and mixed, after the stream splitting, with a solution of 0.033 M sodium sulphate and 10^{-5} M sodium tetrafluoroborate introduced through a side channel at a rate of 0.45 ml/min.

The use of the high dispersion FIA system for analytical determinations in baths justified the evaluation of the calibration parameters for the detectors when inserted in the manifold. By injecting sodium tetrafluoroborate solutions with concentrations between 1 an 6 M, a linear response from the tubular detector was obtained, with a correlation coefficient of 0.9997 and a slope of approximately 59 mV/dec, which leads to the conclusion that the dispersion does not affect the response characteristics of the detector.

In Table 3, the results of tetrafluoroborate determinations covering seven different plating baths samples are presented. The given values are the mean of five determinations performed with two tubular detectors.

Because there is no reference method applicable to the analysis of tetrafluoroborate in electrolytic baths, as far as we know, the quality of the results was assessed by means of recovery method. The mean values obtained were of 98.8% with a variation coefficient of 1.9% ($n = 7$).

The precision of the measurements was evaluated after 20 successive injections of each sample, resulting in standard deviations inferior to ±0.095 mV.

4. Conclusions

The performances obtained with tetrafluoroborate conventionally-shaped electrodes using the same membrane as constructed tubular detectors, leads one to conclude that significant improvements have been achieved when compared with tetrafluoroborate electrodes, previously referred to in literature [2–10]. The improvements obtained were substantially with regard to the stability of potentials, reproducibility, and most especially, their lifetime. These aspects justified the preparation of tubular electrodes and their application to continuous flow analyses.

The above improvements resulted from the use of an appropriate sensor system such as tetraoctylammonium and 2-nitrophenyloctyl ether, and the elimination of the inner reference solution.

By using tubular electrodes, with small dead volumes, the implementation of a mechanically stable albeit more elaborated flow design, was achieved. Moreover, it was possible to perform determinations in electroplating baths with high

concentrations of tetrafluoroborate, if the samples are diluted, on-line, before detection. The setup described with potentiometric detection, allows accurate results and suggest its use to the quantitative determination of other highly concentrated chemical species by detector substitution.

This method may be used either on or off-line and thereby contributes to decreasing the cost of industrial control processes.

Acknowledgements

This work was granted by the Junta Nacional de Investigação Científica (Project No. PBIC/CEN/1107/92). The authors also wish to thank the Departamento de Educación, Universidades e Investigación del Gobierno Vasco, Spain (Project No. 92-37), for its financial support.

References

[1] B.T. Duhart, EPA-600/4-76-005, USEPA, Cincinnati, OH, 1976.
[2] R.M. Carlson and J.L. Paul, Anal. Chem., 40 (1968) 1293.
[3] R.E. Reinsfelder and F. Schultz, Anal. Chim. Acta, 65 (1973) 425.
[4] C. Liteanu, E. Hopirtean and E. Stefaniga, Rev. Roum. Chim., 23 (1978) 653.
[5] E. Hopirtean and E. Stefaniga, Rev. Roum. Chim., 23 (1978) 137.
[6] S.S.M. Hassan and M.A.F. Elmosalmi, Fresenius' Z. Anal. Chem., 325 (1986) 178.
[7] A.G. Fogg, A.S. Pathan and D.T. Burns, Anal. Lett., 7 (1974) 545.
[8] K-Chang, H-C Fu, W.X. Wang, Hou-Chi and Y. Qun, Hua Hsuech Hsuch Pao, 38 (1980) 223.
[9] M. Panoch and M. Semler, C.A., 104 (1986) 1221772.
[10] Q. Yan, C. Lin and J. Luo, Fenxi Huaxue, 12 (1984) 412.
[11] G.J. Moody, J.D.R. Thomas, J.L.F.C. Lima and A.A.S.C. Machado, Analyst, 113 (1988) 1023.
[12] R.A.S. Lapa, J.L.F.C. Lima and A.M.R. Silva, Il Farmaco, 45 (1990) 901.
[13] British Standard Specification for Fluorboric Acid and Metal Fluorborates for Electroplating BS 2657, 1974.
[14] S. Alegret, J. Alonso, J. Bartroli, A.A.S.C. Machado and J.L.F.C. Lima, Quim. Anal., 6 (1987) 278.
[15] F.A. Lowenheim, Electroplating: Fundamentals of Source Finishing, Mac Graw Hill, New York, 1978.
[16] J. Ruzicka and E.H. Hansen, Flow Injection Analysis, Wiley, New York, 1988, p. 25.
[17] S. Alegret, J. Alonso, J. Bartroli, J.L.F.C. Lima and A.A.S.C. Machado, Anal. Lett., 18 (1985) 2291.
[18] IUPAC, Analytical Chemistry Division on Analytical Nomenclature, Pure Appl. Chem., 53 (1981) 1907.

ELSEVIER

Analytica Chimica Acta 293 (1994) 43–48

ANALYTICA CHIMICA ACTA

Nanoband electrodes for electrochemical stripping measurements down to the attomole range

Joseph Wang [a,*], Xu Rongrong [a], Tian Baomin [a], Jianyan Wang [a], Clifford L. Renschler [b], Christine A. White [b]

[a] *Department of Chemistry and Biochemistry, New Mexico State University, Las Cruces, NM 88003, USA,*
[b] *Sandia National Laboratories, Division 1812, Albuquerque, NM 87185-5800, USA*

(Received 29th December 1993; revised manuscript received 23rd February 1994)

Abstract

Small-volume measurements of lead and cadmium have been accomplished using a mercury-coated nanoband electrode. The band electrodes are fabricated from ultrathin carbonized polyacrylonitrile films. The coupling of the inherent sensitivity of stripping analysis, with submicroliter sample volumes and enhanced plating efficiency (due to enhanced diffusional flux) results in remarkably low detection limits of 100 femtograms (5×10^{-16} mole) lead. To our knowledge, this detection limit is significantly lower than previously reported values for electrochemical stripping work. Air-saturated quiescent sample droplets can thus be assayed by the square-wave or potentiometric stripping modes. Variables influencing the stripping response are explored and the stripping performance is characterized. Applicability to direct measurements of lead in microliter blood samples is illustrated.

Key words: Sensors; Stripping voltammetry; Potentiometry; Stripping analysis; Attomole detection limits; Blood; Lead; Microliter analysis; Nanoelectrodes

1. Introduction

Stripping analysis is a very powerful electrochemical technique for monitoring trace metals [1,2]. Traditionally, stripping measurements have been carried out in 10–50 ml cells, in connection with the static mercury drop or rotating mercury film electrodes. However, recently there has been a considerable interest in stripping analysis of very small sample volumes, in connection with microscale determinations of trace elements. Various microcells have been developed for metal measurements in microliter (0.005–0.100 ml) samples [1,3–7]. Such miniaturization has been accomplished through the use of special cell geometries [3,4] or by reducing the size of the working electrode [5–7]. In particular, mercury-coated carbon fiber microelectrodes (7–10 μm diameter) have allowed measurements in sample volumes down to 5 μl [5–7].

This paper describes the utility of mercury-coated nanoband electrodes for performing stripping assays in total sample volumes as small as 500 nl. The use of microelectrodes in stripping

* Corresponding author.

SSDI 0003-2670(94)00098-7

analysis is advantageous not only for microscale measurements, but offers also an improved plating efficiency (due to a greatly enhanced diffusional flux) and assays without supporting electrolytes (due to smaller ohmic drops) [8–10]. Such advantages become more pronounced by further reducing the size of the working electrode into the nanometer regime. The nanoband electrodes, used in the present work, are based on a ultrathin carbon film technology, developed at Sandia National Laboratories [11]. Films of controllable thickness (10–500 nm) can thus be fabricated by spin casting polyacrylonitrile (PAN), followed by high temperature carbonization of the coating. By sandwiching these films between insulating supports and polishing their edge, one can obtain band electrodes of nanoscopic dimensions [12,13]. The resulting carbon-based nanoelectrodes can serve as substrates for the mercury film, as compared to common (metallic) band electrodes, prepared from metal foils or vacuum deposited metal films [14]. (Metallic substrates usually result in an irreproducible stripping behaviour due to the formation of intermetallic compounds, a low hydrogen overvoltage and solubility in mercury [1].) In the following sections we demonstrate that the coupling of the inherent sensitivity of stripping analysis with the reduced (submicroliter) sample volume and the larger edge effect, accrued from the use of nanoband electrodes, results in remarkably low (femtogram) detection limits, as compared to the picogram detectability characterizing stripping work at carbon-fiber based electrodes [5,6].

2. Experimental

2.1. Apparatus and procedure

A TraceLab potentiometric stripping unit (PSU 20, Radiometer) and an IBM PS/2 555 × computer were used to obtain the stripping potentiograms, while a BAS-100A electrochemical analyzer (Bioanalytical Systems (BAS)) was employed for square-wave stripping voltammetry.

The band electrode was constructed by using the quartz/carbon film/glass sandwich assembly, in a manner similar to that used in our laboratories for fabricating enzyme nanoband electrodes [12,13]. The carbon film thickness was 360 nm. A silicone adhesive sealant (Loactite, Cleveland, OH) was placed on the carbon coated quartz plate and smoothed to a thin layer that covered one half of the plate. The glass slide was placed on top and was tightened to the quartz plate (by applying pressure during the curing process). Electrical contact was established to the back of the electrode. The electrode face was smoothed (with alumina slurries down to 0.05 μm) to ensure that only the band surface contributes to the stripping response. Two configurations, for stripping work with microliter and large volumes, were employed (as shown schematically in Fig. 1A and B, respectively). In the former case, a silver wire (0.18 mm diameter) was glued to the working electrode body, ca. 0.4 mm away from the edge of the carbon film, and served as a quasi-reference electrode. The inverted electrode was placed in a covered polyethylene container (2-cm diameter, 3-cm height), to minimize contamination and solution evaporation. Drops were dispensed with an adjustable micropipette (Oxford Benchmate). Large-volume experiments were carried out in a 10 ml cell (Model VC-2, BAS), in connection with a Ag/AgCl reference (Model RE-1) and platinum wire auxiliary electrodes. The

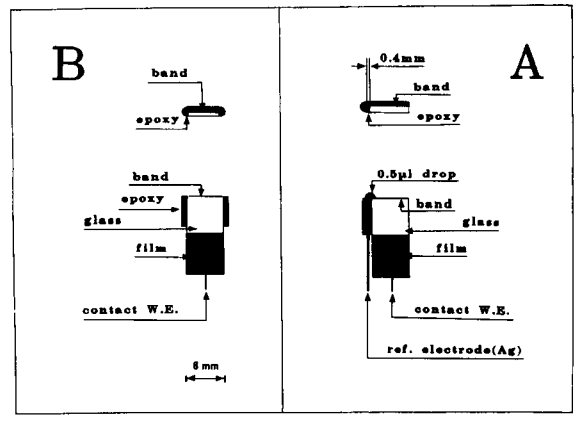

Fig. 1. Schematic diagrams of the carbon-film nanoelectrode used in connection with microliter (A) and large-volume (B) analyses: side and top views (bottom and top, respectively). See text for details.

mercury film was deposited in-situ during the measurement, and was "cleaned" at 0.0 V for 1 min after each cycle.

2.2. Reagents

All solutions were prepared from analytical-grade chemicals and doubly-distilled water. Stock solutions of lead, cadmium and mercury were purchased from Aldrich and diluted daily as required. The supporting electrolyte was an acetate buffer solution (0.1 M, pH 4.2); sodium chloride (1 M) was added in the small-volume experiments (in accordance with the silver wire quasi-reference electrode). The sheep blood was obtained from the College of Agriculture at NMSU, and stored in venojet sterile ampules.

3. Results and discussion

3.1. Large-volume characterization experiments

The stripping performance of the nanoband electrode was first characterized in a conventional (10 ml) cell. Two stripping modes, potentiometric stripping analysis (PSA) and square-wave stripping voltammetry (SWSV), were employed, as neither is prone to oxygen interferences (and hence can use nondeaerated solutions, as desired for the subsequent microliter work). For the same reason, most of the characterization work employed an unstirred solution during the deposition step.

Fig. 2 displays stripping potentiograms (A) and voltammograms (B) for a nondeaerated mixture containing 40 μg/l lead and cadmium, at the nanoband (a), carbon-fiber (b), and glassy-carbon (c) mercury-coated electrodes. A stirred solution was used for the deposition at the macro surface, while quiescent ones were employed in connection with the micro- and nanoelectrodes. Similar to its larger counterparts, the nanoelectrode exhibits a well-defined stripping response, and permits convenient quantitation following short deposition periods. While the voltammetric peak current, and corresponding background, are significantly smaller at the nanoelectrode (note the different current scales), this tiny electrode offers higher current densities (due to improved plating efficiency), e.g. only 40-fold smaller peaks vs. the carbon fiber, despite the 100-fold decrease in surface area. Overall, because of the efficient preconcentration at the nanoelectrode, its stripping operation is within the current range of commercially available instruments. Unlike the voltammetric stripping, the potentiometric stripping response is only slightly influenced by the drastic change in the surface area (note the similar scales), and offers improved resolution between the neighbouring peaks.

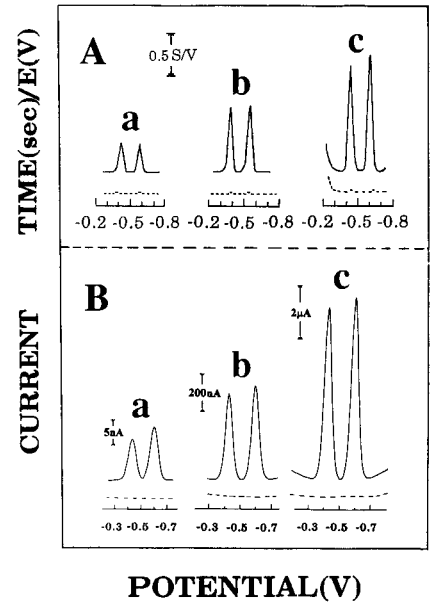

Fig. 2. Stripping potentiograms (A) and voltammograms (B) for 40 μg/l lead and cadmium at the mercury-coated carbon film nanoband (a), carbon-fiber (b) and glassy carbon (c) electrodes. Deposition time and potential, 1 (A) and 2 (B) min at −1.10 and −1.20 V, respectively. Stirring rate, 0 (a,b) and 900 (c) rpm. Electrolyte, 0.1 M acetate buffer (pH 4.2), containing 10 mg/l mercury (10 ml). Square-wave stripping (B) with 20-mV amplitude, 45-Hz frequency and 6-mV step. Dashed curves represent the response for the blank solution.

Fig. 3 examines the effect of solution stirring rate (during the deposition) on the potentiometric stripping lead peak height of the nanoband (A), carbon-fiber (B) and glassy-carbon (C) coated electrodes. The response of the macro glassy carbon electrode is strongly influenced by the con-

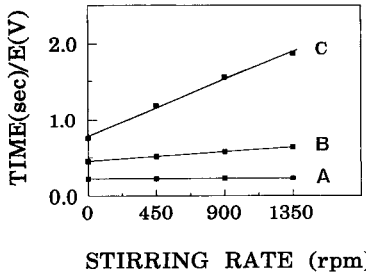

Fig. 3. Effects of stirring rate upon the lead potentiometric stripping peak at the mercury-coated carbon film nanoband (A), carbon-fiber (B) and glassy carbon (C) electrodes. 1 min deposition at −1.0 V. Other conditions, as in Fig. 2A.

vective transport (slope, 0.83 ms/V · rpm). In contrast, and as expected from the smaller dimensions of the working electrode, the micro and nanoelectrodes display a reduced stirring-rate dependence. Yet, while some convection effect is observed at the carbon-fiber electrode (slope, 0.13 ms/V · rpm), the nanoelectrode displays an independence upon the convective transport (slope, 0.01 ms/V · rpm, with similar signals for 0 and 1350 rpm). Such behaviour reflects the enhanced diffusional flux (i.e. plating efficiency) at the nanoscopic surface.

Fig. 4 displays square-wave stripping voltammograms at the nanoelectrode for solutions of increasing cadmium and lead levels [10–80 μg/l (a–h)] following a 2 min deposition. Both peaks

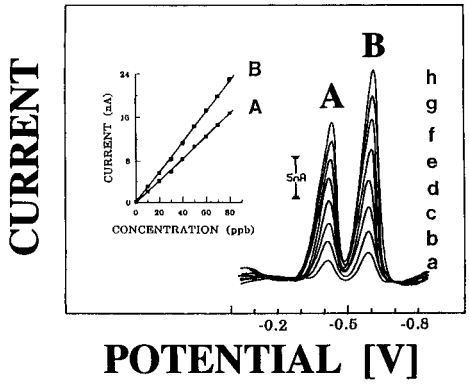

Fig. 4. Stripping voltammograms for mixtures containing increasing levels of cadmium and lead, 10–80 μg/l (a–h). Deposition for 2 min at −1.0 V, using unstirred solutions. Other conditions, as in Fig. 2B(a).

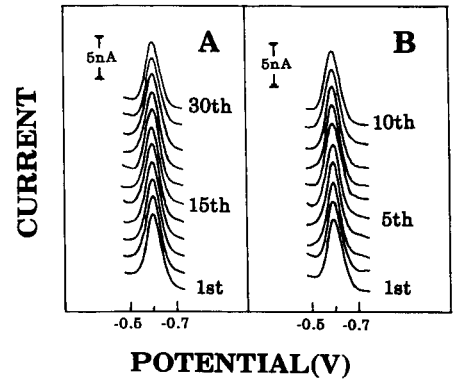

Fig. 5. Microliter volume analysis. Repetitive voltammetric stripping measurements of 10 μg/l lead in the same 1-μl drop (A) and in different drops (B). Deposition at −1.40 V for 1 min. Square-wave stripping with 25 mV amplitude, 100 Hz frequency, and 4 mV step. The electrolyte solution contained also 1 M sodium chloride and 120 mg/l mercury.

increase linearly with the metal concentration over the entire range (see inset). A least-square treatment of these data yields sensitivities of 0.291 and 0.211 nA · l/μg for lead and cadmium, respectively. Note again the well-defined response for low (10 μg/l) concentration following a short deposition period from an unstirred solution. The effect of the deposition time upon the square-wave stripping response for 40 μg/l lead and cadmium was examined over the 0–8 min range (not shown). Both peaks increase linearly with the time up to 5 min, and then more slowly.

3.2. Assays of extremely small volumes

The feasibility of using the nanoelectrode for microliter stripping analysis was examined subsequently. Fig. 5 displays repetitive stripping voltammograms for 10 μg/l lead in the same 1 μl drop (A) and using different drops (B). A well-defined lead response is observed despite the very small (nondeaerated/unstirred) samples and the low analyte concentration. The relative standard deviations over these complete series, 4.0 (A) and 2.0 (B)%, are similar to those of stripping assays of large-volume solutions with conventional electrodes. The stable response obtained for the same drop during the prolonged series of

30 runs (total 90 min) indicated that evaporation from the drop is not significant. The weight of a 1 μl drop decreased by 2% over a 30 min period. No apparent carry over was observed between sequential 2 μl drops, containing 10 and 30 μg/l lead (not shown; conditions, as in Fig. 5). The lead peak was not influenced by the sample volume over the 0.5–5 μl range. (The more negative deposition potential and lead peak potential are in accordance to the quasi reference electrode.)

Fig. 6 displays square-wave stripping voltammograms for 0.5 and 1.0 μg/l lead in a 0.5 μl droplet. While no response is observed without accumulation (a), a well-defined peak is obtained following preconcentration (b–e). The peak increases with the preconcentration time, with some curvature at periods longer than 15 min. The limit of detection – calculated from 3 times the noise [of Fig. 6A(c)] – was found to be 0.2 μg/l. This value means that 100 femtograms (i.e. 500 attomoles!) can be detected in the 0.5 μl of solution used. To the best of our knowledge, such a value is significantly lower than any previously reported for stripping work, in particular, and for trace metal analysis, in general.

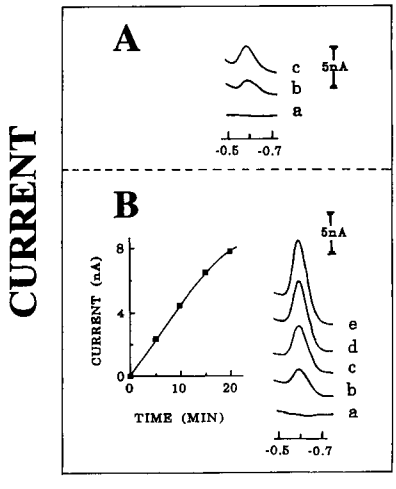

Fig. 6. Stripping voltammograms for 0.5 (A) and 1.0 (B) μg/l lead in 0.5 μl droplets. Deposition time, 0 (A(a), B(a)), 5 (B(b)), 10 (A(b), B(c)), 15 (B(d)) and 20 (A(c), B(e)) min. Other conditions, as in Fig. 5.

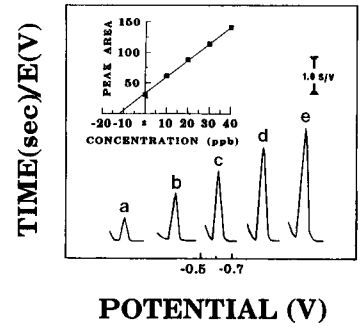

Fig. 7. Determination of lead in a whole blood sample. Potentiograms for the sample (a) and subsequent concentration increments of 10 μg/l (b–e). 2 min deposition at −1.4V. The blood sample was diluted (10-fold) in a 0.3 M HCl solution, containing 125 mg/l mercury ion.

Fig. 7 demonstrates the suitability of the nanoband electrode to the determination of lead in a 5 μl blood sample. With simple (1 : 10) dilution and a short (2 min) accumulation, the electrode exhibits a well-defined lead peak for the spiked sample (a). This peak can be easily quantified following standard additions of 10 μg/l (b–e). The resulting standard addition plot (also shown) yielded a lead level of 118 μg/l (after correction for the dilution), which is in good agreement with the spiked value (100 μg/l) and the original (unspiked) level of 9 μg/l (that was determined in a separate run). Measurements of lead in a diluted (1 : 1) drinking water sample were accomplished in a similar fashion (not shown).

In conclusion, we have demonstrated that the coupling of the remarkable sensitivity of stripping analysis with assays of submicroliter volumes (accrued from the use of nanoband electrodes) extends the detection limit to the attomole range. The volumes used in the present work are significantly smaller than those previously employed in stripping analysis. Such an operation holds great promise for clinical testings for toxic metals, and in particular for screening blood lead in children. Even smaller (thinner) nanoband electrodes can be fabricated to further enhance the plating efficiency, and hence the sensitivity. While the new electrode was demonstrated within the framework of anodic stripping measurements of lead or

cadmium, it could be extended to numerous other trace elements or organic compounds, in connection with different versions of stripping analysis (e.g. cathodic or adsorptive ones).

Acknowledgement

This work was supported through Sandia National Laboratories, under U.S. Department of Energy contract (DE-AC04-94AL85000). Support from the Centers for Disease Control (CDC contract CCR608615-01) is also acknowledged.

References

[1] J. Wang, Stripping Analysis, VCH, Deerfield Beach, FL, 1985.
[2] T. Copeland and R. Skogerboe, Anal. Chem., 46 (1974) 1257A.
[3] T. DeAngelis, R. Bond, E. Brooks and W.R. Heineman, Anal. Chem., 49 (1977) 1792.
[4] R. Eggli, Anal. Chim. Acta, 91 (1977) 129.
[5] W. Frenzel, Anal. Chim. Acta, 196 (1987) 141.
[6] A. Baranski, Anal. Chem., 59 (1987) 662.
[7] J. Peng and W. Jin, Anal. Chim. Acta, 264 (1992) 213.
[8] L. Nyholm and G. Wikmark, Anal. Chim. Acta, 273 (1993) 41.
[9] J. Wang, P. Tuzhi and J. Zadeii, Anal. Chem., 59 (1987) 2119.
[10] S. Daniele and G.A. Mazzocchin, Anal. Chim. Acta, 273 (1993) 3.
[11] C.L. Renschler, A.P. Sylwester and L. Salgado, J. Mater. Res., 4 (1989) 452.
[12] J. Wang, A. Brennsteiner, A. Sylwester and C.L. Renschler, Electroanalysis, 3 (1991) 505.
[13] J. Wang, N. Naser and C.L. Renschler, Anal. Lett, 26 (1993) 1333.
[14] M. Samuelsson, M. Armgarth and C. Nylander, Anal. Chem., 63 (1991) 931.

ELSEVIER

Analytica Chimica Acta 293 (1994) 49–54

ANALYTICA CHIMICA ACTA

Demonstration of an optimised evanescent field optical fibre sensor

Z.M. Hale, F.P. Payne *

Engineering Department, University of Cambridge, Trumpington Street, Cambridge CB2 1PZ, UK

(Received 16th December 1993; revised manuscript received 23rd February 1994)

Abstract

Evanescent field optical fibre sensors have been widely exploited in biochemical assays. The use of multimode fibres has revealed a number of limitations, especially in the case of absorption sensors. In this paper, we describe the use of a tapered single mode optical fibre as an optimised system to act as an evanescent wave absorption sensor, with a calcium detection scheme as a model system.

Key words: Sensors; Evanescent field optical fibre sensor

1. Introduction

Evanescent field sensing with optical fibres has been examined by many researchers [1–6]. This configuration is ideal for the detection of a variety of chemical analytes since the evanescent field extends beyond the fibre core with the bulk of the light remaining within and guided by the core. Sensors have been developed which make use of either evanescent field absorption [7,8], or fluorescent capture [9,10]. In most cases these have been based on multimode fibres, and, in the case of absorption sensors, calibration assumes a modified form of Beer's law

$$P_{out} = P_{in}\, e^{-\alpha\eta l} \qquad (1)$$

where α is the absorption coefficient specific to the bulk material, η is the fraction of light in the evanescent field, l is the length of a reference cell, or extent of interaction of the sensor, and P refers to the optical power. The absorption coefficient is specific to a given solution at a given wavelength. The absorbance, $\log_{10}(P_{in}/P_{out})$, varies linearly with the concentration. As much of the evanescent field as possible must be exposed to the surroundings in order to maximise the device sensitivity. Furthermore, the distribution of optical power amongst the fibre modes is extremely important; higher order modes have evanescent fields which extend further beyond the waveguide than the fields of lower order modes. Selectively exciting the higher order modes can result in high sensitivity. As a result, some multimode fibre devices depend on the selective excitation of high order modes through the use of masks or appropriate launch conditions. In general, these launch conditions are

* Corresponding author.

SSDI 0003-2670(94)00104-T

difficult to repeat reliably. As an alternative, and to avoid these difficulties, some multimode sensors rely on uniformly exciting all the modes in the fibre. However, recent work with such fibre sensors has shown that the results often deviate from Beer's law, and that Eq. 1 does not in fact apply; in particular, Eq. 1 overestimates the absorbance, whilst deviations from a linear variation with concentration are also observed. A careful analysis of the modal distribution in multimode fibres clarifies this considerably [11]. Each mode of the initially uniform distribution experiences different attenuation in the external medium; consequently, an initially uniform distribution of modes is quickly lost. Using a rigorous modal analysis, we have recently shown that under these circumstances the absorption along the fibre is described more precisely by [11]:

$$\frac{P_{out}}{P_{in}} = f(\gamma) \tag{2}$$

where $\gamma = 2\alpha l/V$. The function $f(\gamma)$ is defined by

$$f(\gamma) = \frac{2\pi}{\gamma}[\mathbf{H}_1(\gamma) - Y_1(\gamma)] - \pi[\mathbf{H}_0(\gamma) - Y_0(\gamma)] - \frac{4}{\gamma^2} \tag{3}$$

α is the bulk absorption coefficient, l is the interaction length, $\mathbf{H}_1$ and $\mathbf{H}_0$ are Struve functions, Y_1 and Y_0 are modified Bessel functions [12], and V is the normalised frequency defined by

$$V = \frac{2\pi\rho}{\lambda}\sqrt{n_1^2 - n_2^2} \tag{4}$$

The fibre core refractive index is n_1, the index of the absorbing region surrounding the fibre is n_2, and the radius of the fibre core is ρ. Eq. 2 is in good agreement with experimental data for multimode fibre absorption sensors, and describes reasonably well the observed deviations from Beer's law [7,11].

In Fig. 1 we compare Eq. 3 with the simple Beer's law prediction from Eq. 1. From this it is clear that the design and calibration of a multimode sensor depends critically on the excitation

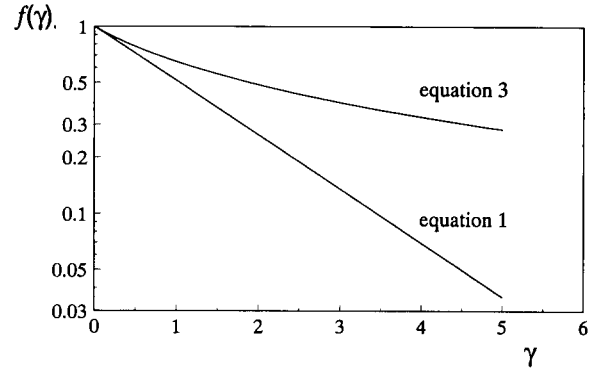

Fig. 1. Fibre absorbance plotted as a function of γ (defined in Eqs. 2 and 3). The prediction of Eq. 1 is plotted for comparison.

scheme of the fibre modes. A natural way to avoid many of these difficulties is to use a single mode optical fibre; this allows the modal field to be well-defined. However, there remains the problem of gaining access to the evanescent field. One possible method is to remove part of the fibre cladding by polishing; characteristically this allows only a small portion of the external field to be available for interaction, unless the external index of refraction is adjusted to match that of the fibre. This would typically require the use of viscous index matching oils, which are not generally compatible with biochemical assays. In this paper we propose an alternative means of gaining access to the evanescent field, based on an adiabatically tapered single mode optical fibre. The taper consists of a region of fibre with decreasing cross-section followed by an expanding section, as illustrated in Fig. 2. The tapers were fabricated in a manner described earlier [13]. A section of the single mode fibre is melted in an oxybutane flame whilst being gradually stretched. Careful control of the tapering process results in an adiabatic taper: the taper angle is small and changes slowly over the extent of the taper (several mm in length). Because of this, the fundamental fibre mode that enters the tapered region does not couple to either cladding or radiation modes [14]. The overall transmission loss across the taper is of the order of 0.1 dB or less. For this work, very small diameter tapers were constructed, of waist

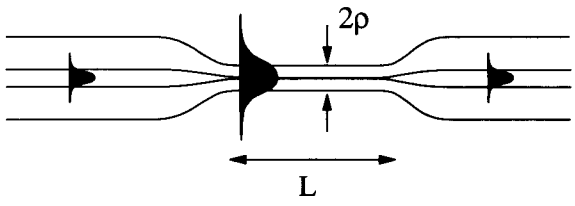

Fig. 2. Idealised geometry of a tapered fibre with the fundamental mode shown propagating. The length of the tapered section is L, and the radius at the taper waist is ρ.

diameter approximately one micron, so that the original core of the fibre no longer makes a significant contribution to the waveguiding. As a result, the evanescent field extends far into the medium surrounding the cladding at the taper waist, where there is a new effective waveguide consisting of the fibre cladding and the external solution. Because the light always remains in the fundamental guided mode, with no lossy coupling to radiation, it is clear that the absorption through the tapered region will be described by Beer's law of the form in Eq. 1.

In this paper, we demonstrate the feasibility of using a tapered single mode fibre as an absorption sensor by designing and testing a sensor for calcium ions in solution. The detection of calcium, as well as magnesium ions, is currently performed in clinical assays, which often require the preparation of standards and numerous dilutions. The use of fluorescence or absorption optical sensors for determination of such ions is of interest particularly because of the potential for real-time results [15–17]. As a preliminary, we verified that the tapered fibre sensor obeys Beer's law by measuring the evanescent wave absorption using an aqueous solution of methylene blue. We then describe a tapered fibre sensor capable of detection down to 2 ppm (w/w) of Ca^{2+} ions.

2. Experimental

The dye used for the confirmation of Beer's law, methylene blue, was purchased from Aldrich. The reagents for the calcium absorption detection, calcium acetate and calmagite, were supplied by Sigma. The pH 10 buffer solution was obtained from Fisons.

The single mode silica optical fibre used for the sensor, SM-450, was specially made and supplied by Fibercore (formerly York Technology). It had a numerical aperture of 0.18, and a cutoff wavelength of 450 nm. The diameter of the nominally circular core of the fibre was about 1.7 μm, whilst the outer cladding diameter was 80 μm. The silica cladding refractive index was 1.458, the core refractive index was 1.469. The tapers used in this study had waist diameters of 1–2 μm. A tungsten white light source and monochromator were used for the spectral absorption measurements of methylene blue in a dye cell, and when circulating around a tapered fibre. A 632.8 nm He–Ne laser was used for the taper absorption measurements over a range of methylene blue concentrations. The calmagite solutions used for the calcium detection were illuminated with the 514-nm line of an air-cooled argon-ion laser from Omnichrome.

The optical detection system used in all the measurements consisted of a large area photodiode (RS Components, data sheet 12508). Signal levels were recorded on a Model SR510 lock-in amplifier from Stanford Research Systems. The lock-in amplifier was linked to a personal computer via an analog-to-digital acquisition card.

3. Results

The absorption characteristics of the tapered fibre were first determined using an aqueous solution of methylene blue. The spectral absorption characteristics of methylene blue were first measured using a bulk dye cell 1 mm thick, with a variety of concentrations of methylene blue that varied from 5×10^{-6} to 2×10^{-3} M, using the experimental arrangement shown in Fig. 3. For these measurements a tungsten white light source and monochromator were used. The absorption spectrum between 640 and 675 nm was measured; a typical result measured at a concentration of 5 μM is shown by the dashed line of Fig. 4. The absorption peak is at 664 nm. The dye cell was then replaced by a tapered fibre immersed in

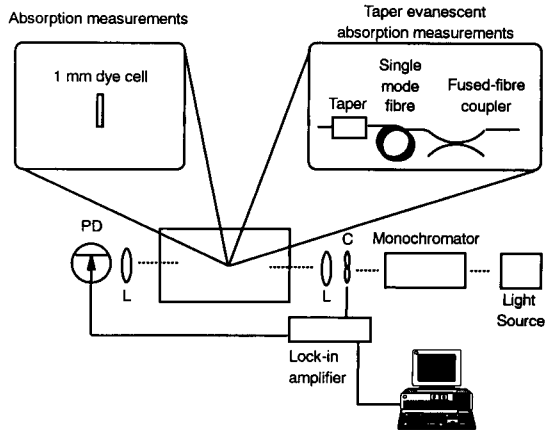

Fig. 3. Apparatus used for absorption measurements. The absorption spectra of the dye cell and of the taper immersed in methylene blue solutions were made with a white light source and monochromator. The variation of absorption with dye concentration for the taper was made at a fixed wavelength using a He–Ne laser (632.8 nm) and with the monochromator removed. PD = Photodiode, L = lens, C = optical chopper.

solutions of methylene blue and spectral absorption measurements were made across the same concentration range using the same configuration shown in Fig. 3. After each measurement, the taper was cleaned with deionised water and a baseline spectrum of water taken and compared to an initial spectrum. All data was thereby rendered comparable. These results are shown in Fig. 4 by the solid line. The response of the taper follows that of the bulk measurements, but with a somewhat lower absorption level, due to an external refractive index of 1.33 around the taper.

The absorption of the taper in aqueous methylene blue was then measured at the specific wavelength of 632.8 nm over a range of concentrations from 5×10^{-6} to 1×10^{-3} M using the arrangement shown in Fig. 3, but with the white light source replaced with a He–Ne laser, and without the monochromator. The data were analysed using a least-squares regression fit to test for a linear and a square root dependence on concentration [18]. The latter is reported as characteristic of multimode evanescent absorption sensors, particularly if surface contamination is noted. A linear fit [$n = 105$ (15 repetitions across 7 concentrations), slope = 26.5 M^{-1}, intercept = 0.11, $r^2 = 0.83$, $\sigma_x = \sigma_y = 0.01$] was confirmed ($\chi^2$ linear = 0.32, χ^2 square root = 4), indicating that Beer's law applies with little measurable deviation.

Having established that the tapered fibre obeys Beer's law, a simple absorption-based sensor was investigated. Calcium ion concentration levels were detected by the use of an indicator, calmagite [1-(1-hydroxyl-4-methyl-2-phenylazo)-2-naphthol-4-sulfonic acid]. Calmagite functions as a typical acid–base indicator, with different colours corresponding to different levels of pH. The indicator conforms to Beer's law [19]. The blue colour of calmagite exhibited in a pH 10 buffer is changed to red by the addition of either calcium or magnesium ions [19]. The absorption maximum for calmagite was found to be at 523 nm. The nearest convenient wavelength available to us was the 514.5 nm line from an argon-ion laser, and this was used for the calcium absorption measurements. All calcium detection with the taper was performed without modifying the refractive index of the test solution. Concentrations of calcium, from calcium acetate, ranging from 40 μM to 5 mM were measured. After each measurement, the taper was cleaned with deionised water and a baseline spectrum taken, as before, to normalise the data as well as to verify that no calcium had become bound to the fibre. The optimised system for calcium ion detection in an optical fibre sensor is shown in Fig.

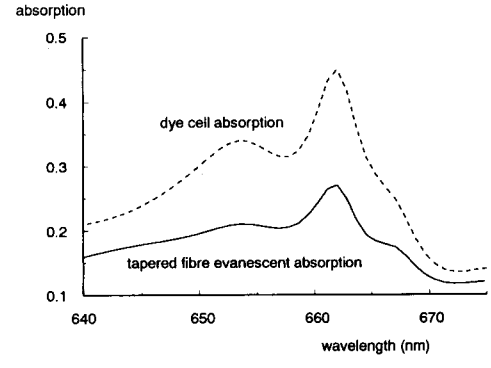

Fig. 4. Absorbance measurements of methylene blue. Dye cell measurements are shown by the dashed line. Taper evanescent absorption is shown by the solid line. The concentration of methylene blue is 5 μM.

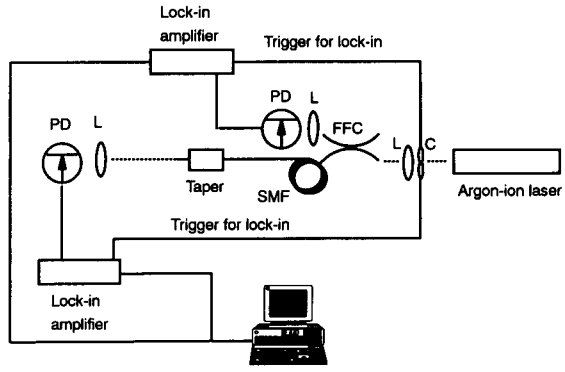

Fig. 5. Optimised configuration for calcium absorption measurements. Both lock-in amplifiers were triggered from the optical chopper. FFC = Fused fibre coupler, SMF = single mode fibre, PD = photodiode, L = lens, C = optical chopper.

5. A fused optical fibre coupler, with the power split between the two output arms in the ratio 55:45, was fabricated in order to monitor the input power and output power simultaneously. This automatically eliminates any laser power fluctuations from the received attenuation data at the far end of the optical fibre. The sensor showed the expected linear response with concentration, confirming that Beer's law is obeyed, with an r^2 value of 0.98 [$n = 90$ (9 repetitions of 10 concentrations), slope of $-45.5\ M^{-1}$, intercept of -0.02, $\sigma_x = 0.03$, $\sigma_y = 0.01$], demonstrating that changes in optical absorption of the indicator dye is a good predictor of the Ca^{2+} concentration. The detection limit is estimated as 2 ppm (w/w) Ca^{2+} ion in solution.

4. Conclusions

We have demonstrated the feasibility of using a tapered single mode optical fibre as an evanescent wave absorption sensor. Our device accurately follows Beer's law, unlike the reported data from multimode fibre sensors. Detecting Ca^{2+} demonstrates that the sensor displays both good sensitivity and linearity. Although the current configuration of the absorption sensor did not have the indicator bound to the surface of the optical fibre, immobilisation techniques are well-documented [20]. In a future paper we will describe a simple scheme to develop an indicator-immobilised fluorescent sensor based on the affinity of penicillinase to glass surfaces [21]. Further, other model systems have been developed using silanisation as the basis for linking reactive proteins directly to the fibre. Our work here confirms the theoretical analysis of evanescent absorption in optical fibres, and lays the basis for optimisation of evanescent field optical fibre sensors.

Acknowledgement

Z.M. Hale would like to thank the United States Air Force Institute of Technology for personal support.

References

[1] B.I. Bluestein, I.M. Walczak and S.-Y. Chen, Trends Biotechnol., 8 (1990) 161–168.
[2] E.E. Carlyon, C.R. Lowe, D. Reid and I. Bennion, Biosensors Bioelectronics, 7 (1992) 141–146.
[3] R.G. Eenink, H.E. de Bruijn, R.P.H. Kooyman and J. Greve, Anal. Chim. Acta, 238 (1990) 317–321
[4] R.G. Heideman, R.P.H. Kooyman, J. Greve and B.S.F. Altenburg, Appl. Optics, 30 (1992) 1474–1479.
[5] B.D. MacCraith, Sensors Actuators B, 11 (1993) 29–34.
[6] R.B. Thompson and F.S. Ligler, in D.L. Wise and L.B. Wingard (Eds.), Biosensors with Fiberoptics, Humana Press, Clifton, NJ, 1991, pp. 111–138.
[7] V. Ruddy, B.D. MacCraith and J.A. Murphy, J. Appl. Phys., 67 (1990) 6070–6074.
[8] M.D. DeGrandpre and L.W. Burgess, Anal. Chem., 60 (1988) 2582–2586.
[9] L.C. Shriver-Lake, R.A. Ogert and F.S. Ligler, Sensors Actuators B, 11 (1993) 239–243.
[10] I.M. Walczak, W.F. Love, T.A. Cook and R.E. Slovacek, Biosensors Bioelectronics, 7 (1991) 39–48.
[11] F.P. Payne and Z.M. Hale, Int. J. Optoelectronics, 8 (1994) 743–748.
[12] M., Abramowitz and I.A. Stegun, Handbook of Mathematical Functions, Dover, 1972.
[13] H.S. MacKenzie and F.P. Payne, Electronics Lett., 26 (1990) 130–132.
[14] Z.M. Hale and F.P. Payne, Sensors Actuators B, 17 (1994) 233–240.
[15] J.R. Lakowicz, H. Szmacinski and K.W. Berndt, SPIE Proc., 1648 (1992) 150–163.

[16] D.C., Ashworth, H.P. Huang, R., Narayanaswamy, Anal. Chim. Acta, 213 (1988) 215–217.
[17] B.P.H. Schaffar and O.S. Wolfbeis, Anal. Chim. Acta, 217 (1989) 1–9.
[18] V. Ruddy, B. MacCraith and J.A. Murphy, SPIE Proc., 1172 (1989) 83–92.
[19] F. Lindstrom and H. Diehl, Anal. Chem., 32 (1960) 1123–1127.
[20] F. Baldini and S. Bracci, Sensors Actuators B, 11 (1993) 353–360.
[21] L.F. Cullen, J.F. Rusling, A. Schliefer and G.J. Papariello, Anal. Chem., 46 (1974) 1955–1961.

ELSEVIER

Analytica Chimica Acta 293 (1994) 55–65

ANALYTICA CHIMICA ACTA

Potentiometric stripping determination of mercury(II), selenium(IV), copper(II) and lead(II) at a gold film electrode in water samples

Eduardo Pinilla Gil [1], Peter Ostapczuk *

Institute of Applied Physical Chemistry, Research Center Jülich, D-52425 Jülich, Germany

(Received 27th September 1993; revised manuscript received 17th January 1994)

Abstract

A potentiometric stripping method for the determination of Se(IV), Hg(II) at the ng l^{-1} level, which also permits the simultaneous determination of Cu(II) and Pb(II) has been developed. Anodic stripping by an oxidative constant current follows the reductive deposition of the elements in atomic form at a gold film working electrode. The performance of the method has been checked on a certified reference water sample. The method was adapted to operate on river water samples, and the results of the determination of mercury at low ng l^{-1} level in sea water are also reported. Typical interferences that can occur in water samples are discussed.

Key words: Potentiometry; Copper; Lead; Mercury; Selenium; Gold film electrode; Waters

1. Introduction

Stripping potentiometry is a powerful electroanalytical technique for the rapid, precise and sensitive determination of trace amounts of metals and some metalloids in solution. The fact that in most cases this technique can be directly applied to liquid samples without previous treatment, and that it is virtually free from the interference of dissolved oxygen, makes it attractive in comparison with stripping voltammetry, the most widely accepted electroanalytical technique for trace element determination. Both techniques are based on the same principle, e.g., the analytes are first deposited (and hence preconcentrated) on the electrode surface while the solution is stirred, and then stripped back to the solution in the measurement step. Stripping potentiometry works on a film electrode, usually made of electrochemically deposited mercury or gold on a glassy carbon support, which is easier to operate and maintain than the mercury drop which is normally employed in stripping voltammetry. Stripping potentiometry can compete with non-electroanalytical techniques for trace element analysis in terms of price and possibility of automation, but its general use is still rather limited.

* Corresponding author.

[1] On leave from Departamento de Química Analítica y Electroquímica, Universidad de Extremadura, 06071 Badajoz, Spain.

SSDI 0003-2670(94)00075-W

The usual material of choice for the working electrode in stripping potentiometry is mercury film on glassy-carbon support. With this electrode many elements can be determined, including those that form amalgams and those that can be adsorbed in some specific form on the mercury surface. Mercury as electrode material has the main drawback of a limited anodic range. This prohibits its use for the determination of those elements that are oxidized at a higher electrode potential than that for the mercury oxidation under the solution conditions. Both this fact and mercury toxicity, with the associated problems of handling and disposal, for example in large-screening clinical programs [1], have promoted an increasing interest to other electrode materials. Gold is a good alternative since it is a noble material that can either be used as a disc or fibre electrode, or deposited from a solution of Au(III) to form a stable and reproducible film. Many elements are soluble in gold, thus enabling its wide use in electrochemical stripping analysis. Our interest has been focused in this work on the simultaneous determination of selenium and mercury at the level they occur in natural waters, typically below 1 $\mu g\ l^{-1}$ for Se(IV) [2] and below 0.1 $\mu g\ l^{-1}$ for Hg(II) [3], and the posibilities of simultaneous determination of other elements.

The electroanalytical determination of mercury has been reported by many authors. The results of the extensive work based on the deposition of metallic mercury on a glassy carbon surface can be found in the work of Gunasingham et al. [4]. For the determination of mercury on a gold working electrode, Andrews et al. [5], found a detection limit of 0.02 ng l^{-1} for Hg(II) by anodic differential pulse stripping voltammetry on a rotating gold disc electrode. However, the method was not applied to real samples. The same technique was applied by Sipos et al. [6] for the simultaneous determination of Hg and Cu in natural water and wine. They used a twin gold electrode for the determination of Hg(II) below 100 ng l^{-1}. Huiliang et al. [7–9] have determined mercury and other elements in a flow system with potentiometric stripping on a gold fibre working electrode. A detection limit of 45 ng l^{-1} (10 min deposition time) was found. The method was proved to be useful in tap water [7] and a certified urine standard [8]. Other methods include adsorption of volatilized mercury metal on a gold disc and subsequent voltammetric stripping in thiocyanate solution [10], with a detection limit of 30 ng of Hg(II), and operation with a gold film electrode modified with tri-*n*-octylphospine oxide [11]. A study on alternating current (AC) anodic stripping voltammetry on a rotating gold disc electrode has been reported [12,13]. Hátle [14] applied differential pulse voltammetry to the determination of mercury in sediments on various working electrodes, including gold disc and film surfaces.

Electrochemical methods for selenium determination on mercury working electrodes, including speciation studies about the selenite and selenate forms, have been reported by many authors in recent years [15–17]. These methods cannot be used if the simultaneous determination of mercury is desired.

Some work on the determination of selenium on gold electrodes has been reported. Andrews and Johnson [18] studied the reductive deposition of Se on a gold surface and found it to be a somewhat complicated process, producing Se in three distinct states of activity accompanied with three anodic voltammetric stripping waves. If the selenium concentration is sufficiently low, so that less than a monolayer is formed during the deposition step, the method was useful for analytical purposes. They reported a detection limit of 0.04 $\mu g\ l^{-1}$ in 0.1 M $HClO_4$ medium. Al-Bakri [19] determined Se(IV) in river water samples by anodic stripping voltammetry on a gold film electrode. Adeloju et al. [20] developed a direct calibration method for the stripping voltammetric determination of Se in biological materials. A similar procedure, with a gold film working electrode, has been proposed by Wu et al. [21] for the determination of Se in hair and flour samples.

The electroactive form of selenium in the presently developed methods is Se(IV), whereas Se(VI) gives no response. This fact is useful for speciation studies, but it has the drawback that a reductive chemical process is needed for the determination of total selenium in environmental samples.

No references have been found about the simultaneous potentiometric determination of low concentrations of Se and Hg on the gold film electrode. The main problems of such a method seem to be the overlapping of the metal signals and the risk of interferences from other elements. Masking of the Se response by the oxidation of the gold film is also a disturbing process. We have found the determination to be feasible under certain conditions and this will be discussed in the following sections.

2. Experimental

2.1. Equipment

An PSU 20 TraceLab potentiometric stripping unit (Radiometer, Copenhagen) with a SAM20 sample station (Radiometer), connected to a personal computer, was used. The system operates on a three-electrode basis, a glassy carbon disc working electrode with a surface area of about 7 mm^2, a calomel reference electrode (sat. KCl) and a platinum wire auxiliary electrode. A gold film was deposited on the glassy carbon surface as described in the Procedures section. To avoid mercury contamination from the calomel material when determining sub $\mu g\ l^{-1}$ levels of mercury, the reference electrode was separated from the sample solution by a quartz tube filled with the electrolyte solution. This solution was replaced at the beginning of every working session. The electrodes fit in the analytical cell (50 ml, made of quarz) by holes in a plastic head. A stirring device consisting of a plastic propeller with adjustable speed (from 300 to 3000 rpm) is included in the system.

A home made UV digestion system was employed for water samples pretreatment. It consists of an air cooled 150 W UV lamp surrounded by twelve 100 ml closed quarz tubes to contain the samples.

2.2. Reagents and glassware

All reagents used were of Suprapur grade (when available) or analytical reagent grade (Merck). Deionized water (resistance higher than 15 MΩ) was obtained from a Milli-Q system (Millipore).

A Au(III) stock plating solution was obtained by dissolving 1 g of Au in minimum amount of aqua regia and then diluting to 1 l with HCl solution. The plating solution used for film formation contained 50 mg l^{-1} of Au(III) and 0.04 M of HCl, and were prepared by dilution of the stock.

Stock standard solutions of the elements of interest were prepared by dilution of Titrisol solutions (Merck), and acidified to pH 2 with $HClO_4$. All standard solutions with element content lower than 1 mg l^{-1} were prepared daily.

All glassware and quarz measurement cells were cleaned in a 1:3 HCl–water solution at 60°C for three days, and then in 1:5 Suprapur HNO_3–water until used.

2.3. Real samples

Standard reference water (SRM 1643b) was obtained from the U.S. National Bureau of Standards and used without any treatment.

Water from the Riachuelo river (Buenos Aires Province, Argentina), was collected in polyethylene bottles, and acidified at the sampling site with 0.1 M Suprapur nitric acid. Once in the laboratory, it was filtered through a 0.45 μm pore size membrane and stored at 4°C in polyethylene bottles.

Sea water samples were collected from the surface of the North Sea at several sampling places and mixed. Samples were acidified with 1% HNO_3 and stored unfiltered in a glass container.

2.4. Procedures

UV digestion of the water samples

This procedure was chosen to decompose dissolved organic matter. A 20-ml water sample was placed in a quarz tube. Acidification to pH 2 was performed by perchloric acid and 20 μl of 30% H_2O_2 were added to enhance the digestion effect

of the UV light. It should be noticed that addition of H_2O_2 will cause most of the Se(IV) to be oxidized to Se(VI). The irradiation was carried out for 6 h. The lamp was switched off for 15 min after 2 and 4 h of operation, to prevent excessive heating of the samples.

Glassy carbon pretreatment

When a glassy carbon electrode that was stored for a long time was taken to perform the analysis, it was pretreated in the following way: first it was polished with decreasing grain size Al_2O_3 powders (1, 0.1 and 0.05 μm) until the surface presented a mirror-like surface. Then the electrode was immersed in a 0.05 M H_2SO_4 solution and cycled for 10 min between -500 and 500 mV at a sweep rate of 10 mV s^{-1}. Then, twenty cycles of 10 s deposition and subsequent stripping were performed from -250 to 900 mV by applying a constant current of 30 μA to the working electrode. This treatment was found to be essential to obtain a smooth and reproducible behaviour of the stripping curves. Once completed, it was not necessary to repeat it if the electrode is in continuous use within the specified potential window (-250 to 900 mV). However, after several measurements in samples with a high chloride content, like sea water, the treatment had to be repeated, starting with cleaning of the surface by sandpaper.

Gold film plating and conditioning

The gold film was plated by immersing the electrodes in a cell containing 20 ml of 50 mg l^{-1} Au(III) in 0.04 M HCl and applying a potential of -100 mV. After 1 min with moderate stirring rate (about 1200 rpm), a homogeneous and mechanically stable film was obtained. After plating, the electrode was conditioned by immersing it in 0.05 M H_2SO_4 solution and applying a potential of +800 mV for 5 min with moderate stirring. This approach was chosen to get a reproducible film surface, especially at the positive tail of the stripping curves, at a potential that corresponds to the gold film oxidation. At unconditioned film, this tail shifts slowly in the positive direction in subsequent runs, thus causing erroneous measurements mainly affecting the Se signals.

Sample analysis

A 40-ml sample was placed in the quarz measurement cell, 100 μl of concentrated sulphuric acid and 25 μl of 3 M KCl were added and the determination was started. After a 5 s conditioning step, where the potential of the working electrode was set at +950 mV, the deposition step was carried out at a potential of -250 mV. The deposition time varied from 1 to 10 min at a stirring speed of 2100 rpm. After an appropriate rest time of 30 s, the stripping curve was recorded by applying a constant current of 2 μA, until the electrode reached a potential of +900 mV. After a second rest period of 30 s, the background curve was immediately recorded. This curve was substracted from the sample curve to give the corrected signal. The analytical signal evaluated was the peak area, given typically in ms. The metal contents in the samples were evaluated by the standard additions method.

3. Results and discussion

3.1. Optimal chemical conditions for the determination

For the electrochemical stripping determination of mercury on a gold electrode the supporting electrolyte must contain a species capable of complexing Hg(II), since the interaction of this element with gold is very strong. Chloride has been generally selected for this purpose, although bromide could be considered as an alternative. In such a medium, the typical response of the proposed method for the four elements involved in this work is shown in Fig. 1. The peaks are well resolved and measurable at μg l^{-1} level. The gold film oxidation appearing just 100 mV more positive than the Se peak, limits the determination of selenium at very low levels.

The influence of the nature of the mineral acid employed for the determination (HCl, HBr, $HClO_4$, HNO_3 and H_2SO_4) was investigated. HCl and HBr concentrations of 0.1 M, required to give pH 1, were found to be unsuitable for the determination of Se(IV) at the low levels to be expected in natural water. Both halide acids

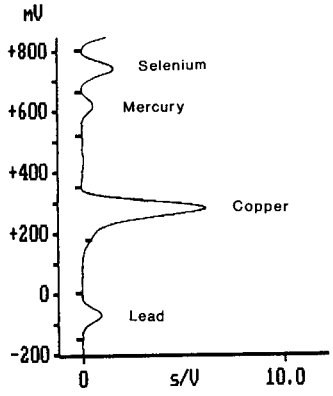

Fig. 1. Typical stripping potentiometric peaks obtained after deposition of the metals on the gold film electrode, in a 40 ml sample solution containing 0.2 μg l^{-1} of Se(IV) and Hg(II), and 2 μg l^{-1} of Cu(II) and Pb(II). Medium: 0.05 M H_2SO_4 and 2 mM KCl; deposition potential, −250 mV; deposition time, 90 s; deposition stirring speed, 2100 rpm; constant current for stripping, 2 μA.

caused a negative shift of the gold oxidation due to the formation of complexes with gold. The lower limit of determination was 1 μg l^{-1} of Se(IV). Moreover, the Hg peak was also shifted in the negative direction so that it tends to overlap with the Cu signal. Among the other three acids checked, HNO_3 gave a somewhat poor reproducibility with increasing amounts of the elements, and was also discarded. $HClO_4$ and H_2SO_4 were found to be the best choices, with the same performance. The only drawback observed for $HClO_4$ was a splitting of the Se signal observed at high concentration, a fact expected from previous reports [18]. In H_2SO_4, the occurrence of the splitting was never observed, so this acid was finally chosen for further work. For Se(IV) concentrations lower than 1 μg l^{-1}, $HClO_4$ can be employed without any problems. A H_2SO_4 concentration of 0.05 M was selected, to ensure a solution pH of about 1. It was found that lowering the acid concentration below 0.01 M caused a decrease in the signals, whereas increasing the acid concentration to 0.1 M or higher did not improve the response attained at 0.05 M.

The effect of changing the chloride concentration in the medium was studied next. As previously mentioned, there must be a complexing agent for Hg(II) in the solution, and the most widely used agent was chloride. This anion was also selected for the present work because some experiments with bromide ions did not show any improvement. Fig. 2 presents the effect of changing the chloride ions concentration on peak potential (A) and area (B) for Se(IV) and Hg(II) signals. The limiting potential due to the oxidation of gold is also presented. The effect on the Cu(II) and Pb(II) signals was less pronounced, and is not shown in the figure. It can be seen in Fig. 2A that the shifting of the gold oxidation potential with increasing amounts of chloride prohibits the proper integration of the 10 μg l^{-1} Se(IV) peak for a Cl^- concentration of about 10

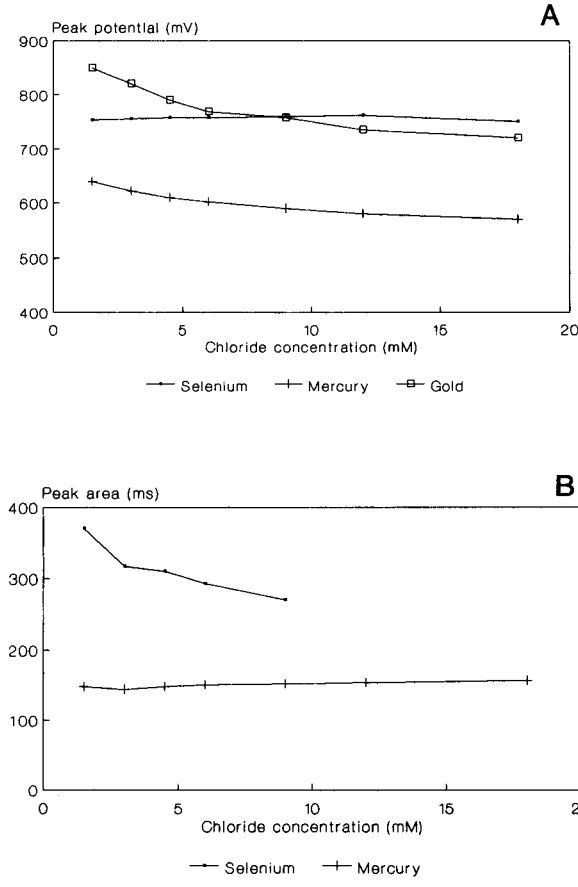

Fig. 2. Influence of chloride concentration on (A) peak potential of selenium, gold and mercury and (B) peak area of selenium and mercury. Concentrations of Hg(II) and Se(IV), 10 μg l^{-1}; deposition time, 30 s. Other conditions as in Fig. 1.

mM or higher. On the other hand, a minimum amount of Cl^- is required to strip the Hg at a sufficiently negative potential which avoids its overlapping with the Se peak. The optimum chloride concentration was 2 mM, although this can be increased up to 10 mM if the Se(IV) concentration to be determined is not lower than 10 $\mu g\ l^{-1}$.

The effect of codeposition of Au with the elements of interest during the accumulation step was also investigated. A first experiment was carried out to check the response with the film plated in situ during the deposition step. In such a situation the response for Se was small and irreproducible. This can be explained by the results of Andrews and Johnson [18] who have shown that the analytically useful stripping signal of Se is coming from an adsorbed monolayer. The in situ approach on the other hand may result in the formation of an electrochemically irreversible intermetallic compound between Se and Au, also described by the same authors. There were also some difficulties in the stripping process of Hg with the in situ plating procedure, mainly because of poor sensitivity and the presence of a mercury signal in the background stripping curve. These facts have been previously reported by Hátle [14] and explained by stronger interaction between gold and mercury during the codeposition process. In view of these results, this mode of operation was discarded, and a preplated film was always used. The addition of Au(III) to the sample solution was also found to be disadvantageous, because the same effect on the Se and Hg signals were observed. A preplated gold film was used for the analysis, with no Au(III) added to the samples. Under these conditions, the film was stable for many determinations if the potential of the electrode is not made too positive for a prolonged period of time.

3.2. *Experimental parameters of the technique*

The influence of the stirring speed on the signals during the deposition step in connection with the cell hydrodynamics, was briefly investigated. The equipment is supplied with two kinds of propellers with different vane sizes. The larger one was more effective. The maximum allowable stirring speed without drawing air into the solution was 2100 rpm when the solution volume in the cell was 40 ml. If the volume of sample available is smaller, the stirring speed has to be adjusted. A minimum volume in the cell of 10 ml is required. The surface of the working electrode was placed as close as possible to the propeller so that the effect of stirring was maximum.

The value of the oxidative constant current employed for the stripping of the elements deposited at the gold film is one of the most decisive factors for the sensitivity of the technique. The theory of potentiometric stripping predicts a linear relationship between inverse current (i^{-1}) and peak area. This fact makes the use of low currents desirable when the concentrations to be determined are low. Unfortunately, the increase of response is accompanied by a corresponding increase of the background noise. The correlation was investigated by running a sample containing 0.5 $\mu g\ l^{-1}$ of Se(IV) and Hg(II), 5 $\mu g\ l^{-1}$ of Cu(II) and 2 $\mu g\ l^{-1}$ of Pb(II). The results for Se(IV) and Hg(II) are shown in Fig. 3. Some deviations from the linear relation were observed for the Se(IV) signal at the lower current values. Cu(II) and Pb(II) gave straight lines, with some deviation for Pb(II) at the low current values. The minimum value of the current that was affordable without a severe increase of background was 2 μA, once the glassy carbon pretreatment described in the Procedures section was completed. Without that treatment, the current should be increased by a factor of 5 or more (at least to 10 μA) to get proper results, with a corresponding loss of sensitivity of the method.

The influence of deposition potential was investigated in the range from -100 to -350 mV. The signals of the four elements, and in particular the Pb(II) peak, tended to increase with a decrease of the deposition potential. At values lower than -300 mV the interference from H_2 generation during the deposition step started because the baseline curve became irregular and irreproducible. A deposition potential of -250 mV was employed for further experiments.

The influence of the deposition time on peak areas was then checked. In accordance with the-

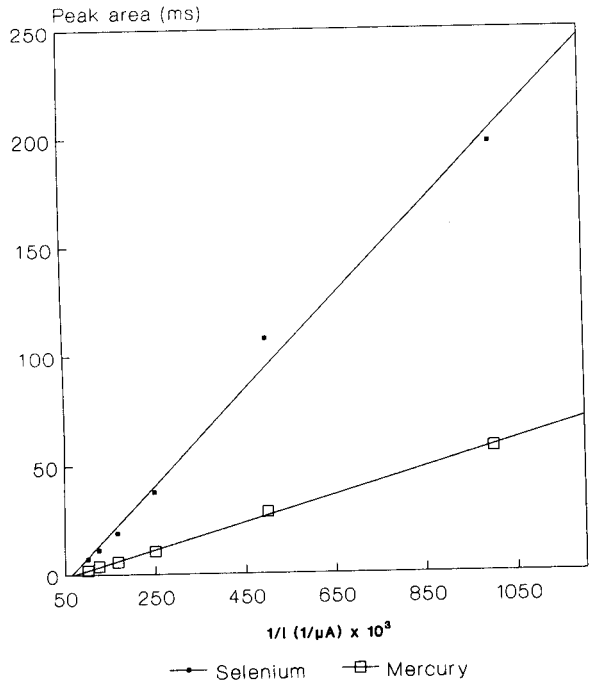

Fig. 3. Influence of constant current value on the peak area in a solution containing 0.5 $\mu g\ l^{-1}$ Se(IV) and Hg(II). Deposition time, 60 s. Other conditions as in Fig. 1.

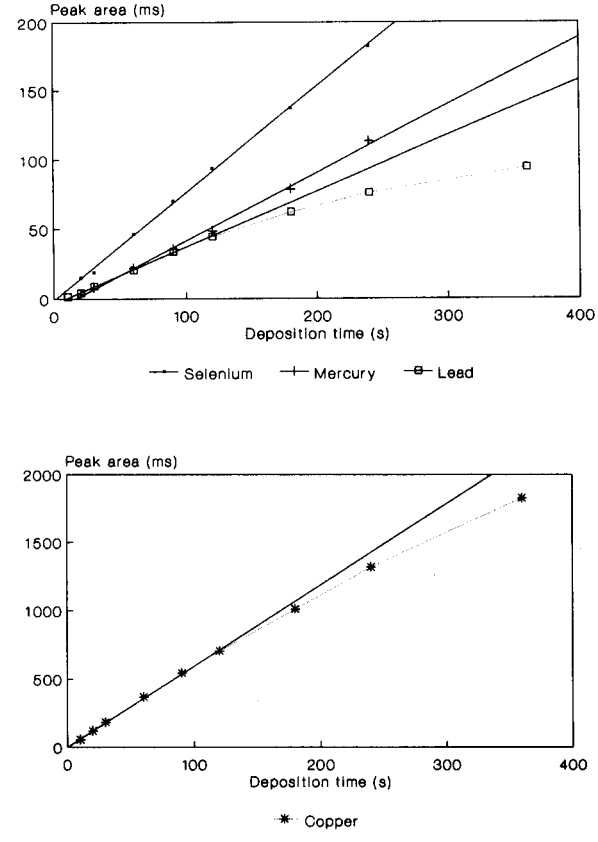

Fig. 4. Influence of deposition time on peak area in a solution containing 0.5 $\mu g\ l^{-1}$ Se(IV) and Hg(II), 5 $\mu g\ l^{-1}$ Cu(II) and 2 $\mu g\ l^{-1}$ Pb(II). Experimental conditions as in Fig. 1.

ory, straight lines were obtained up to the point that the film becomes saturated. This was noticed for Cu(II) and Pb(II), which were present in the water samples at higher concentrations than Se(IV) and Hg(II). Typical lines are shown in Fig. 4.

Linear calibration lines were obtained for the four elements; the main parameters are summarized in Table 1.

The detection limit for Se(IV) is determined by the overlapping of the peak with the gold oxidation signal, which leads to integration errors and irreproducible signals. Despite of the use of very long deposition times, it was not possible to measure reproducible signals from less than 0.1 $\mu g\ l^{-1}$ Se(IV) in the cell, so this was assumed to be the detection limit under the present conditions.

The detection limit for Hg was investigated by running blank solutions with a long deposition time of 10 min with extreme care to avoiding external contamination. The average signal found corresponded to a Hg(II) concentration of 10 ng l^{-1}. The standard deviation was about 5 ng l^{-1}, so the detection limit can be estimated to be 15 ng l^{-1} (3σ level).

Table 1
Main parameters of typical calibration lines obtained in the multielement determination by constant current stripping potentiometry (conditions as in Fig. 4)

Element	Deposition time (s)	Linear range ($\mu g\ l^{-1}$)	Slope (ms/$\mu g\ l^{-1}$)	Intercept (ms)	Regress coef. r
Hg(II)	180	0.05–10.00	114.11	2.13	0.9997
Se(IV)	180	0.20–10.00	525.44	20.68	0.9990
Cu(II)	90	0.50–10.00	96.46	4.64	0.9994
Pb(II)	90	0.50–10.00	12.15	0.67	0.9995

Since Cu(II) and Pb(II) usually occur at higher concentrations than Se(IV) and Hg(II) in natural water samples, no special work was devoted to determine them at very low levels. The determination in the high ng l^{-1} range can be done under the method conditions. The sensitivity can be enhanced if necessary by increasing the deposition time.

3.3. Internal interferences

According to previously reported data obtained during anodic stripping voltammetric studies on the determination of Se(IV) [17,18,20], a mutual interference between that element and Cu(II) is to be expected, since they form an intermetallic compound during their codeposition on the gold film (on a mercury film too). We found an increase of the response of a given Se(IV) concentration for increasing amounts of Cu(II) added to the solution. An average increase of 20% of 0.8 μg l^{-1} Se(IV) signal was observed when increasing the Cu(II) concentration from 2 to 8 μg l^{-1}. At a constant concentration of Cu(II), the Se(IV) signal was found to remain stable, with a relative standard deviation of ca. 3% (six consecutive replicates). From these results, it was not possible to determine all four elements in the same step by the standard additions method. Of course the calibration line approach is not useful since the same concentration of Se(IV) gave very different response in samples with different content of Cu(II). It was decided to determine Cu(II), Pb(II) and Hg(II) first, and then Se(IV), in both cases by standard additions. This scheme was found to be advantageous for the determination of low Se(IV) levels, since the activation of Se deposition caused by Cu(II) from standard addition was utilized to increase the sensitivity.

3.4. Determination in reference water. External interferences

The performance of the method was first checked with an NBS certified reference water sample. The sample contains 0.5 M of HNO_3. Apart from the elements of interest (except mercury, that was not present and thus had to be spiked), the water sample contains many other elements, like arsenic (49 μg kg^{-1}), bismuth (11 μg kg^{-1}), cadmium (20 μg kg^{-1}), iron (99 μg kg^{-1}), manganese (28 μg kg^{-1}), vanadium (45.2 μg kg^{-1}), zinc (66 μg kg^{-1}) or molybdenum (85 μg kg^{-1}). The determinations were performed on 1:10 diluted samples on different days, with the following conditions: concentration of Cl^-, 2 mM; constant current, 2 μA; deposition time, 120 s; deposition potential, −250 mV; end potential, 900 mV. The results of a set of determinations are shown in Table 2. A somewhat low recovery for Se(IV) was achieved. It should be noticed that the concentrations in the cell were ten times lower than those in Table 2 (except for Hg(II) that was spiked directly in the cell), so the accuracy and precision at the actual cell concentration level is acceptable.

Table 2
Determination of Se(IV), Hg(II), Cu(II) and Pb(II) in certified reference water by constant current potentiometric stripping

	Certified (μg/kg)	Found (μg/kg)
Se(IV)	9.7±0.5	8.8 ±0.5
Hg(II)	0.10 (spiked)	0.13±0.04
Cu(II)	21.9±0.4	21.8 ±0.7
Pb(II)	23.7±0.7	23.7 ±1.3

Number of samples assayed = 6.

From the foreign elements present in the sample, only bismuth and arsenic were found to interfere with the determination in this concentration range. Bismuth gave a peak at a slightly more positive potential than copper, as has been previously reported [8]. At a Bi to Cu concentration ratio of 1:2, the determination of Cu(II) was possible with good precision and accuracy. However, additions of Bi(III) cause the determination to be disturbed when the Bi to Cu concentration ratio is higher than 3. However, this is not a case which occurs frequently in natural waters. Arsenic(III) is known to be electroactive at a gold film electrode, and it gave a peak in the potential region between Cu and Pb. The problems associated with the reproducibility of the arsenic stripping signal, that tend to decrease with each replication, are also well documented. No problems were observed for the As–Pb and As–Cu couples

at concentration ratios of 2 in the samples. For concentration ratios larger than 10, the determination of Cu and Pb was affected.

With respect to other elements not present in the reference water that were investigated as possible interferences, only Sb(III) gave a peak at a potential of 500 mV between the Cu(II) and Hg(II) peaks. The signal was anyway well resolved from both other peaks, so the determination was possible even at concentration ratios of 150 in the case of Sb to Hg and 4 for Sb to Cu.

3.5. Determination in river water

The determination of the elements of interest in polluted river water samples was then attempted. A problem was encountered with the tail of the stripping curves, that masked the signal of Se(IV) even when the sample was spiked with 10 ng l^{-1} of Se(IV). This is probably due to the high organic material content of the water. Some attempts of UV digestion of the samples before measurement, according to the protocol described in the Procedures section, improved the curve shape, but unfortunately most of the Se(IV) was oxidized to Se(VI) which is not electroactive under the method conditions. When the treatment was attempted in the absence of H_2O_2, the digestion was not satisfactory. Careful adjusting of the UV digestion conditions may be the choice to obtain proper results. This was not further investigated.

The remaining elements were determined simultaneously with a previous 1:4 dilution of the river water. The results of the determination are shown in Table 3. Good agreement with the spiked concentration was found for Hg(II). For Cu(II) and Pb(II), the results tended to be lower than those obtained by inductively coupled plasma mass spectrometry (ICP-MS).

Other elements found in a general screening of the river water by ICP-MS were not interfering, at least for Hg(II), Cu(II) and Pb(II). Those include iron (596 μg l^{-1}), manganese (100.2 μg l^{-1}), phosphorus (217.3 μg l^{-1}) and sulphur (73.7 mg $^{-1}$).

Table 3
Determination of Hg(II), Cu(II) and Pb(II) in river water by inductive coupled plasma mass spectrometry and constant current potentiometric stripping analysis

	ICP-MS (μg/kg)	CCPSA (μg/kg)
Hg(II) (+)	Not assayed	0.19 ± 0.05
Cu(II)	7.98	6.72 ± 0.52
Pb(II)	9.62	8.40 ± 0.76

Number of samples assayed = 5. (+) Spiked with 0.2 μg/kg.

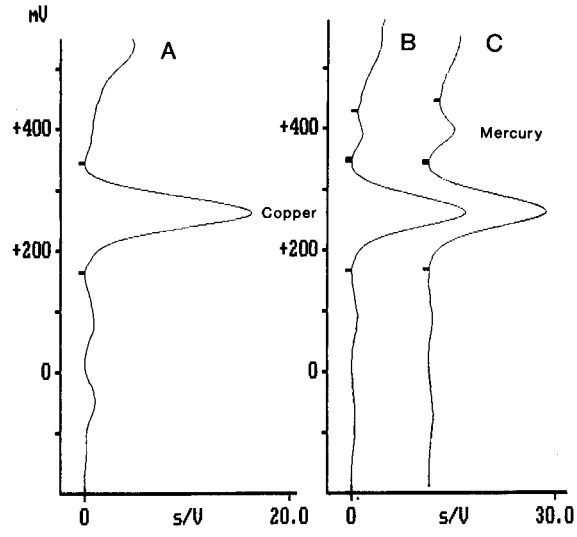

Fig. 5. Potentiometric stripping curves in (A) unfiltered and untreated sea water from the North Sea; (B) same as (A) spiked with 25 ng l^{-1} Hg(II); (C) same as (A) spiked with 75 ng l^{-1} Hg(II). Deposition time, 10 min. Other conditions as in Fig. 1. Note: curves are displaced along the y-axis for clarity.

3.6. Determination of Hg(II) and Cu(II) in sea water

The most important feature of sea water with respect to this method is its high chloride content of about 0.55 M. In this medium, the limiting signal from the gold film oxidation is shifted in the negative direction to a value of about +600 mV, thus masking completely the Se(IV) peak even when present at concentrations higher than 10 μg l^{-1}. The Pb(II) peak is shifted in this medium to about −100 mV, and becomes broad and irreproducible. Fig. 5 depicts the curves obtained in unfiltered sea water after an accumulation time of 10 min. Although the Hg(II) peak

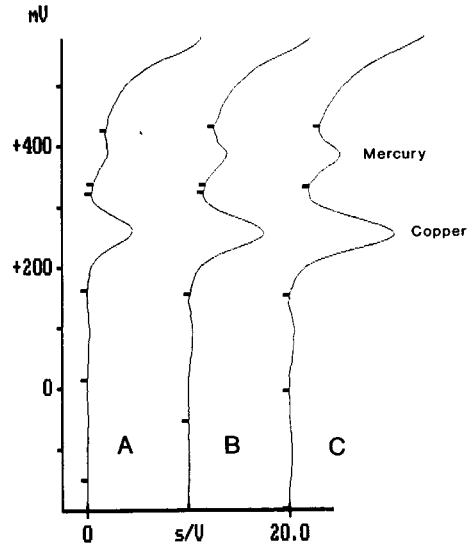

Fig. 6. Potentiometric stripping determination of Hg(II) and Cu(II) in UV digested sea water. (A) Sample curve; (B) and (C), two subsequent standard additions of 0.1 μg l^{-1} of Hg(II) and 0.5 μg l^{-1} of Cu(II). Deposition time, 5 min. Other conditions as in Fig. 1. Note: curves are displaced along the y-axis for clarity.

cannot be directly measured (curve A), there was a clearly different response from standard additions of 25 ng l^{-1} (curve B) and 75 ng l^{-1} (curve C). Since the sea water was analyzed for mercury by cold vapour atomic absorption and gave a value of 25.3 ± 1.2 ng l^{-1}, it was concluded that Hg(II) is probably present in the sea water sample in some chemical form not directly available to be reduced at the deposition potential used in the potentiometric method. To liberate Hg(II) from the binding material, UV digestion was carried out as specified in the Procedures section. After that, it was possible to determine Hg(II) and Cu(II) in the sea water with a deposition time of 5 min. Typical curves obtained during one of the measurements are shown in Fig. 6. The average estimated concentrations after four determinations were 62 ± 19 ng l^{-1} for Hg(II) and 0.79 ± 0.07 μg l^{-1} for Cu(II). The precision of both results can be accepted at this concentration level. The higher concentration of Hg(II) with respect to the cold vapour atomic absorption spectrometry (CVAAS) data can be assigned to the contamination during the manipulation before and after the UV digestion. In any case, the method was proven to operate in the low ng l^{-1} of Hg(II). No reference data for the Cu(II) concentration were available.

4. Conclusions

A constant current stripping potentiometry method on a gold film electrode was reported to be useful for the simultaneous determination of Se(IV) and Hg(II) at the ng l^{-1} level. Cu(II) and Pb(II) can be also determined simultaneously by the same method. Interferences from Bi(III), Sb(III) and As(III) disturbed in some extent the determination of Cu(II) and/or Pb(II), but not for Hg(II) and Se(IV). High content of organic material in the water samples caused a severe interference for Se(IV), which should be overcome in future work. In sea water, Hg(II) can be determined at the low ng l^{-1} level. The method operates in non-deoxygenated solutions, thus making the equipment easily portable or installed in mobile laboratories for fast "in situ" determinations.

Acknowledgements

We thank Patricia Galán for the river water samples and Dr. Karl May for providing the sea water sample. E.P.G acknowledges support received from the Radiometer Analytical A/S Company (Copenhagen, Denmark) during his stay in Germany.

References

[1] J. Wang and B. Tian, Anal. Chem., 65 (1993) 1529.
[2] L. Fishbein, in E. Merian (Ed.), Metals and Their Compounds in the Environment. Occurrence, Analysis and Biological Relevance, VCH, Weinheim, 1991, Chap. II.25
[3] R. Von Burg and M.R. Greenwood, in E. Merian (Ed.), Metals and Their Compounds in the Environment. Occurrence, Analysis and Biological Relevance, VCH, Weinheim, 1991, Chap. II.20.

[4] H. Gunasingham, K.P. Ang and C.C. Ngo, Analyst, 113 (1988) 1533.
[5] R.W. Andrews, J.H. Larrochele and D.C. Johnson, Anal. Chem., 48 (1976) 212.
[6] L. Sipos, J. Golimowski, P. Valenta and H.W. Nürnberg, Fresenius' Z. Anal. Chem., 298 (1979) 1.
[7] H. Huiliang, D. Jagner and L. Renman, Anal. Chim. Acta, 201 (1987) 1.
[8] H. Huiliang, D. Jagner and L. Renman, Anal. Chim. Acta, 202 (1987) 117.
[9] H. Huiliang, D. Jagner and L. Renman, Anal. Chim. Acta, 201 (1987) 269.
[10] F. Scholz, L. Nitschke and G. Henrion, Anal. Chim. Acta, 199 (1987) 167.
[11] J. Lexa and K. Stulík, Talanta, 36 (1989) 843.
[12] M. Leu and H. Seiler, Fresenius' Z. Anal. Chem., 321 (1985) 479.
[13] T. Ozaki, and N. Unohara, Buseki Kagaku, 36 (1987) 479.
[14] M. Hatlé, Talanta, 34 (1987) 1001.
[15] U. Baltensperger and J. Hertz, Anal. Chim. Acta, 172 (1985) 49.
[16] S.B. Adeloju, A.M. Bond and M.H. Briggs, Anal. Chem., 57 (1985) 1386.
[17] V. Stará and M. Kopanica, Anal. Chim. Acta, 208 (1988) 231.
[18] R.W. Andrews and D.C. Johnson, Anal. Chem., 47 (1975) 294.
[19] M. Al-Bakri, Ph.D. Dissertation, University of Leipzig, Germany, 1991.
[20] S.B. Adeloju, A.M. Bond, M.H. Briggs and H.C. Hughes, Anal. Chem., 55 (1983) 2076.
[21] T. Wu, W. Xiang, F. Zangh and J. Dang, Analyst, 113 (1988) 1431.

ELSEVIER

Analytica Chimica Acta 293 (1994) 67–76

ANALYTICA CHIMICA ACTA

Anodic oxidation processes of copper with a mercury electrode in the presence of hydrogen peroxide and in unbuffered sodium chloride solutions

Damir Krznarić

Centre for Marine Research Zagreb, Ruder Bošković Institute, Bijenička 54, 41000 Zagreb, Croatia

(Received 30th August 1993; revised manuscript received 18th January 1994)

Abstract

The oxidation processes of copper with a mercury electrode were investigated in the presence of H_2O_2 and in unbuffered NaCl solutions. The method used was anodic stripping alternating current voltammetry. Owing to the electrocatalytic process of Cu and H_2O_2, the local pH around the electrode increases, resulting in copper(I) oxide formation. It was determined that the anodic peak current relating to Cu_2O deposition on the electrode surface is directly proportional to H_2O_2 concentration. The product of the Cu^{2+} and H_2O_2 concentrations in solution at which the Cu_2O deposit on the electrode surface first appears is constant. These results suggest the possibility of the determination of H_2O_2 or dissolved oxygen in similar systems. The possible structural changes and oxidation processes of the Cu_2O film are discussed.

Key words: Stripping voltammetry; Anodic oxidation; Copper; Mercury electrodes

1. Introduction

In a previous paper [1], it was shown that the voltammetric behaviour of copper in the presence of atmospheric oxygen or hydrogen peroxide is characterized by a catalytic current. Using cyclic voltammetry, a pronounced cathodic current was observed during the potential sweep in the anodic direction. The reactions responsible for this catalytic current were proposed to be

$$Cu^0 \longrightarrow Cu^+ + e^- \quad (1)$$

$$Cu^+ + 2Cl^- \longrightarrow CuCl_2^- \quad (2)$$

$$H_2O_2 + 2CuCl_2^- \longrightarrow 2Cu^{2+} + 2OH^- + 4Cl^- \quad (3)$$

As the electrode potential is still sufficiently negative, the Cu^{2+} formed in reaction 3 is reduced back to Cu^+:

$$Cu^{2+} + e^- \longrightarrow Cu^+ \quad (4)$$

As no buffer was used the local pH around the electrode increased, causing copper(I) oxide (Cu_2O) to precipitate on the electrode surface. Using anodic stripping alternating current voltammetry, at least two anodic peaks were observed. The first was due to the oxidation process given by Eqs. 1 and 2 and the second was proposed to be the oxidation of Cu_2O to some form of Cu(II). The second peak is observable at pH 5 [1]. At pH > 9 the peak appears even in the absence of oxygen or H_2O_2 owing to the high

SSDI 0003-2670(94)00076-X

OH^- ion concentration. However, in buffered solutions the local pH around the electrode surface cannot increase sufficiently through the catalytic process and the precipitation of Cu_2O is hindered. The second peak was not investigated any further at that time. In this work, a more detailed investigation of the process responsible for this second anodic peak was attempted.

Anodic oxidation of copper has been investigated mostly with copper electrodes, as passivation of copper in neutral and alkaline media is of considerable interest in many fields, in particular corrosion, electrocatalysis and double-layer structure research. The literature on the subject up to 1974 has been reviewed [2]. Early work was done by galvanostatic methods [3], but the rotating split ring disc technique or voltammetry offered better resolution [4–17]. Still, electrochemical studies of copper in basic electrolytes present conflicting views about the nature and composition of surface oxides. There is general agreement that the initial species is Cu_2O, but there is still some disagreement as to the nature of the second stage, which can lead to one of several oxides or hydroxides in the +1 or +2 oxidation state.

The second oxidation stage usually gives up to several times larger charges than the Cu_2O formation stage. This was interpreted as the oxidation of Cu_2O as well as bulk Cu to CuO or $Cu(OH)_2$. Both stages could be accompanied by dissolution processes [5–9]. Further, the formation of a double oxide film consisting of an inner Cu(I) and an outer Cu(II) oxide overlayer was also suggested [8,12,13]. Before the Cu_2O film oxidation, one or two small peaks were observed by some workers and were explained as dissolution of Cu(I) [9], as adsorption of oxygen [10,11,17] or the introduction of adatoms/hydrous oxide concept [15]. Depending on the electrochemical conditions, Speckmann et al. [18] found during the potentiostatic oxide formation four different oxide species: CuO_x, Cu_2O, CuO and $CuO_y \cdot zH_2O$.

In addition to electrochemical methods, a number of surface analytical techniques such as x-ray photoelectron spectroscopy (XPS) [19–21], ion-scattering spectroscopy (ISS) [18], x-ray and electron diffraction and scanning electron microscopy (SEM) [22] have been used for the study of the anodic oxidation of copper. In alkaline solutions anodic oxidation of copper proceeds by forming first a base layer of porous Cu_2O via a solid-state process [21]. Within the pores, metal dissolution of Cu^{2+} species occurs in addition to oxidative dissolution of Cu_2O. As local supersaturation with respect to $Cu(OH)_2$ and CuO is achieved, an upper layer of $Cu(OH)_2$ and CuO forms via nucleation and crystal growth from solution. Finally, the whole surface, including pores and exposed Cu_2O, is covered with a CuO layer.

Instead of copper electrodes, Fletcher et al. [9] used copper amalgam electrodes in 0.1 M LiOH. They observed a small anodic peak due to dissolution of Cu(I), which was followed by two sharp, large peaks interpreted as two Cu_2O monolayers. Subsequently further inhibited dissolution of Cu(I) occurred.

In this work, lower concentrations of copper were used in the presence of H_2O_2 and in unbuffered medium, and an attempt was made to elucidate the processes taking place in the anodic region of copper(I) oxide formation and oxidation on mercury electrodes.

2. Experimental

The measurements were carried out with a Princeton Applied Research Model 170 multimode polarographic analyser in a 50-ml Metrohm cell equipped with a three-electrode system. The working electrode was a Metrohm hanging mercury drop electrode (HMDE) with a surface area of 0.022 cm^2. A saturated calomel electrode (SCE) was used as the reference electrode and a platinum electrode as the auxiliary electrode.

All chemicals were of analytical-reagent grade from Merck (Darmstadt) and hydrogen peroxide was obtained from Kemika (Zagreb, Croatia). Solutions were prepared with doubly distilled water and were deaerated with pure nitrogen. If they contained hydrogen peroxide, they were freshly prepared each time from a 30% concentrated solution of hydrogen peroxide.

The method used was anodic stripping phase-sensitive alternating current voltammetry

(ASacV). The in-phase component of the current was always registered. Prior to the anodic potential scan, copper was accumulated into the mercury electrode at -0.5 V (E_D) with stirring of the solution for a time period t_D, which was followed by a quiescent period of 15 s. Unless stated otherwise, t_D was 1 min. The solution was stirred with a PTFE stirrer. The effective diffusion layer thickness, σ, for the stirred solution was calculated to be 3.0×10^{-3} cm in 1×10^{-4} M Cd(II) with 0.1 M NaCl as supporting electrolyte; σ was calculated by the method of Davison [23].

Throughout the measurements 0.5 M NaCl was used as the supporting electrolyte. No buffer was used during the measurements as the intention was to observe the formation and behaviour of copper oxides due to the local pH changes in the vicinity or on the surface of the electrode in the presence of hydrogen peroxide. The influence of sodium hydrogen carbonate buffer on the investigated catalytic process was discussed in a previous paper [1]. The pH of the freshly prepared measured solutions was between 5.5 and 5.9.

During measurements the cell was thermostated at 20 ± 0.5°C. The amplitude of the a.c. potential was 10 mV, the frequency was 70 Hz and the potential scan rate was 10 mV s^{-1}.

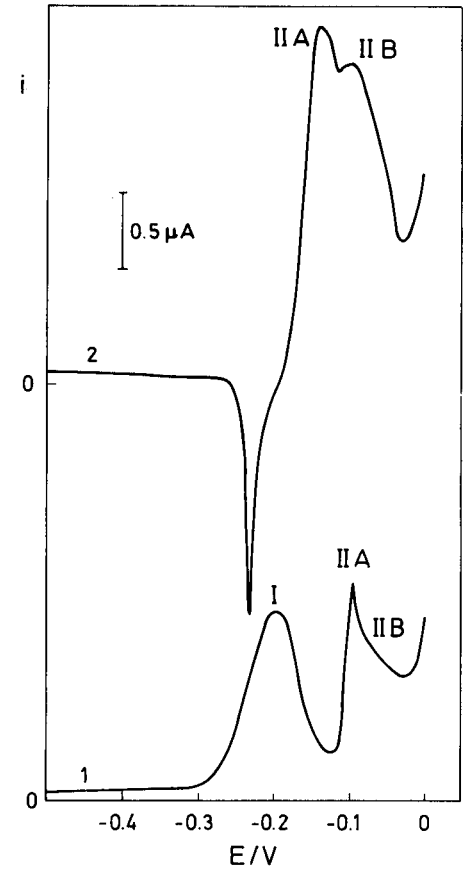

Fig. 1. ASacV curves for 3×10^{-6} M $Cu(NO_3)_2$ in 0.5 M NaCl and (1) 4×10^{-4} and (2) 3×10^{-3} M H_2O_2.

3. Results and discussion

It was determined in previous work (see Fig. 5 in [1]) that oxidation of copper from an amalgam in the presence of H_2O_2 resulted in two anodic waves when the ASacV method was used. With anodic stripping direct current voltammetry (ASV), the same type of solution would give a pronounced cathodic current owing to the described electrocatalytic process. It was stated that current reversal probably could not be observed with ASacV because of the nature of current registration with the alternating current technique. Subsequently it was found that a cathodic catalytic current can be observed even with ASacV if sufficiently high concentrations of Cu or H_2O_2 are measured. In Fig. 1 an example is given of such behaviour. Copper was first accumulated into the mercury electrode for 1 min from 3×10^{-6} M $Cu(NO_3)_2$ solution and was then stripped by applying a potential scan in the anodic direction. With lower concentrations of H_2O_2 in the solution (curve 1) only anodic peaks I and II were observed. In this case peak II is a composite peak containing two peaks designated IIA and IIB. Peak I represents oxidation of Cu(0) to Cu(I) and peak II further oxidation of Cu(I) to Cu(II) together with possible oxidation of H_2O_2 to oxygen. A more detailed discussion follows later. With increase in H_2O_2 concentration (curve 2), a pronounced cathodic current is observed at -0.23 V while peak I almost completely disappears. Hence an electrocatalytic process depicted by Eqs. 1–4 is observed with ASacV, but at higher concentrations than in ASV or differential-pulse anodic

stripping voltammetry (DPASV). As the peak resolution is much better with ASacV than with the other two methods, ASacV was chosen in this work.

As already mentioned, the main interest in this work was to investigate the oxidation of copper from a mercury electrode and the precipitation of copper oxides on the electrode surface in H_2O_2 solutions, i.e., the behaviour of the composite anodic peak II. Owing to the relatively low solubility of copper in mercury, it was important to choose lower concentrations of copper in solution so that the effects observed would not be caused by this phenomenon. Under our experimental conditions this was satisfied in the concentration range between 0 and 3×10^{-6} M $Cu(NO_3)_2$. In this range the peak I current, in the absence of H_2O_2, is always proportional to Cu^{2+} concentration in solution. The investigated H_2O_2 concentrations were usually up to 3×10^{-3} M.

In the given Cu(II) concentration range two main regions of peak II behaviour are observed. One is below ca. 5×10^{-7} M Cu(II), where a single peak IIA appears, and the other is above it, where peak II becomes a composite peak. An example of the behaviour at the first Cu(II) concentration region is given in Fig. 2. If 3×10^{-7} M $Cu(NO_3)_2$ solution is titrated with H_2O_2, a well defined single peak IIA grows and its potential shifts towards more negative values. In Fig. 3 the anodic peak I and IIA currents are plotted against H_2O_2 concentration. At first peak I increases, but subsequently decreases again with the appearance of peak IIA. According to the literature [24], in chloride media peak I is the oxidation of Cu(0) to $CuCl_2^-$ as given by Eqs. 1 and 2. It is not clear what the reason is for the increase of peak I with small additions of H_2O_2. A possible explanation is the disproportionation reaction of Cu^+. Disproportionation of Cu^+ in alkaline media, using copper electrodes, has also been observed by other workers [7] and by us in neutral media in the presence of surfactants [25]. The increase of peak I is not followed by a change in its shape, i.e., the width of the peak at its half-height remains unchanged. Therefore, the increase is not due to the change in reversibility of the oxidation process.

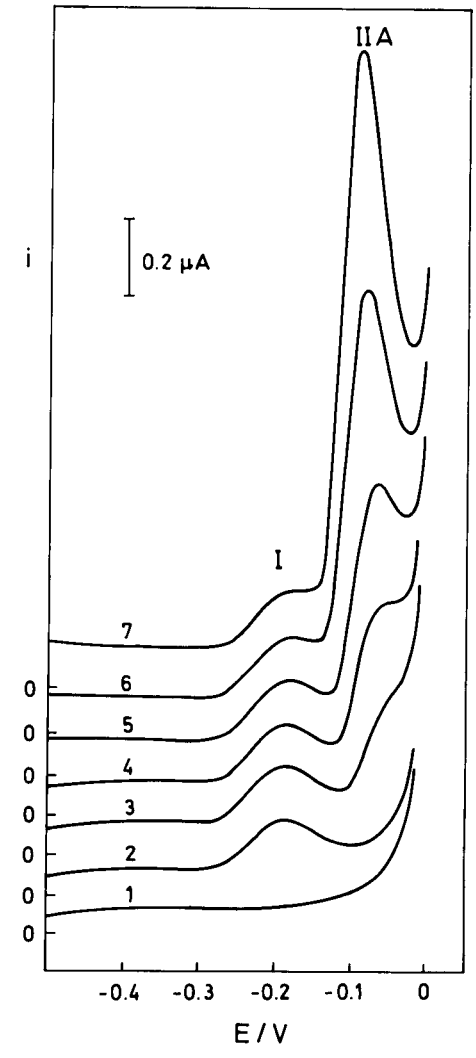

Fig. 2. ASacV curves for 3×10^{-7} M $Cu(NO_3)_2$ in 0.5 M NaCl and (2) 0, (3) 7×10^{-4}, (4) 9×10^{-4}, (5) 1.1×10^{-3}, (6) 1.5×10^{-3} and (7) 1.8×10^{-3} M H_2O_2. Curve 1 is a blank in pure NaCl solution.

With the first appearance of peak IIA, peak I starts to decrease, usually down to a certain plateau value. This suggests passivation of the electrode by a film of Cu_2O deposited on its surface. With the increased H_2O_2 concentration, the pH around the electrode increases owing to the electrocatalytic reaction depicted by Eqs. 3

and 4 and Cu_2O is deposited. The possible reaction is

$$2Cu^+ + 2OH^- \rightleftharpoons Cu_2O + H_2O \quad (5)$$

The partial blocking of the anodic peak, corresponding to peak I, by a passivating film of Cu_2O has also been observed by other workers [8]. Peak IIA increases with increase in H_2O_2 concentration (curve 2) and the curve shows three different slopes. The most characteristic is the first part of the curve with the lowest slope, which goes usually up to a current value of 0.2–0.3 μA. The second part of the curve with an intermediate slope is sometimes not observed. The final part of the curve continues to increase with increasing H_2O_2 concentration with unchanged slope. This behaviour indicates the formation of one or two layers of Cu_2O on the electrode surface. Cu_2O is oxidized to CuO or $Cu(OH)_2$, resulting in peak IIA. Some workers claim that the product is CuO [8,12], whereas others suggest both forms [5–7,13–17,19–21].

Peak IIA in Fig. 3 increases continuously at H_2O_2 concentrations above 1.5×10^{-3} M and becomes more than one order of magnitude higher than peak I. Much higher currents for peak II than peak I have also been observed by other workers [4–9,15,17] using Cu electrodes in alkaline media. Generally it was explained by the simultaneous oxidation of Cu_2O and Cu to CuO or $(Cu(OH)_2$. Fletcher et al. [9] attributed peak II to the nucleation and subsequent crystal growth of Cu_2O. However, in our case such explanations are not applicable because the amount of Cu(0) oxidized from the amalgam electrode is limited by the amount of Cu^{2+} previously reduced, i.e., during the first step of oxidation, given by peak I, Cu(0) is almost completely oxidized to Cu(I). Hence the much higher value of the peak II current cannot be attributed to further dissolu-

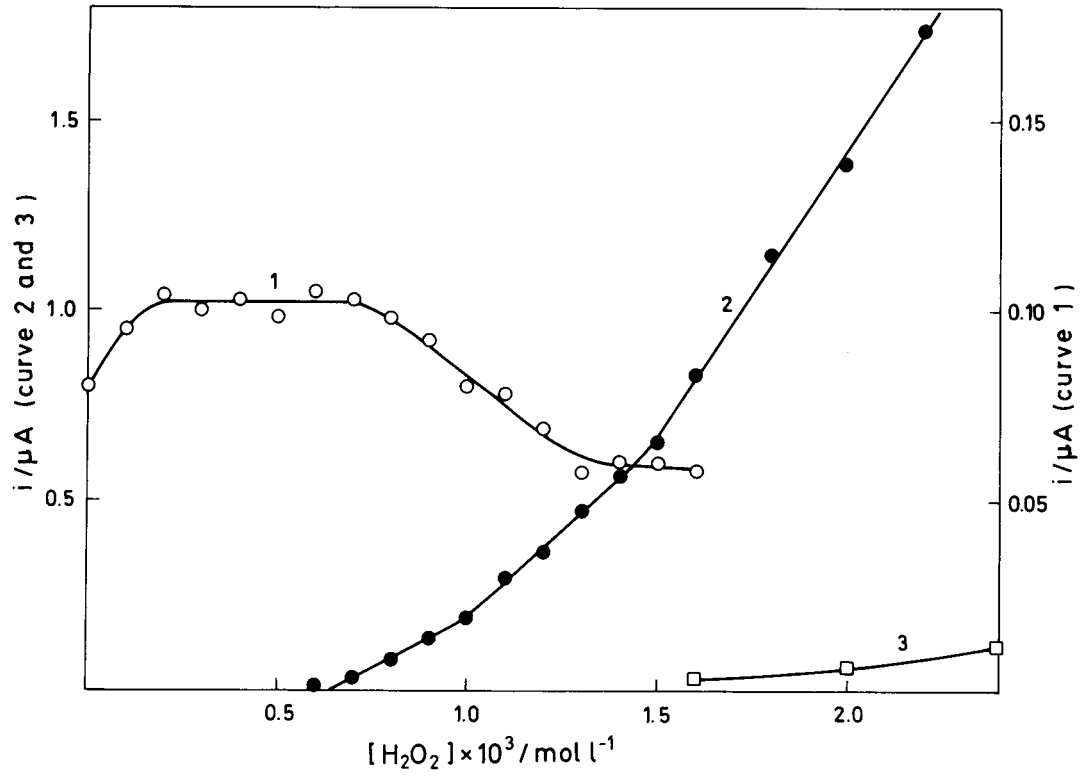

Fig. 3. Dependence of (1) peak I and (2) peak IIA currents on H_2O_2 concentration for 3×10^{-7} M $Cu(NO_3)_2$ in 0.5 M NaCl solution. Curve 3 represents H_2O_2 oxidation current for solution without $Cu(NO_3)_2$.

tion of Cu(0), as in the case with the Cu electrode, as no more Cu(0) is left in the mercury electrode. A possible explanation is the oxidation of hydrogen peroxide to oxygen. Potentials for the oxidation of Cu(I) to Cu(II) and H_2O_2 to oxygen almost coincide under our experimental conditions. Hence the general reaction scheme is that first Cu(0) from the electrode is oxidized through reactions 1 and 2 to $CuCl_2$. As the pH around the electrode increases due to the electrocatalytic process given by reactions 3 and 4 Cu_2O starts to deposit on the electrode surface. One or two layers of Cu_2O are formed and they promote oxidation of H_2O_2 to oxygen. This is supported by the fact that the further increase of curve 2 in Fig. 3 is proportional to H_2O_2 concentration.

The proportionality between H_2O_2 concentration and the peak IIA current could be used for the determination of H_2O_2 concentration. Given the constant Cu^{2+} concentration and experimental conditions, it would be sufficient to determine the peak IIA current and from a curve similar to curve 2 in Fig. 3 the concentration of H_2O_2 could be read. However, when the concentration of Cu^{2+} is 5×10^{-7} M or lower, peak IIA appears only at concentrations of H_2O_2 of ca. 3×10^{-4} M or higher.

The first appearance of peak II is dependent on both the concentration of H_2O_2 and the concentration of Cu^{2+} in solution. In Fig. 4, peak IIA currents are plotted versus H_2O_2 concentration for several concentrations of Cu^{2+}. The curves correspond to the first part of curve 2 in Fig. 3, i.e., the part with the lowest slope, and they are obviously straight lines. We suggest that this part of the curves correspond to the formation of a Cu_2O monolayer on the HMDE surface, and the intercept of the lines with the abscissa is the concentration of H_2O_2 at which Cu_2O starts to deposit. If that concentration of H_2O_2 is plotted on a logarithmic scale against the concentration of Cu^{2+} for such curves, a straight line is obtained (Fig. 5). The proportionality can be expressed as

$$[H_2O_2][Cu^{2+}]^{1.07} = 5.4 \times 10^{-11} \quad (6)$$

Taking into account the experimental error, the line in Fig. 5 can be considered as a non-linear proportionality. Hence the concentration of H_2O_2 in solution at which Cu_2O starts to precipitate on

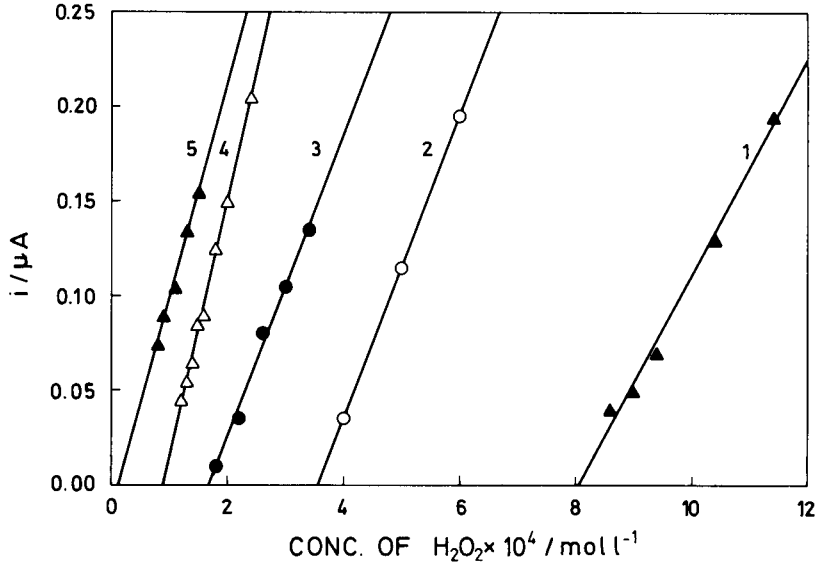

Fig. 4. Dependence of ASacV peak IIA current on H_2O_2 concentration for (1) 2×10^{-7}, (2) 4×10^{-7}, (3) 8×10^{-7}, (4) 1.6×10^{-6} and (5) 2×10^{-6} M $Cu(NO_3)_2$ in 0.5 M NaCl.

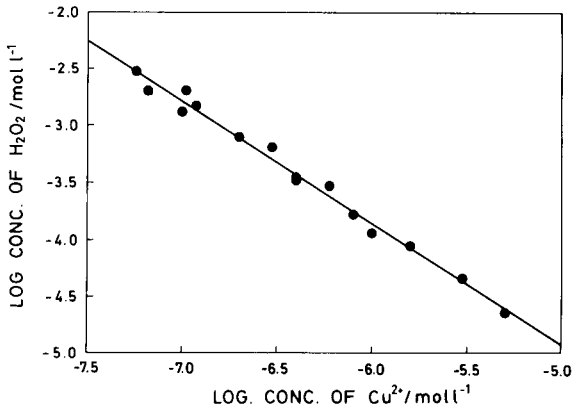

Fig. 5. Dependence of H_2O_2 concentration at which peak IIA first appears on $Cu(NO_3)_2$ concentration in 0.5 M NaCl solution. H_2O_2 values represent intercepts of straight lines, given in Fig. 4, with the abscisa.

the electrode surface is not linearly proportional to the concentration of Cu in the Hg electrode, i.e., to the Cu^{2+} in the bulk of the solution.

The type of experiment illustrated in Figs. 4 and 5 could be used for analytical purposes for the determination of H_2O_2. The procedure would be to add to a solution of unknown H_2O_2 concentration a certain amount of Cu^{2+} and to titrate the solution with H_2O_2 as shown in Fig. 4. The intercept of the straight line with the abscisa would be the concentration of added H_2O_2 C_{ad}, necessary for the first appearance of peak IIA. The total concentration of H_2O_2 at that point would be $C_T = C_{ad} + C_x$ where C_x is the unknown concentration of H_2O_2. Substituting C_T into Eq. 6 for H_2O_2 concentration:

$$C_T = 5.4 \times 10^{-11}[Cu^{2+}]^{-1.07} \quad (7)$$

or

$$C_x = 5.4 \times 10^{-11}[Cu^{2+}]^{-1.07} - C_{ad} \quad (8)$$

The value of the product, i.e. the constant in Eq. 6, is dependent on the experimental conditions such as deposition time and solution composition. Therefore, if they are changed, the curve in Fig. 5 would have to be determined again. The above procedure is also applicable to the determination of dissolved oxygen, as it gives the effects comparable to H_2O_2.

As already mentioned, in the Cu^{2+} concentration region below ca. 5×10^{-7} M, no obvious splitting of peak II was observed, regardless of H_2O_2 concentration. At higher concentrations of Cu^{2+} peak II can split into two peaks depending on H_2O_2 concentration, and above 3×10^{-6} M even more peaks appear. However, no detailed investigations were performed for Cu^{2+} concentrations above 3×10^{-6} M because then additional problems occur with the low solubility of Cu in mercury. In Fig. 6, ASacV curves are given for 1.4×10^{-6} M Cu^{2+} solution to which increasing amounts of H_2O_2 were added. At first on addition of H_2O_2 a small peak corresponding to peak IIA in Fig. 2 starts to grow, but at about 2×10^{-4} M H_2O_2 a second peak IIC appears. In the literature similar peak splitting on copper electrodes was attributed to the formation of soluble and insoluble Cu(II) species [5,8], to the formation of both CuO and $Cu(OH)_2$ deposits [7,15], to the presence of two Cu_2O monolayers [9] or to the oxidation of surface layers of Cu_2O and Cu to $Cu(OH)_2$ [17]. In this work there was insufficient evidence to differentiate between any of the above possibilities. Very tentatively, a pos-

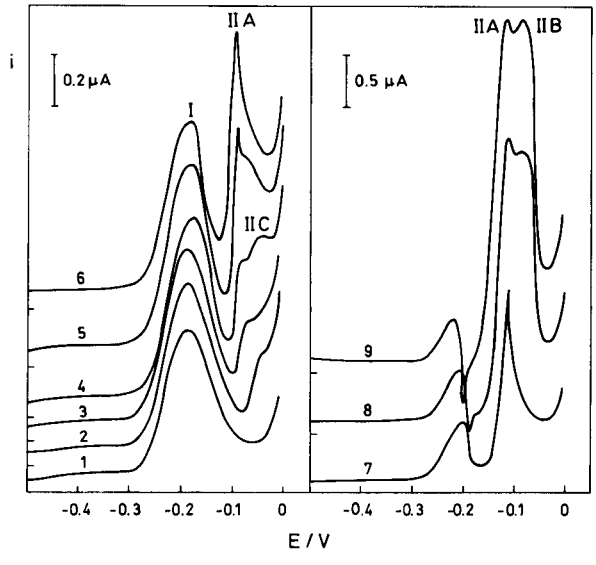

Fig. 6. ASacV curves for 1.4×10^{-6} M $Cu(NO_3)_2$ in 0.5 M NaCl and (1) 0, (2) 1×10^{-4}, (3) 1.6×10^{-4}, (4) 2.6×10^{-4}, (5) 3.4×10^{-4}, (6) 5×10^{-4}, (7) 1.2×10^{-3}, (8) 1.6×10^{-3} and (9) 2×10^{-3} M H_2O_2 solution.

sibility of H_2O_2 oxidation should be mentioned. Further additions of H_2O_2 cause peak IIC to diminish again with a further increase of peak IIA, which at this concentration acquires a sharp form. Peak IIC appears only in a short H_2O_2 concentration range between ca. 2×10^{-4} and 5×10^{-4} M. Subsequently the process given by peak IIC is blocked by the reaction resulting in peak IIA. With further additions of H_2O_2 there is a sudden transformation of the sharp peak IIA into a composite peak IIA and IIB (curve 8 in Fig. 6). As the transformation occurs with the smallest additional increase of H_2O_2 concentration and is not very reproducible, it is indicative of a change in oxide structure. In order for such a change to take place, the concentration of Cu^{2+} in solution should be above 5×10^{-7} M, regardless of H_2O_2 concentration. At the same time, a stronger electrocatalytic reduction process is observed at -0.2 V in curves 8 and 9. What type of structural changes take place and whether peaks IIC and IIB represent the same process are not clear.

Because of the small separation of peaks IIA, IIB and IIC and because of the possible mutual interference of the processes which are occurring in this H_2O_2 and Cu^{2+} concentration region, no attempt was made to give the behaviour of each peak separately. Instead, the total current of the composite peak II was plotted against H_2O_2 and Cu^{2+} concentrations in a three-dimensional representation (Fig. 7). The experiment was performed by taking H_2O_2 solutions with concentrations increasing by 2×10^{-4} M and by titrating each solution with Cu^{2+}. With the first addition of Cu^{2+} only peak IIA is observed as in Fig. 2. At a Cu^{2+} concentration around 5×10^{-7} M a sudden increase for the current occurs together with the characteristic appearance of peak IIB. After a maximum current has been reached at about 8×10^{-7} M Cu^{2+}, the total peak II current decreases again. A two-dimensional representation of the regions in Fig. 7, at which different peaks appear, is given in Fig. 8. The most interesting feature of Fig. 7 is the concentration ridge at 8×10^{-7} M Cu^{2+}. Once a sufficient amount of H_2O_2 is attained, the deposited oxide layer transformation and peak IIB occurrence result in a sharp ridge formation. Further additions of Cu^{2+} diminish the composite peak II, apparently mainly through the decrease of peak IIB. We can only speculate about the nature of peak IIB or oxide

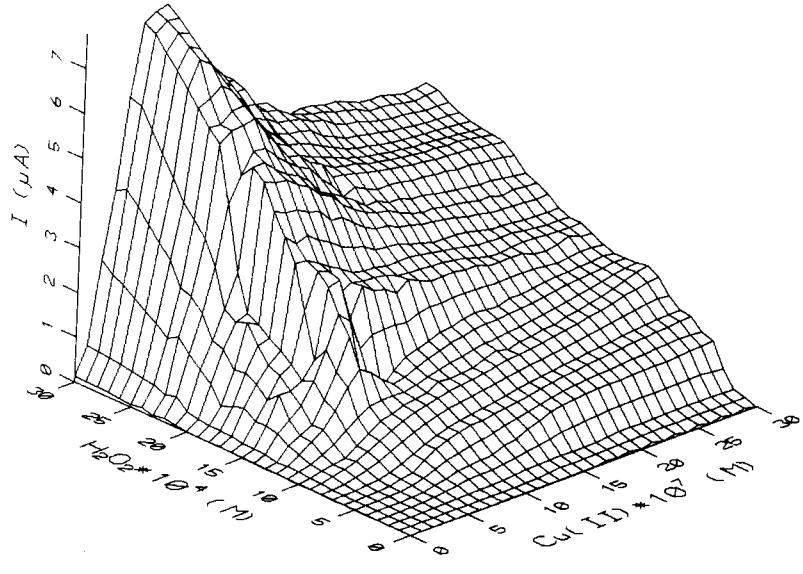

Fig. 7. Dependence of the total ASacV anodic composite peak II current on H_2O_2 and $Cu(NO_3)_2$ concentrations in 0.5 M NaCl solution.

layer transformation. Tentatively we suggest the sudden formation of an ordered crystalline structure when the right amount and ratio of H_2O_2 and Cu^{2+} in solution are attained. Splitting of peak II into two peaks IIA and IIB could be a consequence of different structures of the inner and outer Cu_2O layers or perhaps the oxidation of Cu_2O to CuO and $Cu(OH)_2$.

Measurements were also attempted in $NaClO_4$ supporting electrolyte. In that case Cu(0) is oxidized to Cu(II) by a single two-electron process as shown by a characteristic sharp peak in Fig. 9, curve 1. The first addition of H_2O_2 shifts the peak towards more positive potentials and then suddenly a small increase in H_2O_2 concentration results in peak splitting. A new peak appears at more negative potentials and starts to increase while the more positive peak diminishes. Further, an additional small peak appears around 0.25 V. Similarly to the NaCl supporting electrolyte, if the peak current of the new peak at −0.05 V is plotted against the concentration of H_2O_2 added, a straight line intersecting the abscisa is obtained. However, this time no obvious dependence between the Cu^{2+} and H_2O_2 concentrations at which this peak first appears was observed. This observation and the fact that the new peak appears at more negative potentials than the normal oxidation peak of Cu(0) indicate a basically different behaviour in $NaClO_4$ from that in NaCl supporting electrolyte.

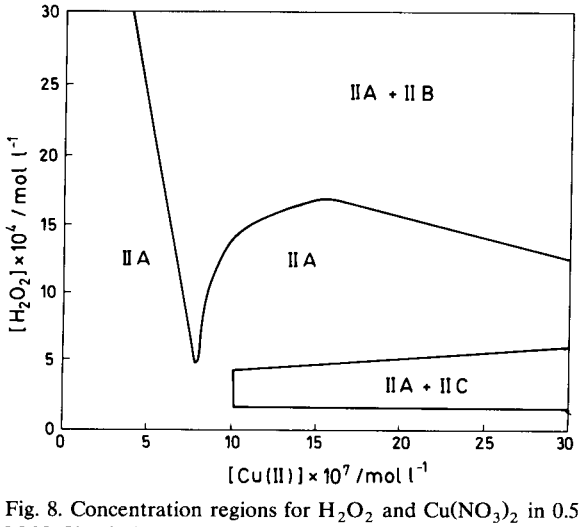

Fig. 8. Concentration regions for H_2O_2 and $Cu(NO_3)_2$ in 0.5 M NaCl solution at which different forms of peak II appear.

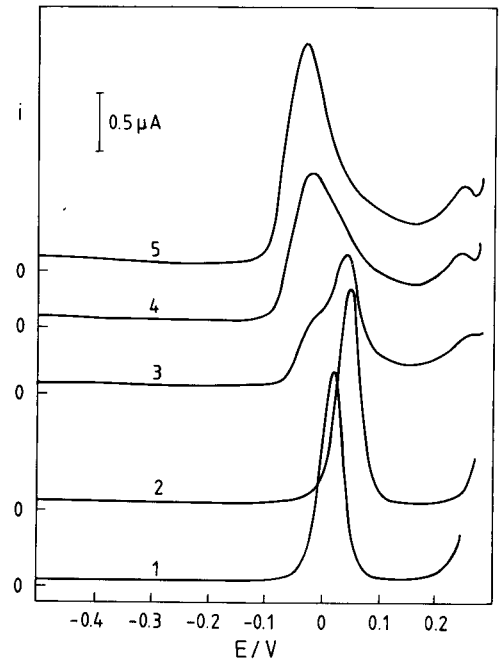

Fig. 9. ASacV curves for 4×10^{-6} M $Cu(NO_3)_2$ in 0.5 M $NaClO_4$ and (1) 0, (2) 1×10^{-3}, (3) 1.1×10^{-3}, (4) 1.2×10^{-3} and (5) 1.3×10^{-3} M H_2O_2 at pH 5.5.

4. Conclusions

Anodic stripping of copper from neutral sodium chloride solutions and in the presence of hydrogen peroxide is characterized by an electrocatalytic process resulting in current reversal. Because of the catalytic process, the local pH around the Hg electrode increases and Cu(I) oxide precipitates on the electrode surface. Further oxidation of Cu_2O gives rise to a second anodic peak when anodic stripping alternating current voltammetry is used. This peak II can be a single peak or a composite one consisting of several superimposed peaks described as peaks IIA, IIB and IIC. At lower concentrations of Cu^{2+} or H_2O_2 in solution a single peak IIA is observed, whose height is proportional to H_2O_2 concentration until a monolayer deposit of Cu_2O is formed. Sometimes deposition of a second layer is observed,

after which H_2O_2 oxidation seems to be promoted.

The first deposition of Cu_2O is dependent on both Cu^{2+} and H_2O_2 concentrations in solution. The product of these two concentrations at which peak IIA starts to appear is a constant. This characteristic can be used for the determination of H_2O_2 or dissolved oxygen concentrations in solution. In this work, the range of H_2O_2 concentrations thus determined was between ca. 2×10^{-5} and 3×10^{-3} M.

At Cu^{2+} concentrations above ca. 5×10^{-7} M, the Cu(I) oxidation peak may become a composite peak. In certain Cu^{2+} and H_2O_2 concentration regions a sudden transformation of deposited oxide structure on the electrode is observed. The presence of two superimposed Cu(I) oxidation peaks is tentatively explained by different structures of the inner and outer Cu_2O layers or by oxidation of Cu_2O to CuO and $Cu(OH)_2$.

Acknowledgement

The financial support of the Authority for Scientific Research of the Republic of Croatia is gratefully acknowledged.

References

[1] D. Krznarić, M. Plavšić and B. Ćosović, Electroanalysis, 4 (1992) 143.
[2] U. Bertocci and D.R. Turner, in A.J. Bard (Ed.), Encyclopedia of Electrochemistry of the Elements, Vol. II, Dekker, New York, 1974, p. 383.
[3] H.P. Leckie, J. Electrochem. Soc., 117 (1970) 1242, and references cited therein.
[4] B. Miller, J. Electrochem. Soc., 116 (1969) 1675.
[5] N.A. Hampson, J.B. Lee and K.I. MacDonald, J. Electroanal. Chem., 32 (1971) 165.
[6] N.A. Hampson, J.B. Lee and K.I. MacDonald, J. Electroanal. Chem., 34 (1972) 91.
[7] J. Ambrose, R.G. Barradas and D.W. Shoesmith, J. Electroanal. Chem., 47 (1973) 47.
[8] D.D. Macdonald, J. Electrochem. Soc., 121 (1974) 651.
[9] S. Fletcher, R.G. Barradas and J.D. Porter, J. Electrochem. Soc., 125 (1978) 1960.
[10] J.M.M. Droog, C.A. Alderliesten, P.T. Alderliesten and G.A. Bootsma, J. Electroanal. Chem., 111 (1980) 61.
[11] J.M.M. Droog and B. Schlenter, J. Electroanal. Chem., 112 (1980) 387.
[12] U. Collisi and H.-H. Strehblow, J. Electroanal. Chem., 210 (1986) 213.
[13] U. Collisi and H.-H. Strehblow, J. Electroanal. Chem., 284 (1990) 385.
[14] M.P. Sanchez, M. Barrera, S. Gonzalez, R.M. Souto, R.C. Salvarezza and A.J. Arvia, Electrochim. Acta, 35 (1990) 1337.
[15] L.D. Burke and T.G. Ryan, J. Electrochem. Soc., 137 (1990) 1358.
[16] W. Kautek and J.G. Gordon, II, J. Electrochem. Soc., 137 (1990) 2672.
[17] S. Dong, Y. Xie, and G. Cheng, Electrochim. Acta, 37 (1992) 17.
[18] H.D. Speckmann, M.M. Lohrengel, J.W. Schultze and H.-H. Strehblow, Ber. Bunsenges. Phys. Chem., 89 (1985) 392.
[19] H.-H. Strehblow and B. Titze, Electrochim. Acta, 25 (1980) 839.
[20] N.S. McIntyre, S. Sunder, D.W. Shoesmith and F.W. Stanchell, J. Vac. Sci. Technol., 18 (1981) 714.
[21] D.W. Shoesmith, S. Sunder, M.G. Bailey and F.W. Stanchell, J. Electroanal. Chem., 143 (1983) 153.
[22] D.W. Shoesmith, T.E. Rummery, D. Owen and W. Lee, J. Electrochem. Soc., 123 (1976) 790.
[23] W. Davison, J. Electroanal. Chem., 87 (1978) 395.
[24] A. Nelson, Anal. Chim. Acta, 169 (1985) 273.
[25] M. Plavšić, D. Krznarić and B. Ćosović, Electroanalysis, submitted for publication.

ELSEVIER

Analytica Chimica Acta 293 (1994) 77–86

ANALYTICA CHIMICA ACTA

Indirect tensammetric method for the determination of non-ionic surfactants Part 3. Properties of the analytical signal of mixtures of non-ionic surfactants [1]

Andrzej Szymanski, Zenon Lukaszewski *

Institute of Chemistry, Technical University of Poznan, PL-60-965 Poznan, Poland

(Received 20th July 1993; revised manuscript received 6th January 1994)

Abstract

Seven binary and three multi-component mixtures of non-ionic surfactants and a mixture of ethylene glycol and PEG 400 were investigated using tensammetry with "normal" recording and one binary mixture by using "reverse" recording. Within the initial section of the Γ-shaped calibration graph, the investigated mixtures show no or small deviations from the plot for the standard (Triton X-100) and most of the mixtures show good additivity. In the case of two mixtures showing deviation from additivity the results deviated less from the plot for the standard than would be expected presuming additivity. Within the range 0.1–1.0 mg l^{-1} the mixtures can be determined using a Triton X-100 calibration graph without serious error. The shape of the calibration graph as a whole depends strongly on the average number of oxyethylene subunits of a mixture, but depends only slightly on the molecular weight distribution of the mixture. Therefore, the behaviour of polydisperse surfactants can be simulated by a mixture of two different polydisperse surfactants.

Key words: Voltammetry; Surfactants; Tensammetry; Waters

1. Introduction

Several hundred different synthetic non-ionic surfactants can be found in sewage and surface water. The determination of each of them is impossible with the present state of trace analysis of surfactants. On the other hand, such a target is excessive from the point of view of routine control of water pollution. Only one common factor is used for the description of the so-called "total concentration" of non-ionic surfactants. BiAS [1,2] in Europe and CTAS in America [3] are used for this purpose.

The indirect tensammetric method (ITM) seems to be a promising alternative to BiAS and CTAS [4,5]. ITM operates within a more convenient range of surfactant concentrations than the methods currently used and it requires a substantially smaller volume of water sample. The cali-

* Corresponding author.

[1] Dedicated to Professor Rolf Neeb, Johannes Gutenberg University, Mainz, Germany, on the occasion of his 65th birthday.

SSDI 0003-2670(94)00072-T

bration graphs for particular surfactants differ less from each other than in the BiAS and CTAS methods and ITM permits the determination of ethoxylates having 1–30 ethoxylene subunits, in contrast to the other methods, which operate with ethoxylates having 4–30 ethoxylene subunits only. An additional advantage of ITM is its low sensitivity to the presence of anionic surfactants [5] and the much simpler separation scheme necessary prior to the determination itself.

The main disadvantage of tensammetry is the complex irregular behaviour of mixtures of surfactants, although ITM uses an indirect tensammetric signal. In adsorptive stripping tensammetry both separate peaks of mixtures and single common peaks can be formed. If separate peaks of components of a mixture appear they can be either suppressed or enhanced or retain their original height depending on the nature of the interaction of the components of the mixture on the electrode surface and on the conditions of the experiment [6–9]. The lowering of the tensammetric peak of ethyl acetate due to competitive adsorption of the analysed surfactants is the analytical signal in ITM. The behaviour of mixtures of non-ionic surfactants in ITM must be carefully checked prior to recommending ITM for routine use. This checking was the aim of this work.

Several binary systems of non-ionic surfactants were selected as representatives. Four representative mixtures of oxyethylated alcohols, i.e., the most often applied group of non-ionics (64% of total production of non-ionics [10]), were selected for examination. The broadest investigations were performed with binary mixtures containing Triton X-100, the most common model non-ionic surfactant, used as a standard in ITM. The other components of these mixtures were surfactants having very short oxyethylene chains. Surfactants having more than ten oxyethylene subunits produce much smaller differences in the ITM analytical signal or none at all [4]. Such mixtures need no wider checking of the additivity of their ITM signals. Except for ethoxylates, a binary mixture of poly(ethylene glycol) of molecular weight 400 and ethylene glycol was selected for examination. Such a mixture approaches the behaviour of the "pure" hydrophilic part of ethoxylates.

In fact, the selected mixtures cannot be considered as binary mixtures in terms of chemical compounds when they are multi-component mixtures obtained by mixing two polydisperse components. In order to check the behaviour of a mixture of homogeneous compounds, the surfactant 18-2 having an average of two oxyethylene subunits was separated into four initial sequential homologues and the behaviour of the unseparated mixture was compared with that of its homogeneous components.

In order to check the conclusions drawn on the basis of this investigation of model binary mixtures and to approach the conditions of real multi-component mixtures of non-ionic surfactants existing in surface waters, two additional mixtures were selected. The first was a ten-component mixture of components representative of the most frequently used classes of non-ionic surfactants according to a recent report concerning the volume of surfactant produced [10]. The other one was a mixture of "native" non-ionic surfactants isolated from river water of unknown composition.

2. Experimental

2.1. Apparatus

A Radelkis OH-105 polarograph was used with a voltage scan rate of 400 mV min^{-1}. The applied amplitude of the alternating voltage was 2 mV. Controlled-temperature hanging mercury drop electrode (HMDE) equipment (Radiometer), having an additional platinum wire auxiliary electrode, was used. All potentials cited were measured versus a saturated calomel electrode (SCE). The beaker of the measuring cell was replaced with a quartz beaker. The ceramic frit on the end of the salt bridge was protected with a polyethylene tube, which decreases the adsorptive loss of surfactant [11].

2.2. Reagents

The following surfactants were used without additional purification (number of oxyethylene

subunits in parentheses): oxyethylated alkylphenols: Rokafenol N-1 (1) (ICSO Blachownia, Poland), Rokafenol N-3 (3) and Rokafenol N-5 (5) (both from Rokita, Poland), Triton X-100 (9.5) (Rohm and Haas); oxyethylated oxo-alcohols having a C_{10-13} hydrophobic part of the molecule: Oxetal T105 (5) and Oxetal C114 (14) (both from Zschimmer und Schwarz); oxyethylated alcohols having mainly an n-C_{12} hydrophobic part of the molecule: Rokanol KO-4 (4) (Rokita) and Brij 35 (20) (Atlas); oxyethylated alcohols having a C_{16-18} hydrophobic part of the molecule: surfactant 18-2 (2) (Technical University of Poznan), Marlipal 1618/10 (10), Marlipal 1618/18 (18) and Marlipal 1618/25 (25) (all from Hüls); oxyethylated amines having a C_{16-18} hydrophobic part of the molecule: Rokamin R-3 (3) and Rokamin R-11 (11) (both from ICSO); oxyethylene–oxypropylene block copolymers: Rokopol 30p10 (10) (Rokita), having an average number of oxypropylene subunits of 30; oxyethylated oleyl ester of sorbitol: Tween 81(5) (Atlas); and poly(ethylene glycols) of M.W. 200 (PEG 200) and 400 (PEG 400) (both from Carl Roth). Homogeneous oxyethylated octadecanols having one, two, three and four oxyethylene subunits were obtained by separation of polydisperse surfactant 18-2 using thin-layer chromatography. Standard Kieselgel 60 plates (Merck) and ethyl acetate–acetic acid–water (35 + 8 + 7.5) as the developing solution were used. Ethyl acetate, specially pure for gas chromatography (POCh, Poland) and ethylene glycol, analytical-reagent grade (POCh) were used.

The sodium sulphate used for the preparation of the base electrolyte was purified by double recrystallization and heating at 600°C. All solutions were prepared in water triply distilled from

Table 1
Analytical signals (mm) of representative oxyethylated alcohols and their 1 + 1 binary mixtures (100 mm = 0.80 μA)

	Concentration of surfactant or surfactants mixture (mg l^{-1})						
	0.2	0.5	1.0	2.0	3.0	4.0	5.0
Oxetal C114(a) and Brij-35(b)							
(a)	30	70	116	170	216	223	226
(b)	33	73	121	180	213	222	230
Av. [a]	31.5	71.5	118.5	175	214.5	222.5	228
Mix [b]	31	70	119	180	215	223	226
	0.1	0.2	0.3	0.5	0.6	0.8	1.0
Marlipal 1618 / 18(a) and Marlipal 1618 / 25(b)							
(a)	13	26	38	62	73	88	102
(b)	14	27	41	63	74	92	104
Av.	13.5	26.5	39.5	62.5	73.5	90	103
Mix.	14	27	39	64	74	91	103
Surfactant 18-2(a) and Marlipal 1618 / 25(b)							
(a)	12	24	35	51	57	67	76
(b)	14	27	41	63	74	92	104
Av.	13	25.5	38	57	65.5	79.5	90
Mix.	13	25	38	57	67	76	86
Rokanol KO-4(a) and Brij-35(b)							
(a)	12	24	36	54	62	76	84
(b)	16	33	46	73	82	103	121
Av.	14	28.5	41	63.5	72	89.5	102.5
Mix.	15	29	41	63	73	87	99

[a] Av. = expected presuming additivity of signals of components.
[b] Mix. = experimental results for the mixture.

quartz. Only freshly distilled water was used. The supporting electrolyte in all the studies was 0.5 M aqueous sodium sulphate.

3. Results and discussion

3.1. Mixtures of oxyethylated alcohols

Four binary (1 + 1) mixtures of oxyethylated alcohols were investigated using "normal" recording of the ethyl acetate curve (i.e. in the cathodic direction). The first two mixtures consisted of surfactants having similar or the same hydrophobic part and a long oxyethylene chain. The other mixtures consisted of compounds having a similar hydrophobic part but a very different length of the oxyethylene chain. The experimental results were compared with those expected presuming additivity of the analytical signal. Expected values were calculated by adding the half-heights of each component (1 + 1 mixture) at the concentration corresponding to the total value. All four mixtures examined behaved almost perfectly additively, as is apparent from Table 1. The small deviations are hardly significant. It must be stressed that two the mixtures discussed contain surfactants that are not detectable by the BiAS or CTAS methods (surfactant 18-2 and Rokanol KO-4).

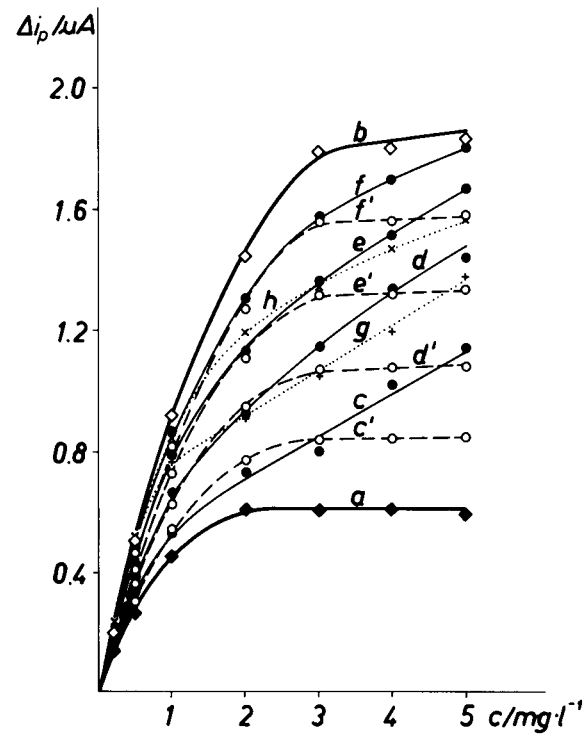

Fig. 1. Dependence of analytical signal on the surfactant or surfactant mixture concentration for (a) Rokafenol N-1, (b) Triton X-100 and their (c) 4 + 1, (d) 3 + 2, (e) 2 + 3 and (f) 1 + 4 mixtures. The dashed curves (c'–f') were calculated for corresponding mixtures presuming additivity of signals of mixture components. The curves for Rokafenol N-3 (g) and Rokafenol N-5 (h) are included for comparison purposes. Concentration of ethyl acetate: 1.5 ml in the sample (25 ml).

3.2. Binary mixtures of Triton X-100 and surfactants having a short oxyethylene chain

Mixtures of Rokafenol N-1 and Triton X-100 were investigated at different ratios of the components. Some of the experiments were performed using "normal" recording of the ethyl acetate curve and the others with "reverse" recording, i.e., in the anodic direction starting from −1.40 V vs. SCE. This will be considered in more detail in the next paragraph. The results are shown in Fig. 1 and compared with the curves calculated on the basis of the expected additivity (dashed lines). This calculation was performed similarly to the case with oxyethylated alcohols taking into account the different ratios of the components in the mixtures examined. The initial sections of the experimental curves are hardly distinguishable in Fig. 1, because of the coincidence of numerous points, so these results are also presented in Table 2. The experimental curves (solid lines) and those calculated on the basis of additivity (dashed lines) roughly coincide for the range of concentrations corresponding to the rising parts of the calibration graphs. However, they differ for higher concentrations. The experimental results are higher (5–10 mm) than those expected presuming additivity and frequently they are the same as for Triton X-100 alone. The paradox is that this deviation from additivity minimizes the error of determination caused by the choice of the standard surfactant.

Table 2
Analytical signals (mm) of binary mixtures of (a) Rokafenol N-1 and (b) Triton X-100 obtained with "normal" and "reverse" recording (100 mm = 0.80 μA)

Recording direction		Concentration of surfactant or surfactant mixture (mg l^{-1})		
		0.2	0.5	1.0
Normal	*Single surfactants*			
	(a)	16	32	55
	(b)	26	61	114
	Mixtures			
	1+4:			
	Av. [a]	24	55	102
	Mix. [b]	27	62	109
	2+3:			
	Av.	22	49.5	90.5
	Mix.	27	60	99
	3+2:			
	Av.	20	43.5	78.5
	Mix.	25	51	83
	4+1:			
	Av.	18	38	67
	Mix.	21	42	67
Reverse	*Single surfactants*			
	(a)	9	16	22
	(b)	26	61	114
	Mixtures			
	1+4:			
	Av.	22.5	52	95.5
	Mix.	25	63	107
	2+3:			
	Av.	19	43	77
	Mix.	25	60	100
	3+2:			
	Av.	16	34	59
	Mix.	23	54	86
	4+1:			
	Av.	12.5	25	40.5
	Mix.	18	40	62

[a] Av. = expected presuming additivity of signals of components.
[b] Mix. = experimental results for the mixture.

In fact, the examined mixtures are not truly binary (in terms of chemical compounds) but a multi-component mixture created by mixing two polydisperse components. From this point of view, the examined mixtures of Rokafenol N-1 and Triton X-100 having proportions of 4 + 1, 3 + 2, 2 + 3 and 1 + 4 can be considered as synthetic polydisperse mixtures with average numbers of oxyethylene subunits of 2.7, 4.4, 6.1 and 7.8, respectively. It is interesting to compare the behaviour of these mixtures with that of oxyethylated alkylphenols having a similar number of average oxyethylene subunits. Therefore, experiments with Rokafenol N-3 (average 3 oxyethylene subunits) and Rokafenol N-5 (average 5 oxyethylene subunits) were performed and the results are included added to Fig. 1 (dotted lines g and h, respectively). The shapes of the additional curves are very similar to the experimental curves for mixtures of Rokafenol N-1 and Triton X-100 and, obviously, they differ strongly from the lines calculated presuming additivity. The line for Rokafenol N-3 (3 oxyethylene subunits) runs near the line for the 4 + 1 mixture of Rokafenol N-1 and Triton X-100, i.e. that corresponding to an average of 2.7 oxyethylene subunits. The line for Rokafenol N-5 (5 oxyethylene subunits) runs between the lines corresponding to 3 + 2 and 2 + 3 mixtures of Rokafenol N-1 and Triton X-100, i.e. those corresponding to averages of 4.4 and 6.1 oxyethylene subunits, respectively. These results show that the behaviour of polydisperse mixtures is strongly governed by the average number of oxyethylene subunits of the mixture, independently of the M.W. distribution of the components. The behaviour of a surfactant having a certain number of oxyethylene subunits can be roughly simulated by a mixture of two components having a similar hydrophobic part and the same average number of oxyethylene subunits.

Two other binary mixtures of Triton X-100 were investigated. The other component was surfactant 18-2 or Rokamin R-3, i.e. surfactants having also a very short oxyethylene chain (2 and 3, respectively) like Rokafenol N-1 but with a hydrophobic part different from that of Triton X-100. The conditions of the experiments including concentration range were the same as before, with the exception of the proportion of components, which was 1 + 1. The results are shown in Figs. 2 and 3, respectively and, for the initial range of concentration, in Table 3. The experimental curve for the 1 + 1 mixture of Triton X-100 and surfactant 18-2 runs over (ca. 15%) the curve calculated with the presumption of additivity (compare curves c and c′ in Fig. 2), whereas within the initial section of the calibration graph

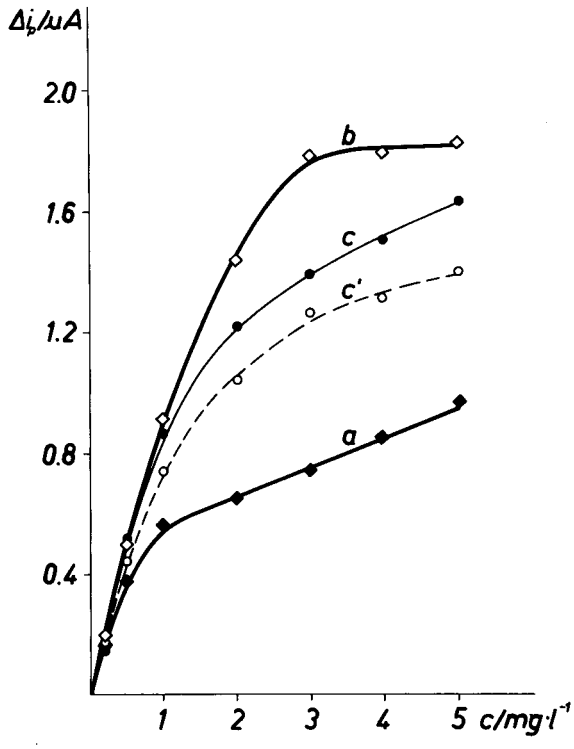

Fig. 2. Dependence of analytical signal on the surfactant or surfactant mixture concentration for (a) surfactant 18-2, (b) Triton X-100 and (c) their 1+1 mixture. The dashed curve (c') was calculated presuming additivity of signals of mixture components. Concentration of ethyl acetate: 1.5 ml in the sample (25 ml).

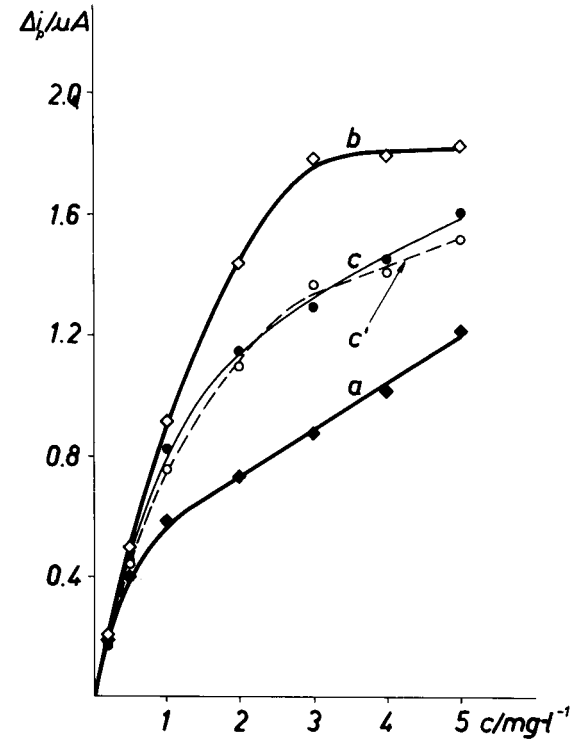

Fig. 3. Dependence of analytical signal on the surfactant or surfactant mixture concentration for (a) Rokamin R-3, (b) Triton X-100 and (c) their 1+1 mixture. The dashed curve (c') was calculated presuming additivity of signals of mixture components. Concentration of ethyl acetate: 1.5 ml in the sample (25 ml).

the experimental results are almost the same as for Triton X-100 (see Table 3). The experimental curve for the mixture of Triton X-100 and Rokamin R-3 runs very close to that calculated presuming additivity (see Fig. 3 and Table 3).

3.3. Behaviour of the mixture of Triton X-100 and Rokafenol N-1 with "reverse" recording

"Reverse" recording of the ethyl acetate curve substantially improves the tolerance to the presence of anionic surfactants in the system [5]. On the other hand, the behaviour of mixtures in tensammetry can become extremely sensitive to the starting potential [6–9]. Therefore, the results of "reverse" recording should be checked and compared with those for "normal" recording.

Table 3
Analytical signals (mm) of (a) Triton X-100, (b) surfactant 18-2, (c) Rokamin R-3 and binary (1+1) mixtures of Triton X-100 with surfactant 18-2 (av.1 and mix.1) and Rokamin R-3 (av.2 and mix.2) (100 mm = 0.80 μA)

	Concentration of surfactant or surfactants mixture (mg l^{-1})		
	0.2	0.5	1.0
(a)	26	61	114
(b)	24	51	76
(c)	26	51	73
Av. 1 [a]	25	56	95
Mix. 1 [b]	23	62	108
Av. 2	26	56	94
Mix. 2	24	58	103

[a] Av. = expected presuming additivity of signals of components.
[b] Mix. = experimental results for the mixture.

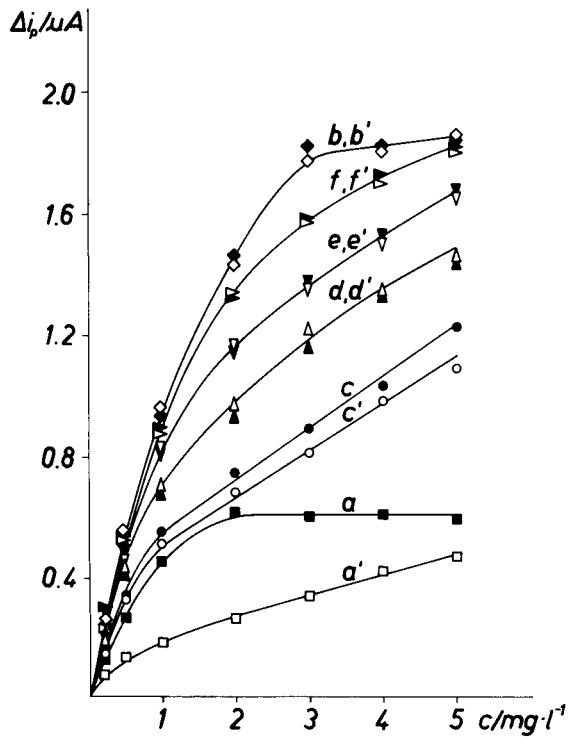

Fig. 4. Dependence of analytical signal on the surfactant or surfactants mixture concentration for (a and a') Rokafenol N-1, (b and b') Triton X-100 and their (c and c') 4+1, (d and d') 3+2, (e and e') (2+3) and (f and f') (1+4) mixtures using "normal" (a–f) and "reverse" (a'–f') recording. Concentration of ethyl acetate: 1.5 ml in the sample (25 ml).

Such a comparison was made with the mixture of Triton X-100 and Rokafenol N-1. Rokafenol N-1 alone is very sensitive to a change in the direction of recording from "normal" to "reverse" and the corresponding change in the starting potential [5]. The results are given in Fig. 4 and the exact values for the lowest concentration range in Table 2. It is apparent from Fig. 4 that only the curve for Rokafenol N-1 alone shows a substantial difference between the two recording directions. A difference is also observed for the results corresponding to the 4 + 1 mixture (corresponding to an average number of 2.7 oxyethylene subunits). The other points concerning the two directions of recording are almost identical. The same conclusion can be drawn by comparing the results for the "normal" and "reverse" directions of recording given in Table 2. The similarity of the results for the "normal" and "reverse" recordings is very fortunate for the determination but unexpected from the point of view of additivity. The lower results obtained for Rokafenol N-1 with "reverse" recording in comparison with those for "normal" recording should cause a proportional decrease in the signals of the mixtures if additivity were be fulfilled. This expected decrease is apparent from comparison of the calculated signals for the "normal" and "reverse" recording (presuming additivity) given in Table 2. However, the results for the mixture are higher than those expected on the basis of additivity and much closer to the calibration graph of Triton X-100. Therefore, the error is much lower than would be expected on the basis of additivity.

3.4. Mixture of ethylene glycol and PEG 400

This mixture was investigated in order to check if the role of the length of the oxyethylene chain is not influenced by the hydrophobic part of the surfactant. The 1 + 1 mixture should roughly correspond to the behaviour of PEG 200 as long as the mixture behaves in a similar way to the mixture of Rokafenol N-1 and Triton X-100. The results are shown in Fig. 5. The curve for PEG 200 (curve c) and that calculated for the 1 + 1 mixture on the basis of additivity of the curves of ethylene glycol and PEG 400 (dashed line d') were added. The reasonable agreement of the experimental results for the 1 + 1 mixture of ethylene glycol and PEG 400 on the one hand and PEG 200 on the other supports the supposition concerning the governing role of the average length of the oxyethylene chain in the ITM behaviour of mixtures.

3.5. Homogeneous oxyethylated n-octadecanols and their mixture

In order to check the behaviour of a precisely defined mixture of ethoxylates, the polydisperse surfactant 18-2 was separated into four homologues. Although surfactant 18-2 is a polydispersed mixture, its hydrophobic part is well defined (*n*-octadecyl). The separation was per-

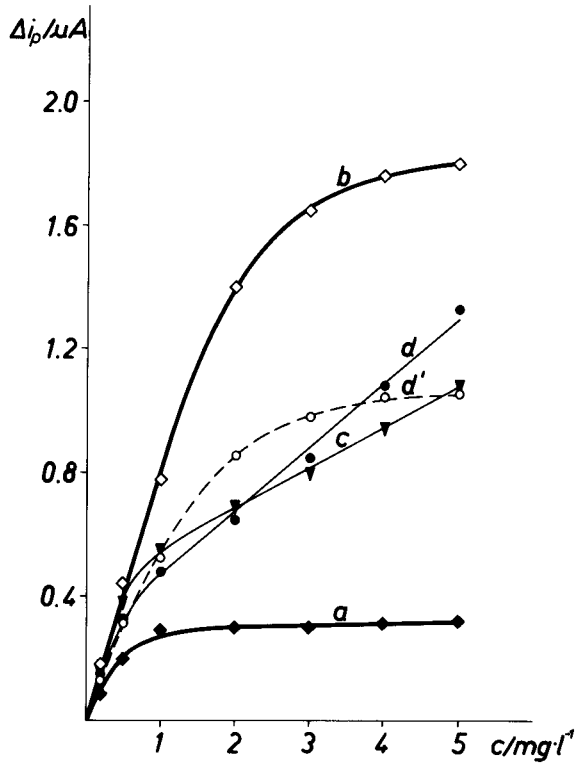

Fig. 5. Dependence of analytical signal on the surfactant or surfactant mixture concentration for (a) ethylene glycol, (b) PEG 400 and (d) their 1+1 mixture. The dashed curve (d') was calculated presuming additivity of signals of mixture components. The curve for PEG 200 (c) is included. Concentration of ethyl acetate: 1.5 ml in the sample (25 ml).

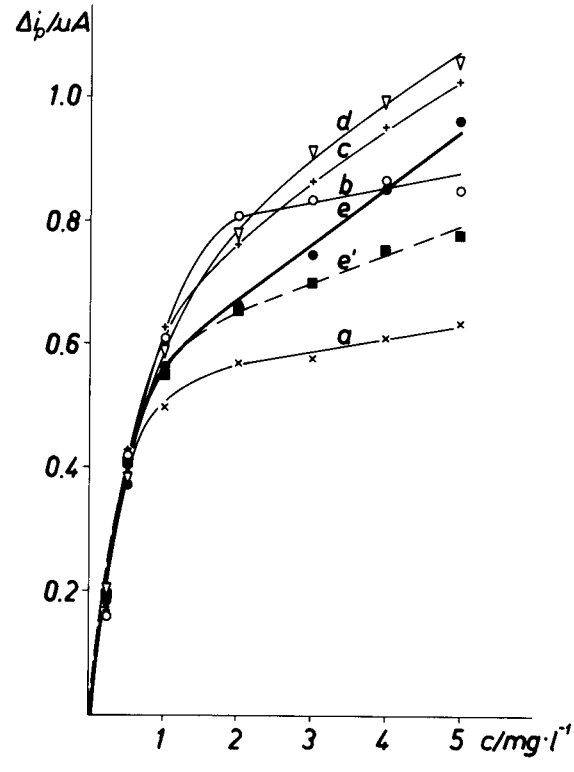

Fig. 6. Dependence of analytical signal on the surfactant concentration for homogeneous surfactants (a) 18-2/1, (b) 18-2/2, (c) 18-2/3, (d) 18-2/4 and (e) their mixture containing 57.6% of 18-2/1, 11.0% of 18-2/2, 18.3% of 18-2/3 and 12.6% of 18-2/4. The dashed curve (e') was calculated presuming additivity of signals of mixture components. Concentration of ethyl acetate: 1.5 ml in the sample (25 ml).

formed using thin-layer chromatography. The behaviour of pure homologues 18-2/1, 18-2/2, 18-2/3 and 18-2/4, having one, two, three and four oxyethylene subunits, respectively, was investigated. The results are shown in Fig. 6, together with the curve for the unseparated polydispersed surfactant 18-2. The curve calculated on the basis of additivity was also added (dashed line e'). The exact results concerning the concentration range 0.2–1.0 mg l^{-1} are additionally given in Table 4. Within the range of concentrations corresponding to the initial part of the calibration graph the mixtures show almost perfect additivity (see Table 4). For higher concentrations corresponding to plateau or pseudo-plateau formation, on the calibration graph for the polydispersed mixture (un-

Table 4
Analytical signals (mm) of single components and multi-component mixture of surfactants (a) 18-2/1 (57.6%), (b) 18-2/2(11.0%), (c) 18-2/3(18.8%) and (d) 18-2/4(12.6%) (100 mm = 0.80 μA)

	Concentration of surfactant or surfactants mixture (mg l^{-1})		
	0.2	0.5	1.0
(a)	24	51	63
(b)	22	50	76
(c)	23	50	80
(d)	24	47	74
Av. [a]	23.5	50	69
Mix. [b]	23	47	71

[a] Av. = expected presuming additivity of signals of components.
[b] Mix. = experimental results for the mixture.

separated surfactant 18-2) additivity of signals is no longer observed (see curves e and e'). The difference has the same character as for mixtures of Rokafenol N-1 and Triton X-100. The curve for the mixture (curve e) having an average of 2 oxyethylene subunits runs differently to the curve for the homogeneous surfactant 18-2/2 (curve b).

3.6. Ten-component mixture of non-ionic surfactants

An artificial mixture consisting of ten different surfactants representative of their classes was formulated, taking the recent report concerning the volume of production as a starting point [10]. The composition of the mixture is given in Table 5. The results are shown in Fig. 7 together with the curve calculated on the basis of additivity (dashed line) and the curve for Triton X-100 (standard surfactant). The exact values for the range 0.2–1.0 mg l^{-1} are given in Table 5. The initial section of the experimental curve runs very close to that calculated and to that of the standard but, in the higher concentration range, the experimental results are lower than the curve for the standard (curve b) and even lower than those expected presuming additive behaviour of the components of the mixture. Such behaviour is different from most other results presented in this paper. In the other mixtures investigated the experimental results are roughly the same as the calculated values (mixture of Triton X-100 and Rokamin N-3) or they run higher than the calculated values. Only the mixture of ethylene glycol and PEG 400 exhibits a similar type of deviation of additivity. The discussed deviation has no serious analytical consequence. More important is the formation of

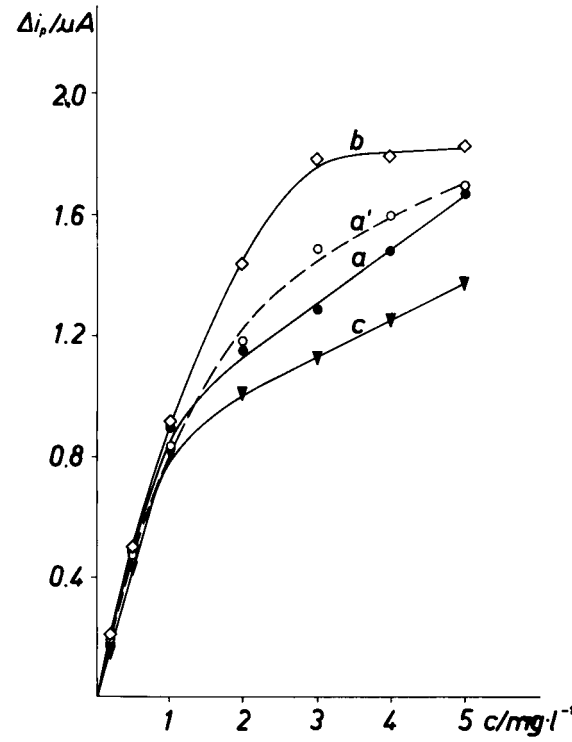

Fig. 7. Dependence of analytical signal on the surfactant mixture concentration for (a) the artificial mixture of Oxetal T105 (1/12), Oxetal C114 (2/12), Brij 35 (1/12), Rokamin R-11 (1/12), Tween 81 (1/12), Marlipal 1618/10 (1/12), Marlipal 1618/18 (2/12), Marlipal 1618/25 (1/12), Rokopol 30p10 (1/12) and Triton X-100 (1/12) and (c) the mixture of "native" surfactants isolated from river water. The dashed curve (a') was calculated presuming additivity of signals of components of the ten-component mixture. The curve for Triton X-100 (standard) (b) is included. Concentration of ethyl acetate: 1.5 ml in the sample (25 ml).

Table 5
Analytical signal (mm) of artificial mixture representing the percentage of certain classes of non-ionic surfactants in the volume of production and analytical signals of the components of the mixture (100 mm = 0.80 μA)

Surfactant	Proportion in mixture	Concentration of surfactant or surfactant mixture (mg l^{-1})		
		0.2	0.5	1.0
Oxetal T105	1/12	32	70	114
Oxetal C114	2/12	30	70	116
Brij 35	1/12	33	73	121
Rokamin R11	1/12	30	60	104
Tween 81	1/12	21	34	52
Marlipal 1618/10	1/12	22	54	84
Marlipal 1618/18	2/12	26	62	102
Marlipal 1618/25	1/12	27	63	104
Rokopol 30p10	1/12	25	63	119
Triton X-100	1/12	26	61	114
Av. [a]		27	62	104
Mix. [b]		25	56	112

[a] Av. = expected presuming additivity of signals of components.
[b] Mix. = experimental results for the mixture.

a pseudo-plateau much below the curve for the standard, which limits the range of analytically useful concentrations. The curve for the mixture is more similar to that for Rokamin R-11 or Marlipal 1618/10 alone than to that of Triton X-100 [4]. It is clear that Triton X-100 can be used as the standard only for concentrations lower than 1 mg l^{-1}.

3.7. Mixture of "native" non-ionic surfactants isolated from river water

Experiments were performed with a mixture of non-ionic surfactants isolated from river water, of unknown composition. Non-ionic surfactants were isolated from the river water sample (Warta River, Czestochowa) by extraction with ethyl acetate. Their total concentration was determined using the BiAS method [2] in a parallel experiment (218 $\mu g\ l^{-1}$). The extract was used for the preparation of series of solutions having "total" concentrations within the range 0.2–5.0 mg l^{-1}. The ITM analytical signals of these solutions were measured and the results are shown in Fig. 7 as curve c. The initial section of this curve is very similar to that for the standard (curve b) and to the experimental curve for the ten-component mixture (curve a). The further section of the curve is similar in shape to the corresponding section of the curve for the ten component mixture but it runs below this curve and much below the curve for the standard. It is apparent from Fig. 7 that Triton X-100 as the standard does not correspond to the mixture of "native" surfactants isolated from river water or to the ten-component mixture above a concentration of 1 mg l^{-1}. Therefore, it cannot be used as a standard for the evaluation of the "total concentration" of non-ionic surfactants for concentrations exceeding this value. In such a case measurements should be repeated with a suitably diluted sample.

Acknowledgements

This work was supported by the Committee of Scientific Research (grant No. 4 4008 92 03). Dr. I. Miesiac is acknowledged for the synthesis of surfactant 18-2 and Dr. Anna Krzyminska for its chromatographic separation into homologues.

References

[1] R. Wickbold, Tenside Deterg., 9 (1972) 173.
[2] D. Brown, H. De Henau, J.T. Garigan, P. Gerike, M. Holt, E. Keck, E. Kunkel, E. Matthijs, J. Waters and J. Watkinson, Tenside Deterg., 23 (1986) 190.
[3] T.M. Schmitt, M.C. Allen, D.K. Brain, K.F. Guin, D.E. Lemmel and Q.W. Osburn, J. Am. Oil Chem. Soc., 67 (1990) 103.
[4] A. Szymanski and Z. Lukaszewski, Anal. Chim. Acta, 260 (1992) 25.
[5] A. Szymanski and Z. Lukaszewski, Anal. Chim. Acta, 273 (1993) 313.
[6] H. Batycka and Z. Lukaszewski, Anal. Chim. Acta, 162 (1984) 215.
[7] Z. Lukaszewski, H. Batycka and W. Zembrzuski, Anal. Chim. Acta, 175 (1985) 55.
[8] M.K. Pawlak and Z. Lukaszewski, Anal. Chim. Acta, 202 (1987) 97.
[9] M.K. Pawlak and Z. Lukaszewski, Chem. Anal. (Warsaw), 30 (1985) 377.
[10] L. Noll, Tenside Surfact. Deterg., 28 (1991) 90.
[11] A. Szymanski and Z. Lukaszewski, Anal. Chim. Acta, 231 (1990) 77.

ELSEVIER

Analytica Chimica Acta 293 (1994) 87–94

ANALYTICA CHIMICA ACTA

Protonation constants of some substituted salicylideneanilines in ethanol–water mixtures

Fitnat Köseoğlu *

Department of Sciences, Faculty of Gazi Education, University of Gazi, Ankara, Turkey

Esma Kılıç, Esin Canel, Nazife Yılmaz

Department of Chemistry, Faculty of Science, University of Ankara, Ankara, Turkey

(Received 3rd September 1993; revised manuscript received 25th January 1994)

Abstract

Protonation constants of some substituted salicylideneanilines have been determined in ethanol–water mixtures at ionic strength of 0.1 M and at 25°C. A potentiometric method was used and calculation was done by Martell's and Motekaitis' PKAS computer programme. The trend in the values of protonation constants of Schiff's bases were explained in terms of the nature of the substituent and the dielectric constant of medium. The applicability of the Hammett equation to the effect of substituents in Schiff's bases is discussed.

Key words: Potentiometry; Titrimetry; Ethanol–water mixtures; Protonation constants; Schiff bases; Substituent effect

1. Introduction

Protonation constants of various compounds can only be determined in mixed solvents because of their insolubility in water [1–6]. The purpose of this research is to determine the protonation constants of Schiff's bases in ethanol–water mixtures and to gain information about the substituent and solvent effects. While a considerable amount of such information has been accumulated particularly during the last few years much less has been done on the Schiff's bases in mixed solvent systems [7]. Furthermore, Schiff's bases are becoming increasingly important in biological, pharmaceutical and other industrial applications. They are also well-known for their complex-forming tendencies [8–12].

In this study, the stoichiometric protonation constants have been determined potentiometrically and the calculation of these constants was carried out by using a computer method recently developed. The effects of methyl, ethyl, methoxy, fluoro, chloro, bromo and iodo groups on the basicity of salicylideneaniline (**I**) when they are in *ortho*, *meta* or *para* position to the azomethine nitrogen have been investigated. It has also been discussed whether the Hammett equation could

* Corresponding author.

SSDI 0003-2670(94)00077-Y

be used to predict the effect of the substituent on the reactivity of salicylideneaniline.

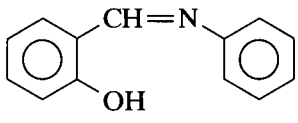

I

2. Experimental

2.1. Materials

All the Schiff's bases were synthesized by condensation of salicylaldehyde with aniline and 2-fluoro, 4-fluoro, 2-chloro, 3-chloro, 4-chloro, 2-bromo, 3-bromo, 4-bromo, 2-iodo, 3-iodo, 4-iodo, 2-methyl, 3-methyl, 4-methyl, 2-ethyl, 3-ethyl, 4-ethyl, 2-methoxy, 3-methoxy and 4-methoxy anilines. The Schiff's bases were purified by recrystallization from ethanol. Stock solutions of them were prepared in ethanol purified as described in Ref. 13.

Salicylaldehyde and all substituted anilines were purchased from Merck and were used as received.

Stock solutions of strong acid and strong base were prepared using analytical reagent-grade perchloric acid and sodium hydroxide, respectively. Acid solutions were standardized by titration against primary standard sodium carbonate. Solutions of standard bases were prepared as 30, 40, 50, 60, 70 and 80% aqueous ethanol solutions (v/v). These solutions were standardized with use of a linear least-squares fit of Gran's plots for end-point determination obtained from titrations of perchloric acid with these bases [14,15]. The water utilized was freshly boiled and twice distilled.

Chemically pure sodium perchlorate was used to maintain a constant ionic strength.

2.2. Equipment and potentiometric measurements

Potentiometric titrations were carried out in a thermostated 80-ml glass vessel. It was equipped with a combined pH electrode (Ingold), nitrogen inlet and outlet tubes, a magnetic stirrer and titrant inlet. The electrode was modified by exchanging its aqueous KCl solution for a solution consisting of 0.01 M NaCl + 0.09 M $NaClO_4$ saturated with AgCl. The cell e.m.f. was measured using an Orion Model 720 A pH ionmeter. The temperature was controlled at 25.0 ± 0.1°C.

The potentiometric cell was calibrated before each experiment to obtain pH (= $-\log[H^+]$) values for each medium studied [16,17]. The ion products ($K_w = [H^+][OH^-]$) were calculated at constant ionic strength of 0.1 M with $NaClO_4$ in all aqueous ethanol solutions based on measurements of $[OH^-]$ and pH in several series of experiments.

Potentiometric measurements were made in aqueous ethanol media containing 30, 40, 50, 60, 70 and 80% ethanol (v/v). Solutions were brought to 0.1 M ionic strength by the addition of sodium perchlorate as background electrolyte.

Titrations were performed at constant temperature and in an atmosphere of nitrogen with CO_2-free standard 0.1 M NaOH in 50.0 ml solution containing 0.1 M $NaClO_4$ with: (i) 2.5×10^{-3} M $HClO_4$ (for cell calibration); (ii) 2.5×10^{-3} M $HClO_4 + 1.5 \times 10^{-3}$ M Schiff's base. During titrations, a potential reading was taken after waiting a suitable time for establishing the equilibrium.

The computations of the protonation constants of Schiff's bases from potentiometric data were carried out with the PKAS computer programme [16].

3. Results and discussion

Table 1 lists the stoichiometric protonation constants for Schiff's bases studied in ethanol–water mixtures. These constants are defined by Eqs. 1 and 2 where HL represents the Schiff's base:

$$L^- + H^+ \rightleftharpoons HL \qquad K_1 = \frac{[HL]}{[H^+][L^-]} \qquad (1)$$

$$HL + H^+ \rightleftharpoons H_2L^+ \; K_2 = \frac{[H_2L^+]}{[H^+][HL]} \qquad (2)$$

Table 1
The stoichiometric protonation constants of substituted salicylideneanilines at 25.0 ± 0.1°C, for different ethanol–water mixtures (μ = 0.1 M $NaClO_4$) and Hammett constants [29]

Schiff's bases	30% Ethanol			40% Ethanol			50% Ethanol			60% Ethanol			70% Ethanol			80% Ethanol			Hammett constants σ
	log K_1	log K_2	Δ log k [a]	log K_1	log K_2	Δ log k [a]	log K_1	log K_2	Δ log k [a]	log K_1	log K_2	Δ log k [a]	log K_1	log K_2	Δ log k [a]	log K_1	log K_2	Δ log k [a]	
Reference	8.50	4.25	0	8.33	4.10	0	8.81	3.95	0	8.99	3.85	0	9.18	3.75	0	9.55	3.83	0	
2-F	8.56	3.01	−1.24	8.40	2.55	−1.55	8.78	2.60	−1.35	8.86	–	–	9.17	–	–	9.32	–	–	–
4-F	8.51	4.20	−0.05	8.51	4.06	−0.04	8.72	3.90	−0.05	8.80	3.74	−0.11	9.12	3.59	−0.14	9.66	3.63	−0.20	0.06
2-Cl	8.64	2.92	−1.33	8.40	–	–	8.76	–	–	8.90	–	–	9.16	–	–	9.40	–	–	–
3-Cl	8.48	3.10	−1.15	8.29	2.97	−1.15	8.73	2.82	−1.13	8.86	–	–	9.07	–	–	9.32	–	–	0.37
4-Cl	8.65	3.73	−0.50	8.38	3.45	−0.65	8.80	3.37	−0.58	8.92	3.25	−0.60	9.10	3.10	−0.65	9.40	3.12	−0.71	0.23
2-Br	8.58	–	–	8.40	–	–	8.85	–	–	8.88	–	–	9.06	–	–	9.31	–	–	–
3-Br	8.69	3.13	−1.12	8.33	2.96	−1.14	8.92	2.84	−1.09	8.90	–	–	9.01	–	–	9.35	–	–	0.39
4-Br	8.60	3.65	−0.60	8.35	3.30	−0.80	8.90	3.18	−0.77	8.96	3.10	−0.75	8.95	2.96	−0.79	9.44	2.98	−0.85	0.23
2-I	8.56	–	–	8.46	–	–	8.85	–	–	8.90	–	–	9.10	–	–	9.37	–	–	–
3-I	8.50	3.16	−1.09	8.45	2.95	−1.15	8.76	2.84	−1.19	8.96	–	–	9.06	–	–	–	–	–	0.35
4-I	8.66	3.50	−0.75	8.71	3.16	−0.94	8.87	3.00	−0.95	8.87	2.90	−0.95	9.11	2.81	−0.94	9.90	2.89	−0.94	0.28
2-CH_3	8.61	4.15	−0.10	8.68	3.94	−0.16	8.80	3.84	−0.09	8.96	3.74	−0.11	9.12	3.64	−0.11	9.50	3.66	−0.17	–
3-CH_3	8.57	4.62	0.37	8.60	4.29	0.19	8.82	4.18	0.23	887	4.07	0.22	8.99	3.95	0.20	9.50	4.00	0.17	−0.07
4-CH_3	8.55	4.96	0.71	8.47	4.60	0.50	8.69	4.50	0.55	8.95	4.39	0.54	9.23	4.22	0.47	9.75	4.22	0.39	−0.17
2-C_2H_5	8.52	4.00	−0.25	8.40	3.64	−0.36	8.68	3.60	−0.35	8.90	3.56	−0.29	9.16	3.50	−0.25	9.52	3.57	−0.26	–
3-C_2H_5	8.50	4.40	0.15	8.32	4.21	0.09	8.73	4.10	0.15	8.97	3.98	0.13	9.18	3.87	0.12	9.45	4.00	0.17	−0.04
4-C_2H_5	8.48	4.68	0.43	8.46	4.48	0.38	8.75	4.38	0.43	8.86	4.30	0.45	9.27	4.18	0.43	9.77	4.21	0.38	−0.15
2-OCH_3	8.66	4.43	0.18	8.31	4.12	0.02	8.71	4.01	0.06	8.72	3.87	0.02	9.15	3.76	0.01	9.32	3.78	−0.05	–
3-OCH_3	8.81	4.11	−0.14	8.30	3.85	−0.25	8.74	3.75	−0.20	8.88	3.66	−0.19	9.08	3.55	−0.20	9.43	3.65	−0.18	0.12
4-OCH_3	8.78	4.95	0.70	8.36	4.70	0.60	8.76	4.60	0.65	8.94	4.50	0.65	9.36	4.40	0.65	10.06	4.47	0.64	−0.27

All errors are 0.03 or lower.
[a] Δ log k = log K_2 − log K_2 (ref.).

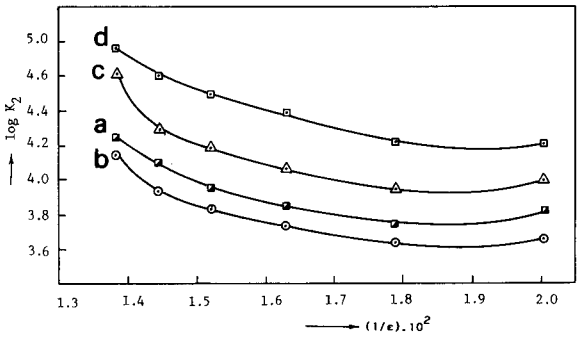

Fig. 1. Plot of log K_2 of (a) salicylideneaniline, (b) salicylidene-2-methylaniline, (c) salicylidene-3-methylaniline and (d) salicylidene-4-methylaniline against the reciprocal of dielectric constants (ε^{-1}) of ethanol–water mixtures.

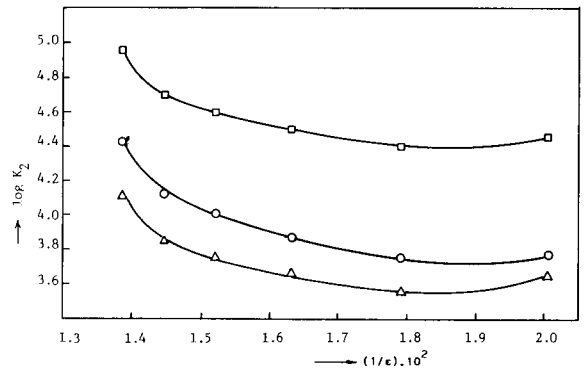

Fig. 3. Plot of log K_2 of (○) salicylidene-2-methoxyaniline, (△) salicylidene-3-methoxyaniline and (□) salicylidene-4-methoxyaniline against the reciprocal of dielectric constants (ε^{-1}) of ethanol–water mixtures.

where K_1 corresponds to the protonation equilibrium of the phenolic hydroxyl group and K_2 to the azomethine nitrogen. The values of log K_1 and log K_2 of all Schiff's bases suggest that the protonations of L^- and HL species take place in two distinct steps.

The effect of the solvent itself upon the protonation constants of various compounds has been studied by several authours [1,4,7,18–22]. Robinson and Stokes [23] have developed a linear relationship based on Born's equation between the logarithm of the acid dissociation constant and the dielectric constant of the solvent.

In Figs. 1–4, log K_2 values of all Schiff's bases have been plotted against the reciprocal of dielectric constants (ε^{-1}) of ethanol–water mixtures. It was observed that these log K_2 values linearly decreased as the concentration of ethanol increased but the values determined in 30% and 80% ethanol did not follow the linear trend observed in the ethanol–water mixtures. These results can be explained by specific solvation effects. As can be seen from Eq. 2, log K_2 values are related to the formation of H_2L^+ species. Since the dielectric constant of the medium decreases with increasing ethanol content, molecular species (HL) would be solvated better than

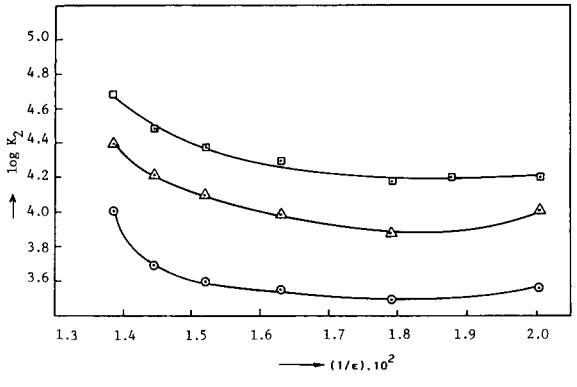

Fig. 2. Plot of log K_2 of (○) salicylidene-2-ethylaniline, (△) salicylidene-3-ethylaniline and (□) salicylidene-4-ethylaniline against the reciprocal of dielectric constants (ε^{-1}) of ethanol–water mixtures.

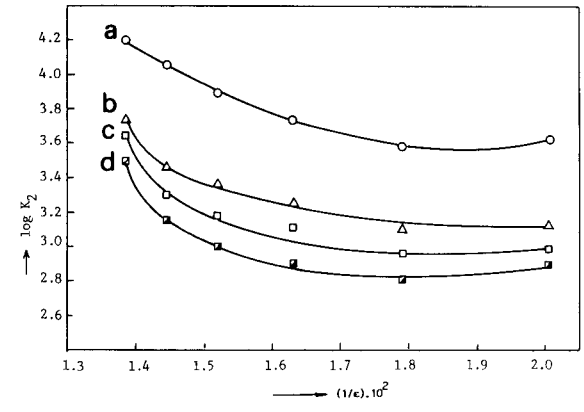

Fig. 4. Plot of log K_2 of (a) salicylidene-4-fluoroaniline, (b) salicylidene-4-chloroaniline, (c) salicylidene-4-bromoaniline and (d) salicylidene-4-iodoaniline against the reciprocal of dielectric constants (ε^{-1}) of ethanol–water mixtures.

ionic species (H_2L^+) in the solvent having a higher percentage of ethanol.

It is seen that an increase in the log K_2 values of all Schiff's bases is obtained in 80% ethanol, that is, these values pass through a minimum while the percentage of water becomes lower, as the curves in Figs. 1–4 show. Bates [24,25] has examined in detail solvent effects which account for the minimum in pK that is characteristic of the dissociation of the charged acids such as ammonium and aniliniums in a number of mixed solvent media. He showed that a major factor is the marked preference of the proton for water and that it is this preference that causes an increase in the pK of all charged acids in solvent mixtures as the percentage of water becomes lower. Thus, when the ethanol content in the solvent exceeds 70%, the upward trend of the curves obtained for all Schiff's bases studied can also be statisfactorily explained by differences in the solvent stabilization of the two type of ions (H^+, H_2L^+), brought about by increasing ethanol content. This preferential solvation can also account for the observed anomalies for log K_2 in 30% ethanol. Another reason why the log K_2 values are much greater than the values expected from the general trend may be the irregular variation of the strength of the intramolecular hydrogen bonding mentioned to exist in Schiff's bases [26,27] with the composition of the solvent. The intramolecular hydrogen bonds should break easier in the water-rich solvent and this should increase the electron density of imine nitrogen and log K_2.

When it comes to the variation of the log K_1 values with the solvent composition, it has been observed that these constants increase as the concentration of ethanol increases from 40 to 80% in ethanol–water mixtures. At first sight these results suggest that the influence of the composition of ethanol–water mixtures on the log K_1 values of Schiff's bases is dependent on the electrostatic effects taken into account in Born's theory. However, the expected linear variation with $1/\varepsilon$ was not observed, thus giving further confirmation of the limitations of the simple Born's theory. Indeed it has become clear that a purely electrostatic treatment is inadequate to account for solvent effects on the protonation constants of the uncharged acids such as HA [25,28]. The curvature of the experimental plot may be explained by non-electrostatic contributions to log K_1 values. Here, an equilibrium of the type $L^- + H^+ \rightleftarrows HL$ is involved where the HL species is more stable in ethanol and the curvature is related with the preferential solvation of L^- species by water. Neither the hydrogen bonding hypothesis considered for log K_2 nor the preferential solvation seems to provide a reasonable explanation of the anomalies for log K_1 in 30% ethanol.

Using the protonation constants obtained in this work, the effects of the substituent on the basicity of the azomethine group of salicylideneaniline (reference compound) have been discussed. The log K_2 values of the Schiff's bases show that the substituents on the phenyl ring of the amine component influence the electron density at the azomethine nitrogen. An inspection of the log K_2 values (Table 1) for the methyl, ethyl and methoxy derivatives of differing pattern of substitution reveals that the orders are:

4-CH_3 > 3-CH_3 > reference > 2-CH_3

4-C_2H_5 > 3-C_2H_5 > reference > 2-C_2H_5

4-OCH_3 > 2-OCH_3 > reference > 3-OCH_3

regardless of the medium.

The log K_2 values of fluoro, chloro, bromo and iodo derivatives show the following orders in the media investigated:

In 30% ethanol:

Reference > 4-F > 2-F

Reference > 4-Cl > 3-Cl > 2-Cl

Reference > 4-X > 3-X (X = Br, I)

In 40 and 50% ethanol:

Reference > 4-F > 2-F

Reference > 4-X > 3-X (X = Cl, Br, I)

In 60 and 70% ethanol:

Reference > 4-X (X = F, Cl, Br, I)

These orders of log K_2 values for all derivatives are as expected in the light of steric, resonance and inductive effects of substituents. Furthermore, when the basicities of halogen derivatives of the same substitution pattern are compared,

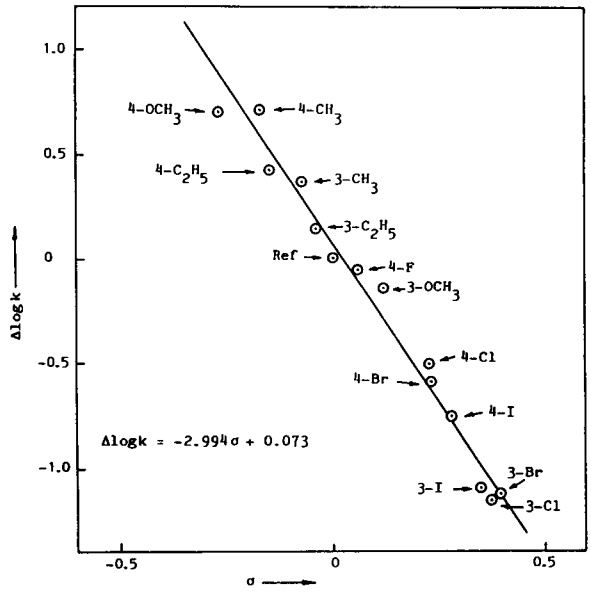

Fig. 5. Plot of Δ log k of substituted salicylideneanilines against Hammett substituent constants (σ) in 30% ethanol–70% water mixture.

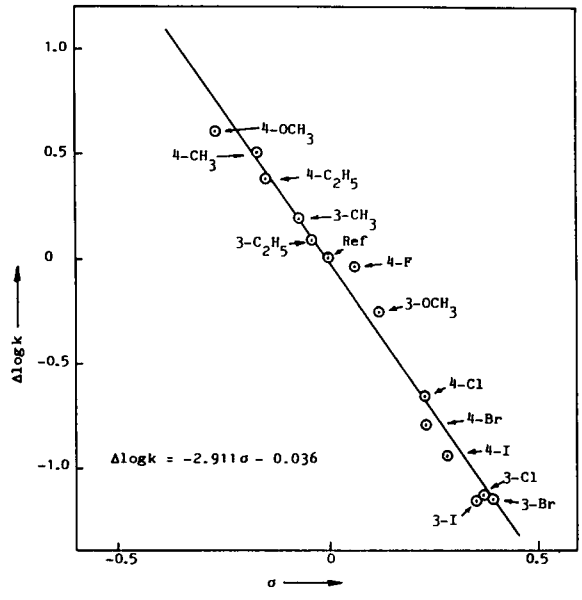

Fig. 6. Plot of Δ log k of substituted salicylideneanilines against Hammett substituent constants (σ) in 40% ethanol–60% water mixture.

orders obtained (for example, 4-I < 4-Br < 4-Cl < 4-F) can be explained by considering total electronic substituent effect (electron-withdrawing and electron-donating effects) [29]. No regularity was observed between the log K_1 values of the phenolic moiety of these Schiff's bases and the type and position of the substituents. This lack of regularity can be due to the fact that the substituents are located far from the phenolic OH group.

There is no systematic discussion to date on the applicability of the Hammett equation to the behaviour of substituents in Schiff's bases in ethanol–water mixtures. For this purpose, Δ log k values in Table 1 are plotted against substituents constants (σ) for each media studied, Figs. 5–10 [30]. The figures show that, to a reasonable approximation, the Hammett equation represents the effects of substituents on the reactivity of azomethine nitrogen of Schiff's bases. The relevant reaction constants (ρ) and the usual parameters describing the precision with which the data are represented by the Hammett equation are given in Table 2. Hoefnagel and Webster [31] studied the variation of the Hammett σ values with solvent composition for a great variety of substituted benzoic acid in ethanol–water and t-butyl alcohol–water. They showed that the sol-

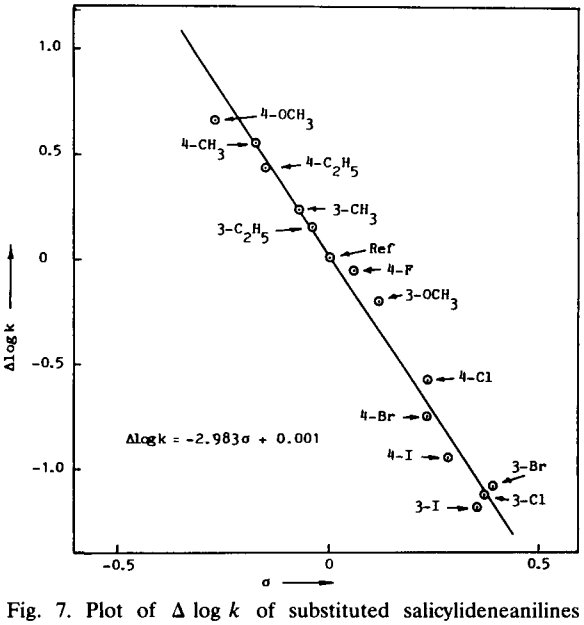

Fig. 7. Plot of Δ log k of substituted salicylideneanilines against Hammett substituent constants (σ) in 50% ethanol–50% water mixture.

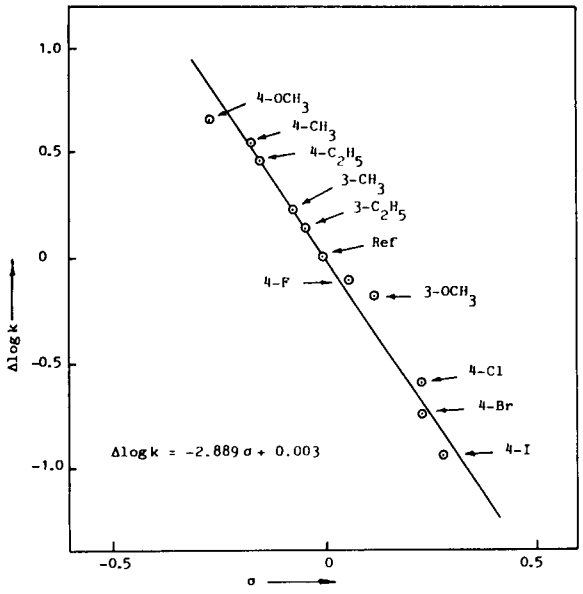

Fig. 8. Plot of Δ log k of substituted salicylideneanilines against Hammett subtituent constants (σ) in 60% ethanol–40% water mixture.

vent mixtures in the ranges 20–60% ethanol and 15–90% t-butyl alcohol introduce more or less serious complications with respect to the Ham-

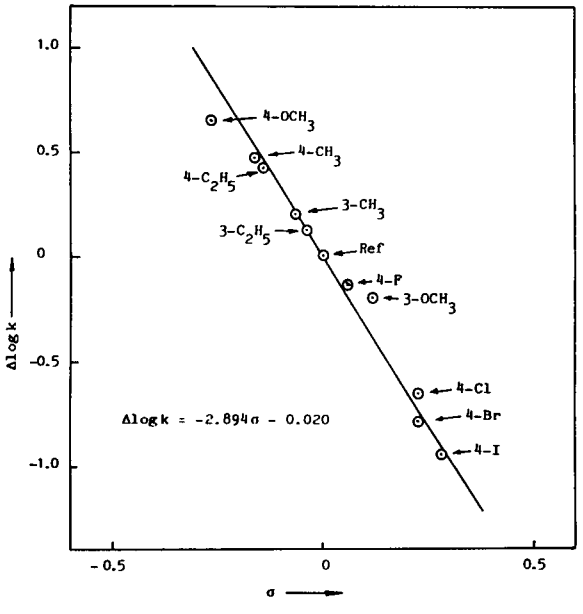

Fig. 9. Plot of the Δ log k of substituted salicylideneanilines against Hammett substituent constants (σ) in 70% ethanol–30% water mixture.

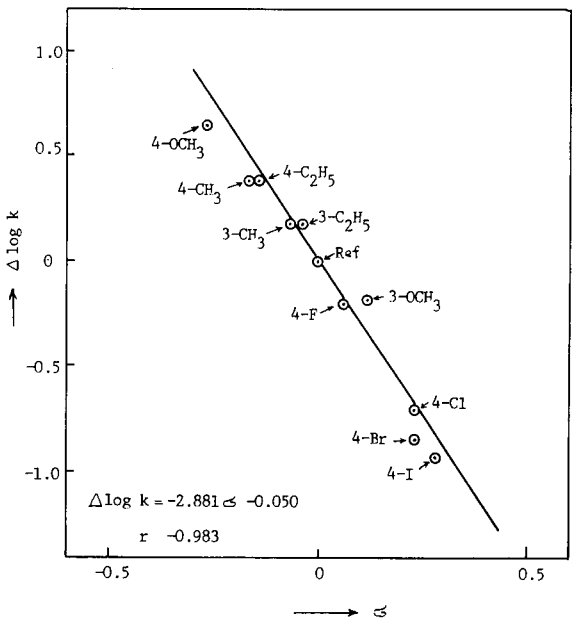

Fig. 10. Plot of the Δ log k of substituted salicylideneanilines against Hammett substituent constants (σ) in 80% ethanol–20% water.

mett equation and that the extended equation, $\Delta = \rho\sigma + h\pi$ (where π is Hansch's hydrophobic constant), covers the experimental data very well. Likewise, using our data on Schiff's bases, we studied how Hammett σ values ($\sigma = \Delta \log k/\rho$, where ρ values were taken from Table 2) vary with the percentage of ethanol to check Hoefnagel and Webster's equation. We observed that the anomalies for substituents studied are not significant and the σ values are nearly equal to

Table 2
Reaction constants for the reactivity of substituted salicylideneanilines at 25°C

Reaction	Ethanol (%)	ρ	s [a]	r [b]	n [c]
$HL + H^+ \rightleftarrows H_2L^+$	30	−2.994	0.050	−0.988	13
	40	−2.911	0.054	−0.990	13
	50	−2.983	0.050	−0.988	13
	60	−2.888	0.046	−0.986	10
	70	−2.894	0.052	−0.988	10
	80	−2.881	0.078	−0.983	10

[a] The standard deviation from the regression line.
[b] The correlation coeficients.
[c] The number of compounds entering the determination of ρ.

the aqueous values for each ethanol concentration. Therefore, it can be concluded that the simple Hammett equation very adequately represents the basicities of substituted Schiff's bases, and that there is no reason to believe that it should not equally apply to basicities of similar compounds. Also, in ethanol–water mixtures, Hoefnagel and Webster stated that the extended Hammett equation could no longer give any improvement for the substituents having a narrow range of π values like the ones studied by us.

Acknowledgement

We gratefully acknowledge the financial support of Ankara University Research Fund (Project No. 92-05-04-04).

References

[1] R.A. Delorenzo and A.D. Kowalok, J. Inorg. Nucl. Chem., 36 (1974) 2329.
[2] L.G. Van Uitert, C.G. Hass, W.C. Fernelius and B.E. Douglas, J. Am. Chem. Soc., 75 (1953) 455.
[3] H. Irving and H. Rossotti, Analyst, 80 (1955) 245.
[4] M.S.K. Niazi and J. Mollin, Bull. Chem. Soc. Jpn., 60 (1987) 2605.
[5] H. Irving and H. Rossotti, Acta Chem. Scand., 10 (1956) 72.
[6] J.F. Coetzee and C.G. Karakatsanis, Anal. Chem., 52 (1980) 59.
[7] T. Gündüz, E. Kılıç, E. Canel and F. Köseoğlu, Anal. Chim. Acta, 282 (1993) 489.
[8] B.L. Kaul, C.A., 104 (1986) 150788t.
[9] M. Butez, L. Rabas and F. Vinet, C.A., 107 (1987) 124755x.
[10] C. Monticelli, G. Brunora, A. Fignani and A. Marchi, Korroz. Figy., 28 (1988) 118.
[11] B. Dash, P.K. Mahapotra, D. Panda and J.M. Pattnaik, Indian J. Chem. Soc., 61 (1984) 1061.
[12] J. Casaszar, J. Morvay and O. Herczeg, Acta Phys. Chem., 31 (1985) 717.
[13] D.D. Perrin and W.L.F. Armarega, Purification of Laboratory Chemicals, Pergaman Press, Oxford, 1966, p. 148.
[14] G. Gran, Acta Chem. Scand., 4 (1950) 559.
[15] G. Gran, Analyst, 77 (1952) 661.
[16] A.E. Martell and R.J. Motekaitis, The Determination and Use of Stability Constants, VCH Publishers, Weinheim, 1988.
[17] M. Meloun, J. Havel and E. Högfeldt, Computation of Solution Equilibria, Wiley, New York, 1988.
[18] Kwan-Kit Mui, W.A.E. McBryde and E. Neiboer, Can. J. Chem., 52 (1974) 1821.
[19] G. Faraglia, F.J.C. Rossotti and H.S. Rossotti, Inorg. Chim. Acta, 4 (1970) 488.
[20] L.G. Van Uitert and C.G. Haas, J. Am. Chem. Soc., 75 (1953) 451.
[21] C.L. Norman, J.M. White and R.L. Yoest, J. Am. Chem. Soc., 78 (1956) 5218.
[22] T. Gündüz, N. Gündüz, E. Kılıç and A. Kenar, Analyst, 111 (1986) 1345.
[23] R.A. Robinson and R.H. Stokes, Electrolyte Solutions, Academic Press, New York, 1959.
[24] R.G. Bates, J. Electroanal. Chem., 29 (1971) 1.
[25] R.G. Bates, Determination of pH, Theory and Practice, Wiley, New York, 2nd edn., 1973.
[26] H.H. Freedman, J. Am. Chem. Soc., 83 (1961) 2900.
[27] J.W. Ledbetter, J. Phys. Chem., 72 (1968) 4111.
[28] G.H. Parsons and C.H. Rochester, J. Chem. Soc. Faraday Trans. I, 71 (1975) 1058.
[29] N.S. Isaacs, Physical Organic Chemistry, Longman, New York, 1986.
[30] H.H. Jaffe, Chem. Rev., 53 (1953) 191.
[31] A.J. Hoefnagel and B.M. Webster, J. Chem. Soc. Perkin Trans. II, (1989) 977.

ELSEVIER

Analytica Chimica Acta 293 (1994) 95–108

ANALYTICA CHIMICA ACTA

Kinetic studies of aluminum and zinc speciation in river water and snow

Yanjia Lu [a], C.L. Chakrabarti [a,*], M.H. Back [b], D.C. Grégoire [c], W.H. Schroeder [d]

[a] *Ottawa-Carleton Chemistry Institute, Department of Chemistry, Carleton University, 1125 Colonel By Drive, Ottawa, Ontario K1S 5B6, Canada*

[b] *Ottawa-Carleton Chemistry Institute, Department of Chemistry, University of Ottawa, Ottawa, Ontario K1N 6N5, Canada*

[c] *Geological Survey of Canada, 601 Booth St., Ottawa, Ontario K1S 0E8, Canada*

[d] *Atmospheric Environment Service, Environment Canada, 4905 Dufferin Street, Downsview, Ontario M3H 5T4, Canada*

Received 21st December 1993; revised manuscript received 31st March 1994

Abstract

Kinetic studies of chemical speciation by the Chelex-100 batch technique revealed aluminum is present both as an aquo ion and as simple complexes of inorganic ligands in snow, but probably bound to macromolecule complexants and/or colloidal substances in the Rideau River surface water. Two kinetically distinguishable components of aluminum having dissociation rate constants of 1.1×10^{-2}, $\leq 5.4 \times 10^{-4}$ s^{-1} and three kinetically distinguishable components of aluminum having dissociation rate constants of 5.5×10^{-3}, 8.4×10^{-4}, $\leq 6.3 \times 10^{-5}$ s^{-1} were observed in snow and river surface water, respectively. One kinetically distinguishable component of zinc having a dissociation rate constant of 9.1×10^{-3} s^{-1}, and three kinetically distinguishable components of zinc having dissociation rate constants of 8.5×10^{-3}, 2.5×10^{-3}, $\leq 6.0 \times 10^{-5}$ s^{-1}, were observed in snow and river surface water, respectively. Use of inductively-coupled plasma mass spectrometry (ICP-MS) with the solution nebulizer to follow the kinetics of the uptake of aluminum and zinc by the Chelex resin in the Chelex batch technique allowed collection of many more data points in the same time range than were obtainable by graphite platform furnace atomic absorption spectrometry (GFAAS) with an automatic sampler, with the result that ICP-MS had a greater ability to resolve labile complexes than GFAAS. ICP-MS is therefore preferable to GFAAS for kinetic studies of metal speciation in aqueous samples.

Key words: Ion exchange; Kinetic analysis; Metal speciation; Snow; River surface water

1. Introduction

Simultaneous kinetic analysis of multicomponent systems is well established [1–5] and extensively used [6–8]. The availability and transport of metal species in waters are controlled by interactions of the metal ions with colloidal ligands, humic substances, hydrous oxides and other macromolecular species [9–11]. It is well known now that the bioavailability of an element depends on both the chemical species in which the element is present in the environment and the

* Corresponding author.

SSDI 0003-2670(94)00166-J

rates of its biological uptake [12–15]. Because different chemical compounds may have different kinetic characteristics, it is possible to differentiate them kinetically by studying their kinetic behaviour. If the metal complexes in freshwaters are not sufficiently labile for the dissociation equilibria to be established during the time-scale of the measurement technique, then the dissociation kinetics of the metal complexes will determine the amount of the metal aquo ions available in the freshwater system. Since many metal complexes in freshwaters are not sufficiently labile, kinetic studies of such metal complexes are important both for understanding bioavailability of metals, metal speciation, and metal transport in the aquatic environment.

Aluminum is the third most abundant element in the earth's crust. As pointed out by Hutchinson [16], there is a long history of the role of aluminum in determining toxicity to aquatic and terrestrial organisms. The recent public concern about the toxicity of aluminum in the natural environment only reinforces its great importance in public health. The available evidence points to a strong correlation between aluminum and toxicity [17,18]. There is considerable evidence to show that cognitive impairment from aluminum is related to aluminum in drinking water [19]. Zinc has been included in this investigation because zinc is one of the heavy metals, the toxicity of which is related to its speciation [20].

Kinetic analysis applied to metal speciation has been reported by a number of authors [21–25]. All these studies were based on the measurement of the kinetics of metal ion transfer from naturally-occurring forms to complexes with a probe ligand, and the concentration of either the product(s) or the reactant(s) was monitored as a function of time. The methods used by the above authors for analyzing the kinetic data were the Guggenheim method [21,23,25] and the kinetic spectrum method [22,24] (Laplace transform), both methods using non-linear regression for the refinement of the kinetic parameters. In another paper [26] by the present authors, the iterative convolution method has been applied to the analysis of kinetic data for speciation of aluminum in synthetic, aqueous solution. The advantage of the iterative convolution method [26] is that it combines data analysis and model assessment together so that more reliable analysis on the kinetics of multi-component systems can be obtained.

The objectives of this research were: (1) to investigate the applicability of the iterative convolution method [26] to kinetic studies of aluminum and zinc speciation in model solutions of aluminum and zinc, each with or without fulvic acid, and the samples of unpolluted river surface water and snow; (2) to compare the performance of the under-named trace-analytical techniques to follow the dissociation kinetics of labile aluminum complexes in the above model solutions: graphite platform furnace atomic absorption spectrometry (GFAAS) and inductively-coupled plasma mass spectrometry (ICP-MS).

2. The kinetic model

The kinetic model [21,22] was developed to study the dissociation kinetics of ML_i, where M is a metal ion, L_i represents a ligand, either a simple inorganic ligand or a simple organic ligand, or a binding site on a polyfunctional complexant, such as humic substance. Consider an aqueous solution containing a mixture of n components in which each component exists in equilibrium with its dissociation products:

$$ML_i \rightleftharpoons M + L_i \quad (1)$$

For simplicity, the charge sign on the metal ion (M) is omitted. When an excess of the strong complexing ligand, Chelex cation exchange resin, is introduced into the mixture, metal ions are taken up by the Chelex resin:

$$\text{Chelex} + M \rightleftharpoons \text{Chelex–M} \quad (2)$$

Eq. 1, then, shifts to the right to restore the metal ions:

$$ML_i \xrightarrow{k_i} M + L_i \quad (3)$$

where k_i is the rate constant for the dissociation of ML_i species. If reaction 2 is much faster than reaction 3, the measured kinetics, then, represents the dissociation kinetics of ML_i, and if each

complex, ML_i, undergoes, independently and simultaneously, a first-order, or pseudo-first-order dissociation reaction, the sum of the concentrations of all components remaining in the solution at time t can be described as

$$C(t) = \sum_{i=1}^{n} C_i^0 \exp(-k_i t) \quad (4)$$

where C_i^0 is the initial concentration of ML_i.

The two assumptions made in the above kinetic model are as follows: (1) Reaction 2 is much faster than reaction 3. (2) Reaction 3 is first-order or pseudo-first-order.

It has been shown in Results and Discussion that the above assumptions are valid.

3. Analytical techniques

Freshwaters contain most, if not all, elements of the Periodic Table, plus a vast number of organic complexants. Innumerable interactions can occur in such systems, whereby an element is distributed in many different forms. The concentrations of trace elements are low, usually at part-per-billion (1 in 10^9) or even lower, in unpolluted freshwaters, and the concentration of each species of an element is even lower. These characteristics of freshwaters require that the analytical techniques used to determine the concentrations of elements in such systems be highly sensitive and also highly selective. Furthermore, the quantity and the quality of the experimental data are crucial for kinetic studies of chemical speciation because the number of kinetically distinguishable components, the dissociation rate constant and the initial concentration of each kinetically distinguishable component must be obtained by curve-fitting of the experimental data.

Two analytical techniques of great sensitivity used for direct, quantitative determination of metal concentrations in freshwaters are compared in terms of their usefulness for following kinetics of metal–complex dissociation: graphite furnace atomic absorption spectrometry (GFAAS) and inductively coupled plasma mass spectrometry (ICP-MS). GFAAS has excellent sensitivity and selectivity and has been shown to be an analytical technique applicable of direct determination of metals for kinetic studies of metal speciation in natural waters [21]. However, the discrete (i.e., non-continuous) sampling required by GFAAS produces data points separated at least by the analysis time (about 1 min) of the measurement technique, and hence, limits the number of data points. Also, the transfer of the sample and the time required for determination by GFAAS introduces risk of contamination and loss of analyte by adsorption (the longer the time the greater the risk of contamination and loss by adsorption, the latter on the wall of the plastic vials), resulting in scatter of data points and hence in lower precision of the results obtained. As well, the time required for analysis by GFAAS limits its application to the study of only those species having a half-life no shorter than minutes. In order to overcome these limitations, the performance of the other analytical technique, an inductively-coupled plasma mass spectrometer (ICP-MS) with solution nebulization mode of sample introduction using a peristaltic pump, was tested. ICP-MS is a simultaneous multielement analytical technique that is used for the determination of over 75 elements in a variety of matrices. The detection limits of ICP-MS are comparable to or better than GFAAS. Its on-line monitoring capability gives real- or near real-time resolution. This feature allows fast kinetics of labile complexes to be readily studied. However, GFAAS is a useful technique for cross-checking the reliability of ICP-MS and for detecting isobaric interferences in ICP-MS.

4. Method for data analysis: the iterative convolution method

In the iterative convolution method, the experimental data are fitted to Eq. 4 by non-linear regression assuming a number of components,

starting with one and increasing until the sum of squares of the weighted residuals, defined as:

Sum of squares of weighted residuals

$$= \sum \left[\frac{C(t) - C_T(t)}{C(t)^{1/2}} \right]^2 \quad (5)$$

where $C(t)$ is the experimental value, and $C_T(t)$ is the calculated value using Eq. 4, achieves a minimum value, and the plot of the weighted residuals over the course of the reaction gives a random and uniform distribution about zero. The values for C_i^0 and k_i for each kinetically distinguishable component are then given by non-linear regression. For detailed information about the iterative convolution method, please see Ref. 26.

5. Experimental

5.1. Materials

Chelex-100 cation exchange resin (Bio-Rad, 100–200 mesh, sodium form) was equilibrated with the NaOAc–HOAc buffer at the pH of the samples. Because the dryness of the resin affected the properties of the resin, and hence changed the pH of the sample during the kinetic measurements, the resin was isolated from the buffer solution immediately before the kinetic measurements. The NaOAc–HOAc buffer was prepared by adding 59.0 ml of concentrated pure acetic acid (ACS grade, Anachemia) to about 1 l of ultrapure water. The pH of the above solution was made 5.0 by adding 6 M NaOH (reagent grade, Fisher Scientific) to it and the solution was diluted to 2 l with ultrapure water.

The Laurentian fulvic acid (FA), supplied by Dr. D.S. Gamble, Agriculture Canada, was prepared following known procedures [27,28] from a sample of a podzol collected from the Laurentian forest preserve of Laval University, Quebec, Canada. Titration revealed 3.03 m mol g^{-1} phenolic group in the above fulvic acid [29], and the phenol content was used for the calculation of the [FA]/[Metals] ratios.

The mixed-metal standard was the ICPMS-2 metal standard (Delta Scientific) containing Al, Zn, Cu, Cd, Ni, Pb and other metals (10 μg ml^{-1} each). Stock solutions containing a single metal (1000 μg ml^{-1}) of Cd, Cu, Ni and Pb were prepared by dissolving an appropriate quantity of CdO (Baker, Analyzed Reagent), copper metal (99.9% pure), nickel metal powder (SPEX, 99.999%) and $Pb(NO_3)_2$ (Fisher, ACS reagent), in nitric acid with heating, and diluting the solution to the appropriate volume with ultrapure water; the final solutions contained 1% (v/v) ultrapure HNO_3. Stock solution (1000 μg ml^{-1}) of aluminum was prepared by dissolving 0.5000 ± 0.004 g aluminum powder (SPEX) in 20 ml 1:1 HCl (Ultrex-brand): H_2O with heating and diluting the solution to 500 ml with ultrapure water. A standard solution (1000 μg ml^{-1}) of Zn was purchased from BDH. Ultrapure water was obtained direct from a Milli-Q-Plus system (Millipore). Screw-capped polyethylene and Teflon bottles (500, 1000 and 2000 ml capacity) were used as reactors and sample storage containers, respectively. These bottles were pre-cleaned following the procedure described in our previous paper [21]. The reactors were equilibrated with the samples before the kinetic measurements.

5.2. Samples

Two sets of model solutions, one contained Al(III) only and the other contained Al(III), Zn(II), Cu(II), Cd(II), Ni(II) and Pb(II), were prepared by spiking ultrapure water or the NaOAc–HOAc buffer solutions of different concentrations with appropriate volumes of standard solutions of metals and of the fulvic acid solution (0.1000 g l^{-1}). The pH (measured with a Fisher Scientific, Accumet 925 pH/ion meter) of the samples was made 5.0 using dilute HNO_3 or NaOH solutions, and the model solutions were left to stand overnight for equilibration. The pH was confirmed after the equilibration.

A surface water sample (5 l) from Rideau River was collected using a precleaned polyethylene water sampler from a site at Carleton University. In order to bring the concentration of the metal analyzed to a detectable level, the sample was spiked with metal standard solutions of Cu,

Ni, Zn, Cd and Pb to contain a few $\mu g\ l^{-1}$ of each, and the pH of the sample was adjusted to 5.0 ± 0.1. After leaving the sample to stand for two days for equilibration, the sample was filtered through a 0.45-μm filter to separate the particulate matter. The filtrate was collected and left to stand for one day for equilibration before making kinetic measurements. The pH was confirmed after the equilibration.

A sample of snow was collected with a pre-cleaned polyethylene pail at a site on the roof top of the chemistry building at Carleton University. The sample was kept in the pail at room temperature inside the laboratory until the snow melted. The snow-melt was filtered through a 0.45-μm filter and the pH was measured before and after the filtration. The concentrations of the metals in the kinetic study described below were determined by ICP-MS.

5.3. Dissociation kinetics of metal complexes

The kinetics of metal uptake in the Chelex batch technique was measured using the following method. Fig. 1 shows the reactor, which was designed in such a way that it allowed the clear sample solution to be withdrawn continuously, through a filter made of nylon membrane, placed in front of the out-let tube, thereby effecting the separation of the sample solution from the Chelex resin. The procedure consisted of adding the pre-treated Chelex resin to a sample solution (400 ml) and the mixture was stirred with a Teflon-coated magnetic stirring bar. The time

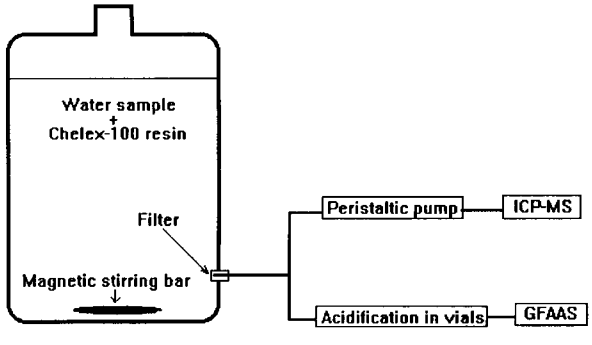

Fig. 1. Schematic diagram of the apparatus for the Chelex-100 batch experiment.

Chelex resin first came in contact with the sample in the reactor was taken as the starting point (time zero). The sum of the concentrations of all the kinetically distinguishable components of the metal remaining in the solution was monitored as a function of time using either ICP-MS or GFAAS. The pH of the sample was also monitored throughout the Chelex-100 batch experiment. Changes in the pH were found to be $< \pm 0.5$ for the unbuffered samples and $< \pm 0.02$ for the buffered samples. In order to ensure that reaction 2 was first-order or pseudo-first-order, various concentrations of Chelex resin of 0.25, 0.50, 0.75 and 1.00% (w/w) in the synthetic aqueous samples were examined for the uptake of the metal ions. The results showed that the uptake of aluminum by Chelex-100 greatly increased when the concentration of Chelex resin was increased from 0.25 to 0.50%, but showed only a small increase with further increase in the concentration of the Chelex resin. The concentration of 1% (equivalent to the Chelex to metal ratio of 100 or higher, depending on the concentrations of the metals in the sample) was therefore used in further studies. Under this experimental condition, the effect of a change in the sample volume during the kinetic measurements was negligible. Chelex resins of 50–100, 100–200 and 200–400 mesh were also examined for their uptake of metal ions from the model solutions. No significant change in the uptake of aluminum was found with the Chelex resins of 100–200 and 200–400 mesh. These results also suggested that any change in the surface area of the Chelex resin due to grinding of the resin by the magnetic stirring bar was not significant.

5.4. Procedure for analysis by GFAAS and ICP-MS

Both the graphite platform furnace atomic absorption spectrometer (Perkin-Elmer Zeeman, Model 5000 equipped with an autosampler) and the inductively-coupled plasma mass spectrometer (Perkin Elmer Sciex Elan-5000) were used to measure the kinetics of metal–complex dissociation. In graphite furnace atomic absorption spectrometry (GFAAS), an HGA-500 graphite furnace, pyrolytically-coated graphite tubes and lab-

Table 1
Instrumental operating conditions and data acquisition protocol for the GFAAS (for aluminum) and for the ICP-MS determination

GFAAS	
Analysis line, nm	309.2
Pyrolysis temperature, °C	1300
Atomization temperature, °C	2400
Atomization duration, s	7
ICP-MS	
RF power	1000 W
Coolant argon flow rate	15.0 l min^{-1}
Auxiliary argon flow rate	850 ml min^{-1}
Carrier argon flow rate	900 ml min^{-1}
Sampler/skimmer	Nickel
Dwell time	100–1000 ms
Scan mode	Peak hop transient
Points/spectral peak	1

oratory-made platforms fabricated from pyrolytic graphite were used. The experimental conditions for GFAAS are given in Table 1. Aliquots of the test solutions (1 ml) were acidified with 10 μl of concentrated nitric acid in small plastic vials. 10–20 μl of this acidified test solution was injected into the graphite furnace and deposited at the same place on the graphite platform (to ensure reproducibility), the solution was dried, pyrolyzed and atomized. The atomic absorbance signal was measured in the peak area mode. The atomization cycle in GFAAS was followed by a 3-s clean-up step of the graphite tube at 2600°C. The argon gas flow was interrupted during the atomization cycle. During the drying, pyrolysis and clean-up cycles, argon gas was passed through the furnace at 300 ml min^{-1}.

In inductively-coupled plasma mass spectrometry (ICP-MS), a peristaltic pump continuously delivered the sample solution to the ICP torch through the nebulizer at a flow rate of 1 ml min^{-1}. The ionic species were analyzed according to their mass/charge ratio by the quadrupole mass analyzer, followed by signal detection with a channel electron multiplier. The signal (counts s^{-1}) was monitored as a function of time. Signals were detected at the mass corresponding to each element to be analyzed. A dwell time for collection of the signal for each element was chosen to give good resolution and low noise. A short dwell time more accurately captures a "snapshot" of the sample spectrum in time, which is especially useful in metal speciation for kinetic study of fast components, but may raise the uncertainty level of the measurement beyond acceptable limits. Therefore, a compromise was made by selecting a dwell time of 100–1000 ms. The interval between successive data points was determined by the dwell time. The experimental conditions and the data acquisition protocol for the ICP-MS determination are listed in Table 1.

6. Results and discussion

6.1. Results of kinetic analysis of the synthetic model solutions of aluminum and zinc

Kinetics of uptake of aluminum species as a function of the NaOAc–HOAc buffer concentrations

Fig. 2 shows the uptake of the aluminum species by the Chelex resin as a function of time for the model solutions containing different con-

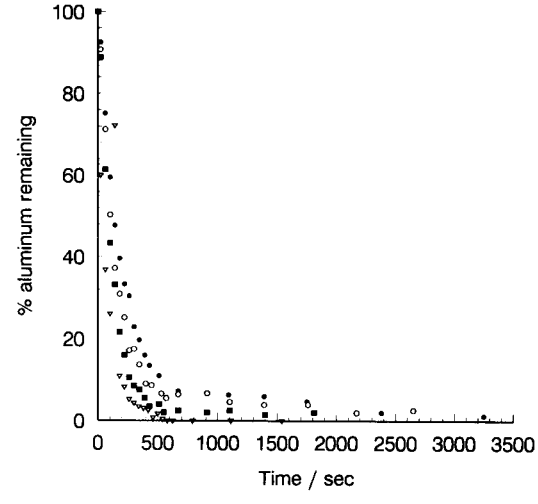

Fig. 2. Percentage of aluminum remaining in the model solutions containing aluminum, as a function of time after uptake of the aluminum by the Chelex-100 resin in the Chelex batch technique, determined by GFAAS. pH 5.0. [Chelex] = 1% (w/w). ●: [NaOAc]:[HOAc] = 0.32:0.18, [Al(III)] = 3.1 μM; ○: [NaOAc]:[HOAc] = 0.16:0.090, [Al(III)] = 2.6 μM; ■: [NaOAc]:[HOAc] = 0.080:0.045, [Al(III)] = 2.3 μM; ▽: [Buffer] = 0.00, [Al(III)] = 0.82 μM.

centrations of the NaOAc–HOAc buffer and aluminum. Although for all of these samples more than 90% of the aluminum species was taken up by the Chelex resin in a few hundred seconds, the time to reach the equilibrium was longer for the buffer of higher concentrations. The rate constants for the uptake of the aluminum by the Chelex resin obtained using the iterative convolution method, as shown in Table 2, decreased with increasing concentrations of the buffer, and a second kinetically distinguishable component appeared when the concentration of OAc^- was increased to 0.16 M. As pointed out by Pai et al. [30], the effect of the salt content on the metal uptake by the Chelex-100 is attributed to the competition of cations of the salt with the metal ions of the sample for the exchange sites on the Chelex resin, and to the complexation reaction between the metal ions and the anions of the salt. A similar explanation would apply to the system with aluminum ions and the sodium acetate buffer. Since the cation, Na^+, in the buffer was the same as that in the Chelex resin, the competition for the exchange sites in the Chelex resin was minimized. The decreased rate constants for the uptake of the aluminum are therefore attributable to the formation of Al–acetate complexes. The appearance of the second kinetically distinguishable component of aluminum at the high concentration of OAc^- was probably due to the formation of more than one Al–acetate complex [31].

Table 3
Kinetics of uptake of the aluminum species by the Chelex resin from the buffered ([NaOAc]:[HOAc] = 0.32:0.18) model solutions containing aluminum, as a function of the initial concentration of aluminum (pH = 5.00 ± 0.02)

$[Al(III)]_{total}$, μM	$k_1 \times 10^{-3}$, s^{-1}	
	GFAAS	ICP-MS
4.7	6.4 ± 0.8	–
3.9	6.4 ± 0.1	–
3.8	–	5.4 ± 0.03
1.2	5.6 ± 0.4	–

Values after ± signs are standard deviations of non-linear regression analysis; $[Al(III)]_{total}$ = the total initial concentration of aluminum.

Kinetics of uptake of aluminum species as a function of the initial concentrations of aluminum

Table 3 shows the rate constants in the Chelex batch process for uptake of the aluminum species by the Chelex resin from the buffered (NaOAc–HOAc) samples containing aluminum only; the concentrations of aluminum were determined by either ICP-MS or GFAAS. The pH changes in the Chelex batch technique were ±0.02. Because ICP–MS cannot tolerate sample solutions having high-salt content such as the buffered solutions for more than a very short period of sample delivery, it was decided to run a single sample with ICP–MS, and hence, there is only a single datum for ICP–MS against three data for GFAAS in Table 3. The concentration of each of the

Table 2
Kinetics of uptake of aluminum species by the Chelex resin from model solutions of aluminum, determined by GFAAS, as a function of the NaOAc–HOAc buffer concentrations (pH = 5.00 ± 0.02 for the buffered samples and 5.0 ± 0.5 for the unbuffered samples)

[NaOAc]:[HOAc]	$[Al(III)]_{total}$, μM	C_1^0, %	$k_1 \times 10^{-3}$, s^{-1}	C_2^0, %	$k_2 \times 10^{-4}$, s^{-1}
0:0	1.1	100	9.9 ± 1		
0:0	0.82	100	10 ± 2		
0.040:0.022	1.6	100	8.9 ± 0.4		
0.080:0.045	2.3	100	7.9 ± 0.4		
0.16:0.090	2.6	93	7.8 ± 0.4	7	≤ 4.2 ± 1
0.32:0.18	3.1	90	6.2 ± 0.3	10	≤ 6.0 ± 0.8

Values after ± signs are standard deviations of non-linear regression analysis; $[Al(III)]_{total}$ = the total initial concentration of aluminum; C_1^0 and C_2^0, % = the initial percentages of the first (the faster) and the second kinetically distinguishable component, respectively.

kinetically distinguishable component of aluminum in the test solutions in the Chelex batch technique (as determined by ICP–MS) was observed to decrease exponentially as a function of time (Fig. 2), indicating first- or pseudo-first order kinetics for the loss process. Also, the rate constants for the fastest kinetically distinguishable component of aluminum were found to be within ±9% of the average value when the initial concentrations of aluminum were varied by a factor of 3 or 4, thus verifying the assumption made earlier that the kinetics of Eq. 3 was first-order or pseudo-first-order.

Kinetics of uptake of aluminum species as a function of the fulvic acid concentration

Fig. 3 shows the uptake of aluminum by the Chelex resin from unbuffered model solutions containing Al(III), Zn(II), Cd(II), Cu(II), Ni(II) and Pb(II), with or without fulvic acid, determined by ICP-MS. The pH changes for the Chelex batch processes were < 0.5 pH unit. More than 96% of the aluminum was taken up within 500 s by the Chelex resin from the sample without fulvic acid, whereas approximately 28%, 32% and 45% of the aluminum in the samples having the ratio of [FA] to [M] of 0.58, 0.87 and 1.2, respectively, still remained in the solutions after 7000 s (where [M] = [Al(III)] + [Cd(II)] + [Cu(II)] + [Ni(II)] + [Pb(II)] + [Zn(II)]). This indicates that the aluminum species associated with the fulvic acid are taken up by the Chelex resin much more slowly. This agrees with the results reported by Campbell et al. [32]. Fig. 3 also validates the

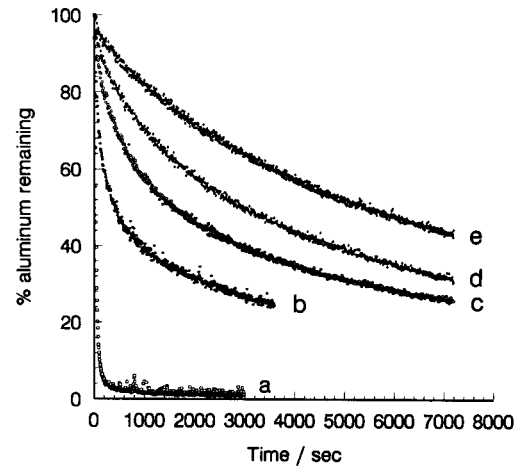

Fig. 3. Percentage of aluminum remaining in the unbuffered model solutions containing Al(III), Zn(II), Cd(II), Cu(II), Ni(II) and Pb(II), as a function of time after uptake of the aluminum by the Chelex-100 resin in the Chelex batch technique, determined by ICP-MS. pH 5.0. [Chelex] = 1% (w/w). [Al(III)] = 1.5 μM. (a) [FA]:[M] = 0.00; (b) [FA]:[M] = 0.29; (c) [FA]:[M] = 0.58; (d) [FA]:[M] = 0.87; (e) [FA]:[M] = 1.2. [M] = Al(III)] + [Cd(II)] + [Cu(II)] + [Ni(II)] + [Zn(II)] + [Pb(II)] = 2.1 μM.

Table 4
Kinetics of uptake of aluminum species by the Chelex resin from the model solutions, determined by ICP-MS, as a function of the concentration of fulvic acid (pH = 5.00 ± 0.02 for the buffered samples, 5.0 ± 0.5 for the unbuffered samples)

[FA]:[M] [a]	$[Al(III)]_{total}$, μM	C_1^0, %	$k_1 \times 10^{-2}$, s^{-1}	C_2^0, %	$k_2 \times 10^{-3}$, s^{-1}	C_3^0, %	$k_3 \times 10^{-4}$, s^{-1}	C_4^0, %	$k_4 \times 10^{-5}$, s^{-1}
Unbuffered samples									
0 [b]	1.5	84	2.7 ± 0.05	14	4.3 ± 0.4	2	≤ 1.8 ± 0.2		
0	1.5	92	2.9 ± 0.09	5	4.5 ± 0.07	3	≤ 2.1 ± 0.3		
0.29	1.5	31	1.9 ± 0.1	27	2.6 ± 0.1	42	≤ 1.6 ± 0.02		
0.58	1.5			18	5.5 ± 0.3	33	8.4 ± 0.3	49	≤ 8.8 ± 0.2
0.87	1.5					30	9.2 ± 0.2	70	≤ 10 ± 0.1
1.2	1.5					23	5.0 ± 0.3	77	≤ 7.7 ± 0.2
Buffered samples									
0 [b]	3.9			92	5.3 ± 0.3	8	4.0 ± 0.2		
4.1 [b]	4.0			23	7.1 ± 0.2	40	17 ± 1	37	≤ 4.9 ± 0.06

Values after ± signs are standard deviations of non-linear regression analysis; [M] [a] = {[Al(III)] = 1.5} + {[Cd(II)] = 0.099} + {[Cu(II)] = 0.16} + {[Ni(II)] = 0.17} + {[Pb(II)] = 0.048} + {[Zn(II)] = 0.15} = 2.1 μM; $[Al(III)]_{total}$ = the total initial concentration of aluminum; C_1^0, C_2^0, C_3^0 and C_4^0, % = the initial concentration (percentage) of the first (fastest), the second, the third and the fourth kinetically distinguishable component, respectively.

[b] The samples contain aluminum only.

assumption made earlier that the rate of the forward reaction of Eq. 2 is much greater than that of Eq. 3, making the latter reaction the rate-limiting step of the overall reaction.

The rate constants of the aluminum uptake by the Chelex resin obtained from the data analysis by the iterative convolution method [26] are listed in Table 4. For the unbuffered model solutions without the fulvic acid, three kinetically distinguishable components of aluminum were resolved, but the slowest component contained only 2–3% of the total aluminum in the sample. The presence of Zn(II), Cd(II), Cu(II), Ni(II) and Pb(II) had no significant effect on the number of kinetically distinguishable components of aluminum present and on the rate constants. For the major components in the samples with a different ratio of [FA] to [M], the initial content (percentage) for the faster component deceased, whereas that for the slower component increased with increasing ratio of [FA] to [M], probably because of formation of Al–fulvic acid complexes. Variation in the dissociation rate constant measured for each component of Al–fulvic acid complex gave the experimental evidence of polyfunctionality of fulvic acid since the dissociation rate constant measured here was an average value of a group of closely-related rate constants. With changing ratios of [FA] to [M], the distribution of aluminum species changed, leading to the change in the dissociation rate constant. For comparison, the results from the buffered solution showed only two kinetically distinguishable components and the rate constant of the major, kinetically distinguishable component of the aluminum in the buffered solution without fulvic acid was smaller than that in the unbuffered solution, probably because of formation of Al–acetate complexes. With increasing concentrations of fulvic acid, the percentage of the slowest, kinetically distinguishable component increased greatly, probably reflecting the fact that most of the aluminum was bound to fulvic acid and the Al–fulvic acid was the slowest component. These results indicate either that the rate of uptake of the aluminum aquo ions by the Chelex resin is much faster than the rate of dissociation of the Al–fulvic complexes (if the dissociation of aluminum complex produces the aluminum ions before their uptake by the Chelex resin), or that the rate of uptake of the aluminum aquo ions by the Chelex resin is much faster than the direct uptake of the Al–fulvic complexes by the Chelex resin. These two mechanisms were described in our earlier paper [26].

Kinetics of uptake of zinc species as a function of the fulvic acid concentration

Fig. 4 shows the uptake of Zn(II) by the Chelex resin from unbuffered model solutions containing Al(III), Zn(II), Cd(II), Cu(II), Ni(II) and Pb(II), with or without fulvic acid. For all of the samples tested, more than 90% of the Zn(II) was taken up by the Chelex resin in 500 s, and the plots of Zn(II) remaining as a function of time showed no significant effect of fulvic acid on the kinetic behaviour of zinc species. The results from the data analysis by the iterative convolution method

Table 5
Kinetics of uptake of zinc species by the Chelex resin from the model solutions, determined by ICP-MS, as a function of the concentrations of fulvic acid (pH 5.0 ± 0.5)

[FA]:[M] [a]	$[Zn(II)]_{total}$, μM	C_1^0, %	k_1, $\times 10^{-2}$, s^{-1}	C_2^0, %	k_2, $\times 10^{-4}$, s^{-1}
0	0.14	98	2.7 ± 0.04	2	≤ 1.0 ± 0.05
0	0.064	98	1.6 ± 0.03	2	≤ 3.8 ± 0.2
3.9	0.089	96	1.1 ± 0.03	4	≤ 2.0 ± 0.2
7.7	0.071	93	0.69 ± 0.02	7	≤ 2.2 ± 0.1

Values after ± signs are standard deviations of non-linear regression analysis; [M] [a] = [Al(III)] + [Cd(II)] + [Cd(II)] + [Ni(II)] + [Pb(II)] + [Zn(II)] = 0.99 μM; $[Zn(II)]_{total}$ = the total initial concentration of zinc; C_1^0 and C_2^0, % = the initial concentration (percentage) of the first (the fastest) and the second kinetically distinguishable component, respectively.

[26] are listed in Table 5. Two kinetically distinguishable components of zinc were resolved for all of the samples, with the faster component comprising more than 90% of the total zinc concentration. The number of kinetically distinguishable zinc components and the distribution of zinc obtained in this study for the samples having the ratio of [FA] to [M] ≤ 3.9 are in general agreement with those from the equilibrium calculation [33]. The addition of small amounts of fulvic acid slightly decreased the dissociation rate constant, but it did not change the distribution of Zn(II) in the samples. However, since the concentration of the second kinetically distinguishable component of zinc counted for only a very small fraction of the total zinc concentration in the samples, its determination would involve much greater uncertainty.

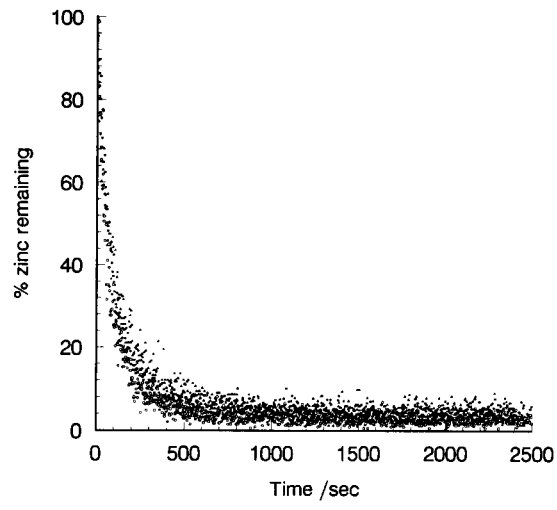

Fig. 4. Percentage of zinc remaining in the unbuffered model solutions containing Al(III), Zn(II), Cd(II), Cu(II), Ni(II) and Pb(II), as a function of time after uptake of zinc by the Chelex-100 resin in the Chelex batch technique, determined by ICP-MS. pH 5.0. [Chelex] = 1% (w/w). •: [FA]:[M] = 0.00, [Zn(II)] = 0.064 μM; ○: [FA]:[M] = 3.9, [Zn(II)] = 0.089 μM; ▲: [FA]:[M] = 7.7, [Zn(II)] = 0.071 μM. [M] = Al(III)] + [Cd(II)] + [Cu(II)] + [Ni(II)] + [Zn(II)] + [Pb(II)] = 0.99 μM.

Comparison of the results obtained by GFAAS and by ICP-MS

Table 3 indicates that the rate constant for the aluminum uptake by the Chelex resin determined by these two techniques is in good agreement. However, comparison of Figs. 2–4 shows that the major difference between Fig. 2 and Figs. 3 and 4 is that ICP-MS is capable of giving a much larger number of experimental data points than GFAAS; this is crucial specially at the beginning of the kinetic measurement where ICP-MS has provided experimental data points, whereas GFAAS has failed to do so. The result is that ICP-MS can reveal the presence of very labile complexes, whereas GFAAS cannot; also, later in the kinetic run, ICP-MS can resolve complexes which are kinetically close to one another, so close as not to be resolvable by GFAAS. Data analysis by the iterative convolution method [26] shows that: (1) three kinetically distinguishable components of aluminum are resolved from the data obtained by ICP-MS, but only one kinetically distinguishable component is resolved from the data obtained by GFAAS for the unbuffered model solutions, as shown in Tables 2 and 4; (2) the standard error of the kinetic parameters, as shown in Tables 2–4, is generally one order of magnitude higher when using the data set obtained by GFAAS. Since the iterative convolution method [26] is based on fitting experimental data, time resolution on the experimental data is essential for obtaining reliable results. If the interval between the experimental data points is too large, as in the case of the GFAAS determination, some kinetically distinguishable components are lost. The larger error on the data set obtained using GFAAS is attributable to (1) the small number of experimental data points; (2) a higher degree of scatter in the data points. Delivery of discrete, sequential samples involving a sample transfer step, inherent in the current GFAAS technology, as opposed to direct, continuous delivery of samples in the ICP-MS solution nebulization technique, limits the number of experimental data points by GFAAS. The much larger number of data points and the smaller scatter in the data points observed in the ICP-MS determination is due to the direct insertion of the sample, which eliminates the sample transfer step and the attendant time of the sample transfer step, resulting in a significant de-

crease in the adsorption loss of the analyte and in the sample contamination, both of which are functions of the time taken by the sample transfer step, and hence, occur in GFAAS, but are almost absent in ICP-MS. In fact with the dwell time of the order of 10 milliseconds for measurements with ICP-MS in principle chemical species with half-lives of this magnitude could be measured. In this aspect ICP-MS has excellent potential for kinetic analysis. Nevertheless, the excellent selectivity of GFAAS, together with its much lower cost per sample and fast, sequential multi-element capability make it a very powerful technique for kinetic studies, especially for cross-checking the reliability of ICP-MS results and for identifying any possible interferences by molecular species in ICP-MS.

6.2. Results of the analysis of a sample of snow

A sample (pH 5.6) of fresh snow was collected on April 1, 1993 at the sample-collection station situated on the roof of the Chemistry Building of Carleton University and analyzed by the Chelex batch technique for Al and Zn. Fig. 5a shows the uptake of aluminum from the snow-melt (pH 5.6). Similar data were obtained for Zn. The logarithmic plot of Fig. 5a, Fig. 5b, indicates that more than one kinetically distinguishable component of aluminum are present in the sample of snow. The iterative convolution method [26] applied to these two sets of data reveals two kinetically distinguishable components of aluminum and one kinetically distinguishable component of zinc, as shown in Table 6. The rate constants for the aluminum species in the snow sample are comparable to those in the model solutions of aluminum without fulvic acid. The rate constant of 9.1×10^{-3} s^{-1} for the zinc species in the snow sample is in good agreement with that (4.1×10^{-3} s^{-1}) for the snow sample presented in our previous paper [21], and these values are comparable to those of the model solutions presented in this paper.

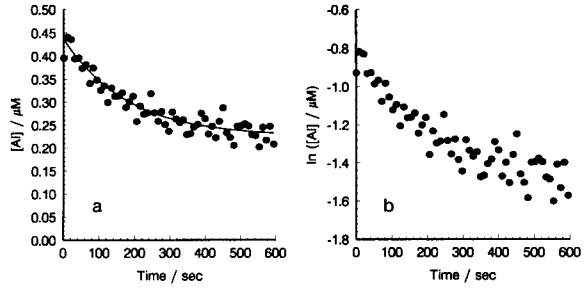

Fig. 5. Aluminum remaining in the snow sample, as a function of time after uptake of aluminum by the Chelex-100 resin in the Chelex batch technique, determined by ICP-MS. pH 5.6. [Chelex] = 1% (w/w). (a) Plot of [Al(III)] vs. time, points are experimental data and the solid line is the least-square line; (b) the logarithmic plot of (a).

Table 6
Chelex-batch-lability of the aluminum and zinc species in the snow sample (pH 5.6) and in the Rideau River surface water sample (pH 5.0 ± 0.5)

Metal	Number of components resolved	C_i^0, μM	C_i^0, %	k_i, s^{-1}
Snow sample				
Al	2	0.14	31	$(1.1 \pm 0.1) \times 10^{-2}$
		0.31	69	$\leq (5.4 \pm 0.7) \times 10^{-4}$
Zn	1	0.050	100	$(9.1 \pm 0.07) \times 10^{-3}$
Rideau river surface water sample				
Al	3	0.068	13	$(5.5 \pm 1) \times 10^{-3}$
		0.076	15	$(8.4 \pm 2) \times 10^{-4}$
		0.37	72	$\leq (6.3 \pm 0.4) \times 10^{-5}$
Zn	3	0.047	55	$(8.5 \pm 0.8) \times 10^{-3}$
		0.032	38	$(2.5 \pm 0.2) \times 10^{-3}$
		0.0059	7	$\leq (6.0 \pm 0.7) \times 10^{-5}$

Values after ± signs are standard deviations of non-linear regression analysis; C_i^0, μM = the initial concentration of the ith kinetically distinguishable component; C_i^0, % = the initial concentration (percentage) of the ith kinetically distinguishable component.

6.3. Results of the analysis of a sample of Rideau River surface water

Figs. 6 and 7 show the uptake of aluminum and zinc from a sample of Rideau River surface water at pH 5.0 in the Chelex batch technique. The curves a in both Figures are the signal vs. time for ultrapure water and serve as blanks, and

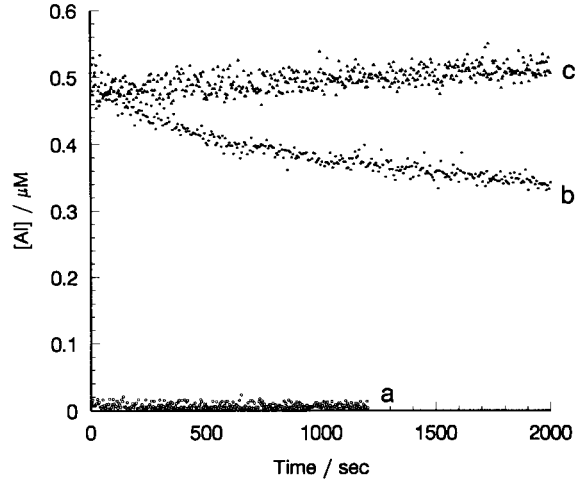

Fig. 6. Aluminum remaining in the sample of Rideau River surface water, as a function of time after uptake of aluminum by the Chelex-100 resin in the Chelex batch technique, determined by ICP-MS. pH 5.0. (a) Ultrapure water without the Chelex resin; (b) [Chelex] = 1% (w/w); (c) the sample without Chelex resin.

show that the noise level for both metals is low and stable, indicating that the whole analytical system including the ICP-MS is performing well. The curve for aluminum has higher noise level

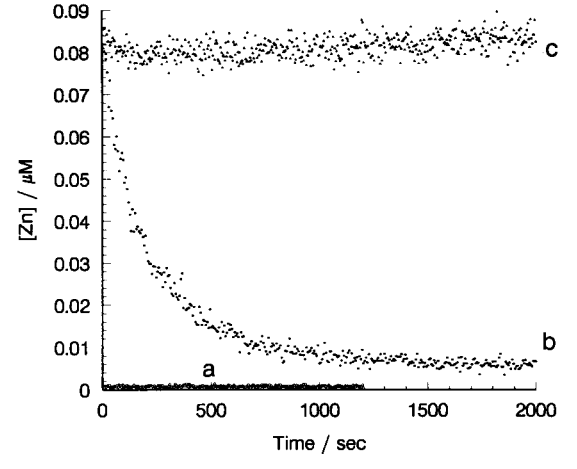

Fig. 7. Zinc remaining in the sample of Rideau River surface water, as a function of time after uptake of zinc by the Chelex-100 resin in the Chelex batch technique, determined by ICP-MS. pH 5.0. (a) Ultrapure water without the Chelex resin; (b) [Chelex] = 1% (w/w); (c) the sample without Chelex resin.

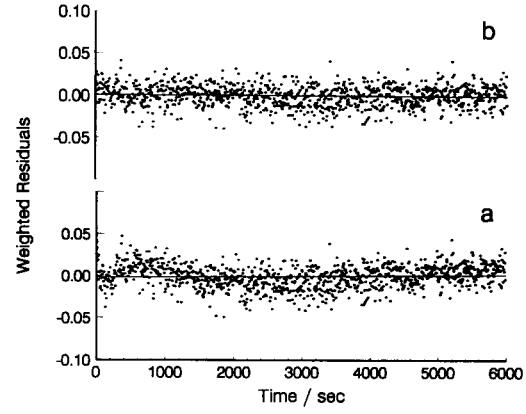

Fig. 8. Plots of weighted residuals as a function of time for the kinetic study of Zn(II) in a sample of Rideau River surface water. pH 5.0. The solid lines are the linear least-square fits. (a) 2-component fitting; (b) 3-component fitting.

than that for zinc. The curves c in both Figures are the plots of signal vs. time for the sample of river surface water without any additions to it and serve as blanks. The purpose of the blank is to correct for adsorption or desorption of the analyte and for contamination from the walls of the reactor. The results show that there is no measurable loss of aluminum and zinc during the kinetic measurements by ICP-MS. A slight contamination (leach-off of aluminum and zinc) from the walls of the reactor was observed, but the effect was within the experimental uncertainty. The very slight increase in the blanks with time (Figs. 6 and 7, curves c) was probably due to leaching of the previously-adsorbed analytes from the walls of the reactor which had been pre-equilibrated with the sample before the kinetic measurements. The curves b in Figs. 6 and 7 show the uptake of Al(III) and Zn(II), respectively, by the Chelex resin from the sample of the river surface water. The weighted residuals as a function of time for the analysis of Zn are presented in Fig. 8. Three-component-fitting gave better normal and random distribution of residuals about zero than two-component-fitting for both aluminum and zinc. Increase of the number of components to 4 did not further improve the distributions. The number of components were, therefore, 3 for both aluminum and zinc in the river surface wa-

ter. The initial concentrations and the rate constants for these components are listed in Table 6.

Table 4 shows the effect of fulvic acid and of the sodium acetate–acetic acid buffer on the removal of aluminum species by the Chelex resin in the batch technique. Fig. 3, curve a, shows that the uptake of aluminum in the absence of fulvic acid (FA) is much faster than that in the presence of fulvic acid. If the mechanism of the aluminum uptake by the Chelex resin is such that the aluminum taken up by the Chelex resin is produced by the pre-dissociation of the aluminum complex, then the results suggest that the rate constant for the dissociation of the aluminum aquo complex is much greater than the rate constants for the dissociation of the aluminum fulvic acid complexes (the higher the [FA] to [Al(III)] ratio, the smaller the rate constant). Table 4 also shows that in the absence of both the buffer and the fulvic acid, the aluminum aquo complex has three kinetically distinguishable components, with the fastest component (which comprises a mean value of about 90% of the $[Al(III)]_{total}$) having a rate constant (mean value) of 2.8×10^{-2} s^{-1}. In the presence of the above buffer (but in the absence of the FA), the fastest of the former three kinetically distinguishable components of aluminum disappears completely, and the two slower components of aluminum now have the rate constant: 5.3×10^{-3} s^{-1} (92% of the $[Al(III)]_{total}$) and $\leq$ 4.0×10^{-4} s^{-1} (8% of the $[Al(III)]_{total}$). The above change is probably due to formation of aluminum monoacetate complexes, which have been studied by Hiraishi et al. [31].

In Table 6, in the snow sample, the faster component of aluminum had a rate constant of similar order of magnitude to that in the model solution of aluminum (without the above buffer and FA) in Table 4, and was probably a similar aquo complex of aluminum; the slower component of aluminum was probably an aluminum complex of simple inorganic ligands, such as carbonate, sulphate and fluoride. The predominant aluminum species (72% $[Al(III)]_{total}$) in the sample of Rideau River surface water had the lowest rate constant $\leq 6.3 \times 10^{-5}$ s^{-1} of the three kinetically distinguishable components of aluminum. All these aluminum species were probably bound to macromolecular, polyfunctional complexant such as humic material, or polymeric colloidal material such as iron oxyhydroxide, all of which tend to give low rate constants for aluminum species in freshwaters. The zinc species in the snow sample was probably a zinc complex of simple inorganic ligands such as carbonate, sulphate and fluoride. The three kinetically distinguishable components of zinc in the sample of Rideau River surface water were probably bound to macromolecular, polyfunctional complexant, such as humic material, or polymeric colloidal material such as iron oxyhydroxide, all of which tend to give low rate constants for zinc species in freshwaters.

7. Conclusions

These kinetic studies of aluminum and zinc speciation in the samples of river surface water and snow yielded valuable information about the dissociation rate constants of the aluminum and zinc species in these samples. The iterative convolution method with the nonlinear least-squares algorithm has been found to be satisfactory for the analysis of kinetic data generated by the Chelex batch technique using ICP-MS with solution nebulization technique.

The use of Chelex as a complexant limits observation of the rate of dissociation reaction by the time taken for the formation of the Chelex–M complex, reaction 2. To estimate this rate, as a first approximation we may assume that there is only one kinetically distinguishable component of aluminum and zinc present in the model solutions without any complexing ligands or the buffer solution. In fact, as shown in Tables 4 and 5, one component accounts for about 90% of the aluminum and up to 98% of the zinc. The half lives of 49 s for the uptake of aluminum and 58 s for the uptake of zinc (Figs. 3 and 4) correspond to formation rate constants for the Chelex–M complexes of 0.014 s^{-1} and 0.012 s^{-1}, respectively. Only complexes of the metal ions whose rate constants for dissociation are approximately 10 times lower than these will be detected by the Chelex batch technique.

The advantages of using the ICP-MS in the Chelex batch technique are: (1) its capability to resolve labile complexes, not resolvable by GFAAS; (2) excellent sensitivity – the limits of detection for some elements can be as low as 10^{-15} g; (3) a true multi-element analytical technique. The alternative analytical technique, GFAAS, has some limitations when applied to kinetic studies; for example, the GFAAS results have more systematic errors and larger scatter of data points. Also, GFAAS involves longer time gaps between the data points, as shown in Fig. 2. In spite of all these limitations, GFAAS also is an extremely useful technique for kinetic studies and can provide an independent check on the ICP-MS results.

Acknowledgments

The authors are grateful to the Natural Sciences and Engineering Research Council of Canada and Environment Canada: Atmospheric Environment Service for financial support of this research project.

References

[1] H.L. Pardue, Anal. Chim. Acta, 216 (1989) 69.
[2] R.G. Garmon and C.N. Reiley, Anal. Chem., 34 (1962) 600.
[3] R.G. Willis, W.H. Woodruff, J.R. Frysinger, D.W. Margerum and H.L. Pardue, Anal. Chem., 42 (1970) 1350.
[4] I. Schechter, Anal. Chem., 64 (1992) 727.
[5] H.A. Mottola, Kinetic Aspects of Analytical Chemistry, Wiley, New York, 1988.
[6] I. Schechter, Anal. Chem., 63 (1991) 1303.
[7] J.A. Larson and H.L. Pardue, Anal. Chim. Acta, 224 (1989) 289.
[8] I. Laios, D.M. Fast and H.L. Pardue, Anal. Chim. Acta, 180 (1986) 429.
[9] C. Mouvet and C.M. Bourg, Water Res., 17 (1983) 641.
[10] G.E. Niembe and G.F. Iee, Water Res., 16 (1982) 1373.
[11] C. Houba, J. Remacle, D. Dubois and J. Throey, Water Res., 10 (1983) 1281.
[12] P.E. White, Plant Soil, 46 (1976) 195.
[13] N.V. Hue, G.R. Craddeok and F. Adams, Soil Sci. Soc. Am. J., 50 (1986) 28.
[14] M.A. Anderson and F.M.M. Morel, Limnol. Oceanogr., 27 (1982) 789.
[15] W.G. Sunda and P.A. Gillespie, J. Mar. Res. 37 (1979) 761.
[16] T.C. Hutchinson, Proceedings of the International Conference on Heavy Metals in the Environment, Heidelberg, September 1983, Vol. 1, CEP Consultants, Edinburgh, 1983. p. 17.
[17] A.J. Dobbs, P. French, A.M. Gunn, T.D.E. Hunt and D.A. Winnard, Environmental Chemistry and Toxicology of Aluminum, Lewis Publishers, Chelsea, MI, 1989, p. 209.
[18] D.R. Crapper, A.J. Dalton and S.S. Krishnan, Science, 180 (1973) 511.
[19] Editorial, Lancet i, 339 (1992) 713.
[20] G.E. Batley (Ed.), Trace Element Speciation: Analytical Methods and Problems, CRC Press, Boca Raton, FL, 1989, p. 25.
[21] C.L. Chakrabarti, Y. Lu, J. Cheng, M.H. Back and W.H. Schroeder, Anal. Chim. Acta, 267 (1993) 47.
[22] D.L. Olson and M.S. Shuman, Anal. Chem., 55 (1983) 1103.
[23] M.K.S. Mak and C.H. Langford, Inorg. Chim. Acta, 70 (1983) 237.
[24] J.A. Lavigne, C.H. Langford and M.K.S. Mak, Anal. Chem., 59 (1987) 2616.
[25] C.H. Langford and D.W. Gutzman, Anal. Chim. Acta, 256 (1992) 183.
[26] Y. Lu, C.L. Chakrabarti, M.H. Back, D.C. Grégoire, W.H. Schroeder, A.G. Szabo and L. Bramall, Anal. Chim. Acta, 288 (1994) 131.
[27] S.M. Griffith and M. Schnitzer, Soil Sci., 120 (1975) 126.
[28] M. Schnitzer and S.I.M. Skinner, Soil Sci., 105 (1968) 392.
[29] V. Tramonti, M.Sc. thesis, Concordia University, Montreal, 1988.
[30] S.-C. Pai, P.-Y. Whung and R.-L. Lai, Anal. Chim. Acta, 211 (1988) 257.
[31] M. Hiraishi, S. Harada, Y. Uchida, H.L. Kuo and T. Yasunaga, Int. J. Chem. Kin., 7 (1980) 387.
[32] P.G.C. Campbell, M. Bisson, R. Bougie, A. Tessier and J.P. Villeneuve, Anal. Chem., 55 (1983) 2246.
[33] A. Duker, A. Ledin, S. Karlsson and B. Allard, Colloidal Carrier Substances – Properties and Impact on Trace Metal Distribution in Natural Waters, Anna Ledin, Kanaltryckeriet i Motala AB, Motala 1993, p. V1.

ELSEVIER

Analytica Chimica Acta 293 (1994) 109–117

ANALYTICA CHIMICA ACTA

Application of solid-phase disk extraction followed by gas and liquid chromatography for the simultaneous determination of the fungicides: captan, captafol, carbendazim, chlorothalonil, ethirimol, folpet, metalaxyl and vinclozolin in environmental waters

Jaume S. Salau, Rosi Alonso, Gloria Batlló, Damià Barceló *

Environmental Chemistry Dept., CID-CSIC, c / Jordi Girona 18-26, 08034 Barcelona, Spain

(Received 8th November 1993; revised manuscript received 18th January 1994)

Abstract

Extraction disks (C_{18} Empore) were used for the isolation and trace enrichment of several fungicides: captan, captafol, carbendazim, chlorothalonil, ethirimol, folpet, metalaxyl and vinclozolin from drinking, river and estuarine water. From most of the pesticides the recoveries (determined by liquid chromatography with diode array detection (LC-DAD) at 210 nm) varied from 68 to 116% with a coefficient of variation (C.V.) of 3–7%. The recoveries observed for carbendazim and ethirimol in natural waters using LC-DAD were 14 and 30%, respectively. These apparent low recoveries were attributed to the measurement (matrix interferences) and values of 40 and 120%, respectively, were achieved when using liquid chromatography thermospray mass spectrometry (LC–TSP-MS) with selected ion monitoring (SIM) and positive ion (PI) mode detection. Analytical determinations were also carried out using gas chromatography with electron capture detection (GC-ECD) for the direct analysis of five fungicides, with the exception of carbendazim, ethirimol and metalaxyl. Confirmation of the identity of the fungicides was carried out by gas chromatography–mass spectrometry (GC–MS) in the electron impact mode and LC–TSP-MS using both positive and negative ion modes and filament-on. The limits of detection at $S/N = 3$ were 5, 10, 100 and 500–2000 ng/l when GC-ECD, GC–MS, LC-DAD and LC–TSP-MS were used, respectively.

Key words: Liquid chromatography; Gas chromatography; Mass spectrometry; Solid-phase disk extraction; Environmental analysis; Fungicides; Waters

1. Introduction

Recently there has been an increasing need for multiresidue analytical methods for the trace level identification and quantitation of pesticides in environmental water matrices, such as surface, estuarine, ground and sea water. Isolation and pre-concentration via liquid–liquid extraction (LLE) and off-line and on-line solid-phase extraction (SPE) are generally used for this purpose [1,2].

* Corresponding author.

SSDI 0003-2670(94)00091-Y

LLE and SPE with benzene [3,4] and dichloromethane [2] using C_{18} bonded-phase cartridges [5,6] has been used for the isolation of fungicide residues from water samples. Analytical determinations of volatile fungicides such as captan, captafol, folpet, chlorothalonil, metalaxyl and vinclozolin are generally carried out by gas chromatography with electron capture detection (GC-ECD) [2,6,7] and gas chromatography–mass spectrometry (GC–MS) [5] giving both much lower limits of detection (LOD) than liquid chromatographic (LC) techniques. However, LC permits the direct analysis of fungicides such as carbendazim [3,4] and ethirimol [8] without the need of derivatization. Since in many water and wine samples several fungicides can be found, the use of LC has to be preferred because it facilitates the simultaneous analysis of all the fungicides. LC methods combined with LLE [4,8], and off-line [5,6,8] and on-line SPE [9,10] have been reported.

The aim of this paper is to establish a method for the isolation, chromatographic analysis and confirmation of selected fungicides in drinking water and river and estuarine water samples from the Llobregat and Ebro (Spain). The fungicides were selected during a joint meeting with the Food and Agriculture Organization of the United Nations Environment Programme and representatives of France, Spain, Italy and Greece. The meeting was held at the International Atomic Energy Agency Laboratories in Monaco (October 1990). On the basis of information on usage, physicochemical properties and persistent data, a list of priority fungicides was made in order to carry out a future pilot monitoring programme in estuarine areas of the Mediterranean region. The proposed list for analysis included the fungicides: carbendazim, ethirimol, metalaxyl, captan, folpet, captafol, vinclozolin and chlorothalonil, which are all used in amounts varying from 20 to 300 tonnes per year in the various Mediterranean countries cited above. Other fungicides, e.g., mancozeb, maneb, ziram and thiram, also used in the same countries but at higher amounts (300–700 tonnes per year) were not included due to the need of developing specific methods of analysis at low μg/l level in water samples [11].

For carrying out a future pilot monitoring programme for fungicides it is needed that a common method is available for all the participating laboratories, so that information and results can be exchanged amongst all laboratories in the future. It is also relevant that when developing such a method, GC and LC techniques are used, making the developed method more versatile. This is a necessity because many laboratories in the Mediterranean region do not have all the chromatographic facilities. Only GC-ECD is present in most of the laboratories. It was agreed that our Department would be responsible for the development of an analytical protocol for the determination of the selected fungicides.

Because SPE disks are very useful for the sampling and analysis of various pesticides (e.g., chlorotriazines and organophosphorus compounds [12]) it was decided to use such disks also for the isolation of fungicides in order to assist the implementation of a monitoring programme. C_{18} Empore disks allow higher sampling flow rates [12] and exhibit better blanks than C_{18} cartridges [13]. The analytical determinations will consist of the combined use of GC-ECD, GC–MS, LC with diode array detection (DAD) and thermospray (TSP) LC–MS. Generally, sufficiently volatile fungicides can be determined in water samples by GC-ECD and GC–MS at the 10 ng/l level [5]. As a complementary technique, LC-DAD and LC–MS can be employed for the determination of the more polar fungicides, e.g, carbendazim and ethirimol. Recommendations for the analysis of the different fungicides in drinking water, river water and estuarine water will be discussed.

2. Experimental

2.1. Chemicals

The Pesticide-Grade solvents ethyl acetate, methanol, acetonitrile, water and dichloromethane (for residue analysis, and for chromatographic quality) were obtained from Merck (Darmstadt). Fungicide analytical standards were obtained from Promochem (Wesel).

2.2. Extraction and concentration of samples

A J.T. Baker 47-mm filtration apparatus was used. The membrane extraction disks were a gift from J.T. Baker (Deventer). The disks used in these experiments were 47 mm diameter and 0.5 mm thick. Each disk contains about 500 mg of C_{18} bonded silica.

The extraction procedure follows a similar procedure previously developed in our laboratory [12]. After spiking 2 l of water with different pesticides, resulting in analyte concentrations of 2 μg/l, the solution was prefiltered using 0.45-μm PTFE fiberglass filters (Millipore, Bedford, MA) to eliminate particulate matter. The disk, placed in the J.T. Baker apparatus, was washed with 10 ml of methanol under vacuum, and then dried and washed with 10 ml of acetonitrile. The disk was not allowed to become dry, and immediately 2 l of water was extracted with the vacuum adjusted to yield a 1 h extraction time. After this operation, the pesticides trapped into the disk were collected with the 2 × 10 ml of acetonitrile. After careful evaporation of part of the solvent, for LC methanol was added up to a volume of 500 μl and 20 μl was injected. For GC isooctane was added up to a volume of 500 μl and 2 μl was injected. Recoveries obtained for the different fungicides are indicated in Table 1.

Table 1
Mean %recovery and coefficient of variation (C.V.) of fungicides (spiking level 2 μg/l ($n = 6$)) in estuarine water samples using Empore extraction disks

Peak No.	Compound	Recovery (%)			
		River water		Drinking water	CV
		A	B		
1	Carbendazim	25	14, 40 [a]	100	5
2	Ethirimol	30	15, 120 [a]	97	5
3	Metalaxyl	104	77	106	3
4	Captan	85	68	103	7
5	Folpet	68	63	94	6
6	Captafol	110	63	84	3
7	Vinclozolin	108	70	101	4
8	Chlorothalonil	107	116	100	6

Water volume: 2 l.
Recoveries were calculated using LC-DAD at 210 nm except [a] by LC–TSP-MS with SIM and PI modes of operation with a C.V. of 25%.
River water A: Llobregat river samples collected upstream. River water B, samples collected in the estuarine area (Ebro river).
C.V.: indicated for river water A and B; C.V. values for drinking water are 2–4%.

GC-ECD

Following the Empore extraction disk preconcentration step, 2 μl of the extracts were injected in the splitless mode (gas hold time = 35 s) with a Hewlett-Packard (Palo Alto, CA) 7673A automatic sampler in a Hewlett-Packard 5890 capillary gas chromatograph equipped with a Ni-63 electron capture detector at 310°C. The DB-5 column used contained 5% phenyl–95% methyl polysiloxane (J&W Scientific, Folsom, CA). The column was programmed from 80°C (2 min) to 290°C (10 min) at 6°C/min. The injector temperature was 270°C.

GC–MS

A Model 8065 GC system and a Model MD 800 GC–MS system from Fison Instruments (Manchester) interfaced with a LAB-BASE data system were used for GC–MS with EI. The same fused silica column as described above was used and directly introduced into the ion source. Helium at 14 p.s.i. was used as the carrier gas. Other chromatographic conditions were identical to those described for the GC-ECD analysis. The ion source and transfer line were kept at 200 and 300°C, respectively. EI spectra were obtained at 70 eV.

LC-DAD

Eluent delivery was provided by Model 600-MS pressure pumps coupled with a Millenium 996 diode array detector, all from Waters–Millipore (Milford, MA). Samples were injected via a 20-μl loop from Rheodyne (Cotati, CA). The extract obtained after isolation of the fungicides through the Empore disks was analysed using a Nova-Pack Phenyl 4-μm column of 3.9 × 150 mm (Waters). Gradient elution was employed with acetonitrile–water (0.02 M KH_2PO_4): 20:80 (5 min) up to 100:0 in 30 min at a flow rate of 1 ml/min. Most of the analyses were performed by LC-DAD using UV absorption at 210 nm.

LC–TSP-MS

A Hewlett-Packard (Palo Alto, CA) Model 5988A LC–TSP-MS quadrupole mass spectrometer and a Hewlett-Packard Model 59970C instrument for data acquisition and processing were employed. The LC eluent and column used are described under chromatographic conditions. The temperatures of the TSP were: 100, 188 and 270°C for the stem, vapour and ion source, respectively. In order to maintain minimum background, the scan range was restricted to m/z values of 150 and 180 for positive ion (PI) and negative ion (NI) modes, respectively, up to m/z 500. In all experiments the filament-on mode (ionization by an electron beam) was used. In this mode of operation, conventional chemical ionization can be carried out using the vaporised mobile phase as the chemical ionization reagent gas. Calibration of the instrument was achieved by using a solution of hydrocortisone (5 mg) which was dissolved in an eluent containing 250 ml of acetonitrile–water (50:50) + 0.05 M ammonium formate. Ions for calibration in the PI mode were at m/z 59, 141 and 363, corresponding to $[(CH_3CN)NH_4]^+$, $[(CH_3CN)_3NH_4]^+$ and $[M+H]^+$ (where M is the molecular mass of hydrocortisone), respectively. In the NI mode, the ions at m/z 91, 137 and 407, corresponding to $[(HCOOH)(HCOO)]^-$, $[(HCOOH)_2(HCOO)]^-$ and $[M+HCOO]^-$, were used [12]. For the confirmation of the samples, the selected ion monitoring mode was employed.

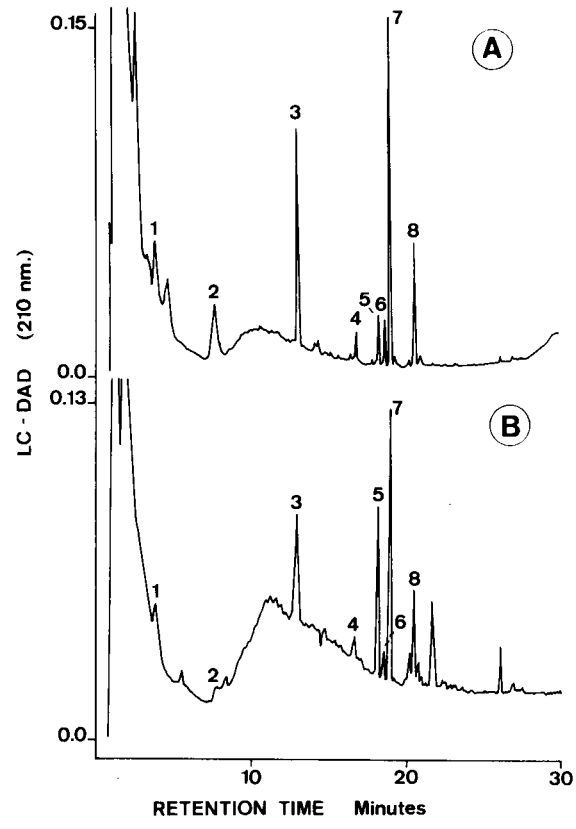

Fig. 1. LC-DAD chromatograms at 210 nm obtained for a 2-l river water extract sample collected upstream (A) and in the estuarine area (B) containing 2 μg/l each of (1) carbendazim, (2) ethirimol, (3) metalaxyl, (4) captan, (5) folpet, (6) captafol, (7) vinclozolin and (8) chlorothalonil. LC eluent: acetonitrile–water (0.02 M of KH_2PO_4) 20:80 (5 min) up to 100% acetonitrile in 30 min; flow rate: 1 ml/min; LC column: Nova-Pack Phenyl 4-μm column of 3.9×150 mm.

3. Results and discussion

3.1. Liquid chromatographic analysis

The recoveries obtained for the different fungicides spiked in three different types of water samples are shown in Table 1. First it should be noticed that recoveries obtained in drinking water were higher than 80% for all the compounds, thus indicating that the use of the disks does not offer a problem for such a type of water.

Problems arise when river water samples need to be analysed. Two types of river water samples were tested. A relatively "clean" river water sample, collected upstream, and an estuarine river water. The two chromatograms of these two types of river water samples are shown in Fig. 1. It is clearly noticed that river water of type B, collected in the estuarine, offers more problems, with higher interferences in the blank samples. The determination of early eluting peaks in both samples (carbendazim and ethirimol) is problematic even while using the present gradient system which has been obtained after various optimization procedures, including the start of the analysis at 100% of water with different buffers. From all the systems investigated, the present one,

starting at 80% phosphate buffer, offers the best separation. The problems of interferences in the preconcentration of real environmental waters spiked with pesticides has been already described by us [12]. These interferences are mainly caused by humic substances present in real environmental water samples which are also trapped by the SPE disks [12] and cartridges [13–15].

However, the recovery for carbendazim and ethirimol could be improved when using LC–TSP-MS under selected ion monitoring (SIM) conditions (this will be discussed below in the LC–MS section), since in this particular case interferences are "artificially" avoided.

A second problem concerns the relatively "low" recoveries obtained for captan, folpet and captafol when isolated from estuarine river water. This may lead to another problem related to the fact that lower recoveries have also been obtained for pesticides when extracted from real river water samples. This was particularly attributed to the formation of pesticide–humic complexes that could not be sufficiently extracted by the C_{18} bonded silica phase [14]. Another aspect that will also contribute to the low recovery of captan concerns the recently reported data about this compound in the sense that it may hydrolyse in the disk due to the remaining water not removed by vacuum filtration [16] and also in the cartridges [5], as noticed for the low recoveries (61%) obtained.

However, we have only noticed low "apparent" recoveries in the case of river water samples, indicating that the presence of humic materials and low particulate matter may trap this residual water into the disk. Because of this it should be indicated that such apparent low recovery is caused by incorrect measurements of the LC-DAD data and not due to the compound of study and sorbent material used. It proved to be useful to calculate the recoveries in relatively clean water samples, e.g., drinking water, and in the other types of water studied here, e.g., river or estuarine water. Using this approach the problem of bad recoveries (if any) caused either by the sorbent used – obtaining low recoveries in drinking water – or the interferences from the water matrix disturbing the quantitation in the analytical determinations used, e.g., LC-DAD, will be understood.

Table 2
Important mass spectral fragments and relative intensities for several fungicides after SPE using Empore disks of 2 l of estuarine river water spiked at 2 μg/l

Mol. wt.	Compounds and ions (m/z and tentative identification)	Relative Intensity PI	NI
191	Carbendazim		
	178 $[M+HCOO-OCOCH_2]^-$		100
	190 $[M-H]^-$		30
	192 $[M+H]^+$	100	
	233 $[M+H+CH_3CN]^+$	15	
209	Ethirimol		
	208 $[M-H]^-$		5
	210 $[M+H]^+$	100	
	251 $[M+H+CH_3CN]^+$	15	
	254 $[M+HCOO]^-$		100
279	Metalaxyl		
	280 $[M+H]^+$	100	
	297 $[M+NH_4]^+$	20	
285	Vinclozolin		
	241 $[M-CO_2]^{-\cdot}$		100
	285 $[M]^{-\cdot}$		40
264	Chlorothalonil		
	264 $[M]^{-\cdot}$		100

3.2. *Liquid chromatography–thermospray-mass spectrometry*

Table 2 shows the important mass fragment ions obtained for the different fungicides at the low spiking level. The different ions formed correspond to typical ions in LC–TSP-MS, which are dependent on the structure of the molecule. The positive ion mode usually gives $[M+H]^+$ as the base peak, as reported for carbendazim [17–19]. When using the NI mode, the formation of adducts with the additive $[M+HCOO]^-$ as base peak is usually the common behaviour, as reported for other pesticides [12]. For carbendazim, the base peak under NI conditions corresponds to the adduct with formate and loss of the $OCOCH_2$ group [17]. Chlorothalonil shows typical electron capture mechanisms with $[M]^{-\cdot}$ as the base peak. Vinclozolin, also under the NI mode, gives rise to a base peak corresponding to a loss of CO_2, which has been also observed with GC–

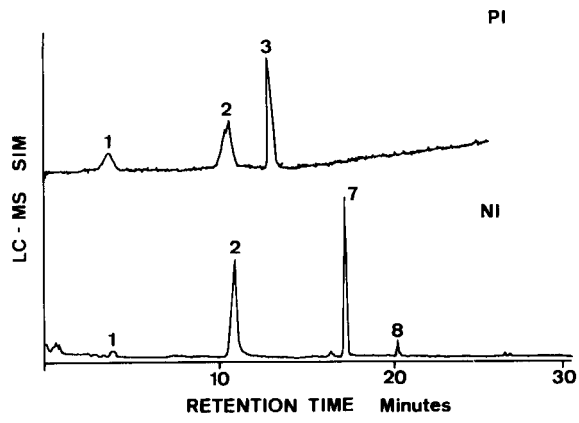

Fig. 2. LC–TSP-MS selected ion chromatogram using PI and NI mode corresponding to the same extract as Fig. 1B. Chromatographic conditions, as in Fig. 1, with the exception of the buffer. In this case 0.05 M ammonium formate was used instead of KH_2PO_4.

MS EI [5]. Its second abundant ion corresponds to an electron capture mechanism.

All the various ions in Table 2 were used in the selected ion monitoring chromatographic procedure shown in Fig. 2. First of all it is shown that the method is not sensitive enough to detect captan, captafol and folpet. Therefore, these compounds can not be detected with SIM-LC–TSP-MS at concentrations of 2 μg/l when preconcentrating 2 l of water sample. In this respect, from the compounds shown in Fig. 2, carbendazim and chlorothalonil are detected probably at their limits of detection (LOD), whereas ethirimol, metalaxyl and vinclozolin have an LOD ca. ten times lower allowing their determination at levels below 0.5 μg/l. The LOD for ethirimol and metalaxyl would then be similar to those observed for other compounds, e.g., organophosphorus pesticides after extraction under similar conditions [12]. The poor sensitivity achieved for captan is not surprising, since this compound has been reported to exhibit a LOD of ca. 10–100 times higher than organophosphorus pesticides in both PI and NI modes of operation in LC–TSP-MS [17].

As indicated above, with LC–TSP-MS using SIM, we were able to obtain better recoveries for carbendazim and ethirimol and consequently we "artificially" avoided the humic substances present in the LC traces. After determination of the recovery values for both pesticides, only for ethirimol we obtained relatively good results, whereas for carbendazim the recovery remained still as low as 40%. The low recoveries obtained for this compound reflect the problems encountered when determining carbendazim under LC–TSP-MS. In a recent interlaboratory study using standard solutions containing pesticides of various chemical groups it was shown that carbendazim was one of the pesticides that offered high interlaboratory variability. This can be attributed to the different operational parameter values in LC–TSP-MS (e.g., adjustment of thermospray tip temperature) that can degrade such a thermally labile compound [20].

3.3. Gas chromatographic techniques

Fig. 3 shows a typical chromatogram obtained after extraction of 2-l river water samples spiked with fungicides at the 2 μg/l level. Due to the selectivity of the detector, no interferences were noticed in the GC-ECD retention time data of these compounds. When compared to LC-DAD (Fig. 1) GC-ECD is more selective, but in contrast, three fungicides cannot be determined. The recoveries of the five volatile fungicides (Table 1) were also calculated by GC-ECD giving similar values.

In a previous paper [21] we have reported the importance of determining the interferences of the disks when analyzing pesticides at a low detection level. It is relevant to determine the different interferences for environmental water samples that will be used for future monitoring studies. Table 3 indicates the interferences found in the GC–MS traces of an extract of 2 l of water after preconcentration with Empore disks (see Fig. 3). We have detected phthalates which may originate from the plasticisers which were added during manufacturing or which are present as contaminants in the polymer components. This is due to the polymeric housing used for the bonded phase materials in both cartridges [22] and disks [21]. Previously we have reported on average blank values of 1 ng/l, when analyzing sea water sam-

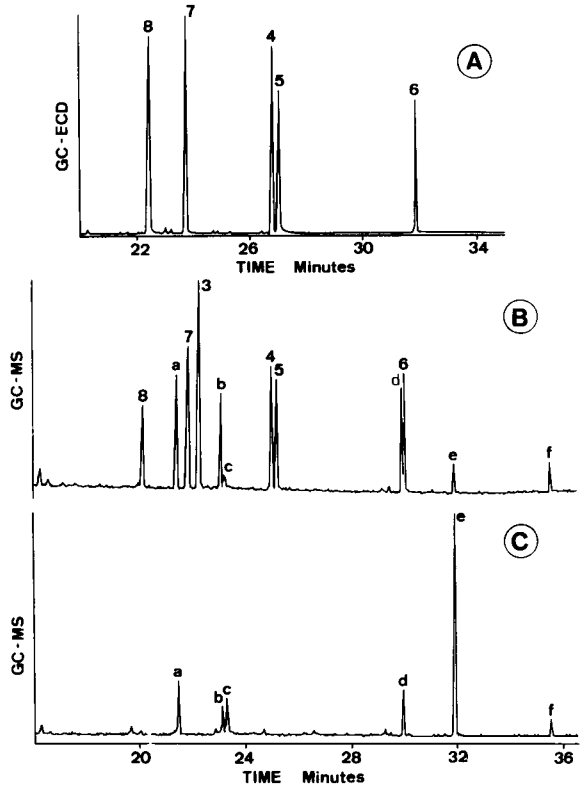

Fig. 3. GC-ECD (A) and GC–MS (B) chromatograms obtained on the same extract as shown in Fig. 1B. (C) Blank river water sample processed under the same experimental conditions. A DB-5 GC column containing 5% phenyl–95% methyl polysiloxane was programmed from 80°C (2 min) to 290°C (10 min) at 6°C /min. For peak numbers, see Fig. 1. Blanks identified in C, see Table 3.

ples of the French coast. The fact that when using the same disks the blanks in the present study are now in the low $\mu g/l$ range suggests that part of the interferences originate from the river itself. Most of the various phthalates detected indeed have been found in these river water samples up to concentration levels for the individual phthalates of 0.5 $\mu g/l$ [23,24].

Using GC–MS, the ions obtained for the different fungicides are shown in Table 4, and are as what would be expected for GC–MS-EI. Similar spectra and relative abundances for captan, captafol and chlorothalonil were found as reported [25–28].

The chromatogram in Fig. 3 shows that it is

Table 3
Compounds eluted from C_{18} empore extraction disks after preconcentration of 2 l of estuarine river water from the Ebro (unknown compounds are indicated by the m/z values and relative abundances (in parenthesis)

Peak No.	Compound
a	Diisobutyl phthalate
b	Dibutyl phthalate
c	Unknown m/z 73 (100), 60 (80), 129 (40)
d	Unknown m/z 129 (100), 57 (40), 147 (30)
e	Di-(2-ethylhexylphthalate)
f	Squalene

recommended to carry out the analysis using SIM. Therefore the interferences caused by the disks and the estuarine waster matrix will be avoided and also the sensitivity of the method will be enhanced. By using SIM, sensitivities in the low ng/l level are achieved, which should permit the unequivocal determination of the volatile fungicides in water samples

3.4. Performance of the analytical system

Table 5 shows the linearity for the different fungicides when plotting peak areas versus amount injected. The LODs using LC-DAD and GC–ECD are also shown. Several comments need to be made. First, the correlation coefficients calculated for the linear regression equations were all above 0.99 except for captafol (0.98). The repeatability relative standard deviation R.S.D. varied for GC-ECD and LC-DAD from 5–10% and 7–14%, respectively. The exception was

Table 4
Main ions (%relative abundance) and retention times of fungicides analysed by GC–MS

Fungicide	Retention time	
	(min)	m/z ions (%relative abundance)
Captan	25.09	79 (100), 149 (25), 264 (4)
Captafol	30.02	79 (100), 313 (5)
Chlorothalonil	20.23	266 (100), 229 (10), 109 (20)
Folpet	25.27	104 (100), 297 (10), 260 (80)
Metalaxyl	22.33	206 (100), 220 (50)
Vinclozolin	21.93	285 (70), 212 (100), 178 (70)

Table 5
Calibration data for fungicides (0.2 – 5 μg/l) after preconcentration of 2 l of estuarine water samples using (a) LC-DAD and (b) GC-ECD (calibration was performed plotting peak area versus amount injected LOD (μg/l) are also indicated. Number of experimental points for each compound, concentration and technique = 4)

Analyte	Calibration equation	r^2	LOD
Metalalxyl	(a) $y = 1.5\ 10^5x - 5.9\times10^5$	0.998	0.02
Captan	(a) $y = 4.2\ 10^4x - 1.7\times10^5$	0.995	0.1
	(b) $y = 1.2\ 10^4x - 6.9\times10^3$	0.994	0.005
Folpet	(a) $y = 1.7\ 10^5x - 6.0\times10^5$	0.998	0.02
	(b) $y = 1.9\ 10^4x - 985$	0.997	0.005
Captafol	(a) $y = 1.5\ 10^4x - 302$	0.988	0.1
	(b) $y = 7.1\ 10^3x - 4222$	0.996	0.005
Vinclozolin	(a) $y = 1.8\ 10^5x - 3.1\times10^5$	0.992	0.01
Chlorothalonil	(a) $y = 5.5\ 10^4x - 1.8\times10^5$	0.998	0.06

captafol with an R.S.D. value of 21%. The second comment refers to carbendazim and ethirimol. These pesticides were not plotted since problems occurred in their accurate determination by LC-DAD when using the river water samples. This was caused by the matrix interferences (see Fig. 1) that lead to very poor recoveries (see Table 1). Such recoveries were only improved by LC–TSP-MS since in this case the analytical measurements were more correctly performed. However we did not plot these two compounds using LC–TSP-MS since the recoveries already showed high coefficients of variation (C.V.) (see Table 1).

The LODs at $S/N = 3$ for the different fungicides were calculated for both GC-ECD and LC-DAD, using the analytical protocol described in the Experimental section. Although for vinclozolin and chlorothalonil, the linearity for GC-ECD was not calculated, their LODs for GC-ECD are within the same range as captan, captafol and folpet. Captan and captafol show poor LOD values for LC-DAD due to the fact that their UV maxima are below 200 nm.

The LODs for LC-DAD were, as usual, worse than with GC-ECD analysis, but it has the advantage of permitting the simultaneous determination of all fungicides, including carbendazim and ethirimol that are not sufficiently volatile to be directly analyzed by GC-ECD. It should also be mentioned that the LODs in river water samples (Table 5) are worse when compared to drinking water samples (a factor of 3 [29]).

For GC-ECD, the LODs were estimated to be at the 5 ng/l level, thus allowing the application of the method for the analysis of relatively "clean" water samples located closer to the sea, where fungicides are expected to be found at ng/l levels (as reported for triazine herbicides [21,30,31]). Indeed, GC-ECD and GC–MS will be the methods of choice recommended for the trace-level determination and confirmation of sufficiently volatile fungicides at trace levels.

4. Conclusions

The research described in this paper comments on a combined method (GC-ECD and LC-DAD followed by GC–MS and LC–MS confirmation) for the trace determination of fungicides in environmental waters.

The use of GC-ECD and GC–MS screening methods is applicable for monitoring most of the fungicides reported in water samples with the exception of carbendazim and ethirimol. The LOD values obtained for GC-ECD are in the 5 ng/l range, thus permitting its use for the analysis of water samples under the restrictions (0.1 μg/l) imposed by the European Community for pesticides in water for human consumption.

The major interferences found in the Empore disks using GC–MS were attributed to the disk material and also to the river matrix, accounting for levels slightly lower than 1 μg/l.

All fungicides studied can be determined in drinking water samples without any problem, using solid-phase Empore disk extraction followed by LC-DAD determinations. For river water samples only metalaxyl, captan, folpet, captafol, vinclozolin and chlorothalonil could be determined at levels varying from 0.01 to 0.1 μg/l. Interferences were found for LC-DAD showing that the early eluting peaks, carbendazim and ethirimol, suffer from coelution with the river water matrix.

Determination of ethirimol could be performed by LC–TSP-MS. Carbendazim could also be identified, although it exhibited a low recovery (40%). Carbendazim is one of the studied com-

pounds that needs further investigation, probably with the use of another interfacing system in LC–(electrospray) MS that provides less degradation.

Acknowledgements

This work has been supported by the Food and Agriculture Organization, the United Nations Environment Programme (FAO-UNEP), the International Atomic Energy Agency (Contract No. 7246/RO/EP) and the Commission of the European Communities (Contract No. CIPA CT92-3005). J.T. Baker (Deventer, Netherlands) is thanked for supplying C_{18} Empore disks.

References

[1] D. Barceló, Analyst, 116 (1991) 681.
[2] D. Barceló, J. Chromatogr., 643 (1993) 117.
[3] R.P. Singh and M. Chiba, J. Chromatogr., 643 (1993) 249.
[4] L.F. López, A.G. López and M.V. Riba, J. Agric. Food Chem., 37 (1989) 684.
[5] E. Benfenati, P. Tremoleda, L. Chiappetta, R. Frassanito, G. Bassi, N. Di Toro, R. Fanelli and G. Stella, Chemosphere, 21 (1990) 1411.
[6] J. Mañes, Y. Picó, J.C. Moltó and G. Font, J. High Resolut. Chromatogr., 13 (1990) 843.
[7] A. Di Muccio, R. Dommarco, D. Attard Barbini, A. Santilio, S. Girolimetti, A. Ausili, M. Ventriglia, T. Generali and L. Vergori, J. Chromatogr., 643 (1993) 363.
[8] E. Bolygó and N.C. Atreya, Fresenius' J. Anal. Chem., 339 (1991) 423.
[9] Ch.H. Marvin, I.D. Brindle, R.P. Singh, C.D. Hall and M. Chiba, J. Chromatogr., 518 (1990) 242.
[10] Ch.H. Marvin, I.D. Brindle, R.P. Singh, C.D. Hall and M. Chiba, J. Chromatogr., 555 (1991) 147.
[11] M. Fielding, D. Barceló, A. Helweg, S. Galassi, L. Torstensson, P. van Zoonen, R. Wolter and G. Angeletti, Pesticides in Drinking Water, Water Pollution Research Report 27, Commission of the European Communities, Brussels, 1992, pp. 56–57.
[12] D. Barceló, G. Durand, V. Bouvot and M.W.F. Nielen, Environ. Sci. Technol., 27 (1993) 271.
[13] D.A. Hinckley and T.F. Bidleman, Environ. Sci. Technol., 23 (1989) 995.
[14] W.E. Johnson, N.J. Fendinger and J.R. Plimmer, Anal. Chem., 63 (1991) 1510.
[15] O. Evans, B.J. Jacobs and A.L. Cohen, Analyst, 116 (1991) 15.
[16] S.A. Senseman, T.L. Iavy, J.D. Mattice, B.M. Myers and B.W. Skulman, Environ. Sci. Technol., 27 (1993) 516.
[17] R.J. Vreeken, W.D. van Dongen, R.T. Ghijsen and U.A.Th. Brinkman, Int. J. Environ. Anal. Chem., 54 (1994) 119.
[18] C-H Liu, G.C. Mattern, X. Yu and J.D. Rosen, J. Agric. Food Chem., 38 (1990) 167.
[19] H. Bagheri, E.R. Brouwer, R.T. Ghijsen and U.A.Th. Brinkman, J. Chromatogr., 647 (1993) 121.
[20] V. Lopez-Avila and T.L. Jones, J. AOAC Int., 76 (1993) 1329.
[21] G. Durand and D. Barceló, Talanta, 40 (1993) 1665.
[22] G.A. Junk, M.J. Avery and J.J. Richard, Anal. Chem., 60 (1988) 1347.
[23] M. Valls, J.M. Bayona and J. Albaigés, Int. J. Environ. Anal. Chem., 39 (1990) 329.
[24] J.I. Gomez-Belinchon, J.O. Grimalt and J. Albaigés, Water Res., 25 (1991) 577.
[25] K. Pfleger, H.H. Maurer and A. Weber, Mass Spectral and GC Data of Drugs, Poisons, Pesticides, Pollutants and their Metabolites, Part 3, VCH, Weinheim, 2nd edn., 1992, p. 1397.
[26] J. Hong, Y. Eo, J. Rhee, T. Kim and K. Kim, J. Chromatogr., 639 (1993) 261.
[27] A. Valverde-Garcia, E. Gonzalez-Pradas, A. Aguilera-Del Real, M.D. Ureña-Amate and F. Camacho-Ferre, Anal. Chim. Acta., 276 (1993) 15.
[28] G.C. Mattern, G.M. Singer, J. Louis, M. Robson and J.D. Rosen, J. Agric. Food Chem., 38 (1990) 402.
[29] S. Chiron, A. Fernandez-Alba and D. Barceló, Environ. Sci. Technol., 27 (1993) 2352.
[30] G. Durand, V. Bouvot and D. Barceló, J. Chromatogr., 607 (1992) 319.
[31] J. Tronczynski, C. Munschy, G. Durand and D. Barceló, Sci. Total Environ., 132 (1993) 327.

ELSEVIER

Analytica Chimica Acta 293 (1994) 119–128

ANALYTICA CHIMICA ACTA

Fourier transform Raman spectroscopic studies of a polyimide curing reaction

Jeffrey F. Aust, Melinda K. Higgins, Peter Gröner, Stephen L. Morgan, Michael L. Myrick *

Department of Chemistry and Biochemistry, The University of South Carolina, Columbia, SC 29208, USA

(Received 27th July 1993; revised manuscript received 22nd February 1994)

Abstract

Fourier transform (FT)-Raman spectroscopy was used to monitor the curing reaction of a polyimide bonding agent, the Ciba-Geigy Matrimid® system. Major Raman bands were assigned by comparison to spectra for small model molecules, by use of ab initio calculations, and by reference to previous literature. The set of FT-Raman spectra taken at various intervals during the curing process was modeled by principal component analysis (PCA). Cure percentage determined by differential scanning calorimetry was then regressed against scores on the first principal component for the different polymer samples. The PCA and regression results summarized significant trends in the FT-Raman spectra and led to a better understanding of the curing mechanism.

Key words: Raman spectroscopy; Principal component analysis; Curing mechanism; Polyimide curing reaction

1. Introduction

Polyimide polymers are frequently used in composites for the electronics and aerospace industries. Polyimides are resistant to high temperatures and have high stability and excellent mechanical and electrical properties. However, polyimide reactions are complex and are less well understood than those of other polymers.

Various optical spectroscopic methods have been applied to the curing of polymers, including UV–visible absorbance, fluorescence [1], near-infrared absorbance (NIRA) [2–4], mid-infrared (MIR) absorbance [5,6], and Raman [7,8]. UV–Visible absorbance is sensitive, but does not give direct information on chemical bonding. Absorbance peaks for the chromophores involved in bonding are broad and shift with temperature. Fluorescence is sensitive to changes in physical state but also does not provide direct chemical bond information. Additionally, the quantum yield of fluorescence for a fluorophore depends on temperature, viscosity, curing, oxygen content, position near interfaces and other factors in a complex way. NIRA gives direct bond information, however, absorbances in the IR-overtone region are weak and broad. NIRA is of limited usefulness if O–H bonds are present in the sample because these vibrations have broad, intense

* Corresponding author.

Elsevier Science B.V.
SSDI 0003-2670(94)00100-Z

overtone absorbances in the near-infrared region. MIR absorbance in the 2 to 15 μm wavelength range is recognized as an important laboratory tool for the analysis of chemical bonding. However, for industrial work the MIR setup is incompatible with most commercial autoclaves. Relevant to our eventual interest in in situ monitoring, MIR does not lend itself to economical remote measurement. For example, the required arsenic germanium selenide chalcogenide fibers manufactured by British Telecom Labs. (Martlesham Heath, Ipswich) cost US$1200 per meter. There has also been a lack of agreement in the literature as to which "imide" bands are most related to changes occurring during curing of polyimides [9].

Raman scattering is a powerful technique for chemical-bonding analysis. The availability of strong monochromatic laser sources and high quality detectors makes Raman spectroscopy practical. Raman has an inherent ability to monitor the temperature of the sample it interrogates by comparing Stokes (lower energy) scattering and anti-Stokes (higher energy) scattering because anti-Stokes scattering is highly temperature dependent. Fourier transform (FT)-Raman is well suited for in situ monitoring of reactions because placement of optical probes directly into materials undergoing polymerization is feasible.

One of our objectives was to investigate principal component analysis (PCA) for modeling changes that occur during curing of polymers. Factor analytic techniques including principal component analysis have been widely used in spectroscopy. Several applications of PCA have been published in the area of materials characterization using FT-IR [10–19]. Factor analysis has been used previously on Raman spectra, but mostly to resolve solution mixtures [20,21]. Recent work by Aries et al. [22] using FT-IR to record spectra during the curing of epoxy resins employed PCA to monitor the reaction progress and to assess spectral changes.

In PCA each spectrum is treated as a data point (or vector) in a measurement space of wavelengths or wavenumbers (the features). Although intensities for a large number of frequencies might be measured, the spectral intensities are not independent. Spectral intensities of adjacent wavelengths tend to be highly correlated. Also intensities at certain other wavelengths may rise and fall together as a consequence of correlation with chemical structures present. These correlations mean that the data matrix will have dominating directions of variability containing most of the information in the data set. The inherent dimensionality of the data is usually much lower than the number of features. Accounting for all the variability in a data set requires a number of principal components (PCs) equal to the smaller of the number of variables or the number of samples [23,24]. Given correlated data, however, a reasonably small number of PCs can reproduce the data adequately. The first PC (PC_1) is the line (linear combination of features) that explains the greatest amount of variability in the data. The second (PC_2) and higher PCs are perpendicular to this axis (PC_1) and are ranked in decreasing order of correlation with the data. This decomposition is obtained by eigenvalue–eigenvector analysis, with the resulting eigenvalues proportional to the variance explained by each PC. As the amount of variability explained by each added PC decreases, a cutoff point may be selected after which remaining PCs are considered to consist of uncertainty. By projecting spectra into the space of the first few important PCs the majority of the variability present in the higher dimensional space is re-expressed in a space of fewer dimensions. Thus PCA may permit relationships or trends among the clusters of samples to be visualized in only two or three dimensions. Further, the spectra projected into the principal component space can be regressed on (fitted to) chemical properties of interest for calibration purposes. This technique is often termed principal component regression [25,26].

Previous Raman studies of interesting polyimides and precursors have included the band assignments for maleimide [27–29] and *N*-phenyl maleimide [30]. Raman spectra from partially cured (190°C, 2 h) samples of methylene dianiline (1,1'-(methylene-4,1-phenylene) bismaleimide, MDA-BMI) were compared to spectra from an uncured sample. Intensity changes were observed for four bands at 3104, 3094, 1585 and

1064 cm^{-1}. These bands correspond to the asymmetric and symmetric C–H stretches, maleimide C=C stretch, and in-plane C–H bend of the maleimide ring, respectively [30]. The Ciba-Geigy Matrimid® 5292 system investigated in this paper is derived from MDA-BMI. It is a two component system consisting of methylene dianiline bismaleimide (component A) and *O,O'*-diallyl bisphenol A (component B). The structures of components A and B along with the mechanism of the curing reaction are shown in Fig. 1. The main curing reaction mechanism is a Michael-type addition. The maleimide alkene functionality is eliminated and the resulting polymer is linear and has a thermoplastic nature [31].

In the present report, we examine the FT-Raman spectroscopy of the Matrimid® cure system, and assign some of the important cure-sensitive vibrations. PCA was employed to summarize the major changes in spectra during curing. To demonstrate that spectral changes can be directly related to the extent of curing, samples were analyzed by differential scanning calorimetry (DSC) to determine cure percentage. These measured cure percentages were then regressed against projections of the spectra in the space of the first principal component to develop a predictive model based on the FT-Raman spectra.

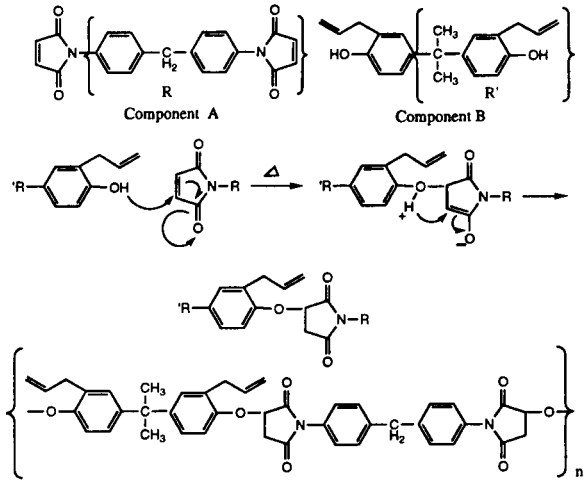

Fig. 1. The components, mechanism, and final product of the Matrimid® 5292 system.

Table 1
Sample identification and curing conditions for Ciba-Geigy Matrimid® 5292 samples

Sample		Cure temperature and time
A.	Control, pre-cure	No curing
B.	Partially cured sample	180°C, 15 min
C.	Partially cured sample	180°C, 30 min
D.	Partially cured sample	180°C, 45 min
E.	Partially cured sample	180°C, 60 min
F.	Partially cured sample	180°C, 120 min
G.	Post-cure sample	180°C, 120 min; then 250°C, 120 min
H.	Post-cure sample	180°C, 120 min; then 250°C, 240 min
I.	Post-cure sample	180°C, 120 min; then 250°C, 360 min

2. Experimental

Maleimide (99%) from Aldrich (Milwaukee, WI) and succinimide from Mallinckrodt (Chesterfield, MO) were used as supplied. Methylene dianiline bismaleimide (component A of the polymer system) and *O,O'*-diallyl bisphenol A (component B) were used as supplied. Formulation of the two-component polymer was a 100:85 (w/w) mixture of components A and B, respectively. The resulting mixture was heated and stirred to 130°C and dispensed into one-dram vials. The vials were placed in an oven equipped with a sand bath and were cured isothermally. Six samples were simultaneously removed at intervals throughout the cure according to the cure temperature and time schedule shown in Table 1. The samples were cooled and refrigerated at 4°C.

FT-Raman spectra were acquired on a Perkin-Elmer 1700X NIR FT-Raman spectrometer (Norwalk, CT). All samples were run over a wavenumber range of 3500 cm^{-1} to 500 cm^{-1} for 16 scans at 4 cm^{-1} resolution and at 1 W of power. DSC thermograms were acquired on a Perkin-Elmer DSC 7 differential scanning calorimeter. All samples were placed in standard aluminum pans and subjected to a temperature range of 50–350°C at a scan rate of 10°C/min. The control sample consisted of an uncured mixture of components A and B (also 100:85, w/w). Percentage uncured was determined by ratio of the sample exotherm (ΔH_{sample}) divided by the

exotherm of the control ($\Delta H_{control}$); this ratio subtracted from one and multiplied by 100 was used as a measure of percentage cure. The last three groups of samples were considered "post cure" since no appreciable exotherm was obtained from DSC.

For multivariate data analysis, 31 peaks of interest were selected. Peak intensities from the spectra of four representative samples of each curing group (A–F in Table 1) were normalized relative to the intensity of the internal standard peak at 1638 cm^{-1}. PCA was performed on this data set consisting of the normalized intensities of 30 peaks (excluding the internal standard peak) for each of 24 samples. Linear regression was used to correlate percentage cure measured by DSC with the projections of the sample FT-Raman spectra in the space of the first principal component. All computations were performed on a MS-DOS compatible computer. Data preprocessing and regression analyses were performed using Microsoft Excel 4.0 (Redmond, WA). Principal component analysis was done using Systat version 5.0 (Evanston, IL).

Ab initio vibrational mode analysis was performed to aid in assignment of peaks in the FT-Raman spectra of initial materials and cured polymer. The optimized structures, associated force fields in Cartesian coordinates, and relative Raman intensities were obtained with the program GAUSSIAN 90 using the 3-21G basis set [32]. All internal force constants were multiplied by a scaling factor of 0.8. The Cartesian force field was converted to a force field in internal coordinates, which was then used to predict the potential energy distribution of the vibrational modes.

3. Results and discussion

3.1. FT-Raman Spectra

As described in the Experimental section, multiple samples of partially cured polyimide were removed from the curing oven/bath after the curing cycles shown in Table 1. FT-Raman spectra of the individual starting components (A and B) are shown in Fig. 2. Representative FT-Raman spectra of a control sample (no cure) and a F sample (76% cure) are shown in Fig. 3.

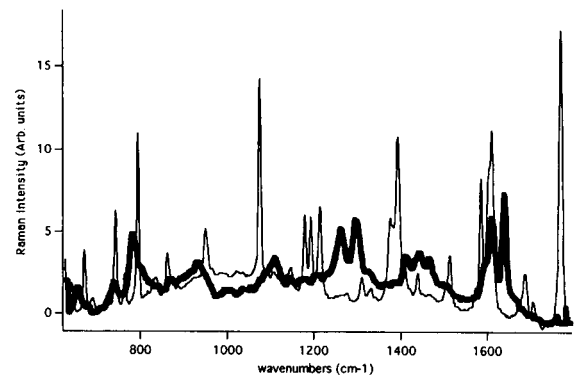

Fig. 2. FT-Raman spectra of Matrimid® 5292 component A (thin line) and component B (thick line).

The 31 peaks selected for data analysis are identified in Fig. 4. Table 2 lists major peak assignments obtained by comparison with model compounds, ab initio vibrational mode analysis and literature sources [27–30]. Any peak that exhibits changes in intensity during the curing process might be selected in an attempt to monitor cure percentage. However, it is advantageous either to use prior knowledge of the chemistry in selecting individual peaks or to use all the com-

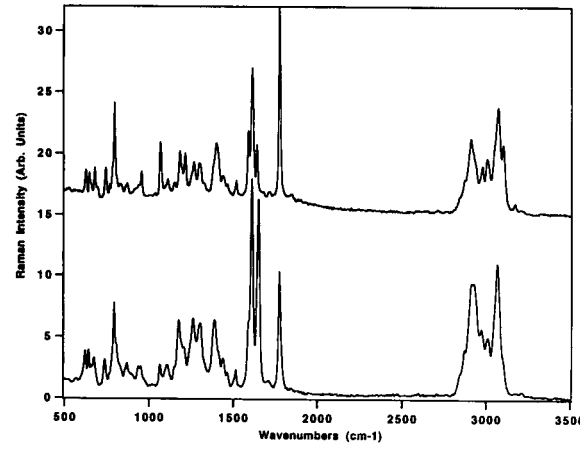

Fig. 3. FT-Raman spectra of a control sample with no curing (top, sample A), and a partially cured (76% cure) sample (bottom, sample F). Refer to Table 1 for sample conditions. Spectra are offset for clarity.

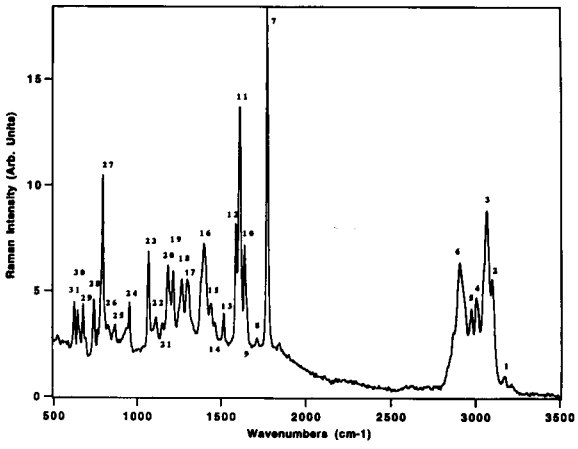

Fig. 4. FT-Raman spectrum for a representative partially cured (sample B) with the 31 peaks selected for principal component analysis. Selected peak assignments are given in Table 2.

bined spectral information with a multivariate data analysis technique such as PCA.

3.2. Correlation of spectral changes with chemical mechanism

Before presenting the results from principal component modeling of the data, it is instructive to discuss how the observed changes in the FT-Raman spectra correlate with our knowledge of the chemical mechanism (Fig. 1).

Table 2
Peak assignments in the FT-Raman spectra of the Ciba-Geigy Matrimid® system

Peak number	Wavenumber, cm^{-1}	Assignment
3	3071	C–H stretch
6	2910	C–H stretch
7	1773	C=O stretch
10	1638	C=C stretch of component B
11	1610	C=C stretch of component B C=C stretch of maleimide
12	1587	C=C stretch of maleimide
16	1398	C–N–C stretch
19	1210	*N*-Phenyl stretch
23	1065	Maleimide C–H in phase bend
27	793	Symmetric ring stretch

The most obvious difference upon curing is the dramatic reduction of the peak at 1773 cm^{-1}, the C=O stretching frequency. This decrease is seen in the comparison of spectra for a control sample (no curing) to a sample spectra shown in Fig. 3. We also observe the expected decrease in the C=C region due to the elimination of the maleimide functionality. The spectrum of the control sample A has a vibration at 1587 cm^{-1} assignable to the C=C maleimide stretch. Bands at 1610 and 1638 cm^{-1} are due to C=C stretches of component B. The band at 1610 cm^{-1} has an overlapping band from the component A maleimide functionality. Sample F (120 min curing) has peaks at 1610 and 1638 cm^{-1}. These peaks represent the remaining C=C stretches of component B, and indicate complete loss of the maleimide alkene functionality associated with a slight shift in the other related peaks.

The reduction of intensity for the C=O stretch (peak 7 at 1773 cm^{-1}) appears to be a unique marker of percentage reaction of the polyimide alkene group. Although the C=O functionality is unaffected by curing, its Raman cross-section is highly cure-dependent. Raman spectra shown in Fig. 5 of the smaller molecules maleimide and succinimide reveals a direct relationship between the existence of a maleimide C=C bond (peak 12 at 1587 cm^{-1}) and the C=O (peak 7 at 1773

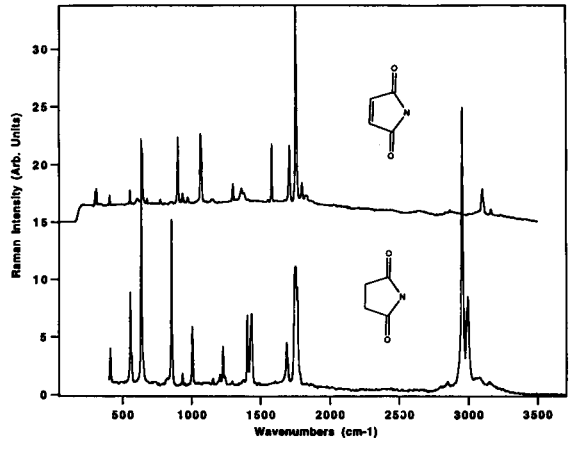

Fig. 5. FT-Raman spectra of maleimide (top), and succinimide (bottom). Spectra are offset for clarity. Selected peak assignments are given in Table 2.

cm^{-1}) intensity. Ab initio calculations predict a similar relationship. We interpret this to mean that the breakage of the maleimide C=C bond disrupts the conjugated π system of the maleimide, reducing polarizability, and decreasing the Raman intensity of the C=O peak.

Because the alkene functionality in component B is unaltered throughout the reaction (see Fig. 1), the relative intensity of the C=C band (peak 10 at 1638 cm^{-1}) was constant. For that reason, this peak was selected as an internal standard. Normalized peak intensities, relative to the standard were determined for the C=O band (peak 7 at 1773 cm^{-1}), component B and A overlapping C=C band (peak 11 at 1610 cm^{-1}), and the maleimide C–H in phase bend band (peak 23 at 1065 cm^{-1}). These particular bands were chosen because they undergo a significant reduction in their intensity during the curing process.

An isothermal analysis was performed on the control to determine theoretical cure percentages as a function of time at a given temperature. These values were then compared to cure percentages based on DSC of the other samples. The DSC analyses of the oven samples (Fig. 6) generally follow the predicted curing curve within experimental error. Figs. 7–9 show plots of normalized intensities versus cure percentage for these peaks. A clear relationship exists between relative peak height of the three cure-sensitive vibrations and the extent of cure. The peak at 1773 cm^{-1} (peak 7, C=O stretch) decreases with relative intensity compared to the reference peak (Fig. 7), but does not disappear. During the curing pro-

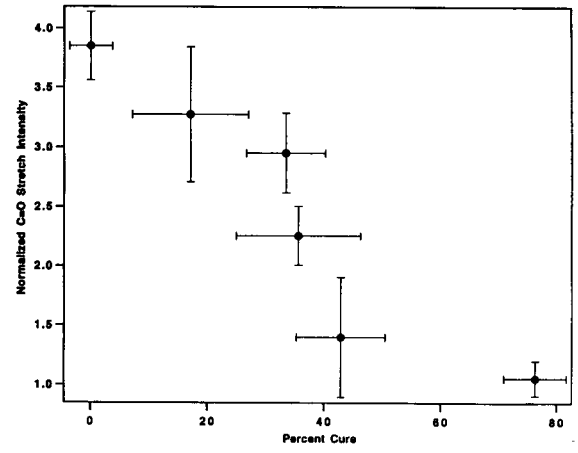

Fig. 7. Normalized FT-Raman intensity for C=O stretch (peak 7 at 1773 cm^{-1}) versus cure percentage derived from DSC. Reference peak for normalization was peak 10 at 1638 cm^{-1}. Error bars represent plus or minus one standard deviation determined from six samples.

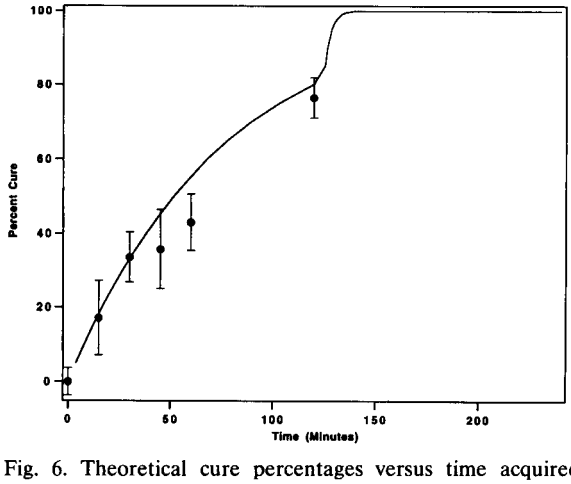

Fig. 6. Theoretical cure percentages versus time acquired from Perkin-Elmer isothermal kinetics software (line) and actual cure from samples from DSC vs. time (markers). Temperature was increased from 180 to 250°C after 120 min. Error bars are standard deviations determined from six samples.

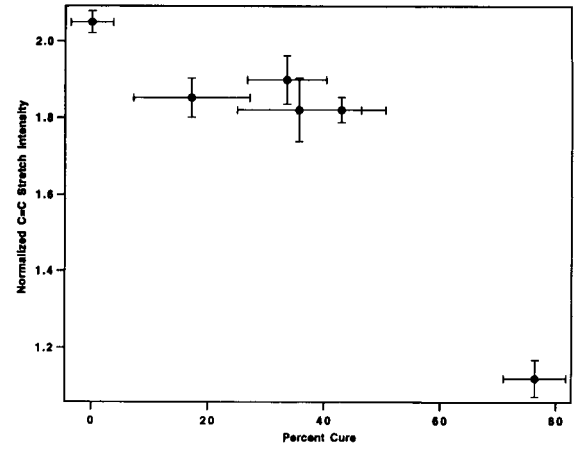

Fig. 8. Normalized FT-Raman intensity for overlapping B and A C=C stretch (peak 11 at 1610 cm^{-1}) versus cure percentage derived from DSC. Reference peak for normalization was peak 10 at 1638 cm^{-1}. Error bars represent plus or minus one standard deviation determined from six samples.

cess, the maleimide C=C functionality is lost. As a result, peaks at 1065 cm^{-1} (peak 23, maleimide C–H bend) and 1587 cm^{-1} (peak 12, maleimide C=C stretch) also decrease in intensity with curing. Figs. 8 and 9 show a similar decrease in the intensity of peaks 11 and 23 relative to the intensity of peak 10 during the curing. Changes in the FT-Raman spectra thus can be directly related to the extent of curing by comparison with DSC results. The error bars plotted in Figs. 7–9 represent the mean values plus or minus one standard deviation for six replicate samples. The relatively large error limits in Figs. 7–9 may be due to inhomogeneous curing of samples cured under replicate conditions.

3.3. Principal component analysis

As discussed above, major differences exist between the FT-Raman spectra of samples cured to a different extent. Subtle intensity changes are also apparent in peaks besides those discussed above. One advantage of a multivariate data analysis technique such as PCA is that the variation of many peaks is taken into account simultaneously. The primary use of PCA in this work was to summarize the trends over the entire curing process more clearly. Score plots, or projections,

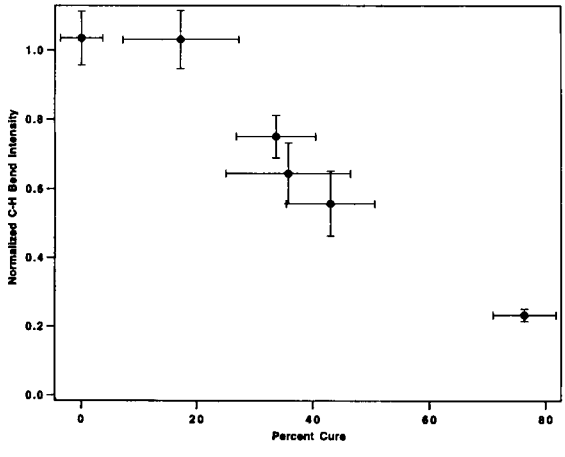

Fig. 9. Normalized FT-Raman intensity for maleimide in-phase C–H bend (peak 23 at 1065 cm^{-1}) versus cure percentage, derived from DSC. Reference peak for normalization was peak 10 at 1638 cm^{-1}. Error bars represent plus or minus one standard deviation determined from six samples.

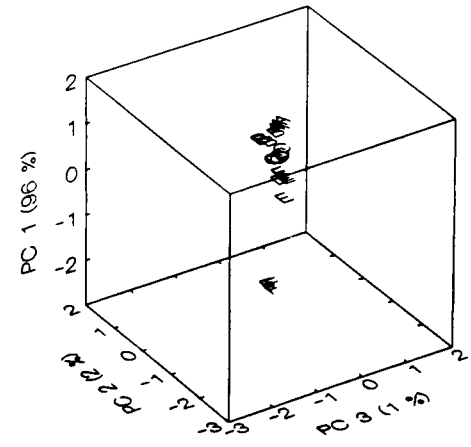

Fig. 10. Projections of FT-Raman spectra into the three-dimensional space of the first three principal components for samples of samples A–F identified in Table 1.

of the FT-Raman spectra onto the first three principal components, are effective for displaying the relationship of each sample spectra to the others. Fig. 10 shows the projection of the 24 FT-Raman spectra into the three-dimensional space of the first three principal components for 4 samples from groups A–F. The changes in the FT-Raman spectra from 0% cure (A) to 76% cure (F) shown in the PCA plot mirror chemical changes during the curing process. The first three principal components of the data set accounted for 99.2% of the variance in the data: 96.3% by PC_1, 2.3% by PC_2, and 0.6% by PC_3. The data lie mostly along a straight line in the three-dimensional PC space and the variability in the data is largely accounted for by a single principal component.

The magnitude of the components of each eigenvector (defining the PCs) gives the relative importance of each feature (wavenumber) in determining that direction of high variability. The six wavenumbers with the largest eigenvector components in the first principal component were associated with peaks 7, 27, 11, 23, 12 and 3 (in decreasing order of magnitude). Three of these six peaks (peaks 7, 11, and 23) were a priori suspected of being related to chemical changes taking place during curing. These three peaks were sensitive to percentage cure as shown by the

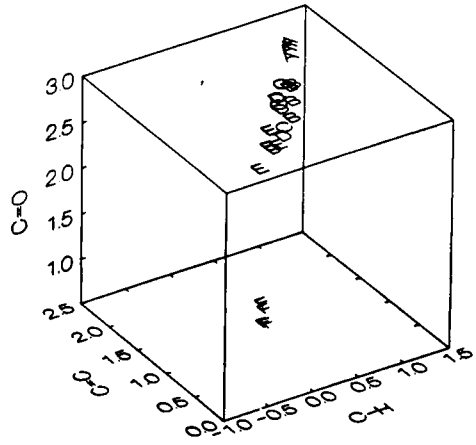

Fig. 11. Three-dimensional plot of the peak intensities related to C=O (peak 7 at 1773 cm^{-1}), C=C (peak 11 at 1610 cm^{-1}), and C–H (peak 23 at 1065 cm^{-1}). See Table 1 for sample identification.

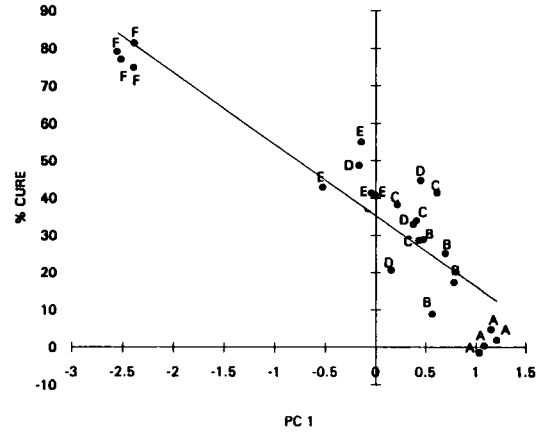

Fig. 12. Plot of percent cure versus projections of the FT-Raman spectra on the first principal component and fitted first order regression line for samples A–F identified in Table 1.

individual plots (Figs. 7–9). Fig. 11 shows a three-dimensional plot of the normalized intensities for peaks 7, 11 and 23. These normalized peak intensities are from the same data set as used for PCA. A linear trend from the initial control samples (A) to the samples of higher cure percentage (F) is apparent. The agreement between these two sets of results confirms the significance of these peaks as measures of percentage cure.

When linear regression is performed on the cure percentage data versus the projections onto the first principal component, a nearly linear fit is obtained with an R^2 of 0.83 (Fig. 12).

PCA results suggest that the entire curing process is not linear. In Fig. 12 the projections for samples having the highest cure percentage (76%, F) are well removed from the cluster of lower cure percentages (A–E). The large separation of the high cure percentages from the lower cure percentages make the data appear linear. There is a suggestion of curvature in the current data set. The later curing reaction and post-cure are marked by cross-linking reactions that consume some of the C=C functionalities of component B. An in-depth investigation of this latter mechanism is currently in progress.

3.4. *"Homopolymerization" of component A*

One further experiment was performed to investigate the polymerization of component A by itself. Parker et al. [30] performed FT-Raman and IR spectroscopy on MDA-BMI before and after 120 min curing at 190°C. Similar changes were observed in the same four bands 3104 and 3094 cm^{-1} (C–H stretches), 1585 cm^{-1} (maleimide C=C stretch), and 1064 cm^{-1} (maleimide

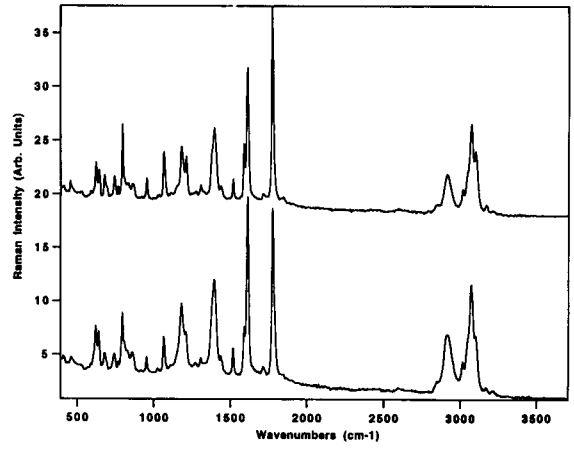

Fig. 13. FT-Raman spectra of Matrimid® 5292 component A cured for 30 min at 180°C (top) and 120 min at 180°C, followed by 1400 min at 214°C (bottom). Spectra are offset for clarity. Peak assignments are given in Table 2.

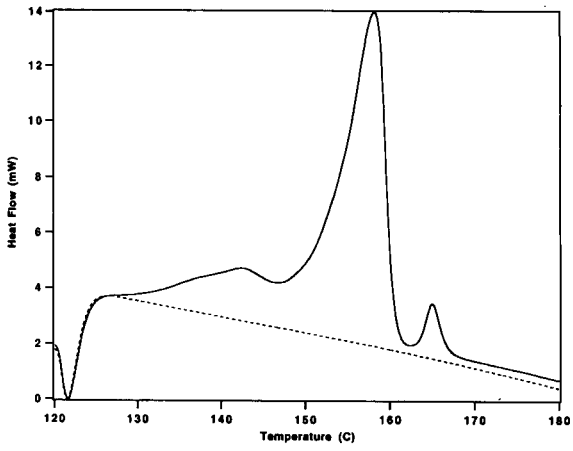

Fig. 14. DSC thermograms of Matrimid® 5292 component A, run from 120 to 180°C at a scan rate of 20°C/min (solid line), and the same sample cooled and rerun (dashed line). Baseline subtraction was performed on both runs. Thermograms were performed in the standard "endotherm up" position.

C–H in phase bend). However, these changes were observed after only 30 min at 180°C, much earlier than by Parker et al. [30]. Fig. 13 compares FT-Raman spectra of component A after 30 min at 180°C (top spectrum) and another spectrum taken after 120 min at 180°C, followed by an additional curing for 1400 min at 214°C. The differences between these two spectra mimic the changes observed during the cure of components A and B together. However, the C=O peak (1773 cm^{-1}) intensity did not reduce dramatically in the current data set. The small reduction in the C=O stretching intensity after a total of 1520 min of curing (observed in Fig. 13) indicates that if the homopolymerization of component A does occur, it is very slow. Since this peak intensity change is due to breakage of the maleimide C=C bond (vide infra) we conclude that the alkene groups in component A are not lost during the initial "reaction". DSC data for component A (Fig. 14) indicate that the reported spectral changes are most likely associated with melting of microcrystallites. Upon cooling, component A appears to form a glass of supercooled liquid, with no apparent phase change in the broad melting range observed on a first scan.

4. Conclusion

We have demonstrated the use of FT-Raman spectroscopy to monitor the curing of polyimide-based polymers. The Ciba-Geigy Matrimid® 5292 system investigated here establishes how characteristic changes in the carbonyl and alkene spectral regions can be monitored and correlated with the degree of curing. Spectral pattern changes were consistent with the known chemical changes occurring in the polyimide material during curing. Principal component analysis of a group of spectra taken at different curing times revealed a clear trend that could be associated with the curing process. Regression analysis of the projections of these spectra on the first principal component was able to provide satisfactory prediction of percent cure independently determined by DSC. The results of this preliminary study support the feasibility of using multivariate data analysis methods for continuous monitoring of curing processes with fiber optic probes.

Acknowledgements

Support for this work was provided by Grant Number N00014-92-J-1813 from the Office of Naval Research (ONR). In addition, thanks go to Dr. Kenneth J. Wynne of ONR for his interest and support of our work. We would also like to thank Dr. Kevin Trainer (Plastics Division, Ciba-Geigy Co., Hawthorne, NY) for supplying us with the Matrimid® 5292 polyimide system, Steve Page (Perkin-Elmer Co., Morrisville, NC) for advice on the DSC studies, Dr. Fredrick C. Wolters (The Clorox Co., Pleasanton, CA) for assistance with molecular modeling calculations, and Dr. Eric Markel (Department of Chemical Engineering, University of South Carolina) for assistance with FT-Raman.

References

[1] N. Sung and D. Wang, Paper 220B, AICHE Annual Meeting, San Francisco, CA, Nov. 6–10, 1989.

[2] T.T. Chiao, E.S. Jessop and H.A. Newey, SAMPE Quarterly, 6 (1975) 112.
[3] T.T. Chiao and R.L. Moore, 29th Annual Technical Conf., Reinforced Plastics/Composites Inst., SPI, Section 16-B, 1–7, 1974.
[4] H. Dannenberg, Proceedings of the 142nd American Chemical Society Meeting, Division Of Organic Coatings and Plastics Chemistry, Atlantic City, NJ, Sept. 1962.
[5] P.R. Young, M.A. Druy, W.A. Stevenson and D.A.C. Compton, 20th Int. SAMPE Technical Conference, Minneapolis, MN, Sept. 27–29, 1988.
[6] D.A.C. Compton, S.L. Hill, N.A. Wright, M.A. Druy, J. Piche, W.A. Stevenson and D.W. Vidrine, Appl. Spectrosc., 42 (1988) 972–979.
[7] C. Johnson and S.L. Wunder, SAMPE J., 26 (1990) 19–25.
[8] C.E. Miller, D.D. Archibald, M.L. Myrick and S.M. Angel, Appl. Spectrosc., 44 (1990) 1297–1300.
[9] C.A. Pryde, J. Polymer Sci., Part A, 27 (1989) 711–724.
[10] M. McCue and E.R. Malinowski, Anal. Chim. Acta, 133 (1981) 125–136.
[11] I.A. Cowe and J.W. McNicol, Appl. Spectrosc., 39 (1985) 257–266.
[12] P.M. Fredericks, J.B. Lee, P.R. Osborn and D.A.J. Swinkels, Appl. Spectrosc., 39 (1985) 303–310.
[13] P.M. Fredericks, J.B. Lee, P.R. Osborn and D.A.J. Swinkels, Appl. Spectrosc., 39 (1985) 311–316.
[14] G. Puchwein, Anal. Chem., 60 (1988) 569–573.
[15] P.J. Gemperline, L.D. Webber and F.O. Cox, Anal. Chem., 61 (1989) 138–144.
[16] H. Mark, Anal. Chim. Acta, 223 (1989) 75–93.
[17] T. Isaksson and T. Naes, Appl. Spectrosc., 44 (1990) 1152–1158.
[18] J.H. Perkins, E.J. Hasenoehrl and P.R. Griffiths, Anal. Chem., 63 (1991) 1738–1747.
[19] E.J. Hasenoehrl, J.H. Perkins and P.R. Griffiths, Anal. Chem., 64 (1992) 656–663.
[20] E.R. Malinowski, R.A. Cox and U.L. Haldna, Anal. Chem., 56 (1984) 778–781.
[21] T. Ozeki, H. Kihara and S. Hikime, Anal. Chem., 59 (1987) 945–950.
[22] R.E. Aries, J. Sellors and R.A. Spragg, in A.M.C. Davies and C.S. Creaser (Eds.), Analytical Applications of Spectroscopy II, Royal Society of Chemistry, Cambridge, 1991, pp. 248–251.
[23] E.R. Malinowski, Factor Analysis in Chemistry, Wiley, New York, 2nd edn., 1991.
[24] S. Wold, K. Esbensen and P. Geladi, Chemom. Intell. Lab. Syst., 2 (1987) 37.
[25] H. Martens and T. Naes, Multivariate Calibration, Wiley, Chichester, 1989.
[26] P.J. Gemperline and A. Salt, J. Chemometr., 3 (1989) 343.
[27] T. Woldbaek, P. Klaboe and C.J. Nelson, J. Mol. Struct., 27 (1975) 283–301.
[28] L. LeGall, J. Lauransan and P. Saumagne, Can. J. Spectrosc., 20 (1975) 136–141.
[29] A.J. Barnes, L. Legall, C. Madec and J. Lauransan, J. Mol. Struct., 38 (1977) 109–120.
[30] S.F. Parker, S.M. Mason and K.P.J. Williams, Spectrochim. Acta, 46A (1990) 315–321.
[31] K. Trainer, personal communication, Ciba-Geigy, Hawthorne, NY.
[32] M.J. Frisch, M. Head-Gordon, G.W. Trucks, J.B. Foresman, H.D. Schegel, K. Raghavachari, M. Robb, J.S. Binkley, C. Gonzalez, D.J. Defrees, D.J. Fox, R.A. Whiteside, R. Seeger, C.F. Melius, J. Baker, R.L. Martin, L.R. Kahn, J.J.P. Stewart, S. Topiol and J.A. Pople, Gaussian, Inc., Pittsburgh, PA, 1990.

ELSEVIER

Analytica Chimica Acta 293 (1994) 129–138

ANALYTICA CHIMICA ACTA

Multicommutation in flow analysis. Part 1. Binary sampling: concepts, instrumentation and spectrophotometric determination of iron in plant digests

Boaventura F. Reis [a,*], Maria F. Giné [a], Elias A.G. Zagatto [a], José Luis F.C. Lima [b], Rui A. Lapa [b]

[a] *Centro de Energia Nuclear na Agricultura Universidade de São Paulo, Box 96, Piracicaba, SP 13418-260, Brazil*
[b] *Faculdade de Farmácia, Universidade do Porto, Porto, Portugal*

(Received 16th November 1993; revised manuscript received 24th January 1994)

Abstract

A novel strategy to handle sample and reagent introduction in continuous flow systems is proposed. Basic features such as the effect of flow cell volume, analytical pathlength and peristaltic pump pulsation on the precision of measurement were studied. The manifold was based on a set of three-way solenoid valves controlled by a microcomputer using software written in QuickBASIC. It could also control the rotation speed of the peristaltic pump. By sampling slugs of sample and reagent solutions synchronized with pulsation of the peristaltic pump, aliquots with volumes as low as 2 μl could be sampled with a relative standard deviation $< 3\%$. Characteristics and performance of the system were studied by using a dye solution to simulate the samples. The feasibility was assessed by spectrophotometric determination of iron in acid plant digests using potassium thiocyanate. Results were in agreement with inductively-coupled argon plasma atomic emission spectrometric determinations. A throughput of 220 samples per hour was achieved and reagent consumption was only 0.7 mg per determination.

Key words: Flow injection; Multicommutation; Binary sampling; Iron determination; Plant digests

1. Introduction

Since flow-injection analysis was introduced eighteen years ago [1], several procedures for solution handling (such as solvent extraction, ion exchange, gas phase generation, standard addition methods, etc.) have been incorporated [2]. Moreover, approaches to save reagent [3,4], to increase residence time with minimum sample dispersion [5,6], and to accomplish zone sampling [7] have also been devised.

In order to implement these tasks, ingenious flow networks have been designed with different devices for sample introduction. Such devices have evolved from the first device equipped with a syringe, as described by Ruzicka and Hansen [1], to a device equipped with an automatic injector with multiple injection sections [8], culminat-

* Corresponding author.

SSDI 0003-2670(94)00090-9

ing today in the widespread employment of six-port valves [9,10].

Loading and injection steps employed by displacing a movable part between two resting positions is a common feature of those devices. With these devices, however, all commutation sections are simultaneously switched, leading to loss in versatility. This limitation can be overcome by designing a flow network with a set of three-way valves, each one acting as an individual commutator [10].

A general characteristic of flow analysis is that carrier and reagent solutions flowing towards the detector, require one pumping channel each. The volume of the injected sample has been defined by the dimensions of the sampling loops, and reagent solutions have been added through confluence into the analytical pathway [2]. With a time-based sampling method, the uncertainty factor in each sample-volume aliquot is associated mainly to precision of time control of the sampling device and to pulsation of the peristaltic pump. Errors related to sampling time have been surmounted by employing electronic devices [11]. Nevertheless, peristaltic pump pulsation is an intrinsic feature of this fluid propeller, and has a remarkable effect on the precision, mainly when small volumes are sampled.

In the present proposal, the manifold is constituted of a set of solenoid valves, each one acting as an independent commutator. Introduction of sample and reagents into the analytical path is performed by aspiration through a single pumping channel. The valves are positioned in the flow network in order to provide facilities to insert small slugs of sample and reagent in an alternated way. Consequently, the inlet end of the analytical path is loaded with a binary string formed by sample slugs in tandem with slugs of reagent. While this string is transported towards the detector, mutual dispersions occur from the liquid interfaces, and an homogeneous mixture tends to be quickly achieved, which affords conditions for development of the chemical reactions.

To undertake the multicommutation approach, a microcomputer was employed to control the lengths of sample and reagent slugs, to select the flow rate, and to synchronize the beginning of each analytical cycle with the pulsation of the peristaltic pump. Software and some necessary interfaces were tailor-made for this project.

The main features of the flow network were studied with a dye solution simulating the sample. Furthermore, iron(III) was determined by the thiocyanate method in acid digests of vegetal materials.

2. Experimental

2.1. Apparatus

The equipment set up consisted of a 432 Femto spectrophotometer (São Paulo) coupled to an ECB 201 (Equipamentos Científicos do Brasil, São Paulo) strip chart recorder, a mp-13R Ismatec peristaltic pump with Tygon pumping tubing, and an IBM-PC 386 compatible microcomputer with a PCL-711 interface card (American Advantech, San Jose, CA).

Flow cells of 15.7, 30.6 (optical path = 5 mm) and 70 μl (optical path = 11 mm) inner volume were constructed from perspex. The lengths of inlet and outlet channels were 10 mm up to the optical path and machined with a cross-section of 0.7 mm (volume ≈ 4 μl). The flow cells with volumes of 70.0 and 30.6 μl were machined with the same cross-section and those of 15.7 and 30.6 μl with the same optical path.

The flow network consisted of a set of NResearch 161T031 three-way solenoid valves (Stow, MA), reaction coil and flow lines of polyethylene tubing (i.d. = 0.8 mm) and three-way connecting pieces made of perspex.

All tubing junctions were airtight sealed because the flow network to implement the binary sampling process worked with an inner pressure lower than atmosphere. Small air bubbles could be delivered from the solutions and could adhere to the inner wall of the flow cell, then causing a drift in baseline. To overcome this drawback, all solutions were degassed before use and the bottles were lifted 30 cm higher than the flow cell level.

The electronic interfaces required to drive the solenoid valves, to control the rotation speed of

peristaltic pump and to detect the pumping pulsation, were developed as described in the following section.

2.2. Reagents and solutions

All chemicals were of analytical grade and freshly distilled and deionized water was used throughout. Buffer solution (0.25 M ammonium acetate) was prepared by dissolving 19.3 g in 600 ml of water, adjusting the pH to 4.7 with glacial acetic acid and water was added up to 1000 ml. A 0.2% (w/v) Eriochrome cyanine R solution was prepared by dissolving the dye in the acetate buffer solution. Working dye solutions were prepared by appropriate dilution with the acetate buffer. A 2% (w/v) potassium thiocyanate solution was prepared by dissolving it in water.

Plant materials were mineralized by employing the nitric and perchloric acid digestion procedure carried out on 40-place digestor blocks [12]. Iron(III) standard stock solution was prepared by dissolving 1.000 g of metallic iron in 20 ml of a 1:1 (v/v) nitric and hydrochloric concentrated acids solution and heating to 80°C. After complete dissolution, the volume was made up to 1000 ml with water. Working standards were prepared by appropriated dilutions of the stock in 0.25 M perchloric acid.

2.3. Hardware and software

The equipment was assembled in order to be controlled by an IBM 386 compatible microcomputer equipped with a PCL-711 Advantech interface card attached to its mother board. This interface provided sixteen input and sixteen output digital lines, an analog-to-digital converter (ADC) and a digital-to-analog converter (DAC) both with twelve bits of resolution.

The rotation speed of the peristaltic pump was proportional to the electric current loop situated in the range from 4 to 20 mA applied at the input control. By employing the DAC of the interface card, differences in electric potential within the suitable range (0.5 to 4.6 V) could be generated, which was converted to the appropriate electric current intensity by the conditioning interface

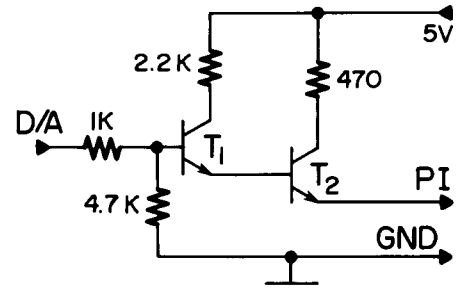

Fig. 1. Electronic diagram of the interface to control the speed of peristaltic pump. D/A = digital to analog converter (DAC) output from PCL-711 interface card; T1 and T2 = BC547 and TIP31A transistors, respectively; PI = peristaltic pump input control; GND = ground reference. All resistors expressed in Ohm.

depicted in Fig. 1. By means of this interface and suitable software, it was possible to settle the pumping flow rate and also, to change it whenever required.

To synchronize the starting of the sampling step with pumping pulses, a spindle was installed to slid on the rollers of the peristaltic pump, and an emitter and detector of infrared (IR) radiation was positioned over the rollers, so that when the pump was working, the spindle was displaced to up and down positions following the passage of each roller. These displacements caused interruptions of the radiation beam, leading the IR detector to generate an electrical pulse which was converted for the TTL level and read by the microcomputer through the interface card digital input port. This was done using the interface of which the electronic diagram is shown in Fig. 2.

The solenoid valves required a difference in electric potential of 12 V and a current intensity of about 100 mA to be activated, which cannot be provided through the PCL-711 interface from the microcomputer power supply. To overcome this obstacle, the interface (Fig. 3) was designed to accomplish the appropriated matching.

When the microcomputer is running, the control software written in QuickBASIC 4.5 inquires about the pump speed, and the timing course for each solenoid valve. These parameters were entered by means of the keyboard. Data concerning pump speed were processed and sent to DAC

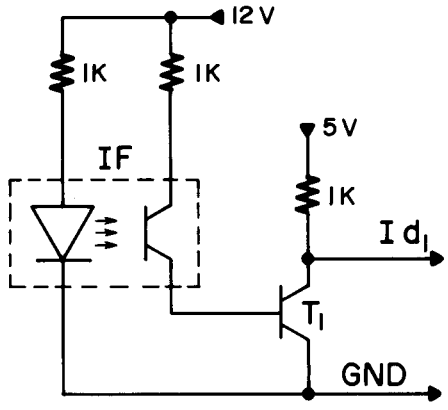

Fig. 2. Electronic diagram of the interface to synchronize the sampling steps. IF = PCST2103 infrared emission and detection system; T1 = BC547 transistor; Id1 = bit d1 of the digital input port of the PCL-711 interface card. Other symbols as in Fig. 1.

which generated a difference of electric potential, further converted to a loop of electric current by the conditioning interface (Fig. 1). Afterwards, the microcomputer read through the digital input port the electrical signal generated by the optic sensor as indicated in Fig. 2. When the TTL low level data was read, the microcomputer carried out a waiting loop until the TTL high level was attained, and then, the solenoid valves timing courses were carried out. On the other hand, if initially the read signal was the TTL high level signal, the microcomputer waited for the TTL low level and then accomplished the timing events sequence as described before. This logic was always followed before the start of each analytical cycle, in order to assure that the sampling step began with the pump roller at the same position. In this way, the duty cycle of solenoid valves was synchronized with the peristaltic pump pulsation.

2.4. Flow diagrams

The strategy for sample and reagent introduction in the analytical pathway as proposed here, is quite different with respect to common flow systems. Therefore, it was mandatory to verify the influence of analytical path length, volumes of sample and carrier slugs, and sampling time on the reproducibility and sample throughput. These features were studied with the manifold outlined in Fig. 4.

As indicated by the timing course of the solenoid valves, when the valves were switched on, the sample solution (S) flowed instead of the carrier solution (CS). By alternately commuting these valves, aliquots of sample and carrier solutions were sampled and inserted in tandem into the inlet of the analytical pathway.

With water instead of the sample, the microcomputer was programmed to settle the rotation speed of the peristaltic pump corresponding to a flow-rate of 930 μl/min. The time intervals for the duty cycle of the solenoid valves were varied from 0.1 to 1.0 s in steps of 0.1 s and from 1.2 to 3.0 s in steps of 0.2 s. For each time interval, 5 sets of 40 aliquots were collected and weighted, and the volume was calculated after considering the water density and temperature. The experiments were repeated for a flow-rate of 1510 μl/min. Average values and standard deviations of

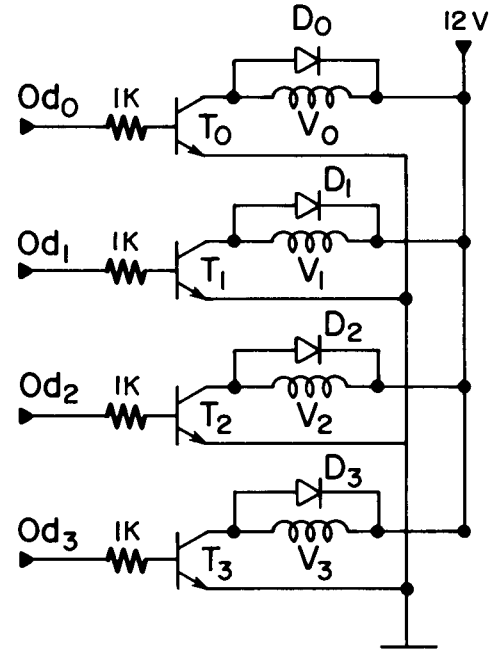

Fig. 3. Electronic diagram of the interface to switch the solenoid valves. V0, V1, V2 and V3 = solenoid valves; T0, T1, T2 and T3 = BC547 transistors; D0, D1, D2 and D3 = 1N4002 diode; Od0, Od1, Od2 and Od3 = digital output lines from the PCL-711 interface card. Other symbols as in the Fig. 1.

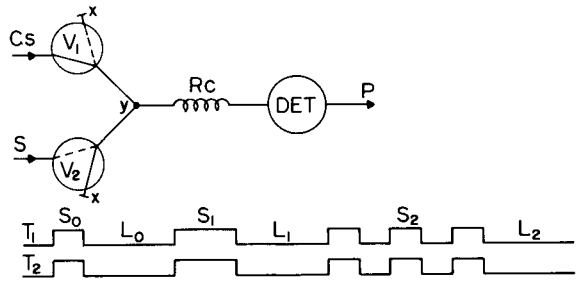

Fig. 4. Flow diagram to investigate the binary sampling process. V1 and V2 = three-way solenoid valves; Rc = reaction coil; DET = spectrophotometer at 540 nm; S = sample; Cs = carrier solution, 0.25 M ammonium acetate buffer; y = perspex junction point; x = stopper made by melting the end of a little piece of polyethylene tubing; P = connection to the peristaltic pump. Arrows indicate the direction; solid lines in the valve symbols indicate actual paths of fluid, and the broken lines indicate the path after the valve switching. T1 and T2 = timing courses of solenoid valves V1 and V2, respectively. The high level indicates the switching of valves. S0 and S1 = sampling with time base units 1 and 2, respectively. S2 indicates the loading of 3 slugs of sample in tandem with slugs of carrier solution; and L0, L1 and L2 indicate the time interval elapsed between consecutive samplings. Time base unit = 0.1.

these data were calculated in order to ascertain the precision of the binary sampling process.

With the dye solution simulating the sample and a 0.25 M ammonium acetate buffer solution as carrier stream, experiments were carried out to study the influence of flow cell volume and the sample aliquot on the magnitude of the recorded signal and system performance. To minimize sample dispersion, the outlets of the solenoid valves were attached 1 cm from the flow cell inlet.

To investigate the influence of pump pulsation on the precision of the selected aliquot, experiments were repeated without synchronization, employing flow cells of 15.7 and 30.6 μl, flow rates of 930 and 1510 μl/min and analytical path lengths of 2, 25 and 50 cm. For these experiments, the valve timing course was programmed with on/off ratios of 0.1:0.1; 0.2:0.2; and 0.4:0.4 s.

The flow network depicted in Fig. 5 was designed in order to demonstrate the feasibility of the approach involving chemical reactions. As indicated by the valve timing courses, in the first step all solenoid valves were off, so that only the carrier solution flowed through the analytical path. In the second step (Wt), V1, V2 and V3 valves were simultaneously switched on. Therefore, the flow of carrier solution was stopped and the sample was aspirated through V2 and V1 by-passing the reaction coil and detector. This was done to wash the flow conduit up to the confluence point y with the sample. Afterwards, V1 was turned off (Sp) and a string of electric pulses was sent to the V2 and V4 valves, so that while V2 was on, V4 was off and vice versa. In this instance, the analytical pathway was loaded with a binary string formed by slugs of sample in tandem with slugs of reagent. The timing course for solenoid valves was programmed to change the V2 duty cycle from 0.1 to 0.6 s, while the V4 duty cycle was maintained in 0.1 s throughout. Once the sampling step was completed, both valves were switched off (L), and the carrier solution again flowed through the analytical pathway, displacing the string towards the detector.

The reaction of iron with thiocyanate was elected as model to demonstrate the feasibility of

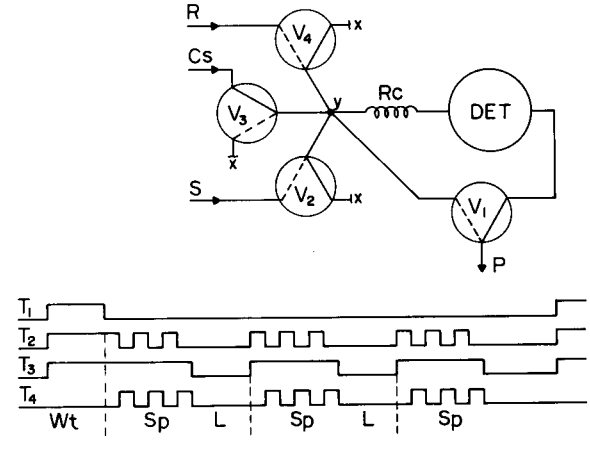

Fig. 5. Flow diagram for spectrophotometric determination of iron. DET = spectrophotometer at 480 nm; Rc = reaction coil (25 cm×0.8 mm i.d.); Cs = carrier stream, 0.25 M perchloric acid solution, flow-rate at 2.3 ml/min; R = 2% (w/v) thiocyanate solution; Wt = washing time with sample; Sp = time for loading the slug of sample; and L = time elapsed between two consecutive analytical cycles. Other symbols as in Fig. 4. The vertical broken lines indicate the beginning of each analytical cycle.

the approach mainly because it is fast, requires dilute solutions, and permits automation with a single reagent. Experiments were then carried out by reacting a 5.0 mg/l iron(III) standard solution with thiocyanate; the pumping rate of 2.3 ml/min was settled, and the duty cycle of valve V2 was changed from 0.1 to 2 s. From these experiments, the conditions for reaction development were established, i.e., 0.3 and 0.1 s as duty cycle for V2 and V4 valves, respectively, a 25-cm analytical pathway and a 70-μl flow cell. Thereafter, iron(III) was determined in acid digests of plant samples within a concentration range of 0.0–10.0 mg/l.

3. Results and discussion

With a dye solution simulating the sample, it was easier to understand the properties of the flow system.

When a long sequence of electric pulses was sent to the solenoid valves, the analytical pathway was filled with a string of sample slugs in tandem with slugs of the carrier solution, so attaining a steady state condition analogous to that of a sample of infinite volume. In this way, the effect of dispersion was suppressed, but some variation

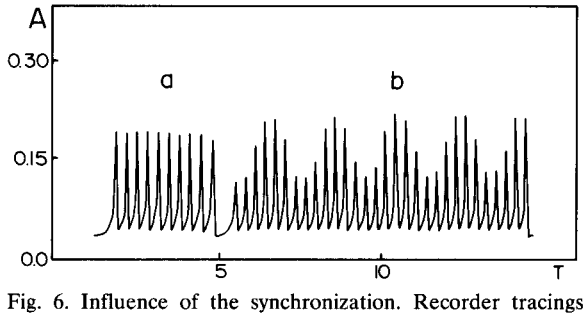

Fig. 6. Influence of the synchronization. Recorder tracings obtained with the flow set up of Fig. 4. Rc = 10 cm; flow rate = 930 μl/min; flow cell volume = 15.7 μl, sampling time = 0.2 s; S = 0.07% (w/v) dye solution in 0.25 M acetate buffer solution; Cs = 0.25 M acetate buffer solution. The two sets of recorder tracings a and b obtained with and without synchronizing. A = absorbance and T = time in min.

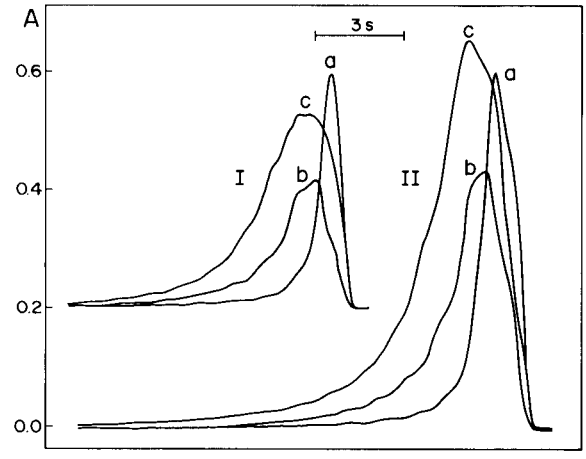

Fig. 7. Influence of the volume of flow cell. Peak profiles a, b and c were obtained with the flow cells of 15.7, 30.6 and 70 μl, respectively, by employing the flow network of Fig. 4, with a 1510 μl/min flow-rate and a 1 cm analytical path. Sets I and II were achieved by sampling aliquots of 13.8 and 29.9 μl respectively. Dye solution and carrier stream as in Fig. 6.

can occur due to incomplete mixing between sample and carrier solutions, and to pump pulsation.

Pulsation of the peristaltic pump as function of time presents a delivering fluid pattern analogous to a rectified full-wave. The volume of each sampled aliquot will be affected by the switching of the valves, impairing the precision of measurements (Fig. 6). In this figure it can be seen that this obstacle was overcome by synchronizing the loading step. Fig. 6 shows the effect of pumping pulsation and further experiments revealed that when either sampling time or pumping flow-rate were changed, different magnitudes of recorded peaks were noticed. A set of peaks with a pattern that was repeatable whenever necessary was obtained.

This drawback could also be avoided by employing a piston pump, considering the fact that in a hydrodynamic view, this flow network behaves as a single channel system.

The flow set up made it easy to study the effects of flow cell dimensions on the magnitude of measurement and on the washing time. As can be seen in Fig. 7, both geometry and dimension of the flow cells exert remarkable influence on

the peak profile. When an aliquot with of 13.8 μl was sampled, the peak profiles I were obtained. The 15.7 μl flow cell yielded a sharp profile (a), 70 and 20% higher than those for the flow cells with volumes of 30.6 (peak b) and 70.0 μl (peak c), respectively. The signal attenuation observed for the 30.6 μl flow cell can be ascribed to the more pronounced dispersion effect as could be expected. The volume of this aliquot was five times lower than the volume of the flow cell (70.0 μl), and therefore high dispersion was obtained as indicated by the broadened peak profile (c). Notwithstanding this fact, this peak height was only 20% lower than that obtained with the 15.7 μl flow cell. The other recorder tracings (set II) refer to a sample aliquot of 29.9 μl. This volume was practically equal to that of the 30.6 μl flow cell, the associated recorder tracing was again the lowest, while the maximum height of that produced with the 70.0 μl flow cell increased by a factor of two. This result indicates that the length of the optical path of the flow cell affects the magnitude of measurement in a higher propor-

Table 1
Influence of the volume of sampled aliquot

Sampling time (s)	Flow-rate = 930 μl/min		Flow-rate = 1510 μl/min	
	Sampled volume (μl)	Standard deviation	Sampled volume (μl)	Standard deviation
0.1	2.26	0.07	4.24	0.07
0.2	4.01	0.12	6.67	0.11
0.3	5.29	0.16	8.50	0.13
0.4	6.73	0.18	10.25	0.15
0.5	8.09	0.20	12.04	0.17
0.6	9.36	0.21	13.78	3.0
0.7	10.62	0.21	16.11	0.21
0.8	11.94	0.22	18.52	0.24
0.9	13.30	0.20	20.88	0.25
1.0	14.49	0.21	24.25	0.24
1.2	17.77	0.24	29.96	0.33
1.4	21.74	0.30	33.95	0.31
1.6	25.76	0.33	37.41	0.26
1.8	28.72	0.37	41.68	0.33
2.0	32.14	0.39	47.33	0.34
2.2	35.84	0.43	53.38	0.27
2.4	38.87	0.43	58.01	0.29
2.6	41.08	0.45	61.20	0.25
2.8	43.57	0.48	64.86	0.19

Each data is the average of 5 sets of measurements, each one comprising 40 aliquots of water.

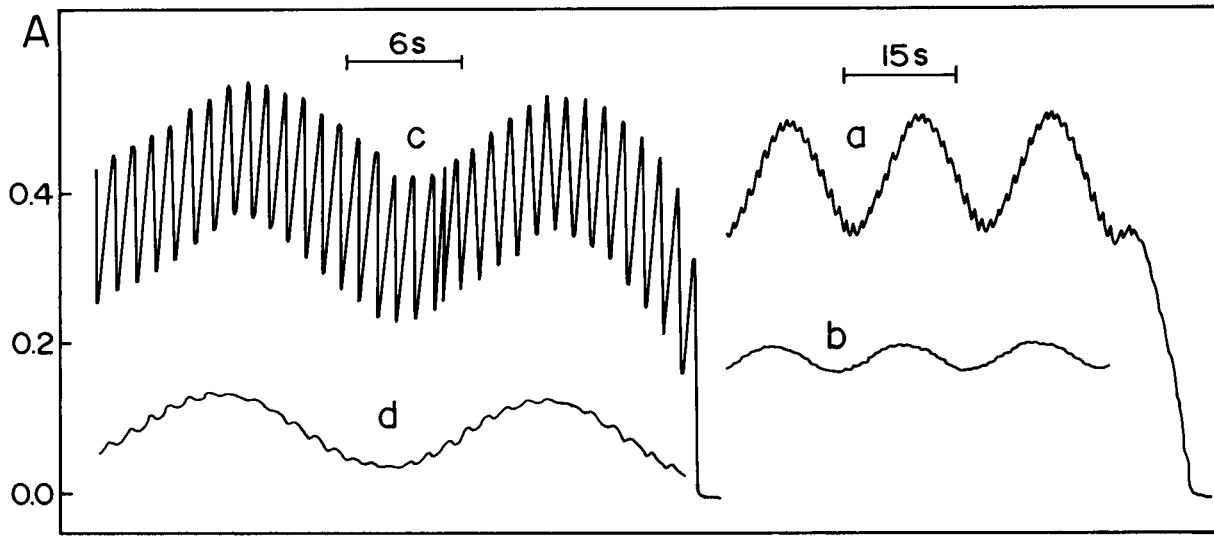

Fig. 8. Influence of flow cell volume and analytical path length. Recorder tracing a and b were achieved by employing a flow cell of 30.6 μl and analytical pathways of 1 and 25 cm length, respectively. Tracings c and d refer to flow cells of 15.7 μl and analytical pathways of 1 and 50 cm length, respectively. The valves duty cycles (Fig. 4) for loading both sample and carrier solution slugs were 0.4 s. Other parameters as in Fig. 7.

tion than the attenuation caused by the dispersion occurring inside the flow cell.

Measurement precision was largely improved when the synchronization device was employed (Fig. 6). Considering that the sampling step is the cornerstone of this process, several experiments were carried out in order to verify the precision of the aliquots sampled. As described in the Experimental section, the aliquots were weighed and converted to volume, the results being summarized in Table 1. The results seem to correspond to those expected, taking into account earlier reported results dealing with time based sampling [10], i.e., the precision was improved when the volume of aliquots was increased. In this case, the less precise result presented a relative standard deviation of 3% for aliquots of 2.26 μl.

Data associated with flow rates of 930 and 1510 μl/min were obtained with the same pumping tubing by changing the rotation speed of the pump. Precision was even better with the flow rate of 1510 μl, which can be easily assessed by comparing the relative standard deviations corresponding to aliquots with volumes of about 4, 10 and 20 μl (obtained with both flow rates). It is remarkable that for aliquots with volumes higher than 25 μl, the relative standard deviation in both cases was lower than 1.4%.

Another important feature to be considered in analysing Table 1, is the relationship between volume of aliquots and sampling time. The volumes of the aliquots (2.26, 4.24 μl) corresponding to flow rates of 930 and 1510 μl/min and a time interval of 0.1 s for sampling, could suggest flow rates higher than the nominal values. This apparent discrepancy was caused by the switching of

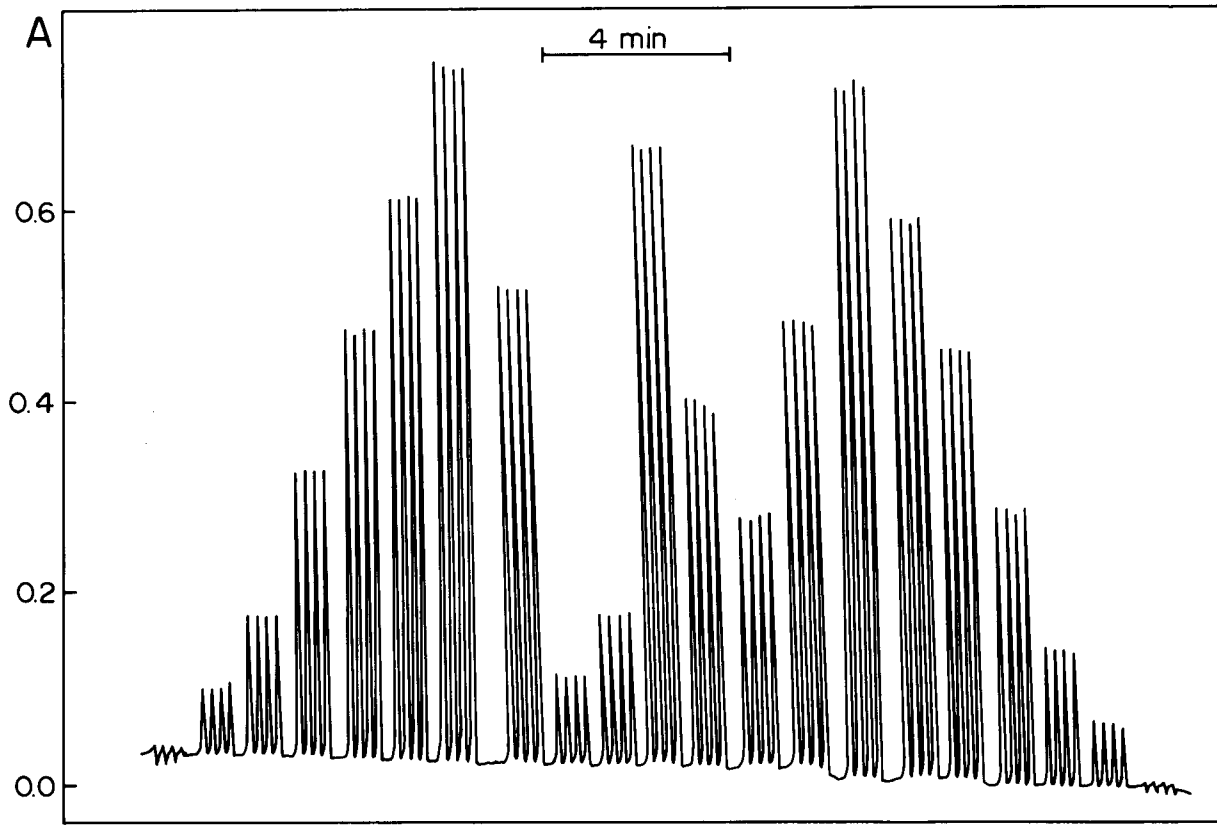

Fig. 9. Recorder tracing of routine analysis. From left to right, seven iron standard solutions (0.0, 1.0, 2.0, 4.0, 6.0, 8.0 and 10.0 mg/l) in quadruplicate followed by seven samples and the standards again. A = absorbance.

the solenoid valves taking place when the roller of the peristaltic pump was in the position of maximum compression. When the programmed time was longer, the sampled aliquot comprised also the position of lower compression, and the proportionality between the sampled volume and time was lessened. For sampling times higher than 0.5 s, the sampled aliquots comprised several positions of maximum and minimum compression. Therefore, the measured flow-rates for the sampling time of 0.1 s tend to values around the averages values of 15.51 and 23.66 μl/s, corresponding approximately to the programmed flow-rates of 930 and 1510 μl/min.

Since in the proposed flow system sample and reagent were inserted into the analytical pathway in a quite different way with regard to the usual flow systems, it is necessary to assess the capability of the system to provide a good mixing. Considering this fact, experiments were done and the results are shown in Fig. 8. The recorded tracings in this figure were achieved by inserting a long string of slugs of the sample in tandem with slugs of the carrier solution into the analytical pathway. The sinusoidal pattern indicates the state of fluid delivery as a function of time, which could become the main source of error when the time-based sampling process was implemented without synchronization. The variation observed along the recorded tracings in spite of the smoothing produced by the flow cell of 30.6 μl reveals that a good mixing inside the flow cells was not attained. Both sample and carrier solution aliquots were 65 and 33% lower than the flow cell volumes of 15.7 and 30.6 μl, respectively, but the magnitude of the fluctuation related to the 15.7 μl flow cell was 7 times higher. While for the 30.6 μl flow cell, and with a 25-cm analytical pathway, the fluctuation was completely smoothed, for the 15.7 μl flow cell it was necessary to increase the pathlength to 50 cm. When the aliquot volume aliquot was diminished, the magnitude of the variation also decreased, so that, when the volume of aliquots was 4.3 μl the fluctuation observed for the results of the small flow cell, was the same as that yielded for an aliquot of 10.3 μl and a flow cell of 30.6 μl.

The feasibility of the binary sampling process performed by multicommutation was demonstrated by using the flow manifold depicted in Fig. 5 which was designed for the spectrophotometric determination of iron(III). Results are shown in Fig. 9. In Fig. 9 a throughput of 220 determinations per hour can be deduced. For each determination, 35 μl of the reagent solution was used, corresponding to a consumption of 0.7 mg of potassium thiocyanate. The results were compared with those obtained by inductively coupled plasma atomic emission spectrometry, and an agreement better than 98% was observed. A relative standard deviation of 0.8% was estimated after 10 consecutive measurements of a typical sample digest with a concentration of 6.8 mg/l.

This paper demonstrated the feasibility of handling in tandem the insertion of sample and reagent slugs into the analytical pathway of a flow system. Implementation of the designed flow system by employing a single pumping channel is also a profitable characteristic.

Acknowledgements

The authors are grateful to FAPESP (Fundação de Amparo à Pesquisa do Estado de São Paulo), CNPq (Conselho Nacional de Desenvolvimento Científico e Tecnológico), FINEP (Financiadora de Estudos e Projetos) and the European Communities (SI1T 92-0052).

References

[1] J. Ruzicka and E.H. Hansen, Anal. Chim. Acta, 78 (1975) 145.
[2] J. Ruzicka and E.H. Hansen, Flow Injection Analysis, Wiley, New York, 2nd edn., 1988.
[3] E.A.G. Zagatto, A.O. Jacintho, L.C.R. Pessenda, F.J. Krug, B.F. Reis and H. Bergamin F°, Anal. Chim. Acta, 125 (1981) 37.
[4] A.O. Jacintho, E.A.G. Zagatto, B.F. Reis, L.C.R. Pessenda and F.J. Krug, Anal. Chim. Acta, 130 (1981) 361.
[5] C. Pasquini and W.A. Oliveira, Anal. Chem., 57 (1985) 2575.
[6] B.F. Reis, M.A.Z. Arruda and E.A.G. Zagatto, Anal. Chim. Acta, 206 (1988) 253.

[7] B.F. Reis, A.O. Jacintho, J. Mortatti, F.J. Krug, E.A.G. Zagatto, H. Bergamin F° and L.C.R. Pessenda, Anal. Chim. Acta, 123 (1981) 221.
[8] B.F. Reis, E.A.G. Zagatto, A.O. Jacintho, F.J. Krug and H. Bergamin F°, Anal. Chim. Acta, 119 (1890) 305.
[9] O. Jones, R. Stanley and M. Barnett, Anal. Chim. Acta, 249 (1991) 539.
[10] B.F. Reis and H. Bergamin F°, Quim. Nova, 16 (1993) 517.
[11] M.F. Giné, B.F. Reis, E.A.G. Zagatto, F.J. Krug and A.O. Jacintho, Anal. Chim. Acta, 155 (1983) 131.
[12] F.J. Krug, H. Bergamin F°, E.A.G. Zagatto and S.S. Joergensen, Analyst, 102 (1977) 503.

ELSEVIER

Analytica Chimica Acta 293 (1994) 139–146

ANALYTICA CHIMICA ACTA

Continuous-flow chemiluminescence detection comprising a rotating reactor

Zhang-Hua Lan, Horacio A. Mottola *

Department of Chemistry, Oklahoma State University, Stillwater, OK 74078-0447, USA

(Received 8th December 1993; revised manuscript received 23rd February 1994)

Abstract

This paper describes the implementation of chemiluminescence detection in an unsegmented continuous-flow system by using a detection cell comprising a rotating disk reactor. Rotation introduces convectional movement and facilitates reaction with concomitant enhancement of the chemiluminescence signal. The rotating disk reactor can also be used as a carrier for immobilized rate modifier (catalyst or promoter) of the luminescence reaction. The overall system has been characterized by means of the luminol–H_2O_2 reaction with hexacyanoferrate(III) ions and cobalt phthalocyanine as rate modifiers. The versatility of the device for analytical chemiluminescence measurements is illustrated.

Key words: Chemiluminescence; Flow system; Sensors; Continuous-flow chemiluminescence detection; Rotating reactor

1. Introduction

Together with fluorescence and phosphorescence, chemi- and bioluminescence can be classified as methods based on the detection of a transient light emission and are, consequently, kinetic-based measurements [1]. Chemiluminescence in particular has attracted increased interest since the mid-1970s, and such interest has been substantial among analytical chemists [2]. Its relatively simple implementation has contributed greatly to the increased popularity of chemiluminescence. Instrumentation for chemiluminescence measurements consists of three basic units: (1) reagent addition device, (2) sample cell, and (3) light measurement (detection) system. Depending on the method of reagent addition, the measurement is made under *batch*, *continuous-flow*, or *stopped-flow* conditions. Although most commercial *luminometers* are based on batch systems [3], the use of continuous flow has received increased attention in recent years. A variety of sample cells have been used in continuous-flow systems [4] and some, have incorporated vibration or magnetically activated balls to aid in mixing. Rapidly mixing reagents results in higher luminescence intensity, and a good flow cell should efficiently retain the emitting medium in the view of the detector. Therefore this paper reports the design and evaluation of a rotating reactor/cell that fulfils these requirements, utilizing small vol-

* Corresponding author.

0003-2670/94/$07.00
SSDI 0003-2670(94)00097-6

umes, and easily incorporating and efficiently utilizing catalysts or promoters of the chemical reaction leading to luminescence.

2. Experimental

2.1. Cell

Fig. 1 shows details of the cell design, which is an adaptation to chemiluminescence detection of a recently introduced strategy to bioreactor/sensor integration [5]. The cell body was constructed of PTFE and the external surface was painted black. The upper part accommodates two inlets and one outlet for solution(s) passage. The PTFE disk (its surface smoothly polished to reduce light scatter and to increase light reflection) contains embedded a miniature stirring bar (PTFE-coated Micro Stir bar from Markson Science, Phoenix, AZ). A PTFE needle is attached to the PTFE disk at bottom center. The needle's point rests on a machined inverted conical indentation that permits smooth disk rotation driven by a common laboratory magnetic stirrer. The upper and lower parts of the detector are made light- and fluid-tight by fastening them with six screws and a concentrically placed O-ring 5.85 cm in diameter (Fig. 1). The cell volume is 133 μl but can be varied simply by changing the disk's thickness.

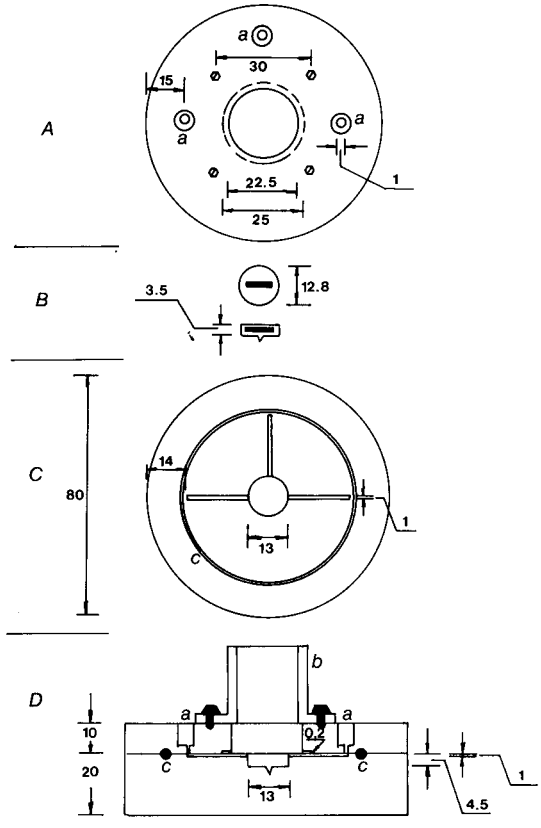

Fig. 1. Schematic representation of the flow-through cell containing the rotating disk. A: Upper cell body. B: Rotating disk showing positioning needle point and embedded magnetic stirring bar. C: Lower cell body showing solution inlet/outlet channels. D: Cross-sectional view showing the flow path and optical connector. (a) Solution inlet/outlet points. (b) Optical connector to photomultiplier tube. (c) O-ring. All measurements in mm.

The center part of the upper portion of the cell has a circular opening for a microscope slide circular cover made of chance microsheet glass (Arthur Thomas, Philadelphia, PA), which provides the optical window. Just above this glass window is located the photo-detector (a RCA 1P28A side-on 9-stage photomultiplier tube). The photomultiplier tube housing and the cell are interconnected with Canon-type optical connectors. A Model 204-10L high-voltage power supply (Pacific Precision Inst., Concord, CA) powers the photomultiplier tube.

2.2. Apparatus

Fig. 2 shows a block diagram of the custom-assembled unit used in the work reported here. The auxiliary electronics components (AE) were built around two chopper-stabilized operational amplifiers (McKee Pedersen, Danville, CA, Model MP-1031) to provide current-to-voltage conversion and an active low-pass filter circuit. The active low-pass filter is needed because disk rotation with the magnetic stirring bar embedded in it produces an AC-like noise which is dependent on rotation velocity: the higher the velocity the higher the noise frequency. A compromise between noise reduction and signal acquisition speed is necessary and can be dictated by the velocity of the chemiluminescence process. The hexacyanofer-

rate(III) rate-modification of the luminol–H_2O_2 chemiluminescence, for example, is relatively low, and data acquisition can tolerate slower response times; but the modification by the cobalt phthalocyanine complex, resulting in a considerably faster process, requires smaller response times. A 14.7-μF capacitor was used in combination with a 10-KΩ resistor (frequency cut-off of 1.06 Hz) in this work. Large capacitance values, however, increase the response time, defined as the time needed for 99.7% full response [6].

As already mentioned, an increase in the disk rotation velocity increases the sinusoidal noise frequency. It was observed that signal and baseline became smoother with increased disk rotation velocity. The improvement was significant at rotation velocities equal to or higher than 258 rpm.

All tubing used for solution transport was of Tygon (rated at 1.0 ml min^{-1} from Alpkem, Clackamas, OR). Whenever a second pump was needed, a FIAtron SHS-200 microprocessor-controlled solution-handling system (FIAtron Systems, Milwaukee, WI) was used (e.g., to implement programmed continuous-flow/stopped-flow/continuous-flow operation).

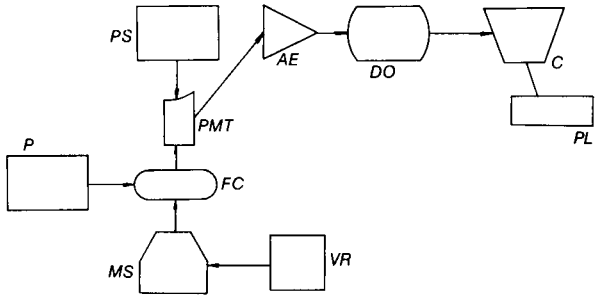

Fig. 2. Instrumental setup used to measure chemiluminescence. P = pump (Minipuls 2); PMT = photomultiplier tube (see text for type); PS = power supply (see text); AE = auxiliary electronics (see text for details); DO = digital oscilloscope [Nicolet 2090A with 94A plug-in and Model D amplifier (Nicolet, Madison, WI)]; C = desk top computer [Hewlett-Packard 9825A (Hewlett-Packard, Palo Alto, CA)]; PL = plotter (Hewlett-Packard 7470A); MS = magnetic stirrer (custom made to rotate a magnet with a Dayton Model 3M247 motor from Dayton Electric, Chicago, IL. This magnetic stirrer was designed to generate no heat, a problem common with most commercially available stirrers); VR = variable transformer [output between 0 and 140 V and 7.5 maximum amperage (The Superior Electric Co., Bristol, CT)].

2.3. Reagents and solutions

The water used for solution preparation was deionized and further purified by distillation in an all-borosilicate-glass still with a quartz immersion heater. Except as noted, all reagents used were of analytical reagent grade. When cobalt phthalocyanine was used in solution, this was prepared from a complex obtained from Pfaltz and Bauer (Flushing, NY) and by shaking excess solid with a 0.10% aqueous solution of ethanol. After standing for several hours the supernatant liquid was decanted into a clean container and this saturated solution used as working catalyst. The 1.00×10^{-2} M aqueous solution of $Fe(CN)_6^{3-}$ was prepared from $K_3Fe(CN)_6$ (Fisher Scientific, Fair Lawn, NJ). Luminol, obtained from Lancaster Synthesis (Windham, NH), was used as a 5.00×10^{-3} M solution in a 0.10 M phosphate buffer adjusted to pH 11.4 with sodium hydroxide. This solution was used when cobalt phthalocyanine served as catalyst. When $Fe(CN)_6^{3-}$ was used as promoter, a 2.00×10^{-3} M solution was prepared in 0.10 M sodium carbonate and the pH adjusted to 10.5 with sodium hydroxide. All luminol solutions were allowed to stand for at least one day to attain stability before use. The H_2O_2 working solution, 8.80×10^{-6} M, was prepared daily from 3% H_2O_2 stock solution (Mallinckrodt, St. Louis, MO).

Immobilization of the cobalt phthalocyanine catalyst was accomplished by first dissolving a small amount of the solid complex in toluene and then equilibrating (by shaking) this solution with controlled-pore glass, CPG (surface area: 24 m^2 g^{-1}, mean pore diameter: 1273 A. Electro-Nucleonics, Fairfield, NJ). Prior to equilibration, the CPG was washed with 2.0 M HCl to remove possible metal oxides, washed thoroughly with distilled water, and dried in an oven at 70°C overnight. After equilibration, the toluene was evaporated and the CPG-immobilized (by adsorption) cobalt phthalocyanine air dried.

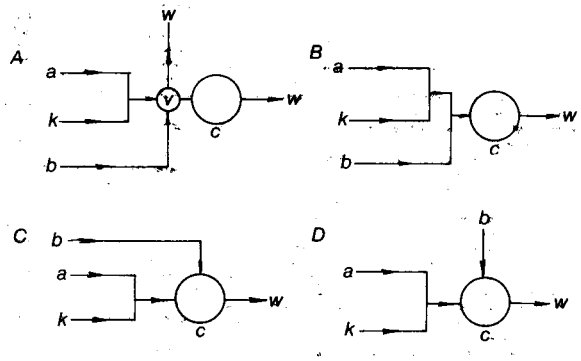

Fig. 3. Schematic representation of the different unsegmented flow configurations used to characterize the flow cell illustrated in Fig. 1. A: Configuration with intercalation of a small plug of sample solution. B and C: Configurations for continuous flow and mixing of all reactants and catalyst/promoter solutions. D: Configuration for stopped-flow operation. (a) Line for introduction of main reagent (luminol), (b) line for introduction of second reactant (H_2O_2), (k) line for introduction of rate modifier (catalyst or promoter), (w) waste line, (v) switching valve, (c) flow cell with rotating disk.

3. Results and discussion

The flow cell presented here is versatile, and different flow configurations can be achieved simply by changing connections. The basic configurations discussed here are illustrated in Fig. 3. The continuous-flow strategies illustrated in this figure have been evaluated mainly with regard to: (1) relevance of disk rotation (a unique characteristic of the flow cell presented here is the rotating disk to help thoroughly mix reactants and to serve as a bed for immobilized reagents), and (2) signal-to-noise ratio of acquired chemiluminescence signals. The chemical reaction used as model for these evaluations is the most popular one in chemiluminescence measurements: luminol (5-amino-2,3-dihydrophthalazine-1,4-dione) + H_2O_2. The rate of this reaction has been found to increase by at least 20 metal ions and some metal complexes. These rate-increasing effects are many times termed *catalytic*, but this designation is questionable since catalytic cycles are difficult to envision in most cases or the rate-affecting species is consumed during reaction. Consequently, most of these effects should be better designated as *promotions* [7]. Two rate modifiers have been used in this work: hexacyanoferrate(III) and cobalt complexed with phthalocyanine. The hexacyanoferrate(III) rate modification is a typical promotion, but the cobalt–phthalocyanine complex seems to behave, under certain conditions, as a true catalyst; studies are being conducted to elucidate its rate-modifying effect. The rate enhancement by the cobalt complex (both in solution and immobilized) is significantly more efficient than that of hexacyanoferrate(III). The background signal, especially when using hexacyanoferrate(III) ions as rate modifiers, was rather strong if the rate modifier and luminol were not mixed before entering the cell. Consequently, luminol and the rate modifier were pre-mixed in a 20-cm long tube when any of the flow configurations illustrated in Fig. 3 were used.

3.1. Continuous-flow operational mode of Fig. 3A

In this mode, the luminol, catalyst, and H_2O_2 solutions were delivered by a single peristaltic pump using tubing for reagents and sample with the same internal diameter. Injection was accomplished by means of a two-way injection valve. The luminol and catalyst solutions were pre-mixed with a T-piece mixing element before entering the injection valve. The mixture of luminol and catalyst served as carrier for the injected H_2O_2 sample. It is very important to make the connecting tubing between injection valve and flow cell as short as possible to minimize consumption of H_2O_2 before detection as well as dispersion. In this work a 2-cm connecting tube was used as the shortest possible connection. The flow rate of the luminol/catalyst mixture also influenced the intensity of chemiluminescence. Lower flow rates resulted in longer residence times and greater consumption of H_2O_2 before the cell was reached. The intensity of chemiluminescence, for instance, increased from a signal of 0.707 V at 1.80 ml min^{-1} (luminol–cobalt phthalocyanine mixture) to 3.904 V at 4.50 ml min^{-1}. Further increase in flow rate resulted in a slight increase in signal but much more consumption of reagents and sample. The flow rate of the H_2O_2 solution giving the best signal when the flow rate of the luminol/rate modifier solution was 4.50 ml min^{-1}, was 2.40 ml min^{-1}. For the slower luminol–H_2O_2–$Fe(CN)_6^{3-}$

reaction, the effect of flow rate was not as pronounced as when cobalt phthalocyanine is used as modifier. Flow rate, on the other hand, had no effect on noise.

The effect of sample size was different with the two different rate modifiers. Using the cobalt phthalocyanine complex required about twice the sample size as did using the $Fe(CN)_6^{3-}$ for maximum signal. In general, the signal vs. time profile became wider as the sample size increased; and, with long sampling loops, although the signal did not decrease, double and even triple peaks were observed. Optimum sampling loops were found to be 14.7 cm when using cobalt phthalocyanine and 7.6 cm when using $Fe(CN)_6^{3-}$.

The effect of disk rotation is illustrated in Fig. 4. Maximum peak signal was observed with 664 rpm and 258 rpm when cobalt phthalocyanine and $Fe(CN)_6^{3-}$ were used as rate modifiers, respectively.

Quantitative measurements made under these conditions can be based on the height of the peak signal. The reproducibility of measurement depends to a great extent on sample injection reproducibility. By using careful manual injection, the relative standard deviation for 11 measurements of a 8.80×10^{-6} M H_2O_2 was 1.6%.

3.2. Continuous-flow operational mode of Fig. 3B and C

In these modes the reagents and the hydrogen peroxide solutions are continuously sent through the cell until a steady state signal is reached. A typical signal vs. time profile observed on the oscilloscope screen is shown in Fig. 5. Before making measurements, the reading on the oscilloscope was adjusted to zero by adjusting a variable resistor in the current-to-voltage conversion portion of the auxiliary electronics unit when water was introduced into the flow cell instead of hydrogen peroxide.

When the flow-cell was operated as illustrated in Fig. 3B, two separate inlets delivered reagents and H_2O_2. The luminol and catalyst mixture was sent to the flow cell through one inlet and the hydrogen peroxide through the other one. This prevents the chemiluminescence reaction from

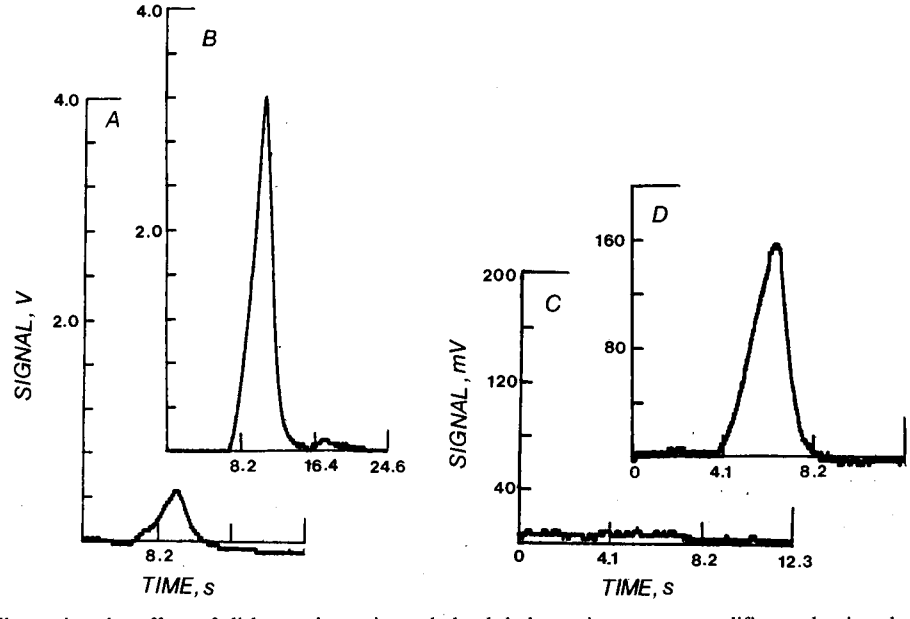

Fig. 4. Signals illustrating the effect of disk rotation using cobalt phthalocyanine as rate modifier and using the continuous-flow strategy of Fig. 3A. A and B: Rate modifier in solution. C and D: Rate modifier immobilized on controlled-pore glass. A and C: No rotation. B, Disk rotating at 664 rpm. D, Disk rotating at 452 rpm. Other experimental conditions as described in text.

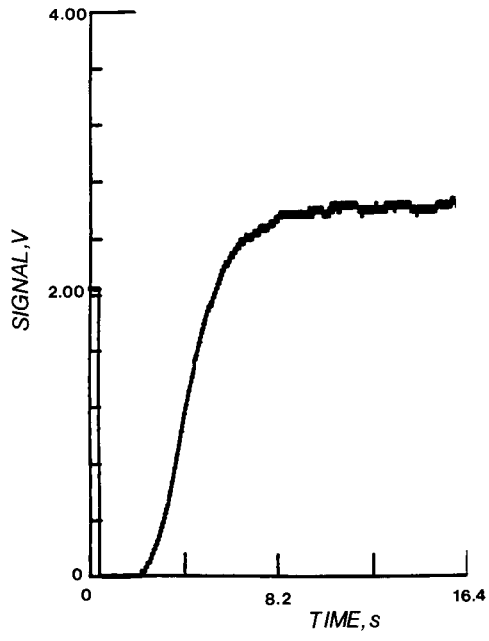

Fig. 5. Typical signal obtained by using the continuous-flow system illustrated in Fig. 3B. Disk rotation velocity: 452 rpm.

taking place before it enters the detector's view. As with any of the configurations used in this work, the effect of disk rotation was dramatic; typical signal levels for 8.80×10^{-6} M H_2O_2 and cobalt phthalocyanine as rate modifier were 0.80 V at 58 rpm, 2.40 V at 258 rpm, and 11.36 V at 874 rpm. The flow rate, as expected, also affected signal level. Optimum signal-to-noise values were obtained by pumping the luminol–catalyst mixture at 3.90 ml min^{-1} and the H_2O_2 solution at 2.00 ml min^{-1}.

In the continuous-flow operation represented in Fig. 3C, luminol and rate modifier were mixed together before mixing with H_2O_2 at another T-piece element. The mixture travelled through a short connection tube (1 cm in length) before entering the cell. In this configuration, fast flow favours a better yield in chemiluminescence detection because it reduces the loss of chemiluminescence outside the view of the detector. In our case the highest flow rates provided by the pump (6.60 ml min^{-1} for the reagent mixture and 3.50 ml min^{-1} for the H_2O_2 solution) provided the best conditions. Disk rotation, however, resulted in different effects with the fast chemiluminescence reaction in presence of cobalt phthalocyanine and the slow with $Fe(CN)_6^{3-}$. The fast chemiluminescence decreased somewhat with rotation (10.8% less signal at a 664-rpm rotation compared with no rotation). The noise level, on the other hand, decreased with rotation; and, on average, the signal-to-noise level was about the same with or without rotation. For the slow chemiluminescence reaction, rotation at 452 rpm produced a signal 21% larger than without rotation, and the noise decreased.

3.3. Stopped-flow operational mode of Fig. 3D

Two pumps were used in the stopped-flow configuration. The pump for the delivery of H_2O_2 was a FIAtron SHS-200 sample delivery system, which permitted control of the amount of hydrogen peroxide in the cell at the moment of measurement.

In order to make the measurement, the second pump, delivering the mixture of luminol and rate modifier, was stopped when the cell was filled and a predetermined volume of H_2O_2 solution was subsequently introduced in the cell. Rotation of the disk provided mixing. Between measurements, the cell was flushed with the mixture of luminol and rate modifier and the injection of H_2O_2 repeated.

In this operational mode, the flow rate of reagent mixture (luminol + rate modifier) does not affect the intensity of chemiluminescence. The amount of H_2O_2 in the cell (controlled by the volume of solution introduced in the cell), however, does affect signal intensity. At the same time, the higher the flow rate used to deliver the H_2O_2 solution, the shorter the injection time needed to reach maximum intensity (Fig. 6).

Just as in the other cases discussed here, disk rotation enhanced chemiluminescence. At optimum velocity, the increase was greater for the fast chemiluminescence reaction utilizing cobalt phthalocyanine as rate modifier.

Stopped-flow operation makes it possible to record the entire intensity vs. time profile (Fig. 6). In order to obtain this type of profile, mixing of reagents and sample must be very efficient.

Care should also be taken that the disk rotation is as high as possible, certainly higher than 258 rpm because slower rotation introduces noise. Quantitative measurements based on signal height of 11 replicates (8.80×10^{-6} M H_2O_2) yields relative standard deviations of 1.4%.

3.4. Use of the rotating disk as carrier for immobilized reagents

The rotating disk, besides aiding in mixing, provides an ideal support surface for immobilized reagents. If a given chemical species acts as a true catalyst, neither consumed nor rendered inactive in the cycling process, its use can be repeated from injection to injection of sample plugs. Use of the rate modifier immobilized on the surface of the disk [5] permits the reaction to take place only inside the cell and only until sample/reagents are in contact with the immobilized rate modifier.

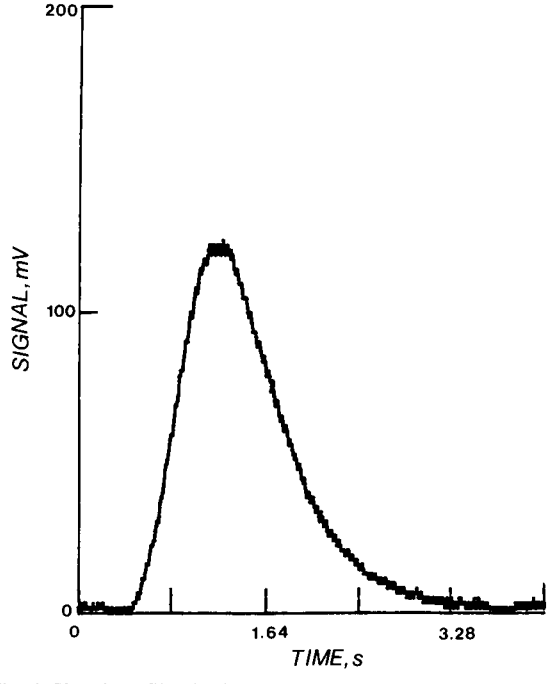

Fig. 6. Signal profile obtained by using the stopped-flow mode of Fig. 3D, showing the entire signal profile for the chemiluminescence of the luminol + H_2O_2 reaction using cobalt phthalocyanine in solution as rate modifier. Disk rotation velocity: 874 rpm.

Table 1
Signal-to-noise ratios observed with the different configurations illustrated in Fig. 3

Operational mode [a]	A	B	C [b]	D
Signal, mV [c]	3094	14500	13280	12480
Noise, mV	4	12	45	4
Signal-to-noise	976	1208	295	3120

[a] For description of each mode see Fig. 3.
[b] Data obtained without rotation.
[c] Concentration of $H_2O_2 = 8.80 \times 10^{-6}$ M.

We have found the rate modification of the luminol + H_2O_2 reaction by cobalt phthalocyanine to entail, under certain experimental conditions, catalytic cycles. This species is only very slightly soluble in water and can be easily adsorbed on controlled-pore glass. The procedure used to attach the complex to the disk was similar to the one described earlier [5] using a double-sided tape. Without disk rotation, practically no chemiluminescence was observed; but when the disk carrying the immobilized catalyst was rotated at 452 rpm, the enhancement of chemiluminescence observed was notable (Fig. 4C and D).

3.5. Signal-to-noise ratios

Table 1 compares signal-to-noise ratios observed with the different configurations discussed in this paper. As can be seen, the stopped-flow mode (using the FIAtron SHS 200 unit) offers the highest signal-to-noise ratio. Pump pulsation greatly increases noise level. The extent of pulsation depends on the construction of the peristaltic pump head and the quality of the tubing. Pulsation cannot be completely eliminated, but it can be considerably reduced by adding a simple dampener consisting of a T-piece (one inlet for flow in, a second for flow out, and the third for the pulsation dampening device). This consists of a piece of 30-cm Tygon tubing with an i.d. of 2.5 mm. The end of this tubing is clamped before starting operation of the pump, trapping air inside the tubing. The air chamber, acting as a buffer, reduces pulsation considerably. Each de-

livery tube used in the work described here was equipped with this device.

Acknowledgements

The authors thank Mike Lucas (Oklahoma State University machine shop) for the construction of the cell. Partial support from the Oklahoma State University Water Research Center is gratefully acknowledged.

References

[1] H.A. Mottola, Kinetic Aspects of Analytical Chemistry, Wiley, New York, 1988, Chap. 8.
[2] H.A. Mottola, Analyst (London), 118 (1993) 675.
[3] A. Townshend, Analyst (London), 115 (1990) 495.
[4] W.R. Seitz, CRC Crit. Rev. Anal. Chem., 13 (1981) 1.
[5] K. Matsumoto, J.J. Baeza Baeza and H.A. Mottola, Anal. Chem., 65 (1993) 636.
[6] J.D. Ingle, Jr. and S.R. Crouch, Spectrochemical Analysis, Prentice-Hall, NJ, 1988, p. 124.
[7] V.V.S. Eswara Dutt and H.A. Mottola, Anal. Chem., 46 (1974) 1090.

ELSEVIER

Analytica Chimica Acta 293 (1994) 147–153

ANALYTICA CHIMICA ACTA

Studies on a flow-injection system as a tool for on-line monitoring of cellulose hydrolysis and amygdalin containing effluents

Enobong F. Umoh, Karl Schügerl *

Institut für Technische Chemie, Universität Hannover, Callinstrasse 3, 30167 Hannover, Germany

(Received 26th November 1993)

Abstract

A presentation is being made of a flow-injection system which can be applied for on-line monitoring of cellulose hydrolysis and amygdalin concentration processes in industrial effluents. The system consists of glucose oxidase and β-glucosidase immobilized on a polymer carrier packed into a cartridge. By consecutive injections of the sample, the system could be used to determine the glucose concentration and total sugar from which the cellobiose concentration can be evaluated. Simultaneous injection of the samples enables the determination of total amygdalin concentration in industrial effluents and the fraction that has been converted into glucose by the inherent β-glycosidase. The system gave reliable readings in practical applications and is very selective.

Key words: Flow injection; Amygdalin; Cellulose hydrolysis; On-line monitoring

1. Introduction

Cellulose exists in vast quantities both in plants and different kinds of waste. As a polymer of glucose units, it has a potential of meeting the glucose needs for the production of single-cell protein, organic chemicals, enzymes and biopolymers. Enzymatic hydrolysis of the cellulose to obtain glucose requires continuous monitoring for attaining optimal yield and to guarantee the economy of the process.

It has been widely agreed that the breakdown of cellulose into glucose is mainly through cellobiose [1,2], which is further converted into glucose by the action of cellobiase; yet cellobiose, the major intermediate product, has been reported to inhibit cellulose-hydrolysing enzymes [3–5]. For efficient control of the process, the concentration of cellobiose must be determined separately and fast enough to facilitate immediate measures to be taken.

The usual methods of monitoring cellulose hydrolysis are performed off-line either by weighing the solid cellulose or by photometric determination of the entire soluble sugars. These methods cannot offer information on the concentration of the inhibiting intermediate products. The concentration of glucose, the desired product of the hydrolysis, is an important parameter in determining the extent of the hydrolysis. The latter,

* Corresponding author.

SSDI 0003-2670(94)00093-2

measured through weighing the solid cellulose requiring treatment of the sample to remove the hydrolysis products and adsorbed protein, is prone to error and is time-consuming. Obtaining it via photometric measurement of soluble sugars is unreliable, since a calibration curve of one sugar will be used to interpret the data of a mixture of sugars.

The flow-injection analysis (FIA) system presented in this work measures the glucose concentration in the sample and the total sugar content separately, thereby enabling the concentration of the intermediate products to be determined. Applied on-line, it renders an immediate measurement.

The cellobiose in the sample and other possible intermediate products are converted into glucose by β-glucosidase, and the glucose is measured through its reaction with glucose oxidase (GOD).

Amygdalin, a toxic component of wastewater from almond paste manufacturing plants is decomposed into glucose, benzaldehyde and hydrogen cyanide (Fig. 1) by β-glucosidase. Hence, its concentration in the effluent can be measured with the system. A complete conversion of the measured substances into glucose is necessary for accurate measurements, hence, the system must be operated at optimal conditions. The measurements must be free from interference by other substances.

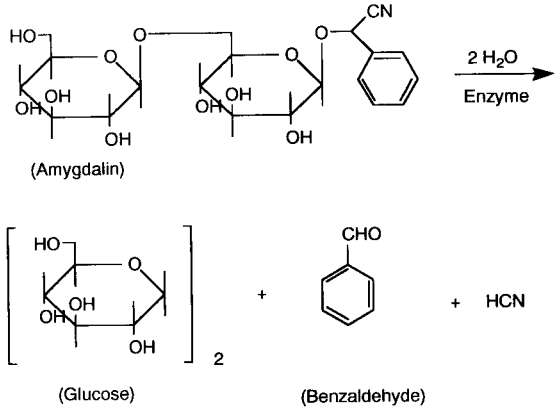

Fig. 1. Decomposition of amygdalin.

2. Experimental

2.1. Materials

The materials used were Glucose oxidase (from *Aspergillus niger*, EC 1.1.3.4, 232 U mg^{-1}, Serva), β-glucosidase (from almonds, EC 3.2.1.21, 5.5 U mg^{-1}, Sigma), cellulase (from *Trichoderma viride*, EC 3.2.1.4, 7.8 mg^{-1}, Sigma) and avicel cellulose (pH 105, Serva).

The substances tested with the system regarding interference were xylobiose, xylotriose, xylotetraose (obtained from the Institute für Biotechnologie, Jülich), β-lactose (Fluka), sucrose (Sigma), maltose (Difco), raffinose (Aldrich), potato starch (10% soluble in cold water, Fluka), xylan (from Birchwood, Sigma), pectin (from citrus fruit, Fluka), xylose (Sigma) and carboxymethylcellulose (CMC) (Fluka).

The buffer solution was composed as follows: K_2HPO_4 (4.3 g l^{-1}), NaH_2PO_4 (1.9 g l^{-1}), NaCl (3.0 g l^{-1}), EDTA (1.5 g l^{-1}) and was adjusted to the desired pH values with 25% HCl

2.2. Enzyme immobilization

The enzymes were immobilized on synthetic polymer beads (VA-Epoxy Biosynth, Riedel de Haen), packed in cartridges (mobicoils, Mobitec). The details of the immobilization procedure are described elsewhere [6].

2.3. Equipment

The major components of the measuring system were a compact FIA unit (Fiamat, laboratory-build) and a recorder. The compact unit consisted of pump, selector and injector valves, a programmable timer and a thermostated block which housed the enzyme cartridges, pulse absorber and oxygen electrode which served as the detector.

2.4. Determination of the amount of immobilized glucosidase

The actual amount of β-glucosidase immobilized on the carrier and the maximum amount the

Table 1
Amount of enzyme immobilized on the cartridges

Original amount in solution (mg)	Amount immobilized (mg)
20 (110 U)	15 (82.5 U)
40 (220 U)	28 (154 U)
60 (330 U)	33 (181 U)

carrier surface can accommodate were investigated by using enzyme solutions with concentrations of 20 mg l^{-1}, 40 mg l^{-1} and 60 mg l^{-1} for immobilization. After the immobilization, the unbound enzyme was washed off completely from the carrier surface. Bradford's test [7], slightly modified [6], was used to measure the extinction of the washwater. The measured extinction was then used to calculate the amount of enzyme in the wastewater from a standard curve constructed by using β-glucosidase, under the same conditions. The difference between the concentrations in the enzyme solution and the concentration in wastewater was regarded as the amount immobilized on the carrier (Table 1).

2.5. Interference test

Sugars from non-cellulosic material and substances of plant origin were tested for interference with the system measurements. Each substance (1 g l^{-1}) was tested for the signal, and the height of the signal was normalized against the height of the signal of 1 g l^{-1} cellobiose (single analysis). Equal volumes of the cellobiose and substance solutions were mixed and analysed, and the signal was normalized against the signal of 0.5 g l^{-1} pure cellobiose solution (mixed analysis). The interference test results are presented in Table 2.

2.6. On-line monitoring of cellulose hydrolysis

The system was applied in monitoring the hydrolysis of 10 g l^{-1} avicel cellulose with 1 g l^{-1} cellulase at 50°C. The system was set up as depicted in Fig. 2.

The sample was pumped from the reactor and diluted by the buffer carried by the dilution stream in order to bring down the sample concentration to a measurable range.

Table 2
Results of interference test

Substances	Single analysis	Mixed analysis
Lactose	0.02	1.01
Sucrose	0.00	1.00
Maltose	0.02	1.02
Raffinose	0.00	1.00
Starch	0.00	1.00
Xylane	0.00	1.00
Pectin	0.00	1.00
Xylose	0.00	1.00
Xylobiose	0.00	0.98
Xylotriose	0.00	0.98
Xylotetraose	0.00	(no test)
Carboxymethylcellulose	0.00	1.01
Glucose	0.98	2.00

A portion of the diluted sample was pumped with one stroke through the β-glucosidase cartridge and was maintained at 50°C at a rate of 0.27 ml min^{-1}, while the excess sample was collected as waste. During its passage through the β-glucosidase cartridge, cellobiose was converted into glucose.

The converted sample was then injected into a buffer stream which transported it through the GOD cartridge maintained at 30°C at a flow rate of 2.0 ml min^{-1} to measure the total sugar content of the stream recorded as a peak. Using a glucose-based calibration curve, the concentrations corresponding to the peaks were calculated. After a short time interval programmed into the timer and with the help of the selector valve, the diluted sample stream was pumped, by-passing the β-glucosidase cartridge, into the injector

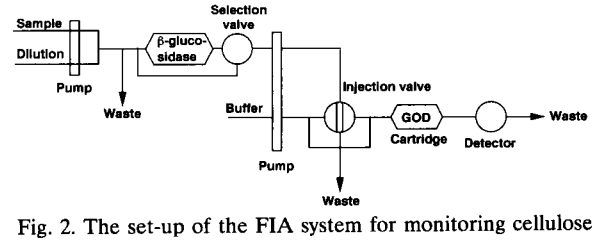

Fig. 2. The set-up of the FIA system for monitoring cellulose hydrolysis.

valve, where it was injected. The sugar concentration measured from this stream corresponded to the glucose concentration in the reactor. The difference between the two sugar measurements was regarded as the concentration of the intermediate product (cellobiose).

2.7. On-line monitoring of the amygdalin concentration

The system set-up having two injectors for analysing the extraction water of apricot kernels soaked in a reactor is shown in Fig. 3. The sample from the reactor diluted with buffer of an optimal pH value was injected simultaneously into two different buffer streams.

The buffer stream which transported the sample from the first injector flowed through both the β-glucosidase and GOD cartridges. At the β-glucosidase cartridge, amygdalin was converted into glucose. The sample from the second injector was simply passed through GOD to measure the glucose content of the sample emanating from the action of inherent β-glucosidase on the amygdalin. The two reactors were operated at 30°C, and the flow rate for the sample was maintained at 1.7 ml min^{-1}. The concentrations from the measurements were calculated from standard curves constructed for the two streams using glucose.

3. Results and discussion

The results in Table 1 show that the surface of the carrier was almost saturated as the amount of

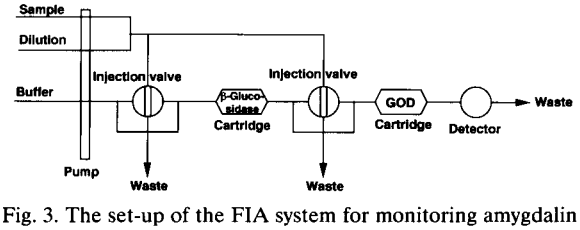

Fig. 3. The set-up of the FIA system for monitoring amygdalin concentration.

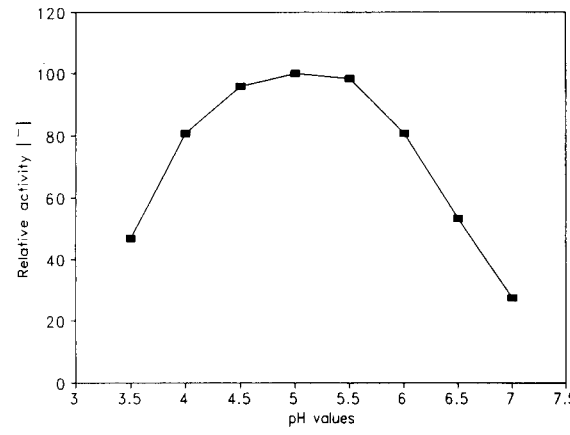

Fig. 4. Relative activity as function of pH for β-glucosidase.

enzyme was increased from 40 to 60 mg. Therefore, the activity of the immobilized enzyme could no longer be increased by raising the enzyme amount in the solution rather than by using an enzyme preparation with a higher specific activity (U mg^{-1}).

Table 1 gives the theoretical activity of the enzyme in each cartridge, since loss of activity due to the immobilization process should be expected.

3.1. Optimal pH and temperature

The optimal pH of the β-glucosidase investigated at 40°C (Fig. 4) with cellobiose as the substrate shows its maximum activity at pH values of 5.0 to 5.5. As the pH values were increased to 6.0, a rapid decrease in activity started, hence, the system was operated between a pH of 5.0 and 5.5. At a pH of 5.5, the enzyme optimal temperature was found to be 60–65°C, beyond which a fast denaturation occurred (Fig. 5). A small slope of the temperature curve between 50 and 65°C shows that any temperature lower than the optimal one in this region can be chosen without much compromise in terms of activity, while a longer life-span of the enzyme is obtained. Thus, 50°C was chosen as the operation temperature of the enzyme cartridge.

3.2. Interference

No interference was observed from the test substances. Therefore, in the application of the system to monitor the cellulose hydrolysis, interference with the measurements by xylose, which is usually a side product in the process [8], is not expected, and sucrose, which exists along with amygdalin in the effluent from apricot kernels [9], will not interfere with the amygdalin measurement. The absence of the signal for the CMC indicates that a soluble, but unhydrolysed cellulose will not be detected by the system.

3.3. Conditions for complete conversion of cellobiose

Although cellobiose is the major route to the formation of glucose, the hydrolysis mixture may contain other cellosugars as well. For accurate determination of the extent to which the solid cellulose has been hydrolysed, all of them must be converted into glucose by β-glucosidase. Since β-glucosidase has the highest Michaelis constant (K_m) with cellobiose compared to other cellodextrins [2], any conditions which achieve a complete conversion of cellobiose into glucose would also accomplish the conversion of the cellodextrins into glucose.

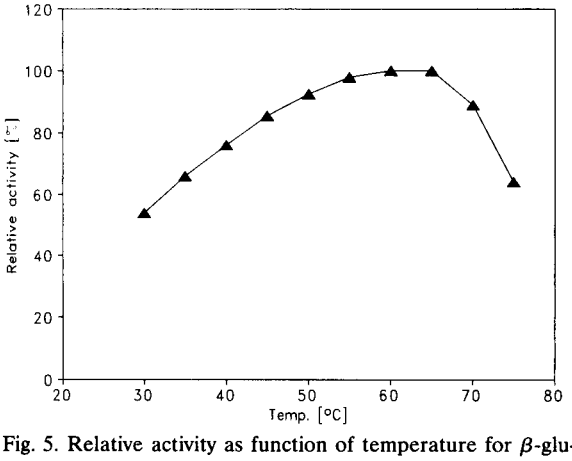

Fig. 5. Relative activity as function of temperature for β-glucosidase.

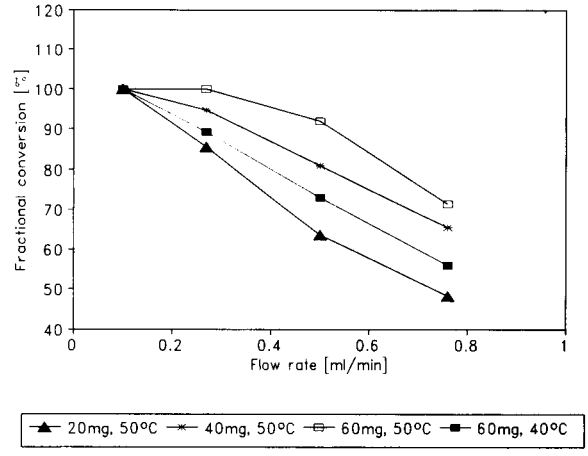

Fig. 6. Effects of enzyme amount, flow rate and temperature on fractional conversion of cellobiose.

Fig. 6 shows the fractional conversion of 1 g l^{-1} cellobiose using the cartridges with different enzyme quantities at different temperatures and different flow rates of the cellobiose solution through the β-glucosidase cartridges.

At 40°C with 60 mg enzyme cartridge, complete conversion was only attained at a flow rate of 0.1 ml min^{-1}. As the temperature was increased to 50°C, complete conversion was attained also at the rate of 0.27 ml min^{-1}. The other enzyme cartridges rendered complete conversion at 50°C only at a flow rate of 0.1 ml min^{-1}. The results in Fig. 6 reveal that increasing the temperature improved the conversion.

Since too high a temperature will result in enzyme denaturation, the system was maintained at 50°C and a flow rate of 0.27 ml min^{-1} was applied. If an enzyme preparation with a higher specific activity is used, a complete conversion can be obtained at a higher flow rate, and possibly with a lower temperature using less enzyme.

3.4. Conditions for complete conversion of amygdalin

The experiments with cellobiose were repeated using amygdalin. In all cases, equal peak heights were obtained, meaning that a complete conversion into glucose was achieved. A further

experiment with a 20 mg enzyme cartridge at a flow rate of 1.7 ml min^{-1} and temperature of 30°C (which were conditions for simultaneous operation of a similar system [6]) also produced the same peak height.

3.5. On-line monitoring measurements

The on-line measurements made during cellulose hydrolysis are shown in Fig. 7. During monitoring, the streams passing through β-glucosidase and the stream by-passing it delivered the same measurements. This was interpreted as that the samples leaving the reactor had already been converted into glucose. The results of the off-line analysis of the samples, drawn from the reactor at various times using the pHBAH [10] method, are also plotted in Fig. 7. Since glucose was used as standard in the pHBAH analysis, the agreement between the on-line and off-line measurements confirms that no cellobiose was present in the sample. If the sample had contained cellobiose which was not measured with the system, its extinction contributed in the pHBAH method would have resulted in higher glucose concentrations in the off-line measurements.

Normally, the stream passing through β-glucosidase should give the concentration of the total sugar in the medium and, hence, how much of

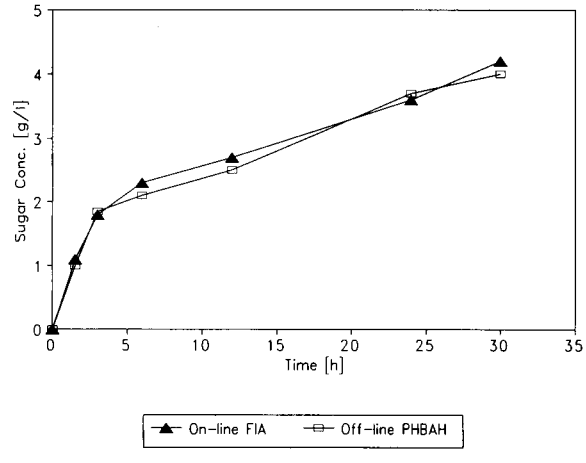

Fig. 7. On-line and off-line measurements during cellulose hydrolysis.

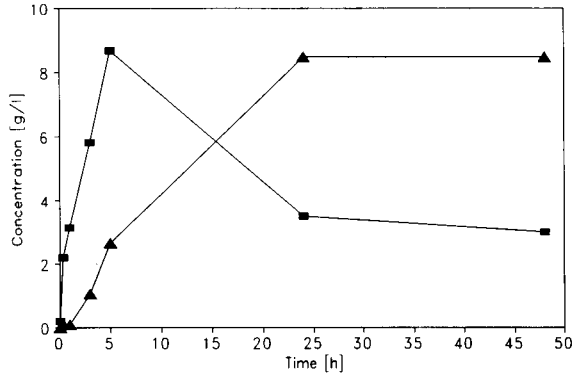

Fig. 8. On-line monitoring of amygdalin containing effluent.

the solid cellulose had been hydrolysed, while the stream which by-passed the β-glucosidase should measure the extent of hydrolysis in terms of the desired product (glucose). The difference between the two concentrations should give information on the accumulation of the intermediate product, which is usually cellobiose, since its conversion into glucose is often the limiting step in the process [11,12]. However, determination of glucose as the sole hydrolysis product is possible with cellulase having high β-glucosidase activity. This has actually been reported in [1,8,13].

In Fig. 8, the measurements of amygdalin and glucose concentrations from the effluent of the apricot kernels are depicted. They initially show an increase in both the concentrations of glucose and amygdalin. While the increase in the amygdalin concentration was due to its extraction from the apricot seeds, the glucose concentration was a result of the action of β-glucosidase inherent in apricot seeds [9,14] on the amygdalin. The conversion of amygdalin into glucose reached a state where further conversion was no longer observed.

From the above results, it can be seen that determining the toxic content of the amygdalin-containing effluent by measuring only the amygdalin concentration of the effluent [14] will exclude the fraction that had already been converted into glucose. Also, basing the toxicity as-

sessment on the cyanide content of the sample [15] will fail to account for the cyanide content of the undecomposed amygdalin.

4. Conclusion

This work shows that an FIA system is a useful tool for monitoring the hydrolysis of cellulose and industrial effluent. The selectivity of the system eliminates the tedious process of sample preparation and makes it economical. Immediate information on the state of the process or effluent is obtained from the system measurements, thus enabling timely action to control the process.

The system developed for cellulose hydrolysis can as well be used for cellulose assay and kinetic studies on the enzymatic degradation of cellobiose and cellodextrins.

Acknowledgement

E.F.U. thanks the German Academy Exchange Service (DAAD) for his scholarship.

References

[1] P. Toussaint and P.F. Bataille, J. Chem. Technol. Biotechnol., 35B (1985) 205.
[2] J.G. Shewale, Int. J. Biochem., 14 (1982) 435.
[3] A.A. Huang, Biotechnol. Bioeng., 17 (1975) 1421.
[4] Y.H. Lee and L.T. Fan, Biotechnol. Bioeng., 25 (1983) 939.
[5] M. Holtzapple, M. Cognata, Y. Shu and C. Hendrickson, Biotechnol. Bioeng., 36 (1990) 275.
[6] E.F. Umoh, Ph.D. Thesis, University of Hannover, 1993.
[7] M.M. Bradford, Anal. Biochem., 72 (1976) 248.
[8] S. Wald, C.R. Wilke and H.W. Blanch, Biotechnol. Bioeng., 26 (1984) 221.
[9] S.E. Godtfredsen, A. Kjaer, J.O. Madsen and M. Sponholtz, Acta. Chem. Scand., B32 (1978) 588.
[10] C.M. Mundie, M.V. Chesire, H.A. Anderson and R.H.E Inkson, Anal. Biochem., 71 (1976) 604.
[11] J.A. Howell and J.D. Stuck, Biotechnol. Bioeng., 17 (1975) 873.
[12] Y.H. Lee and L.T. Fan, Biotechnol. Bioeng., 24 (1982) 2383.
[13] D. Herr, Biotechnol. Bioeng., 22 (1980) 1601.
[14] C.F. Mandenius, L. Bülow and B. Danielsson, Acta Chem. Scand., B37 (1983) 739.
[15] Test 31 cyanide 04, German standard methods for the examination of water, wastewater and sludge (DIN 38405-D13-2-3).

ELSEVIER

Analytica Chimica Acta 293 (1994) 155–162

ANALYTICA CHIMICA ACTA

Analysis of total dissolved nitrogen in natural waters by on-line photooxidation and flow injection

I.D. McKelvie [a,*], M. Mitri [b], B.T. Hart [a], I.C. Hamilton [c], A.D. Stuart [c]

[a] *Chemistry Department and Water Studies Centre, Monash University, Caulfield East, Victoria 3145, Australia*
[b] *School of Chemistry, University of Melbourne, Parkville, Victoria 3052, Australia*
[c] *BHP Research, Wallsend, NSW 2287 Australia*

(Received 6th July 1993; revised manuscript received 24th February 1994)

Abstract

A sensitive automated method for the determination of total dissolved nitrogen (TDN) is described. This method is based on the complete conversion of inorganic and organic nitrogen species to nitrate by photooxidation in an alkaline peroxodisulphate medium. Following on-line photooxidation, sodium metabisulphite is added to reduce excess peroxodisulphate reagent, and a portion of the resultant solution is injected into a flow-injection manifold for the measurement of nitrate by cadmium reduction to nitrite, diazotization, coupling and detection at 540 nm. The method is comparatively fast (ca. 25 determinations h^{-1}), has a detection limit of 0.03 mg l^{-1} N, and is linear up to 3 mg l^{-1} N. The PTFE tubing photoreactor is simple to construct, and because detection is by visible spectrophotometry, the method could be readily employed using either commercial or low-cost laboratory-built flow-injection analysis systems.

Key words: Flow injection; Nitrate; Nitrite; Photooxidation; Peroxodisulphate; Waters

1. Introduction

The total dissolved nitrogen (TDN) content of natural and marine waters is an important water quality parameter, given that nitrogen is an essential nutrient for primary production, and in some cases may be limiting. Dissolved nitrogen species in natural waters include inorganic species (nitrate, nitrite, ammonia) and organic moieties such as amino acids, enzymes, nucleic acids, vitamins and alkaloids [1]. Historically, analysis of TDN has involved the Kjeldahl determination, although strictly this measures only dissolved organic nitrogen (DON) plus ammonia, and to obtain TDN, the oxidized forms nitrate and nitrite must be measured separately.

Alternative approaches to the determination of TDN have been the use of UV-induced photooxidation using hydrogen peroxide at low pH [2], or alkaline peroxodisulphate [3], and thermal oxidation using alkaline peroxodisulphate [4]. Both methods involved the conversion of DON to nitrate/nitrite, and while slow (30 min to 3 h conversion time) offered a significant improve-

* Corresponding author.

SSDI 0003-2670(94)00101-Q

ment over analysis by the Kjeldahl method. In both cases, the nitrate/nitrite formed by the oxidation step was determined by reduction on a copperized cadmium column, followed by diazotization and coupling to form an azo dye.

UV photooxidation methods for TDN have often been criticised because they give poor recoveries for some N-containing model compounds, especially those containing N–N and N≡N bonds (the so-called "recalcitrant" compounds). However, a study of batch UV photooxidation and high temperature combustion (HTC) methods for TDN has shown that the UV method gave a mean recovery of 60% for recalcitrant N-compounds, and 90% to 95% for a range of other reference N-compounds compared with the HTC method [5]. However the UV method gave an average recovery of 98% compared with the HTC method for seawater samples, a result which reflects the paucity of the recalcitrant N-compounds in natural samples.

More recently, attempts have been made to automate these approaches using flow injection analysis. Aoki et al. [6] have described a manifold involving the high temperature (175°C) digestion of TDN with alkaline peroxodisulphate containing selenium. Nitrate formed was converted to ammonia with titanium(III) chloride. After diffusion through a microporous membrane, the ammonia was mixed with *o*-phthalaldehyde and 2-mercaptoethanol, and measured by fluorimetry. This method was capable of six determinations per hour, and had a detection limit of 9 $\mu g\ l^{-1}$ N.

Rapid on-line photooxidation flow-injection methods have been described for dissolved organic phosphorus (DOP) [7] and dissolved organic carbon (DOC) [8]. A similar approach has been applied to the determination of TDN by Hinkamp and Schwedt [9] who used UV spectrophotometry to detect nitrate produced by UV photooxidation over a range of 1–50 mg l^{-1}. While this detection method is very sensitive for nitrate, the absorbance of the peroxodisulphate oxidizing reagent and its photolysed products resulted in a high blank, and the effective detection limit was constrained to ca 0.5 mg l^{-1}.

This paper describes a similar TDN method, based on the UV photooxidation method previously described for DOP [7], and which uses the more commonly applied Cd reduction–diazotization method with visible spectrophotometry. However, the alkaline peroxodisulphate photooxidation reagent was found to have an adverse effect on the Cd reduction column, and some modifications to the manifold and post-oxidation chemistry are described to overcome this problem.

This method is more sensitive, and probably more widely applicable than that using UV spectrophotometry, given that most commercial flow-injection instruments have the capability only for visible spectrophotometry, and has the advantage that even simple LED photometric detectors may be employed. The rate of sample throughput is also favourable compared with the batch photooxidation procedure.

2. Experimental

2.1. Reagents

Alkaline peroxodisulphate solution

Alkaline peroxodisulphate solutions were prepared by suitable dilution of a 40 g l^{-1} stock of twice recrystallized low-nitrogen potassium peroxodisulphate (Ajax Chemicals, AnalaR) in 34 g l^{-1} sodium tetraborate (Ajax Chemicals, Laboratory Grade).

Sodium metabisulphite

The working solution of sodium metabisulphite was prepared by appropriate dilution of a 40 g l^{-1} stock solution (BDH General Purpose Reagent).

Buffer solution

Ammonium chloride (Ajax Chemicals, AnalaR) (75 g) was dissolved in Milli-Q water, the pH adjusted to 8.5 with concentrated ammonia, and diluted to 500 ml.

Diazotizing agent

Sulphanilamide (5 g) was dissolved in a solution of 26 ml conc. HCl and 300 ml of Milli-Q water and diluted to 500 ml.

Coupling reagent

N-1-Naphthylethyenediamine dihydrochloride (NED) (0.5 g) was dissolved in 500 ml Milli-Q water. The reagent was stored in a dark bottle at $\leqslant 4°C$, and was stable for up to eight days when stored under these conditions.

Nitrate stock

A stock solution of 100 mg NO_3-N was prepared by dissolving 0.6070 g $NaNO_3$ in Milli-Q water and diluting to 1 l.

Model N compounds

These included ammonium chloride, urea, glycine, aminobenzoic acid, nicotinic acid, ethylenediamminetetraacetic acid, oxamic acid, barbituric acid and aspartic acid, and were chosen because of their range of stability to photooxidation. Best available reagents were used, and all were 95 to > 99% pure.

Cadmium column

Activated cadmium granules (0.3–0.8 mm particle size, Merck Coarse Cd Powder) [10] were packed in a 120 × 2 mm i.d. PVC tubing plugged with cotton wool, and placed in-line by the use of connecting nipples.

2.2. Manifold

The photooxidation system comprises an Oliphant G36NU germicidal U-tube which was housed in a fan-ventilated, light-tight enclosure. A 3 m × 0.3 mm PTFE tubing served as the photoreactor. Two Ismatec pumps (Mini S840 and S820) were used for sample and reagent delivery, and a pneumatically actuated PTFE injection valve assembly (Rheodyne 5020/5701/7163-003) was employed for sample and reagent injection. An Applied Biosytems variable wavelength detector (Model 759) was used to monitor absorbance.

Debubbling of the sample/reagent stream was achieved by the use of 10-cm ENKA AG Accurel microporous tubing (S6/2), as previously described [7].

Nitrate formed by photooxidation was determined by adapting the FIA method [11] involving conversion of nitrate to nitrite by reduction in a column of Cu-coated cadmium granules, diazotization with sulphanilamide, followed by coupling with *N*-1-naphthylethylenediamine. The absorbance of the pink azo dye thus formed was measured at 540 nm [12–14].

3. Results and discussion

3.1. Manifold design

Initial experiments involving the manifold shown in Fig. 1 (Manifold A) highlighted two major deficiencies, viz. the large concentration of alkaline peroxodisulphate used in the photooxidation step (40 g l^{-1} $K_2S_2O_8$) gave an extremely high blank, and rapidly degraded the Cd column.

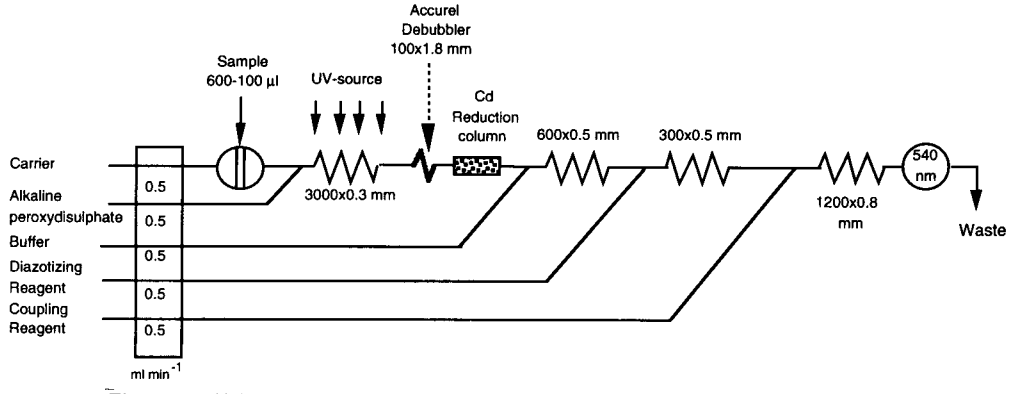

Fig. 1. Manifold A used for initial investigations of flow-injection TDN determination.

The formation of a white precipitate on the surface of the Cd granules was noted, and was presumed to be cadmium hydroxide formed following oxidation of the Cd granules by peroxodisulphate. The addition of a line to deliver sodium metabisulphite was done in an attempt to destroy excess peroxodisulphate following photooxidation of the organic nitrogen species, but this proved unsuccessful because the metabisulphite interfered with the detection chemistry, giving an extremely large blank signal.

In order to overcome these difficulties, the manifold shown in Fig. 2 (Manifold B) was developed. This configuration involves photooxidation of the sample, removal of bubbles of O_2 gas, and subsequent reaction of excess peroxodisulphate with sodium metabisulphite. A portion of the photolysed stream, containing oxidized nitrogen species, was then injected into a buffered carrier reduced to nitrite, followed by diazotization, coupling, and detection of the dye formed at 540 nm.

A preliminary assessment of the effectiveness of photooxidation on a number of model nitrogen compounds, and a USEPA Quality Assurance standard was performed using this manifold. Photooxidation efficiency was expressed as percentage N recovery after photooxidation, and was determined by comparison of the peak heights of organic nitrogen compounds with a calibration graph prepared from sodium nitrate standards. Relative standard deviations for %N recovery values were estimated from the standard deviation values of the nitrate and model compound peak heights using the standard method for multiplicative expressions [15]. For ammonium chloride, urea, glycine, EDTA and aspartic acid, recoveries were all greater than 90%. Given that urea and EDTA are relatively refractory organic nitrogen compounds [4], commonly used as standards for %recovery, these preliminary results were encouraging. Improvement in the recovery of nicotinic acid and other more recalcitrant compounds was expected following optimization of the manifold.

3.2. Photo-oxidation conditions

Influence of peroxodisulphate and metabisulphite concentration

A lower concentration of alkaline peroxodisulphate than that reported necessary for DOP digestion [7] was found to be adequate for near or total photooxidation of N-compounds to be achieved. Fig. 3 shows that high recoveries for a number of model compounds were obtained for a manifold in which a photooxidation reagent of 5 g l^{-1} potassium peroxodisulphate/4.25 g l^{-1} sodium tetraborate was used in conjunction with a 5 g l^{-1} sodium metabisulphite solution, under non-optimized flow rate conditions. The recalcitrant compounds, nicotinic acid and aminobenzoic acid, both showed recoveries of ca. 60% under these conditions, while complete recovery was achieved for urea. When a photooxidation

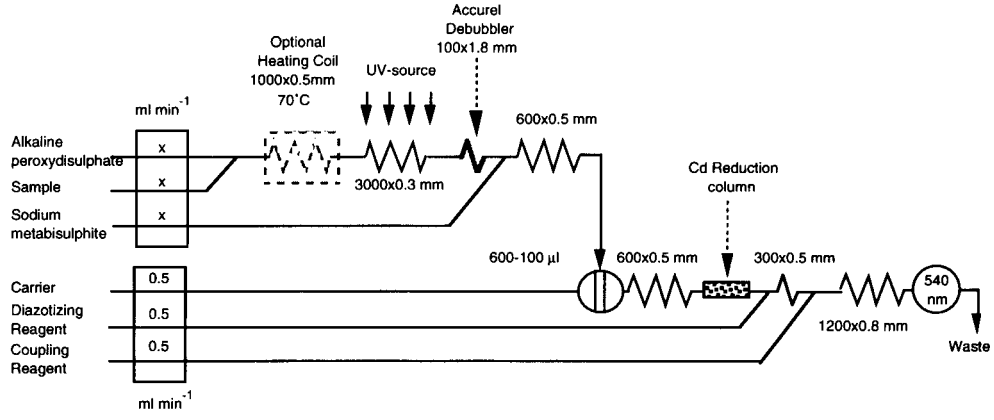

Fig. 2. Manifold B adopted for flow-injection TDN determination.

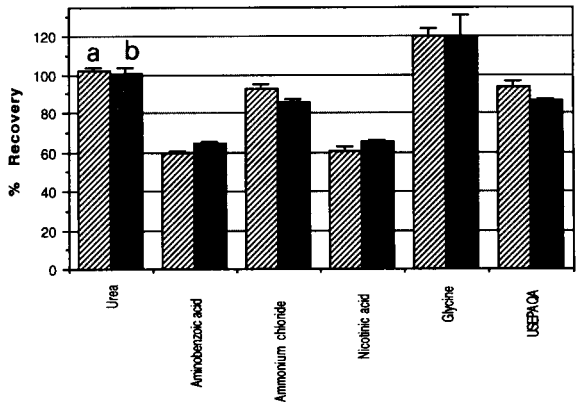

Fig. 3. Comparison of model compound recoveries at different potassium peroxodisulfate concentrations. Error bars shown are $\pm 1\sigma_{n-1}$ for $n = 3$. (a) 5 g l^{-1} potassium peroxodisulphate, 5 g l^{-1} sodium metabisulphite; (b) 10 g l^{-1} potassium peroxodisulphate, 10 g l^{-1} sodium metabisulphite.

reagent with 10 g l^{-1} potassium peroxodisulphate/8.5 g l^{-1} sodium tetraborate was used with a 10 g l^{-1} sodium metabisulphite solution, slight improvement in the recovery of nicotinic and aminobenzoic acid was achieved, and this combination of reagents was adopted as the digestion reagent for use in all subsequent optimization and analysis.

The completeness of conversion of model compound species to nitrate using these photooxidation conditions was also tested. The Cd reduction column was removed and the peak response of a variety of organic nitrogen model compounds and of nitrate after photooxidation was monitored for nitrite using the system described. No nitrite was detected following photooxidation of a number of easily oxidized or even more refractory nitrogen species.

Predictably, increasing the sodium metabisulphite concentration had no beneficial effect on N recovery, and served only to increase the size of the blank signal.

Influence of alkaline peroxodisulphate flow rate

The effect of different flow rates of both the alkaline peroxodisulphate and metabisulphite streams on recovery of model organic nitrogen compounds was investigated. Progressive improvement in recovery for some dissolved organic nitrogen species was observed (Fig. 4) when the residence time in the photoreactor was increased by reducing the flow rate though the photoreactor from 0.9 ml/min to 0.3 ml/min. The photoreactor has a volume of ca. 210 μl, and the residence time of an element of sample under this latter flow condition would be approximately 0.7 min which still permits fairly rapid sample throughput.

Effect of preheating on recovery

A heating coil was included in the manifold immediately following the mixing point of the sample and peroxodisulphate to determine whether better recovery of refractory organic nitrogen compounds could be achieved by thermal action and photooxidation, as opposed to photooxidation alone. However, heating at 70°C resulted in a decrease in recovery for some compounds, and this step was abandoned. One possible explanation for this behaviour is that peroxodisulphate degrades more rapidly at temperatures greater than 50°C [16], which could lead to a reduction in the active concentration of peroxodisulphate available in the photooxidation step following.

3.3. Detection chemistry

Influence of diazotizing and coupling reagent concentrations

The effect of differing concentrations of NED and sulphanilamide on the signal detected was investigated by increasing the concentration of both these reagents by up to five times that specified by Karlberg and Pacey [11] and used in these experiments. No improvement in peak heights was observed, indicating that there was an initial excess of chromogenic reagents.

Carrier buffer conditions

Some FI nitrate/nitrite determinations utilizing Cd reduction have used a carrier of 0.1 M ammonium chloride at ca. pH 5 [11]. However, a number of other workers [4,14,17] have suggested

that the efficiency of the copperized Cd column is best in the pH range 8.0–8.5. For Manifold B, ammonium chloride carrier solutions of 2.8, 1.4 and 0.7 M were adjusted to pH 8.5 with concentrated ammonia. The most concentrated carrier gave the largest analytical response, whereas when the 1.4 M buffer was used, a 50% decrease in signal was observed. Use of the 0.7 M buffer yielded doublet peaks of further reduced peak height.

Effect of injection volume

The influence of injection volume on measured analytical signal was investigated. For injection volumes of 600 to 200 μl, doublet peaks were obtained, but for 100 μl injections, singlet peaks of greater height, but similar area to those of the doublets were observed. Doublet peaks in FIA are usually associated with incomplete reaction of the central portion of the sample bolus because of inadequate radial dispersion or chromogenic reagents of insufficient concentration [18]. In this instance, chromogenic reagent concentration did not appear to influence peak shape, and existence of doublet peaks appears related to sample dispersion in the detection section of the manifold. The injection volume of 100 μl is large in comparison with those used by other workers for nitrate analysis using this detection chemistry and unsplit systems [12,19].

Influence of digest reagent purity on blank value

The magnitude of the blank signal was largely dependent on the purity of the peroxodisulphate used. Recrystallized laboratory-grade and low-nitrogen potassium peroxodisulphate gave blank peaks equivalent to ca. 0.18 and 0.13 mg N l^{-1}, respectively. This blank value was further reduced to ca 0.06 mg N l^{-1} when double recrystallized low-nitrogen peroxodisulphate was used.

The purity of sodium tetraborate, used in the digestion at a constant concentration of 8.5 g l^{-1}, appeared to have no influence on the magnitude of the blank signal, and both Laboratory and Analytical grade reagents were used at various times. Only General Purpose grade sodium

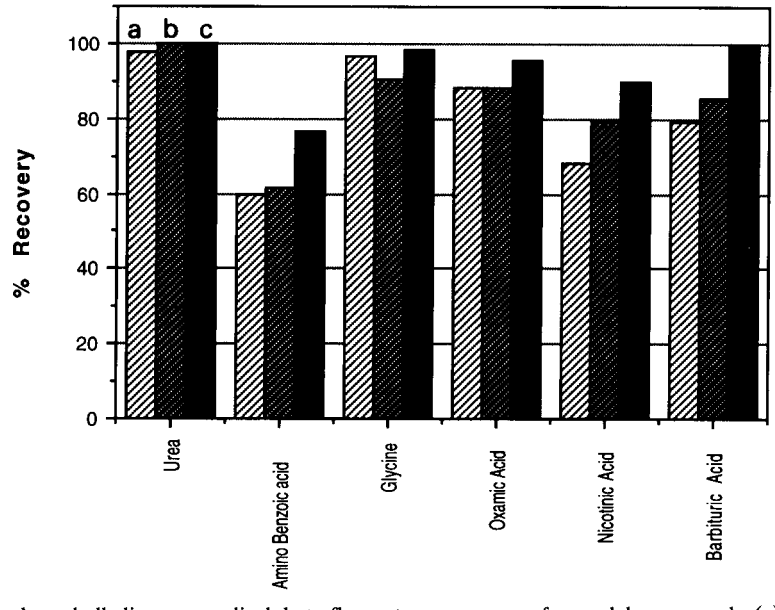

Fig. 4. The effect of sample and alkaline peroxodisulphate flow rates on recovery for model compounds. (a) Sample: 0.9 ml min^{-1}; peroxodisulphate and metabisulphite: 0.7 ml min^{-1}, (b) sample: 0.5 ml min^{-1}; peroxodisulphate and metabisulphite: 0.45 ml min^{-1}, (c) sample: 0.3 ml min^{-1}; peroxodisulphate and metabisulphite: 0.2 ml min^{-1}.

metabisulphite was used, and the effect of the purity of this reagent on the blank signal requires further investigation.

3.4. Analytical performance measures

Linearity and sensitivity

A typical calibration data obtained using Manifold B (Fig. 2) and a series of nitrate standards yielded a straight line; regression analysis of these data gave the highly linear best-fit equation:

$$\text{Peak height (mm)} = 60.7\ [\text{mgl}^{-1}\text{TDN-N}] + 9.1$$

for which $r^2 = 0.998$. The sensitivity of this method was estimated at 0.037 AU (mg l^{-1} TDN-N)$^{-1}$.

The calibration graph was tested for linearity only up to 3 mg l^{-1} N, but with reduced injection volume could be expected to have a somewhat greater linear range. The calibration also displayed significant absorbance associated with the blank (0.003–0.005 AU) which was predominantly due to the presence of nitrogenous impurities in the digestion reagents.

Limit of detection and reproducibility

A limit of detection value of 0.05 mg l^{-1} was determined from the calibration graph using the method of Miller and Miller [15]. This value is probably conservative compared with that determined by the method described by Skoog and Leary [20]. Using the standard deviation of the blank for 10–20 measurements, and the calibration sensitivity from the calibration graph, a detection limit of 0.03 mg l^{-1} NO_3-N was obtained. Injection reproducibility was acceptable, with a relative standard deviation of 0.47% for eight injections of 1 mg l^{-1} NO_3-N.

Sample throughput and long term operation

Using Manifold B and optimal N-recovery conditions, 30 + injections per hour are feasible once sample has been merged with alkaline peroxodisulphate reagent and transported into the photoreactor. However, the loading time causes some delay, and sample throughput is conservatively estimated at ca. 8 samples/hour using triplicate injections.

Long term detection stability was of concern in developing this method, especially as the lifetime of the Cd reduction column could potentially be shortened because of the alkaline peroxodisulphate conditions used. Using Manifold B, the dry weight mass of the Cd in the reduction column was noted to decrease from 1.36 to 1.23 g over a period of six days, during which time an estimated 400 injections were made. No diminution in nitrate reduction efficiency was observed during this period.

Validation against Kjeldahl and alkaline peroxodisulphate batch methods

A number of estuarine, marine, fresh and waste water samples were analysed by the proposed method, following appropriate dilution, and compared with results for total Kjeldahl nitrogen (TKN) and the commonly used alkaline peroxodisulphate (AP) batch digestion [4]. Good agreement was achieved for most samples between methods over a wide range of concentrations and salinity conditions (Fig. 5), with the following regression equations being obtained:

$$\text{TDN(FIA)} = 1.06\ \text{TDN(AP)} - 0.25$$

$$r^2 = 0.995,\ n = 16$$

$$\text{TDN(FIA)} = 0.92\ \text{TDN(TKN)} + 0.05$$

$$r^2 = 0.995,\ n = 8$$

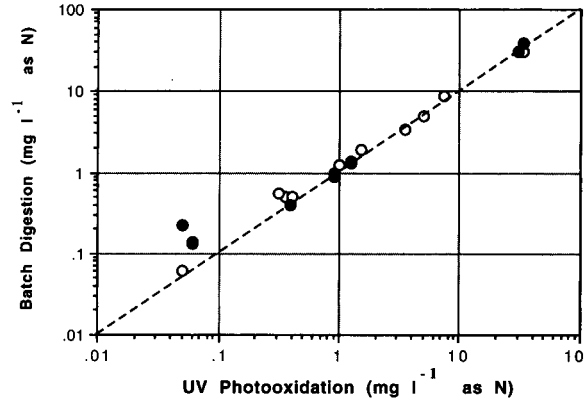

Fig. 5. Comparison of flow-injection UV photooxidation TDN with batch alkaline peroxodisulphate (○) and Kjeldahl (●) digestion methods for water and waste waters.

The proposed flow-injection method has been shown to be a rapid, sensitive alternative to the Kjeldahl and alkaline peroxodisulfate batch digestions which are most frequently used. The reduction step involving the Cd column is potentially the most problematic, and other reduction techniques may need to be investigated if this method is to be implemented for long-term field or monitoring applications.

Acknowledgements

The authors are indebted to Tony Puclin and Paul Freeman for their helpful suggestions, and to BHP Research for financial support of this work.

References

[1] L.L. Ciaccio, in S. Ahuja, E.M. Cohen, T.J. Kneip, J.L. Lambert and G. Zweig (Eds.), Chemical Analysis of the Environment, Vol. 5, Plenum Press, New York, 1973, p. 384.
[2] F.A.J. Armstrong, P.N. Williams and J.D.H. Strickland, Nature, 211 (1966) 481.
[3] L. Gustaffson, Talanta, 31 (1984) 979.
[4] L. Solórzano and J.H. Sharp, Limnol. Oceanogr., 25 (1980) 751.
[5] T.W. Walsh, Mar. Chem., 26 (1989) 295.
[6] T. Aoki, S. Uemera and M. Munemori, Bunseki Kagaku, 35 (1986) 32.
[7] I.D. McKelvie, B.T. Hart, T.J. Cardwell and R.W. Cattrall, Analyst, 114 (1989) 1459.
[8] R.T. Edwards, I.D. McKelvie, P. Ferrett, B.T. Hart, J.B. Bapat and K. Koshy, Anal. Chim. Acta, 261 (1992) 287.
[9] S. Hinkamp and G. Schwedt, Z. Wasser-Abwasser-Forsch., 24 (1990) 60.
[10] APHA, Standard Methods for the Examination of Water and Wastewater, American Public Health Association, Washington, DC, 1989.
[11] B. Karlberg and G.E. Pacey, Flow Injection Analysis – A Practical Guide, Elsevier, Amsterdam, 1989, p. 372.
[12] L. Andersson, Anal. Chim. Acta., 110 (1979) 123.
[13] M. Giné, H. Bergamin F°, E.A.G. Zagatto and B.F. Reis, Anal. Chim. Acta., 114 (1980) 191.
[14] K.S. Johnson and R.L. Petty, Limnol. Oceanogr., 28 (1983) 1260.
[15] J.C. Miller and J.N. Miller, Statistics for Analytical Chemistry, Ellis Horwood, Chichester, 1988, p. 227.
[16] I.M. Kolthoff and I.K. Miller, J. Am. Chem. Soc., 73 (1951) 3055.
[17] F. Nydahl, Talanta, 23 (1976) 349.
[18] J. Ruzicka and E.H. Hansen, Flow Injection Analysis, Wiley, New York, 1988, p. 498.
[19] J.F. Van Staden, Anal. Chim. Acta., 138 (1982) 403.
[20] D.A. Skoog and J.J. Leary, Principles of Instrumental Analysis, Saunders, New York, 1992, p. 700.

ELSEVIER

Analytica Chimica Acta 293 (1994) 163–170

ANALYTICA CHIMICA ACTA

Direct determination of ammonium in solid samples by automatic flow procedures

Zheng-liang Zhi [a], Angel Ríos, Miguel Valcárcel *

Department of Analytical Chemistry, University of Córdoba, E-14004 Córdoba, Spain

(Received 22nd September 1993; revised manuscript received 18th January 1994)

Abstract

Two new approaches to the determination of ammonium in solid samples using flow systems and photometric detection are presented. Both allow the direct determination of this analyte as gaseous ammonia, and simplify the treatment of the samples by reducing their manual manipulation. One of the manifolds used incorporates an absorbing solution held in a mini-chamber, whereas the other is based on a flow-through gas-diffusion probe. Both methods allow the ammonium to be determined at $\mu g\ g^{-1}$ level with relative standard deviations between $\pm 3\%$ and $\pm 5\%$. The performance of the two methods was tested by analysing both synthetic and real (soil) samples. Nitrogen availability and extractable ammonium nitrogen in soil were determined by using the proposed methodologies.

Key words: Flow injection; Flow system; Spectrophotometry; Ammonium; Solid samples

1. Introduction

Continuous-flow systems in general, and flow-injection analysis (FIA) in particular, are very useful methodologies for automating analyses of liquid samples. Thus, much attention has lately been paid to the analysis of a wide variety of water samples, which can be performed with a high degree of automation and simplicity. These techniques also allow a number of specific analytical problems to be solved [1], particularly in relation to direct analyses of gaseous and solid samples. Several approaches to the analysis of gaseous samples have so far been developed: closed-loop systems with debubbling units [2], iterative flow-reversal methodology [3], and gas-diffusion through a suitable membrane [4], among others. Direct analyses of heterogeneous or solid samples by use of automatic systems cause special difficulties. This is why only a few applications have so far been reported. Bergamin F° et al. developed direct FIA determinations for aluminium [5] and molybdenum [6] in steels by carrying out a brief electrolysis in a sample cylinder functioning as the anode and in contact with an acid stream which partially dissolved the electrode, thus providing a dissolved sample plug that was subsequently analyzed. Ultrasonic irradiation has also been applied to the direct determination of iron in plant materials and available boron in

* Corresponding author.

[a] Permanent address: China Pharmaceutical University, Nanjing, 210009, China.

SSDI 0003-2670(94) 00074-V

soils [7]. Recently, McLeod developed a micro-distillation unit as a module for coupling to continuous-flow analyzers, where ammonium and nitrate nitrogen can be determined in a variety of digest extracts [8] and soils [9].

In this work, simple flow procedures were used to determine ammonium nitrogen in solid samples as ammonia gas, which was retained in an absorbing mini-chamber or permeated through a porous membrane accommodated in a probe. An acceptor stream flowing through the probe was employed to collect the ammonia. Nessler's reagent was used for the photometric detection of the analyte. These approaches provide a simpler methodology than existing alternatives.

2. Experimental

2.1. Apparatus

A Hewlett-Packard 8452A diode array detector interfaced to a Vectra ES/12 computer and furnished with a HP Think-Jet printer was used.

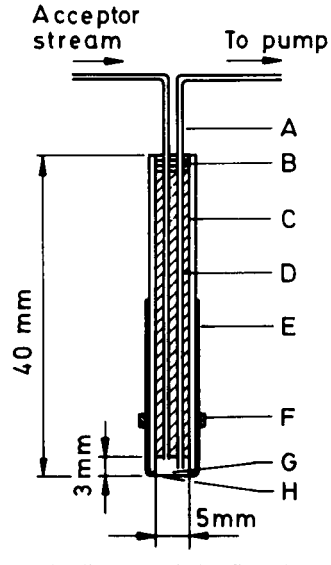

Fig. 1. Schematic diagram of the flow-through gas-diffusion probe: (A) 0.5 mm i.d. PTFE tubing; (B) adhesive sealant; (C) 5 mm i.d. glass tubing; (D) PTFE support; (E) Parafilm; (F) O-ring; (G) internal acceptor solution; and (H) microporous hydrophobic PTFE membrane.

A Gilson Minipuls-3 peristaltic pump, a Hellma 178.12 QS flow-cell (inner volume 18 μl; path length 10 mm), Tecator L100-1 and Rheodyne 5301 three-way injection valves were also used.

A laboratory-made flow-through gas-diffusion probe was built, which scheme is shown in Fig. 1. It consisted of a glass tube (40 mm $\times$ 5 mm i.d.), two PTFE tubings (0.5 mm i.d.) and a PTFE support, along which the tubes reached the internal mini-chamber (ca. 60 μl), sealed with a PTFE hydrophobic membrane from Millipore (Fluoropore) through an O-ring, and sealed tightly with Parafilm in order to avoid any leakage. Membranes of pore size 0.45 μm and 1.0 μm were also employed.

2.2. Reagents

All reagents were of analytical grade and distilled water was used throughout.

Nessler's reagent. To 4.0 g of potassium iodide in 40 ml of distilled water is added slowly 4% mercury(II) chloride solution, with gentle stirring until the appearance of a red precipitate. Then, 100 ml of 10 M sodium hydroxide solution are added and the solution is diluted to 500 ml with distilled water. Finally, a small amount of mercury(II) chloride is added until permanent turbidity is observed. The solution is allowed to stand overnight, then decanted and stored in topaz coloured bottles.

Ammonium standard solution. A stock solution containing 1000 μg ml^{-1} of ammonium nitrogen was prepared from ammonium chloride (Merck) and diluted as required to prepare samples of known concentrations.

Aqueous solutions of sodium hydroxide (10 M) and 2% (w/v) of both potassium permanganate and boric acid were also used.

2.3. Manifolds and procedures

Two different manifolds were designed and tested for determining ammonium directly in aqueous suspensions of the solid soil samples (Fig. 2).

Manifold using an absorbing vessel (Fig. 2a)

The solid sample was weighed in a mini-container (10 ml) that was subsequently incorporated into the flow system after adding 4.0 ml of 2.5 M NaOH in order to remove ammonium as NH_3 gas. The process was favoured by heating the vessel in a thermostatic water bath at 100°C and continuously stirring the suspension inside the vessel with a magnetic stirrer. This sample vessel was connected to another one containing 1.5 ml of 2% boric acid that absorbed the gas through a 0.5 mm i.d. PTFE tube. A peristaltic pump was used to aspirate air bubbles into the sample solution in order to facilitate the release of ammonia, and a switching valve was used in order to assemble an open–closed flow system in which the sample and absorbing vessels were included as shown in Fig. 2a. This open–closed system was kept in its closed position as long as required to boast the NH_3 release. Then, the switching valve was turned and the boric acid solution in the absorbing vessel was aspirated to fill the loop of the injection valve located in a simple flow system, where ammonium was determined with Nessler's reagent [10]. At this moment, both the mini-container and the boric acid absorber vessel were replaced by new ones containing the following sample and a fresh solution of boric acid, respectively (a set of two mini-containers and two absorber vessels was used).

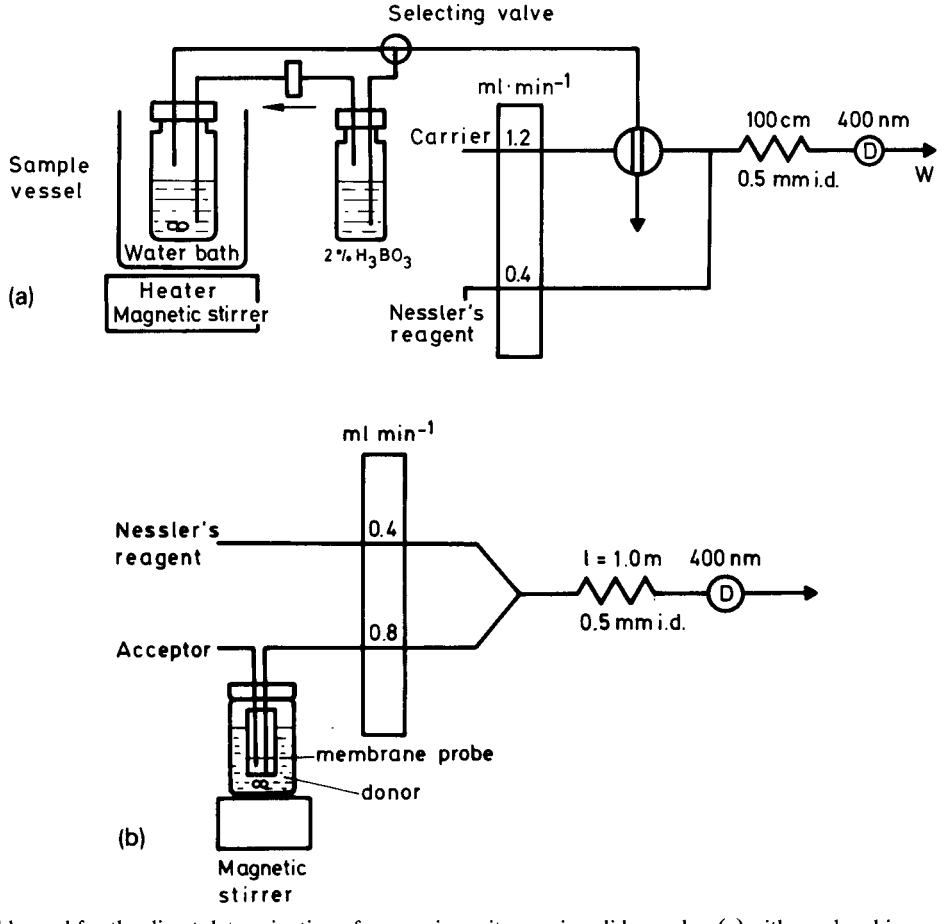

Fig. 2. Manifolds used for the direct determination of ammonium nitrogen in solid samples: (a) with an absorbing solution held in a mini-chamber; and (b) with a flow-through gas-diffusion probe. For details, see text.

Manifold using a flow-through gas-diffusion probe (Fig. 2b)

The probe used is depicted in Fig. 1; it functioned as a pseudo-injection valve. The mini-chamber of the probe was filled with acceptor solution and this probe was immersed in the donor solution (NaOH) containing the sample in a screw-capped vessel (10 ml) with the inlet and the outlet. This solution (or suspension) was continuously stirred. At the beginning, the acceptor solution was continuously pumped through the probe chamber at a constant flow-rate for 2 min in order to obtain a stable base-line from the photometric detector after mixing with the Nessler's reagent stream. Then, the flow was stopped over the interval needed to collect a sufficient amount of ammonia from the donor solution. Finally, the flow was resumed and the acceptor plug merged with the reagent to obtain the coloured product, which was monitored at 400 nm.

3. Results and discussion

Preliminary assays revealed that Nessler's reagent provided more reproducible results for ammonium than did coloured acid–base indicators and required less critical control of experimental conditions. The reaction was monitored photometrically at 400 nm. The results obtained by using each manifold described under Experimental are discussed below.

3.1. Manifold using an absorbing solution

The manifold is depicted in Fig. 2a. The sensitivity to ammonium was mainly determined by the efficiency of ammonia gas release from the sample and its absorption by the acceptor solution. The influence of the duration of the absorption step, NaOH and boric acid concentrations, and volume of this last solution used were obtained from peak height data. Fig. 3 shows graphically the effect of these variables. Thus, a 2.5 M NaOH solution was adequate to ensure maximum release of NH_3 from the sample, but the process was very slow (Fig. 3a) and the signal increased

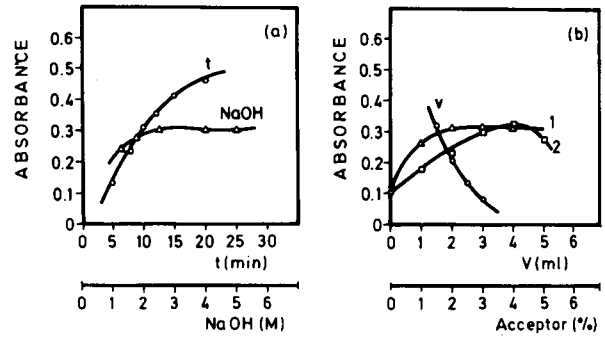

Fig. 3. (a) Influences of the NaOH concentration (releasing time 10 min) and time needed to perform the analysis (1.7 M NaOH) on measured signal; (b) influence of the type (1 = boric acid; 2 = hydrochloric acid), volume and concentration of acceptor solution employed (b) with the manifold using an absorbing solution in a mini-chamber.

with time (10 min was chosen as a compromise between sensitivity and sampling frequency). Boric and hydrochloric acid were tested as acceptor solutions (Fig. 3b). The former was chosen because a lower concentration was needed to obtain the same signal (2%, w/v). Moreover, the sensitivity increased dramatically on reducing the volume of the acceptor solution because of the preconcentration effect and the high signal enhacement observed by increasing the ammonium concentration (sensitivity of the method). Thus, a final volume of 1.5 ml boric acid was adopted. The temperature plays a major role in the release of NH_3, so the sample-donor vessel was thermostated by means of a water bath. The higher the temperature, the more efficient the NH_3 release. Thus, for example, an absorbance increase of ca. 130% was observed for 10 μg ml^{-1} of ammonium nitrogen when 100 ± 1°C was used instead of 90 ± 1°C. Obviously, the sensitivity could be improved by using a larger amount of sample.

FIA variables

FIA variables were optimized for the submanifold used for ammonium determination with Nessler's reagent. A sample loop volume of 180 μl and a reaction coil length of 100 cm provided optimum signals. The carrier solution was 2%

boric acid flowing at 1.2 ml min^{-1}, whereas Nessler's reagent was pumped at 0.4 ml min^{-1}.

Calibration graph

First, a calibration graph was run from liquid samples containing 0–10 μg ml^{-1} of ammonium nitrogen in order to check the reliability of the method. An aliquot of 2 ml standard solution and 2 ml 5 M NaOH were taken and mixed in the sample vessel to release ammonia. The linear determination range was 0.4–10.0 μg ml^{-1} (r = 0.9987, for $n = 6$), and conformed to the following equation:

$$A = 0.167[NH_4^+ - N] - 0.051$$

where A is the absorbance and the concentration of ammonium nitrogen ($NH_4^+ - N$) in the orignal standard solution is expressed in μg ml^{-1}. The relative standard deviation (R.S.D.) was 4.9% and 3.3% ($P = 0.05$; $n = 10$) for the determination of 1.0 and 3.0 μg ml^{-1} ammonium nitrogen, respectively. The sample frequency was 5 h^{-1} (more than one sample vessel was used in order to avoid dead time between samples), but can be increased by increasing the concentration of ammonium in the sample vessel. In that case a lower percentage of ammonia has to be transferred to generate a sufficiently large amount for detection. Thus, if the concentration of ammonium in the samples or the amount of sample taken is increased by a factor of 10, the sample throughput is raised to ca. 20 h^{-1}. Analogous results were obtained by using readily soluble solid samples (inorganic synthetic salts prepared from NH_4Cl, NH_4NO_3, and $(NH_4)_2SO_4$). The overall contents of $NH_4^+ - N$ added were 6.0 μg; other types of inorganic ions (potassium, sodium, calcium, magnesium, manganese and phosphate) were also added as common co-existing ions in soils. The results obtained for these synthetic samples are shown in Table 1. The recoveries were between 95 and 105%.

Application to soil samples

Soil samples were taken as models for real solid samples. Preliminary experiments showed that only inorganic ammonium and part of organic nitrogen in soil samples could be released slowly by using NaOH alone; also, the results obtained under the conditions described above were not comparable to those provided by the Kjeldahl distillation method. Consequently, an alkaline permanganate solution was used, which can release all ammonia instantaneously, and thus the nitrogen availability was determined in this case [11]. The influence of the $KMnO_4$ concentration added (in 2.5 M NaOH) was studied and a 2% (w/v) concentration was finally chosen in order to ensure almost complete transformation of organic nitrogen to inorganic ammonium in a reasonably short time. By using this procedure, a standard calibration graph showing no significant differences from the original one was obtained. In this case, about 0.03 g of air-dried soil sample was exactly weighed. The recovery of the proposed method was tested by applying the standard addition method to four different samples. The results obtained are given in Table 2, where – except for sample number 1 – the differences between the proposed method and the reference method are very small.

Table 1
Determination of ammonium nitrogen in synthetic samples by using the manifold depicted in Fig. 2a

Sample	Standards	Ammonium nitrogen ($n = 3$)		
		Added (μg)	Found (μg)	Recovery (%)
1	NH_4Cl	6.0	6.0 ± 0.1	100 ± 2
2	NH_4NO_3	6.0	6.0 ± 0.2	100 ± 3
3	$(NH_4)_2SO_4$	6.0	5.8 ± 0.2	97 ± 3
4	$NH_4NO_3 + (NH_4)_2SO_4$ (1 : 1)	6.0	5.9 ± 0.1	98 ± 2
5	$NH_4NO_3 + NH_4Cl$ (1 : 1)	6.0	6.3 ± 0.3	105 ± 5
6	$(NH_4)_2SO_4 + NH_4Cl$ (1 : 1)	6.0	5.9 ± 0.2	99 ± 3
7	$NH_4Cl + NH_4NO_3 + (NH_4)_2SO_4$ (1 : 1 : 1)	6.0	6.2 ± 0.2	103 ± 0.4

Synthetic matrix prepared from 200 μg Na^+, 200 μg K^+, 600 μg Ca^{2+}, 300 μg Mg^{2+}, 6 μg Mn^{2+} and 20 μg PO_4^{3-}.

3.2. Manifold using a flow-through gas-diffusion probe (Fig. 2b)

The flow system variables and the concentration of Nessler's reagent were optimized by directly pumping 0.5 and 1.0 μg ml^{-1} ammonium nitrogen solutions through the internal chamber of the probe. The effect of the Nessler's reagent concentration was studied by diluting the initial solution (see Experimental section) from 100 to 25% (v/v) and keeping a constant NaOH concentration of 2.5 M. A dilution of 55% provided maximal absorbance; more concentrated reagent solutions decreased the sensitivity through higher base-lines. An additional enhancement of the signal was observed by using a 3.0 M NaOH concentration.

Flow system variables

The effect of the overall flow-rate was tested from 0.6 to 2.5 ml min^{-1}, and a value of 1.2 was finally selected as a compromise between sensitivity and sample throughput. A reagent/carrier flow-rate ratio of 1:2 provided the best results. The length of the reaction coil had only a slight effect on the absorbance; a coil of 100 cm was long enough for reproducible results to be obtained with maximum sensitivity.

Sample treatment and ammonia collection

The effect of the NaOH concentration added to the sample vessel was studied over the range 0.1–5 M. Although above 0.1 M NaOH no enhancement of ammonium transfer can be expected because more than 99% is in the form of ammonia at that pH, a concentration of 0.32 M in the NaOH donor solution provided the maximal peak height. The permeation of ammonia from the donor solution to the acceptor (carrier) solution also depended on the composition of the acceptor solution. Several experiments showed that boric acid was the best choice; its concentration was optimized by using 0–5% aqueous solutions. A concentration of 2% (w/v) was finally selected. Using Nessler's reagent as direct acceptor stream was inadvisable as the membrane pores were clogged gradually by the precipitate deposited on the membrane inside the chamber.

Table 2
Determination of ammonium nitrogen availability in soil samples by using the absorbing mini-chamber method

Sample	Nitrogen availability [$NH_4^+ - N$] ($n = 3$)	
	Proposed method ($\mu g\ g^{-1}$)	Reference method [a] ($\mu g\ g^{-1}$)
1	768 ± 22	712 ± 8
2	308 ± 7	292 ± 7
3	302 ± 13	305 ± 5
4	184 ± 9	185 ± 3

[a] Distillation method [11].

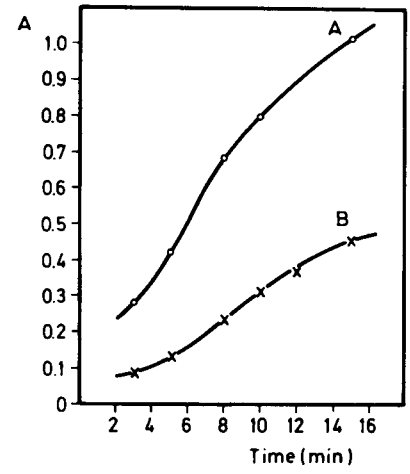

Fig. 4. Influence of the membrane pore size and stopped-flow time on the efficiency of ammonia permeation through the flow-through gas-diffusion probe. Membrane pore size: A = 1.0 μm, and B = 0.45 μm. An amount of 35 μg of ammonium was used in all cases.

Enhancement of ammonia permeation

The membrane pore size and the stopped-flow time of the acceptor solution were found to have a dramatic effect on the efficiency of ammonia permeation, as shown in Fig. 4. An increase in pore size from 0.45 to 1.0 μm resulted in an increase in sensitivity of ca. 2.6 times, so the larger pore size was chosen. The stopped-flow time could be selected according to the sensitivity required for each type of sample, while achieving the maximum possible sampling frequency. A time of 10 min was chosen for general purposes. Although heating and the use of ultrasonic energy

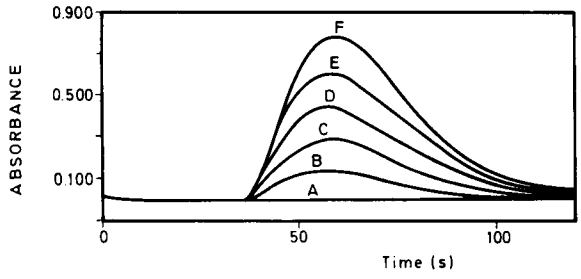

Fig. 5. Absorbance–time recordings obtained at different standard ammonium concentrations: (A) 0.32 M NaOH or 10 μg ml^{-1} NH_4^+ –N at pH 2; (B) 2.0; (C) 4.0; (D) 6.0; (E) 8.0; and (F) 10.0 μg ml^{-1} NH_4^+ –N.

have been recommended for increasing gas (CS_2) permeability across membranes in CS_2 determination in air by flow-injection with a membrane separation unit [12], it proved useless in this system because the membrane service life was shortened through early deterioration at temperatures above 45–50°C or under the action of ultrasonic waves.

Calibration graph

Synthetic samples of ammonium (prepared from ammonium sulphate salt) were used in order to test the performance of the method and construct a calibration curve. First, two different blanks were tested: a single 0.32 M NaOH solution, and a sample containing 10 μg ml^{-1} of ammonium nitrogen at pH 2. No differences between their signals and the base-line were observed, thus indicating the blank had a zero absorbance and no dialysis of NH_4^+. Fig. 5 illustrates these phenomena and the responses obtained for different amounts of ammonium in the samples. The absorbance (A)–ammonium nitrogen concentration (in μg ml^{-1}, in orignal standard solution) relation obtained was:

$$A = 0.0836[NH_4^+ - N] - 0.053$$

$$(r = 0.9992, \quad \text{for } n = 6)$$

for a determination range from 0.5 to 10 μg ml^{-1}; the R.S.D. was 4.3% for 3.0 μg ml^{-1} ammonium nitrogen ($n = 10$). The base-line to base-line time was ca. 60 s under the above conditions, but the resulting overall sampling frequency was ca. 5 h^{-1} (including sampling time used) because the expeditiousness of the process was determined by the duration of the ammonia permeation step.

Several synthetic samples prepared from ammonium chloride, nitrate and sulphate, whether mixed or pure, containing different inorganic ions (sodium, potassium, calcium, magnesium, manganese and phosphate) were analysed by using the proposed methodology. The results obtained are listed in Table 3. As can be seen, the recoveries were quite favourable in all cases.

Application to soil samples

The proposed method was used for the direct determination of extractable ammonium in soil extracts without pretreatment. In each case, 0.5 g of air-dried powdered sample was weighed out precisely into the 10-ml sample vessel, and 7.0 ml of 0.32 M NaOH were added, the mixture being allowed to release ammonia gas. The standard addition method was used for calibration. Table 4

Table 3
Determination of ammonium nitrogen in synthetic samples by using the manifold depicted in Fig. 2b

Sample	Standards	Ammonium nitrogen ($n = 3$)		
		Added (μg)	Found (μg)	Recovery (%)
1	NH_4Cl	10.5	10.5 ± 0.5	100 ± 5
2	NH_4NO_3	10.5	10.3 ± 0.2	98 ± 2
3	$(NH_4)_2SO_4$	10.5	10.9 ± 0.4	104 ± 4
4	$NH_4NO_3 + (NH_4)_2SO_4$ (1:1)	10.5	10.1 ± 0.6	96 ± 6
5	$NH_4NO_3 + NH_4Cl$ (1:1)	10.5	10.7 ± 0.2	102 ± 2
6	$(NH_4)_2SO_4 + NH_4Cl$ (1:1)	10.5	10.7 ± 0.3	102 ± 3
7	$NH_4Cl + NH_4NO_3 + (NH_4)_2SO_4$ (1:1:1)	10.5	10.8 ± 0.3	103 ± 3

Synthetic matrix prepared as described in Table 1.

Table 4
Determination of ammonium in soil samples by using the gas-diffusion probe method

Sample	Ammonium nitrogen ($n = 3$)	
	Proposed method ($\mu g\ g^{-1}$)	Reference method [a] ($\mu g\ g^{-1}$)
1	10.8±0.4	11.0±0.4
2	9.2±0.4	9.1±0.3
3	4.0±0.4	4.2±0.3
4	12.0±0.5	13.4±0.5

[a] Exchanged ammonium extracted with 2 M KCl.

shows the results obtained for four different soil samples. When the analysis was finished, the probe was carefully rinsed with distilled water. Normally, this membrane probe can be used continuously for at least two days with no loss of reproducibility or sensitivity.

4. Conclusions

Two simple automatic methods were developed for the direct determination of nitrogen availability and extractable ammonium respectively, in solid samples with no manual treatment. After the sample is weighed, it is introduced into the flow system and ammonium is released as ammonia gas, which is subsequently determined photometrically. Both methods allow the partial automation of preliminary operations of the analytical process, which are rarely dealt with systematically in unsegmented continuous-flow systems. These steps are crucial because they are tedious, time-consuming and the source of major errors affecting the final results. Therefore, the automation of these operations is one of the chief current goals of analytical chemistry. The proposed approaches presented are among the few reported so far for the direct analysis of solid samples, and can be expanded to other analytes, even if no gas is released when the probe approach is used, because depending on the nature of the membrane used, transfer of the analyte from the sample to the acceptor solution should take place by gas diffusion or dialysis. No significant differences in the analytical results provided by each of the proposed methods were observed; however, the method using the gas-diffusion probe is simpler and seemingly provides more accurate results.

References

[1] M. Valcárcel and M.D. Luque de Castro, Fresenius' J. Anal. Chem., 337 (1990) 662.
[2] S.M. Ramasamy and H.A. Mottola, Anal. Chem., 54 (1982) 283.
[3] F. Cañete, A. Ríos, M.D. Luque de Castro and M. Valcárcel, Anal. Chim. Acta, 224 (1989) 127.
[4] W. Frenzel, Fresenius' J. Anal. Chem., 342 (1992) 817.
[5] H. Bergamin F.°, F.J. Krug, E.A.G. Zagatto, E.C. Arruda and C.A. Coutinho, Anal. Chim. Acta, 190 (1986) 177.
[6] H. Bergamin F.°, F.J. Krug, B.F. Reis, J.A. Nobrega, M. Mesquita and I.G. Souza, Anal. Chim. Acta, 214 (1988) 397.
[7] F. Lázaro, M.D. Luque de Castro and M. Valcárcel, Anal. Chim. Acta, 242 (1991) 283.
[8] S. McLeod, Anal. Chim. Acta, 266 (1992) 107.
[9] S. McLeod, Anal. Chim. Acta, 266 (1992) 113.
[10] F. Cañete, A. Ríos, M.D. Luque de Castro and M. Valcárcel, Analyst, 113 (1988) 739.
[11] S.E. Allen, H.M. Grimshaw, J.A. Parkinson and Ch. Quarmby, Chemical Analysis of Ecological Materials, Blackwell, Oxford, 1974, p. 205.
[12] I.C. van Nugteren-Osinga, M. Bos and W.E. van der Linden, Anal. Chim. Acta, 226 (1989) 171.

ELSEVIER

Analytica Chimica Acta 293 (1994) 171–181

ANALYTICA CHIMICA ACTA

Determination of lead by flow-injection inductively coupled plasma mass spectrometry comparing several calibration techniques

Jan Goossens, Luc Moens, Richard Dams *

Laboratory of Analytical Chemistry, Institute for Nuclear Sciences, Ghent University, Proeftuinstraat 86, B-9000 Ghent, Belgium

(Received 26th November 1993; revised manuscript received 17th January 1994)

Abstract

In this paper we have evaluated the coupling of a modular flow-injection system to an inductively coupled plasma mass spectrometer for lead determinations by direct analysis of wines and urine samples. The flow-injection system used allows an on-line sample dilution and an on-line addition of internal standard and calibrant solution. It was found that particular attention should be paid to the adjustment of the nebulizer gas flow rate in order to obtain maximum sensitivity and precision. In this way and for the experimental set-up described, R.S.D. values $\leqslant 1\%$ on the $^{208}Pb^{+}$ signal for 5 consecutive injections could readily be achieved. The relative merits of external calibration, standard additions and isotope dilution for the calibration of the transient lead signals were compared. It appeared that from the viewpoint of accuracy, precision and flexibility, the standard additions method is the most preferable procedure. Further, it was found that the precision of isotope ratio determinations is degraded in comparison to continuous nebulization. However, matrix-induced mass fractionation on the lead isotope ratios as observed for the continuous nebulization of an aqueous ethanolic (wine) matrix did not occur in flow-injection analysis. The quantitation of lead by direct analysis of undiluted wine and urine samples using this flow-injection method in combination with standard additions calibration resulted in very accurate results (compared to certified and reference values). Excellent relative standard deviations (for 5 consecutive determinations) were obtained ranging from 1% (50 $\mu g\ l^{-1}$ Pb in white wine) to 5% (3.6 $\mu g\ l^{-1}$ Pb in urine).

Key words: Flow injection; Inductively coupled plasma MS; Lead; Urine; Wine

1. Introduction

From a recent review by Evans and Giglio [1], covering a decennium of problems with and solutions to interferences in inductively coupled plasma mass spectrometry (ICP-MS), one can immediately asses the susceptibility of the technique to so-called non-spectral interferences, also referred to as matrix effects. Unlike spectral interferences, caused by the limited resolution of the quadrupole mass analyzer, matrix effects are associated with factors influencing sample transport, ionization in the plasma, ion extraction and

* Corresponding author.

SSDI 0003-2670(94)00089-5

ion throughput in the resultant ion beam. The combination of these effects results in an ion signal enhancement or suppression, the relative extent of which (generally) is identical for isotopes of the same element and often fairly similar for elements with a comparable mass number [2–4]. The nature and concentration of the sample matrix has a direct bearing on the severity of the matrix effects. Many problems are related to the analysis of solutions containing high amounts of dissolved solids and organic solvents.

Albeit somewhat arbitrarily, matrix effects can be subdivided in reversible and irreversible contributions. Reversible matrix effects only occur while the sample is being measured and will disappear when it is replaced by a diluted standard or a rinsing solution. Irreversible matrix effects are clogging of the nebulizer and sampling orifices, carbon deposition on the torch and even a salt build-up in the ion lens stack. These can only be obliterated by interrupting the analytical procedure. However, both categories share a common cause and can, at least partially, be avoided by lowering the amount of sample to which the nebulizer, plasma and sampling devices are exposed. The scope for alternative sample introduction systems therefore being obvious, considerable effort has been made to couple hydride generation [5–9], electrothermal vaporization [10–14], chromatographic systems [15–17] and flow injection [18–28] directly to the ICP-MS system.

In this paper, flow injection (FI) is described as a powerful tool for the direct analysis of wine and urine which can be considered as an aqueous organic solution and a high salt content solution respectively. The FI system allowed an on-line sample dilution and on-line internal standardization. On-line isotope dilution, on-line standard additions and external calibration were compared for their accuracy, precision and flexibility. Furthermore the importance of careful nebulizer gas flow rate adjustment, particularly in wine analysis, is illustrated. Results could be compared to certified values and concentrations, previously determined in the same matrices in this laboratory using continuous nebulization (CN) after appropriate sample dilution.

2. Experimental

2.1. ICP-MS instrumentation

The instrument used was a VG PlasmaQuad ICP mass spectrometer (VG Elemental, Winsford, UK) equipped with a Fassel torch, a Meinhard-type Tr-30-A3 concentric glass nebulizer and a double-pass Scott-type spray chamber with surrounding liquid jacket, the temperature of which was controlled at 10°C with a recirculating refrigeration-heating system. The interface from the standard configuration was replaced by a "high performance interface" supplied by VG Elemental. From a diversity of experiments carried out at this laboratory, the main features of this new type of interface seem to be an increased sensitivity (5×10^7 cps per ppm (mg l^{-1}) for $^{115}In^+$ can be achieved) and a decreased ion signal dependence on some of the ion lens settings. However, an increased susceptibility to matrix effects was also observed and the optimization of some instrumental parameters (such as the torch position and the argon gas flow rates) turned out to be very critical. The operating conditions and main acquisition parameters (see also the section: acquisition parameters adjustment) are summarized in Table 1.

2.2. FI instrumentation

The flow-injection instrument used was a modular system purchased from EVA (the EVA product line is a joint development of FIAtron Systems, Oconomowoc, WI and Eppendorf-Netheler-Hinz, Hamburg). It consists of 4 modules (injector, selector, pump and manifold), 3 of which can control or be controlled by other units or a host computer. The injector module is responsible for the sample injection and contains an 8-port rotary injector valve. The peristaltic pump module enables the use of 4 channels, pumped at an identical rotation speed. The manifold module is a reaction unit, basically consisting of 2 T-junctions and a mixing coil from which the degassing unit was removed.

A scheme of the experimental flow-injection set-up is presented in Fig. 1. Three different

streams, pumped at equal flow rates (0.6 l min^{-1}), are merged using two consecutive T-junctions and are homogenized in a 500 μl mixing coil before they are provided to the injector valve. When the selector valve is set at position A, sample, internal standard (50 $\mu g\ l^{-1}$) and a secondary carrier (0.14 mol l^{-1} HNO_3) are mixed. At selector valve position B the secondary carrier is replaced by an identical flow of calibrant solution. The primary carrier solution (0.14 mol l^{-1} HNO_3) is pumped at 1.5 ml min^{-1} and streams to the nebulizer via the injector valve when this is set at loading position. Meanwhile, the sample mixture flushes the sample loop (70 μl) and is transported to a waste container. On a regularly basis the injector valve is set at the injection position so that a sample loop volume of mixture in inserted into the carrier stream and transported to the nebulizer.

2.3. Reagents and samples

A Pb standard solution (1 g l^{-1}) was prepared by dissolving an appropriate amount of $Pb(NO_3)_2$ (UCB, Brussels) in 0.14 mol l^{-1} HNO_3. Pb metal (NIST SRM-981) was dissolved in 1.4 mol l^{-1} HNO_3 to prepare a Pb standard solution with certified natural isotopic composition. A spike solution for isotope dilution was obtained by dissolving isotopically enriched (^{206}Pb: 92.15%) Pb metal (NIST SRM-983) in 1.4 mol l^{-1} HNO_3. A commercial Tl standard solution (Johnson-Mat-

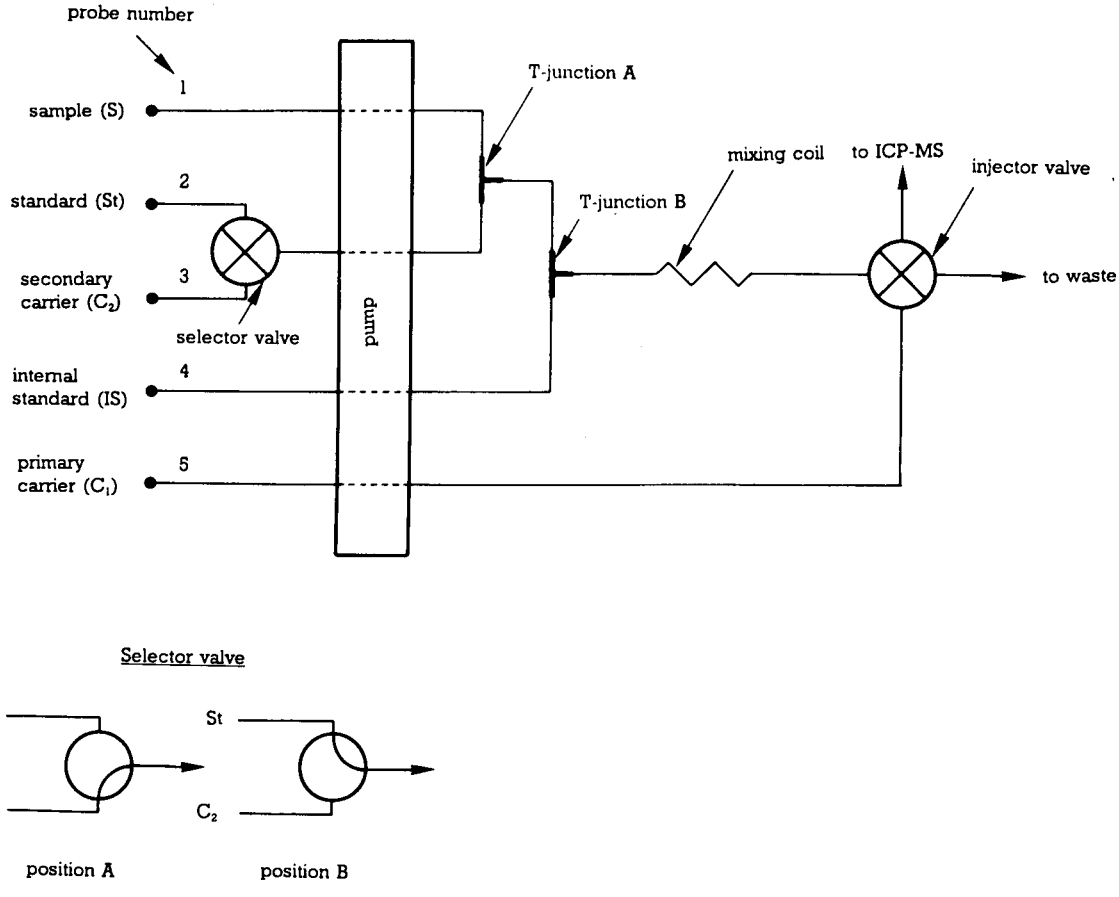

Fig. 1. Schematic representation of the modular flow-injection system used. All flows are pumped at 0.6 ml min^{-1} except the primary carrier, pumped at 1.5 ml min^{-1}.

Table 1
VG PlasmaQuad operating conditions and acquisition parameters

Operating conditions	
Plasma	
R.f. power	Forward: 1350 W
	Reflected: 0 W
Gas flow rates	Plasma: 13.0 l min^{-1}
	Nebulizer: variable
	Auxiliary: 0.85 l min^{-1}
Ion sampling	
Skimmer cone	Nickel, 1.0-mm orifice
Sampling cone	Nickel, 0.75-mm orifice
Vacuum	
Expansion stage	2.0 mbar
Intermediate stage	1.0×10^{-4} mbar
Analyzer stage	2.3×10^{-6} mbar
Acquisition parameters	
Mass range	200–210 u
Number of channels	512
Dwell time	160 μs
Number of sweeps	500
Total acquisition time	35 s [a]

[a] The actual acquistion time may differ to a small extent from the acquistion time as set in the VG PlasmaQuad software.

they, Royston, UK) was used to prepare an internal standard solution. All dilutions were carried out with 0.14 mol l^{-1} HNO_3 using glass pipettes and glass volumetric flasks. Immediately after preparation, all solutions were transferred to polyethylene recipients for storage. Nitric acid (14 mol l^{-1}, purified by sub-boiling distillation of reagent grade acid from quartz apparatus), absolute ethanol (Merck, Darmstadt) and Millipore (Milford, MA) milli-Q water were used.

Three wine samples (white, rosé and red) that have been analyzed in a previous study [29] had been poured from the bottle into polyethylene recipients and were stored at 4°C. No further sample pretreatment was carried out.

Two freeze-dried human urine reference materials (NIST SRM 2670 Low Level and Elevated Level Toxic Metals in Human Urine) were reconstituted with 20 ml of water. Additionally, for methodical development, first void (morning) urine was sampled from the author, cooled down to room temperature and analyzed immediately without any further pretreatment.

Reference values for the lead content of wines and urine samples were obtained by continuous nebulization of 10-fold diluted samples and performing external calibration (wine samples) [29] or standard additions (urine samples).

2.4. Parameter adjustment and calibration control

Acquisition parameter adjustment

Due to the dispersion of the sample plug into the carrier stream the analyte signal obtained from the FI–ICP-MS has a Gaussian transient nature, typically of 10 s duration at peak half-height for the experimental set-up described. As the FI system allowed the timing of injection and sample volumes to be accurately controlled, data could readily be acquired by ICP-MS in the multi-element scanning mode. In particular when relatively small mass regions are selected the number of scans in this mode is sufficiently high to accurately integrate the peak area of the relatively broad-shaped time-resolved profiles. A measuring time that is only slightly higher than the transient signal duration will yield a maximum signal-to-noise ratio while allowing minor fluctuations on the sample transport rate and on the synchronization between the FI instrument and the ICP-MS. The duration of the transient signal was therefore graphically determined from plots obtained in the single ion monitoring mode and the total measurement time was set at 120% of this value, approximately 35 s. As the injections from the FI system were synchronized with the measurements by the ICP-MS instrument, a certain delay time before the actual data acquisition had to be selected covering the period in which the analyte plug is transported from the FI injection valve to the plasma. The optimum value for this parameter (defined in the VG PlasmaQuad software as sample uptake time) was determined by gradually increasing it (at a fixed measuring time) until the transient signal is well covered by the measuring time window of 35 s. During this study the delay time was set at 5 s. Because a deterioration of the pump tubing can exert an influence on the injection characteristics, both time parameters were checked daily. However, re-adjustment never was necessary. The 200–210 u mass range was scanned entirely thus

covering the analyte isotopes (^{204}Pb, ^{206}Pb, ^{207}Pb and ^{208}Pb), both isotopes of the internal standard (^{203}Tl and ^{205}Tl) and the ^{202}Hg isotope used for mathematical isobaric overlap correction of ^{204}Hg on ^{204}Pb. The dwell time per channel was set at 160 μs. During 1 measurement approximately 500 scans were performed.

Nebulizer gas flow rate adjustment

For each sample type, the nebulizer gas flow rate was optimized. Therefore it was gradually increased in 0.02 l min^{-1} steps and at each setting the $^{205}Tl^+$ signal intensity of the internal standard was determined by consecutive flow injections of the sample. As will be demonstrated further, the optimum nebulizer gas flow rate can vary as a function of the sample matrix under consideration and the sample introduction system (FI or CN) applied. This is particularly important for the analysis of aqueous ethanolic mixtures.

Optimization of the ion lens stack

Next, for each sample type, the ion lens potentials were adjusted for maximum $^{205}Tl^+$ signal intensity at the optimum nebulizer gas flow rate by continuous nebulization of a 50 $\mu g\ l^{-1}$ Tl standard solution.

Calibration control procedure

Whatever the type of calibration used, its accuracy is dependent on the merging process in T-junction A (cf. Fig 1). The sample and the calibrant (or the replacing carrier) solution are pumped at equal flow rates and the mixture leaving T-junction A and flowing to T-junction B has to contain exactly the same amounts of both. The merging process of this mixture with the internal standard in T-junction B is less critical and does not affect the accuracy when it is performed in a reproducible way, i.e., the relative amounts of sample + calibrant vs. internal standard should be constant, but not necessarily equal. The accuracy and reproducibility of the mixing processes was checked daily by the analysis of a lead standard solution using single standard addition. In practice, the standard solution probe (2) and the sample solution probe (1) were put in the same lead standard solution (100 $\mu g\ l^{-1}$) and 3 consecutive injections at selector valve position A and 3 injections at selector valve position B were performed. For both positions (A and B resp.) the mean ($n = 3$) $^{208}Pb^+/^{205}Tl^+$ signal ratios were determined. The ratio of the first to the second signal ratio has to equal 0.5 within the experimental uncertainty. Both objectives were commonly achieved if excessive deterioration of the pump tubing was avoided by regular replacement.

2.5. Measurement and calibration procedures

For each sample analyzed, 3 independent calibration procedures were performed. Determination of the lead isotopic composition was carried out for the wine samples only.

Standard additions

At selector valve position A, 5 consecutive injections of a blank solution and 5 consecutive injections of a sample solution [both mixed with equal amounts of internal standard solution (IS) and secondary carrier solution (C_2)] were performed by putting probe 1 in water and undiluted sample solution respectively. Next, the selector valve was set at position B and again 5 consecutive injections of sample (mixed with equal amounts of internal standard and a 100 $\mu g\ l^{-1}$ lead standard solution) were performed.

Stable isotope dilution

An identical procedure as described for the standard additions method is carried out, replacing however the lead standard solution by an ^{206}Pb enriched lead spike solution of an appropriate concentration. The $^{208}Pb^+/^{206}Pb^+$ signal ratio was experimentally determined in the sample solutions and the sample mixed with spike solution. Blank correction was carried out by subtracting the normalized blank signals from the corresponding normalized $^{206}Pb^+$ and $^{208}Pb^+$ signals obtained for the samples. The theoretical (certified) $^{208}Pb/^{206}Pb$ isotope ratio for the spike solution was used in the subsequent calculations, hence neglecting mass discrimination effects for this ratio. This, however, does not significantly affect the accuracy of the results. The optimum concentration of spike to be added was calculated for every sample using a computer program developed in-house and based on a statistical analy-

sis by van Heuzen et al. [35]. Then for each sample the standard solution, the concentration of which matched best the calculated optimum value, was selected from a series of standards ranging from 1 to 500 $\mu g\ l^{-1}$ Pb.

External calibration

At selector valve position A, 5 consecutive injections of a blanc solution and 5 consecutive injections of a sample solution [both mixed with equal amounts of internal standard solution (IS) and secondary carrier (C_2)] are performed by putting probe 1 in water and undiluted sample solution respectively. Next, the sample solution again is replaced by a blank solution (water) and the selector valve is set at position B. The blank solution (water), standard solution (100 $\mu g\ l^{-1}$ Pb) and internal standard solution are mixed and 5 injections are performed.

Determination of the lead isotopic composition

An identical procedure as described for the external calibration method is carried out, however increasing the number of injections to 10 for each mixture and replacing the lead standard solution for a 100 $\mu g\ l^{-1}$ lead solution with certified natural isotopic composition (SRM-981). The latter was used for the experimental determination of fractionation coefficients as described elsewhere [30–34]. A relatively small mathematical correction for the ^{204}Hg overlap on ^{204}Pb was systematically carried out for all determinations. Therefore, the net signal at m/z 202 ($^{202}Hg^+$) was multiplied by 0.229 (the $^{204}Hg/^{202}Hg$ natural abundance ratio) and then subtracted from the signal at m/z 204 ($^{204}Hg^+$ and $^{204}Pb^+$).

In practice, switching the calibrant solutions can be avoided by defining additional selector valve positions and extending the number of probes to the selector so that the use of each probe is restricted to a single calibrant solution (not shown in Fig. 1).

2.6. Fundamental experiments

Ion signal dependence on the nebulizer gas flow rate

Synthetic aqueous ethanolic mixtures of varying composition [0, 10, 20, 30, 40 en 50% (v/v) ethanol] were analyzed at approximately 14 different nebulizer gas flow rates (between 0.5 and 0.9 l min^{-1} or 0.6 and 1.0 l min^{-1}) using both CN and FI. For the FI analysis these experiments were carried out in the single ion monitoring mode as well as in the mass scanning mode. In this instance, CN was performed by switching the injector valve in such a way that the mixture leaving the mixing coil flows directly to the detector. Some of these experiments were repeated for real sample solutions however limiting CN as much as possible in order to avoid irreversible matrix effects.

Mass fractionation effects

Mass fractionation for the Pb isotopes and its dependence on the sample matrix was studied. This is of particular importance for the determination of the isotopic composition of lead in wine and for the use of isotope dilution in general. Therefore synthetic samples, containing 0, 2.5 and 10% ethanol and wines were repeatedly analyzed by FI at the optimum measurement conditions using the mass scanning mode.

3. Results and discussion

3.1. Fundamental studies

Ion signal dependence on the nebulizer gas flow rate

In a number of experiments, the $^{205}Tl^+$ signal was monitored as a function of the nebulizer gas flow rate, the sample matrix and the sample introduction system used. Thallium, rather than Pb was monitored since it was more convenient to control the Tl concentration in different solutions. The main objective of this study was to evaluate the merits of nebulizer gas flow rate optimization for FI analysis using CN which is preferable for practical reasons. In Fig. 2, plots of the Tl^+ signal intensity as a function of the nebulizer gas flow rate are presented for a reference matrix (0.14 mol l^{-1} HNO_3) and a red wine matrix, introduced in the ICP-MS by 2 different techniques (FI and CN). It appears that the optimum nebulizer gas flow rate obtained for CN of a

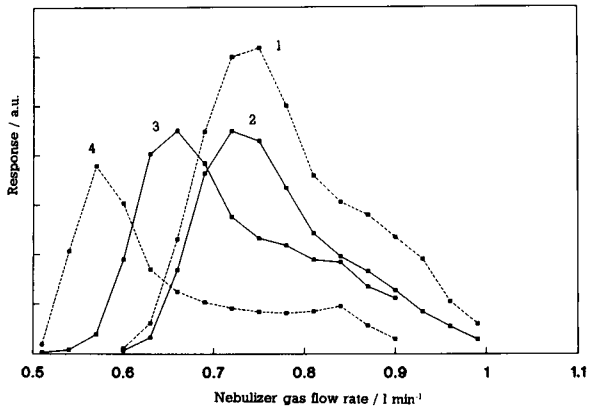

Fig. 2. Dependence of the $^{205}Tl^+$ signal intensity of the nebulizer gas flow rate for 2 different matrices and 2 different sample introduction techniques: (1) CN of 0.14 mol l^{-1} HNO_3, (2) FI of 0.14 mol l^{-1} HNO_3, (3) FI of red wine, (4) CN of red wine. For ease of survey, the signal intensities obtained by CN are normalized to the sensitivity by FI.

0.14 mol l^{-1} HNO_3 matrix approximately coincides with that for FI of the same matrix whereas a considerable shift is observed for FI of the wine matrix. The shift of the optimum nebulizer gas flow rate to lower values is caused by the ethanol present in the wine sample. This has also been observed for other elements and other organic solvents using CN [29,36–38] and was recently explained by Vanhaecke et al. [38] as being caused by a shift of the zone of maximum M^+ density in the plasma. Further, the shift for FI analysis of wine is smaller compared to CN probably due to the lower ethanol content of the sample nebulized into the plasma caused by ethanol dispersion into the carrier. The dependence of the optimum nebulizer gas flow rate (for FI analysis) on the matrix composition of the sample is presented in Fig. 3 showing that the optimum nebulizer gas flow rate almost linearly decreases with increasing ethanol content of aqueous ethanolic mixtures.

Similar experiments were carried out for the urine matrix but it was observed that the optimum nebulizer gas for FI analysis of urine did not differ significantly from the one obtained by CN of the same urine matrix or even a 0.14 mol l^{-1} HNO_3 reference matrix. As a consequence, in this instance, the nebulizer gas flow rate can be optimized by continuous aspiration of an appropriate standard solution.

Mass fractionation effects

Ketterer et al. [39] have reported that the measurement of Pb isotope ratios can be significantly affected by both instrumental and sample induced sources of bias. It was observed that substantial changes in mass discrimination could be brought about by the presence of concomitant elements such as Na, Rb, Cs and U. In this work, this phenomenon was not further examined for the urine matrix but experiments were carried out by FI in order to investigate the influence of an aqueous ethanolic matrix on the determination of Pb and Tl isotope ratios. In contrast to the results obtained by similar experiments using CN [40], no significant or systematic changes were observed in the determined Pb and Tl isotope ratios by FI analysis of 0.14 mol l^{-1} HNO_3, 2.5% or 10% (v/v) ethanol, indicating that only instrumental bias occurs. This can, at least partially, be attributed to the dilution of the sample matrix (merging processes and dispersion) before it is provided to the ICP-MS although former experiments showed a significant mass fractionation on lead isotope ratios for CN analysis of an equally diluted ethanolic aqueous solution. As a result, the mass fractionation occurring in the FI analysis of the wine samples could be calculated from

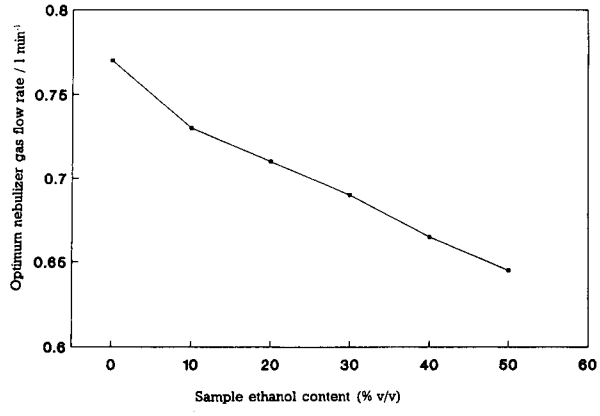

Fig. 3. Optimum nebulizer gas flow rate for FI analysis as a function of the ethanol content (%, v/v) of the synthetic aqueous ethanolic matrix analyzed.

Table 2
Analysis of wines by FI–ICP-MS using on-line standard additions, on-line isotope dilution and external calibration

	Standard additions	Isotope dilution	External calibration	Reference method [29]
White wine	49.46 (0.63)	50.31 (1.53)	48.38 (0.41)	49.61 (0.32)
Rosé wine	43.45 (0.85)	45.39 (1.47)	41.89 (1.14)	43.92 (0.63)
Red wine	50.52 (0.77)	51.06 (0.62)	49.10 (0.50)	50.72 (0.18)

Concentrations are in $\mu g\ l^{-1}$. Uncertainties are expressed as standard deviations on 5 injections, except for the reference method (CN–ICP-MS) where the uncertainty is expressed as the standard deviation on 3 replicates, each measured 5 times.

the analysis of a SRM-981 lead standard solution in a 0.14 mol l^{-1} HNO_3 matrix. Additionally, as Tl was mixed to all solutions as an internal standard, the $^{205}Tl^+/^{203}Tl^+$ ratio was continuously monitored as a check for the absence of matrix-induced bias.

3.2. Analysis of wines

Three different wine samples (white, rosé and red), the content of which was determined in a previous study [29] were now analyzed by FI–ICP-MS. Since the nebulizer gas flow rate was optimized by FI analysis of the wine matrix itself, a 30–50% signal enhancement of the $^{205}Tl^+$ internal standard signal on switching the blank solution for the wine sample was not unexpected. The reproducibility of the absolute $^{208}Pb^+$ signals (i.e., before normalization to $^{205}Tl^+$) was excellent and typical R.S.D. values for 5 consecutive injections were $\leqslant 1\%$. In Table 2, the results obtained using 3 different calibration methods and an ICP-MS reference method of proven accuracy [29] are summarized. Statistical analysis (t-test, 95% confidence level) indicated that the results obtained by each of the calibration methods do not differ significantly from the reference value. Moreover, the good agreement between the external calibration results and those by the other calibration techniques indicates that the matrix-induced Pb^+ signal enhancement is well compensated for by normalization to the $^{205}Tl^+$ signal. This was previously also observed for continuous nebulization analysis and seems to be related to the similar behaviour of the Tl^+ and Pb^+ signals as a function of the nebulizer gas flow rate for the aqueous ethanolic matrix under consideration [29]. The average R.S.D. values obtained by standard additions (1.6%) and external calibration (1.5%) are slightly better than those by isotope dilution (2.5%). The reason for this is the better precision on the determination of the $^{208}Pb^+/^{205}Tl^+$ signal ratios for the standard addition and external calibration calibrant solutions (typically 0.7% for 5 consecutive injections) compared to the $^{208}Pb^+/^{206}Pb^+$ measurements of the sample + spike mixture in isotope dilution (typically 1.4%). The latter is probably to be attributed to differences in concentration between the respective calibrant solutions and hence in the ion counting statistics.

The determination of lead isotope ratios in samples of biological [32], clinical [30,33] geological [31,34,41] and environmental [30,39,42] origin

Table 3
Isotope ratios (corrected for mass fractionation) and calculated Pb abundances for 3 different European wine samples

Wine	Lead isotope ratios			Lead abund.			
	204 : 208 (R.S.D., %)	206 : 208 (R.S.D., %)	207 : 208 (R.S.D., %)	Θ(204)	Θ(206)	Θ(207)	Θ(208)
White	0.02446 (6.3)	0.4725 (1.5)	0.4056 (1.2)	0.01313	0.2499	0.2149	0.5221
Rosé	0.02524 (5.2)	0.4694 (1.7)	0.4040 (1.9)	0.01358	0.2488	0.2145	0.5232
Red	0.02507 (5.3)	0.4737 (1.4)	0.4043 (1.7)	0.01345	0.2505	0.2141	0.5219

R.S.D. values are calcultated from 10 injections

received considerable attention. Dean et al. [43] found that European wines could be distinguished from Australian wines grown in regions where the endogenous lead isotopic composition is significantly different from that in Europe. The results on the isotopic characterization of lead in the 3 (European) wine samples analyzed by FI–ICP-MS are summarized in Table 3. Typical R.S.D. values (10 consecutive injections) on the $^{207}Pb/^{208}Pb$ and $^{206}Pb/^{208}Pb$ ratios vary from 1 to 2% while worse precision is obtained for the $^{204}Pb/^{208}Pb$ ratio (5 to 7%), presumable entirely due to poor counting statistics on the ^{204}Pb isotope. For unclear reasons, considerable better precision was obtained for the $^{205}Tl^+/^{203}Tl^+$ signal ratio (generally $< 1\%$, often down to 0.5%) at a comparable concentration level. There were no significant differences in the abundances of the respective Pb isotopes between the wine samples and the Pb standard solution used as a calibrant for standard additions and external calibration.

3.3. Analysis of urine samples

Four different urine samples, two of which were standard reference materials, were analyzed and the results are summarized in Table 4. It can be seen that the mean values obtained by external calibration are systematically lower than those obtained by the standard additions (significant at the 95% confidence level for all 4 samples) and isotope dilution method (significant at the 95% confidence level for 3 samples out of 4) which are in good agreement with the reference values. It appears that whereas Tl corrects well for the Pb^+ signal enhancement caused by the wine matrix, it only partially compensates for the Pb^+ signal suppression induced by the urine matrix. The suppression of the absolute Tl^+ signals is approximately 35%. The reproducibility of the absolute $^{208}Pb^+$ signals depended on the lead content of the urine samples and the R.S.D. values obtained varied from 1.8% (107 $\mu g\ l^{-1}$) to 7.1% (3.6 $\mu g\ l^{-1}$) for 5 consecutive injections. Generally the RSDs on the results by standard additions are comparable to or, at low lead contents, considerably better than those obtained by isotope dilution. Again this appears to be caused by a better precision on the determination of the $^{208}Pb^+/^{205}Tl^+$ signal ratios (standard additions) compared to the determination of $^{208}Pb^+/^{206}Pb^+$ (isotope dilution). Additionally, at very low contents, the blank has a considerable contribution to the total Pb^+ signal which has to be taken into account twice for isotope dilution ($^{208}Pb^+$ and $^{206}Pb^+$) but only once ($^{208}Pb^+$) for standard additions calibration.

3.4. Comparison of external calibration, standard additions and isotope dilution

Referring to the applications discussed and the experimental set-up described, it appears that the relative advantages and drawbacks of the 3 calibration techniques for FI–ICP-MS are similar to

Table 4
Analysis of urine samples by FI–ICP-MS using on-line standard additions, on-line isotope dilution and external calibration

	Standard additions	Isotope dilution	External calibration	Reference value
SRM-2670 (elevated level)	107.1 (2.2)	107.9 (2.4)	101.8 (1.0)	109 ± 3 [a] 109.9 ± 0.3 [b]
SRM-2670 (low level)	7.74 (0.36)	7.96 (0.41)	6.93 (0.31)	10 [c] 8.25 ± 0.12 [b]
Urine sample A	3.61 (0.18)	3.58 (0.46)	3.14 (0.22)	–
Urine sample B	4.44 (0.08)	4.05 (0.36)	2.95 (0.12)	–

[a] Certified value.
[b] Mean value of 2 replicates determined by CN–ICP-MS.
[c] Indicative value. Concentrations are in $\mu g\ l^{-1}$. Uncertainties are expressed as standard deviations on 5 injections except the reference values which are expressed as 95% confidence intervals.

those for CN–ICP-MS. The accuracy of external calibration (in combination with the on-line addition of Tl as an internal standard) for lead determinations by FI–ICP-MS depends on the matrix under consideration and, at any rate, should be carefully checked. The method however is advantageous (compared to standard additions calibration) for the analysis of large amounts of samples as all sample signals can be calibrated using a single analysis of a standard solution. The number of analyses is also limited for isotope dilution if it is assumed that the isotopic composition of lead in the samples analyzed does not differ significantly from the theoretical value so that unspiked samples do not have to be analyzed. Additionally, isotope dilution appears to guarantee accurate results both for wine and urine analysis. However, the precision is considerably worse compared to the standard additions method, in particular for low lead contents. Further, isotope dilution has a poor flexibility since the relative amount of spike added is very critical and therefore a preliminary semi-quantitative analysis is necessary. The use of FI partially eliminates this drawback as it is possible to perform a number of injections of sample solution without the addition of spike from which the lead content immediately can be estimated so that a spike solution of appropriate concentration can be selected. However, the fact remains that several spike solutions have to be prepared in a concentration range covering the sample lead contents expected. Additionally, experience shows that particular care has to be taken to avoid contamination when preparing spike solutions of low lead content [27].

From the analysis of wines and urine samples, the standard additions method was proved to be the preferable method from the viewpoint of accuracy and precision. Further, all lead contents can be determined using a single standard solution, thus offering maximum flexibility. On the other hand, the number of injections is double compared to external calibration or isotope dilution (the latter on the conditions mentioned above). This is disadvantageous when large amounts of samples are to be analyzed. However, in some instances only one sample to which standard was added on-line probably can serve as a calibrant for a series of samples with comparable matrix composition.

4. Conclusions

The coupling of a flow-injection system to an ICP-mass spectrometer enables the direct analysis of wines and urine samples. After careful optimization of the acquisition parameters and operating conditions, in particular the nebulizer gas flow rate, R.S.D. $\leqslant 1\%$ on 5 consecutive injections can readily be achieved. The precision of lead isotope ratio determinations in wine samples however is degraded compared to continuous nebulization but when using flow-injection no matrix-induced mass fractionation has been observed. The use of the standard additions method for calibration of the Pb^+ signals seems to be the most preferable method from the viewpoint of accuracy, precision and flexibility.

References

[1] E.H. Evans and J.J. Giglio, J. Anal. At. Spectrom., 8 (1993) 1.
[2] W. Dohorty, Spectrochim. Acta, 44B (1989) 263.
[3] J.J. Thompson and R.S. Houk, Appl. Spectrosc., 41 (1987) 81.
[4] F. Vanhaecke, H. Vanhoe, R. Dams and C. Vandecasteele, 39 (1992) 737.
[5] H. Jin, Y. Shibata and M. Morita, Anal. Chem., 63 (1991) 986.
[6] D.T. Heitkemper and J.A. Caruso, Appl. Spectrosc., 44 (1990) 228.
[7] X. Wang, M. Viczian, A. Lasztity and R.M. Barnes, J. Anal. At. Spectrom., 3 (1988) 821.
[8] M. Janghorbani and B.T.G. Ting, Anal. Chem., 61 (1989) 701.
[9] C. Haraldsson, M. Pollak and P. Öhman, J. Anal. At. Spectrom., 7 (1992) 1183.
[10] N. Shibata, N. Fudagawa and M. Kubota, Anal. Chem., 63 (1991) 636.
[11] J.M. Carey, E.H. Evans, J.A. Caruso and W.-L. Shen, Spectrochim. Acta, 46B (1991) 1711.
[12] N. Shibata, M. Fudagawa and M. Kubota, Anal. Chim. Acta, 265 (1992) 93.
[13] E.H. Baily, A.J. Kemp and K.V. Rognarsdottir, J. Anal. At. Spectrom., 8 (1993) 551.
[14] P.G. Wittaker, T. Lind, J.G. Williams and A.L. Gray, Anal. Chem., 114 (1989) 675.

[15] D. Beauchemin and S.S. Berman, Anal. Chem., 61 (1989) 1857.
[16] M.R. Plantz, J.S. Fritz, F.G. Smith and R.S. Houk, Anal. Chem., 61 (1989) 149.
[17] M.E. Ketterer, Anal. Chem., 62 (1990) 2522.
[18] H. Mukai, Y. Ambe and M. Morita, J. Anal. At. Spectrom., 5 (1990) 75.
[19] S.J. Hill, J. Hartly and L. Ebdon, J. Anal. At. Spectrom., 7 (1992) 895.
[20] Y. Israel, A. Lasztity and R.M. Barnes, Analyst, 114 (1989) 1259.
[21] J. Wang, W.-L. Shen, B.S. Sheppard, E.H. Evans, J.A. Caruso and F.L. Fricke, J. Anal. At. Spectrom., 5 (1990) 445.
[22] G.H. Vickers, B.S. Ross and G.M. Hieftje, Appl. Spectrosc., 43 (1989) 1330.
[23] J.R. Dean, L. Ebdon, H.M. Crews and R.C. Massey, J. Anal. At. Spectrom., 3 (1988) 349.
[24] D. Beauchemin, K.W.M. Sui and S.S. Berman, Anal. Chem., 60 (1988) 2587.
[25] J. Wang, E.H. Evans and J. Caruso, J. Anal. At. Spectrom., 6 (1991) 605.
[26] Z. Peng, H. Klinkenberg, T. Beeren and W. Van Borm, Spectrochim. Acta, 46B (1991) 1051.
[27] M. Viczian, A. Lasztity, X. Wang and R.M. Barnes, J. Anal. At. Spectrom., 5 (1990) 125.
[28] R.C, Hutton and A.N. Eaton, J. Anal. At. Spectrom., 3 (1988) 547.
[29] J. Goossens, T. De Smaele, L. Moens and R. Dams, Fresenius' J. Anal. Chem., 347 (1993) 119.
[30] M.J. Campbell and H.T. Delves, J. Anal. At. Spectrom., 4 (1989) 235.
[31] A.R. Date and Y.Y. Cheung, Analyst, 112 (1987) 1531.
[32] J.R. Dean, L. Ebdon and R. Massey, J. Anal. At. Spectrom., 3 (1987) 343.
[33] H.T. Delves and M.J. Campbell, J. Anal. At. Spectrom., 3 (1988) 343.
[34] T.A. Hinners, E.M. Heitmar, T.M. Spittler and J.M. Henshaw, Anal. Chem., 59 (1987) 2658.
[35] A.A. van Heuzen, T. Hoekstra and B. van Wingerden, J. Anal. At. Spectrom., 4 (1989) 483.
[36] H.P. Longerich, J. Anal. At. Spectrom., 4 (1989) 665.
[37] J. Goossens, F. Vanhaecke, L. Moens and R. Dams, Anal. Chim. Acta, 280 (1993) 137.
[38] F. Vanhaecke, R. Dams and C. Vandecasteele, J. Anal. At. Spectrom., 8 (1993) 433.
[39] M.E. Ketterer, M.J. Peters and P.J. Tisdale, J. Anal. At. Spectrom., 6 (1991) 439.
[40] J. Goossens, unpublished results.
[41] M.E. Ketterer, J. Anal. At. Spectrom., 7 (1992) 1125.
[42] A. Miyazaki and R.A. Rumer, J. Anal. At. Spectrom., 8 (1993) 449.
[43] J.R. Dean, L. Ebdon and R.C. Massey, Food Addit. Contam., 7 (1990) 109.

ELSEVIER

Analytica Chimica Acta 293 (1994) 183–189

ANALYTICA CHIMICA ACTA

Data analysis in the chemical laboratory Part 1. Analysis of indirect measurements

Milan Meloun [a,*], Jiří Militký [b]

[a] Department of Analytical Chemistry, University of Chemical Technology, 532 10 Pardubice, Czech Republic
[b] Department of Textile Materials, Technical University, 461 17 Liberec, Czech Republic

(Received 30th March 1993; revised manuscript received 10th November 1993)

Abstract

Response quantities of analytical chemistry investigations of, for instance, concentration or content of substances, viscosity, stability constants or solubility, can be obtained as a non-linear transformation of directly measured quantities or signals. The goal of the indirect measurements analysis is estimation of basic statistical parameters of analytical results from the known non-linear transformation and from the statistical parameters of measured variables. The analysis is based on Taylor series expansion, two-point approximation and Monte Carlo simulation. An algorithm may be applied on any chemical, physical, biological or medical result.

Key words: Error propagation; Indirect measurements; Monte Carlo simulation; Taylor series expansion; Two-points approximation

1. Introduction

A result of a chemical analysis y is often calculated as the known functional transformation $y = G(x_1, \ldots, x_m)$ from a number of directly measured experimental quantities $x_1, \ldots x_m$. Due to various kinds of errors the measured quantities x_i, $i = 1, \ldots, m$, are random variables. Using a basic statistical treatment of measured data the sample means $\bar{x}_i$ and sample variances $s^2(x_i)$, $i = 1, \ldots, m$, are computed. To project these errors into the resultant y is a topic treated in many analytical chemistry texts and is known as error propagation. The well-known formula for the random errors propagation

$$s^2(y) \simeq \left(\frac{dG(x_i)}{dx_i} \right)^2 s^2(x_i) \qquad (1)$$

is based on a number of assumptions: (a) the random variables x_i are uncorrelated; and (b) if y is not a linear function of x_i, then each $s(x_i)$ must be sufficiently small relative to the corresponding mean values of x_i so that the function $G(x_1, \ldots, x_m)$ can be reasonably linearized. If one or more of these assumptions is invalid, Eq. 1 can be suitably corrected but only when making use of a computer. A more difficult problem occurs when the function G(**x**) is differentiable

* Corresponding author.

SSDI 0003-2670(94)00086-2

with great difficulty only. This problem, however, can be solved by numerical methods.

This article compares the Taylor series expansion, the two-point approximation, and the Monte Carlo simulation for a calculation of the mean $\bar{y}$ and the variance $s^2(y)$ of a response quantity (i.e., an analyte concentration or an analyte content).

2. Theory

The treatment of the indirect measurements under consideration in this paper leads to the following problems:

(1) The estimation of the result of the chemical analysis, i.e., the mean value $\bar{y}$.

(2) The estimation of the total error expressed as a standard deviation of chemical analysis, $s(y)$, from known errors of several measured quantities, $s(x_i)$.

(3) The inverse estimation of limiting errors of measured quantities, $s(x_i)$, from the allowed error of the chemical analysis, $s(y)$.

To express the absolute error of the ith variable x_i, the standard deviation $s(x_i)$ is convenient; for the relative error of x_i the relative standard deviation (or the coefficient of variation) is used

$$\delta(x_i) = s(x_i)/x_i \tag{2}$$

For the first problem, if the experiment and computation of $G(\cdot)$ could be done repeatedly to generate a reasonable statistical sample of y_i values, the information on the random uncertainty in y would be within reach. The computer offers a convenient way of simulating the repetition. It is only necessary to generate new sets of x_i data, and the estimates of mean $\bar{x}_i$, variance $s^2(x_i)$, skewness $g_{1,i}$ and kurtosis $g_{2,i}$ are used, cf. p. 101 in [1].

For the second problem the expression for variance $s^2(y)$ as a function of individual variances $s^2(x_i)$ is used. A simplification can often be achieved using the relative errors.

For the third problem the expression for variance $s^2(y)$ or variation coefficient $\delta(y) = s(y)/\bar{y}$ is used. The basic assumption is that individually measured quantities x_i have the same relative effects.

To solve all three problems the mean $\bar{y}$ and corresponding variance $s^2(y)$ of a function $y = G(x_1, \ldots, x_m)$ must be known. The estimates $\bar{y}$ and $s^2(y)$ may be obtained by any of the following methods: (1) Taylor series expansion of the function $y = G(x_1, \ldots, x_m)$; (2) two-points approximation; and (3) Monte Carlo simulation.

Whereas the method of Taylor series expansion requires knowledge of at least first and second derivatives of the function $G(x_1, \ldots, x_m)$, the remaining two methods can be computer-assisted.

2.1. Method of Taylor series expansion

When a function of random variables is analyzed it should be realized that each non-linear transformation of the random variable distorts its distribution, and therefore changes the dependence of variance on the mean value. In the case when the single measured variable x has a constant variance $s^2(x)$, the results of analysis $y = G(x)$ have a non-constant variance $s^2(y)$, Eq. 1. Moreover, in the multivariate case the sample mean $\bar{y}$ cannot be estimated by direct substitution of sample mean $\bar{x}$ into the function $G(\bar{x})$, i.e.,

$$\bar{y} \neq G(\bar{x}) \tag{3}$$

To estimate the mean $\bar{y}$, the variance $s^2(y)$ and higher statistical moments, the Taylor series expansion of function $G(x)$ can be used.

Suppose that the function $y = G(x_1, \ldots, x_m)$ is known. Let $G(\mathbf{x})$ be doubly differentiable at least. When writing the Taylor series expansion in the neighbourhood of the vector of means $\bar{\mathbf{x}} = (\bar{x}_1, \ldots, \bar{x}_m)^T$ we obtain

$$y \approx G(\bar{\mathbf{x}}) + \sum_{i=1}^{m} \frac{\delta G(\mathbf{x})}{\delta x_i}(x_i - \bar{x}_i) + \frac{1}{2}\sum_{i=1}^{m} \frac{\delta^2 G(\mathbf{x})}{\delta x_i^2}(x_i - \bar{x}_i)^2 + \sum_{i=1}^{m-1}\sum_{j=i+1}^{m} \frac{\delta^2 G(\mathbf{x})}{\delta x_i \delta x_j}(x_i - \bar{x}_i)(x_j - \bar{x}_j) + \ldots \tag{4}$$

where all first and second derivatives are calculated for the vector of mean values $\bar{\mathbf{x}}$. By using a mean value operator $E(\cdot)$ at both sides of Eq. 4 the expression for the estimate of mean $\bar{y}$ may be written as

$$\bar{y} \approx G(\bar{\mathbf{x}}) + \frac{1}{2}\sum_{i=1}^{m}\frac{\delta^2 G(\mathbf{x})}{\delta x_i^2}s^2(x_i) + \sum_{i=1}^{m-1}\sum_{j>i}^{m}\frac{\delta^2 G(\mathbf{x})}{\delta x_i \delta x_j}\mathrm{cov}(x_i, x_j) \quad (5)$$

where $\bar{y} = E(y) = E(G(\mathbf{x}))$, $s^2(x_i) = E[(x_i - \bar{x}_i)^2]$ and where $E[(x_i - \bar{x}_i)] = 0$. The symbol $\mathrm{cov}(x_i, x_j)$ stands for the covariance which gives a measure of "linear dependence" between the two variables x_i and x_j.

For computation of variance $s^2(y)$ the linearization based on Taylor expansion is obviously used. More precise is to apply approximation 4 with neglecting the higher moments. (i.e., the skewness and curtosis). The resulting approximate relation for variance is termed the rule of propagation of absolute errors and can be expressed by

$$s^2(y) \approx \sum_{i=1}^{m}\left[\frac{\delta G(\mathbf{x})}{\delta x_i}\right]^2 s^2(x_i) + 2\sum_{i=1}^{m-1}\sum_{j>i}^{m}\frac{\delta G(\mathbf{x})}{\delta x_i}\frac{\delta G(\mathbf{x})}{\delta x_j}\mathrm{cov}(x_i, x_j) + \sum_{i=1}^{m-1}\sum_{j>i}^{m}\frac{\delta^2 G(\mathbf{x})}{\delta x_i \delta x_j}s^2(x_i)s^2(x_j) \quad (6)$$

When the resulting error $s(y)$ is formed from m sources of additive errors, i.e., $G(x_1, \ldots, x_m) = \Sigma x_i$ is linear combination of x_i and each source has its own variance $\delta_i^2(x)$, the following expression for the estimate of error can be used

$$s^2(y) = \sum_{i=1}^{m}\delta^2(x_i) + 2\sum_{i=1}^{m-1}\sum_{j>i}^{m}\mathrm{cov}(x_i, x_j) \quad (7)$$

where $\mathrm{cov}(x_i, x_j)$ again is a measure of linear dependence between the two variables x_i and x_j. There are two limiting cases of estimation of total error of measurements, $s(y)$ from Eq. 7:

(1) The sources of errors are quite independent, so that the covariances $\mathrm{cov}(x_i, x_j)$ are equal to zero. The resulting estimate of an error will be proportional only to the quadratic mean of errors $\delta(x_i)$ coming from m sources,

$$s(y) = \sqrt{\sum_{i=1}^{m}\delta^2(x_i)} \quad (8)$$

(2) The sources of errors are linearly dependent. Then covariances $\mathrm{cov}(x_i, x_j)$ are given by

$$\mathrm{cov}(x_i, x_j) = \sqrt{s^2(x_i)s^2(x_j)}$$

The resulting estimate of the total error will be proportional to the arithmetic mean of errors $\delta(x_i)$ coming from m sources

$$s(y) = \sum_{i=1}^{m}\delta(x_i) \quad (9)$$

For various analytical operations and signal measurements in a chemical laboratory, the function $G(\mathbf{x})$ can be expressed by a power-type relationship

$$y = G(\mathbf{x}) = x_1^{a_1} \cdot x_2^{a_2} \cdot \cdots \cdot x_m^{a_m} = \prod_{i=1}^{m} x_i^{a_i} \quad (10)$$

where a_i are known coefficients usually equal to ∓ 1. The estimation of the absolute error $s(y)$ or $s^2(y)$ by Eq. 6 is then rather complicated. The logarithmic transformation leads to the simpler expression

$$\ln G(\mathbf{x}) = \sum_{i=1}^{m} a_i \cdot \ln x_i \quad (11)$$

Then

$$\frac{\mathrm{d}\ln G(\mathbf{x})}{\mathrm{d}x} = \frac{1}{G(\mathbf{x})}\frac{\mathrm{d}G(\mathbf{x})}{\mathrm{d}x} \quad (12)$$

Substitution of Eq. 12 to Eq. 6 and rearrangement leads to a simplified form for the relative error (variation coefficient)

$$\delta(y) \approx \sqrt{\sum_{i=1}^{m} a_i^2\delta^2(x_i) + 2\sum_{i=1}^{m-1}\sum_{j>i}^{m} a_i a_j r_{ij}\delta(x_i)\delta(x_j)} \quad (13)$$

where r_{ij} represents the correlation coefficient expressing the closeness of linear dependence between variables x_i and x_j. Eq. 13 is called the rule of propagation of relative errors. The quality of estimates $\bar{y}$, $s^2(y)$ and $\delta(y)$ is dependent on the quality of quadratic approximation of the function G(**x**).

Although the estimate $\bar{y}$ is normally sufficiently accurate, some inaccuracy may be found in the estimation $s^2(y)$ [2].

Eq. 13 may be used for estimation of relative errors $\delta(x_i)$ such that a relative error of chemical results $\delta(y)$ will not be greater than the selected value for H in %, i.e., $100 \cdot \delta(y) \leq H$. In solving this inversion problem, the independence of the measured variables x_i and the principle of the same relative influence

$$|a_1|\delta(x_1) \approx |a_2|\delta(x_2) \approx \ldots \approx |a_m|\delta(x_m) \approx H/m$$

are assumed. Here a_i, $i = 1, \ldots, m$, are coefficients of function G(**x**), Eq. 10. For the case of a ratio $G(x_1, x_2) = x_1/x_2$ an estimate of the mean $\bar{y}$ is controlled only by the variance $\delta^2(x_2)$ and not by the variance $\delta^2(x_1)$.

2.2. Method of two-points approximation

Manly's procedure [3] of two-point approximation is based on replacement of the probability distribution of function G(**x**) by the two-points distribution with the same mean and variance. For the case of single x the estimate of the mean is expressed as

$$\bar{y} \approx \{G[\bar{x} + s(x)] + G[\bar{x} - s(x)]\}/2 \quad (14)$$

and the estimate of variance by

$$s^2(y) \approx \{G[\bar{x} + s(x)] - G[\bar{x} - s(x)]\}^2/4 \quad (15)$$

Both simple relations give better results than Taylor's formula for a function of the type in (Eq. 10).

When the function G(**x**) is a function of m independent random variables $x_1, \ldots, x_m$, the summation of Eqs. 14 and 15 can be used

$$\bar{y} \approx \sum_{i=1}^{m} \{G[\bar{x}_i + s(x_i)] + G[\bar{x}_i - s(x_i)]\}/2m \quad (16)$$

and

$$s^2(y) \approx \sum_{i=1}^{m} \{G[\bar{x}_i + s(x_i)] - G[\bar{x}_i - s(x_i)]\}^2 /4m \quad (17)$$

2.3. Method of Monte Carlo simulation

The mean $\bar{y}$ and its variance $s^2(y)$ as a function G(**x**) of random variables x, may be determined by computer-assisted Monte Carlo simulation method. Schwartz [2] showed that this general procedure is well suited for simulation of statistical behaviour of even rather complicated systems. The following steps can be formulated:

(1) Selection of the function G(**x**): for many chemical problems the function G(**x**) is usually known. The great advantage of Monte Carlo simulation method is that the function G(**x**) need not necessarily be expressed in explicit form.

(2) Distribution of measured variables: in chemistry it is usually assumed that measured variables are independent and have normal distribution. Then the Monte Carlo simulation method requires numerical values of quantities $\bar{x}_i$, $s(x_i)$, $i = 1, \ldots, m$, only.

When these values are not available, two limiting values of interval [A,B] in which the variables x_i are expected should be supplied. The approximate probability density function can be then expressed by the parabolic distribution

$$f(x_i) = 6(x_i - A)(B - x_i)/(B - A)^2$$

for $A < x_i < B$. The situation is more complicated when some correlation among the input variables exists. Then the simultaneous distribution of all variables x_i, $i = 1, \ldots, m$, should be specified; this will be simple only for the case of the normal distribution.

(3) Generation of random numbers: most computer software contains a function that will generate pseudo-random numbers from rectangular distribution $R(0,1)$. For two independent random numbers R_j, R_{j+1} the Box–Müller transformation is used to generate two independent random

numbers N_j, N_{j+1}

$$N_j = \sqrt{(-2 \ln R_j)} \sin(2\pi R_{j+1}) \quad (18)$$

$$N_{j+1} = \sqrt{(-2 \ln R_j)} \cos(2\pi R_{j+1}) \quad (19)$$

which have standardized normal distribution. The jth simulated value of the ith variable x_i will be expressed by

$$x^*_{i,j} = N_j s(x_i) + \bar{x}_i \quad (20)$$

(4) The choice of the number of simulations: the rules for the determination of the necessary number of simulations are the same as for the determination of sample size. The minimum number of simulations for the requested $100(1-\alpha)\%$ confidence interval D of the mean is expressed by the relation

$$n_{\min} = \left[4u_{1-\alpha/2} s^2(y)\right]/D^2 + 1 \quad (21)$$

where $u_{1-\alpha/2}$ is the quantile of standardized normal distribution and $s^2(y)$ is the estimate of variance from the first 50 simulations.

(5) The display of results: this step includes a graph of an empirical probability density function of simulated data $\{y_j^*\}$, $j = 1, \ldots, n_{\min}$, and a calculation of the estimates of location and spread, $\bar{y}^*$ and $s^2(\bar{y}^*)$.

3. Computation

The program Propagation-of-Errors calculates the results of indirect measurements or the analytical quantity (concentration, content, etc.) $\bar{y}$ and the variance $s^2(y)$ as a result of several errors concerning various experimental and instrumental operations. In addition to the classical method of Taylor series expansion, two computer-assisted methods can be applied, i.e., the two-points estimation method and the Monte Carlo simulation method. The function G(**x**) is inserted in the one-row panel using the usual algebraic notations. The maximum number of directly measured variables $(m) = 10$. For these variables the value $\bar{x}_i$ and error $s(x_i)$ are required. For all methods the approximate mean $\bar{y}$, variance $s^2(y)$ and variation coefficient $\delta(y)$ are computed. For Taylor expansion all required derivatives are computed using difference formula. For Monte Carlo simulation the kernel probability density function is also creacted created. The probability density function of normal distribution $N[\bar{y}, s^2(y)]$ is calculated and drawn.

The program Propagation-of-Errors in the package CHEMSTAT is available from the authors up on request.

4. Results

The following samples illustrate the application of the computational Propagation-of-Errors technique.

4.1. Sample 1: error in arsenic content in isotope dilution

Arsenic was determined by the isotope dilution method. The initial specific activity was $a_2 = 3.7 \times 10^4$ s^{-1}. After addition of the standard $m_1 = 5 \times 10^{-7}$ g of arsenic, the specific activity was $a_1 = 5.3 \times 10^6$ s^{-1}. The relative error of the arsenic content in the sample should be estimated supposing that the relative error of weighing is $\delta(m) = 0.03\%$, and the relative error of the activity measurement $\delta(a_1) = \delta(a_2) = 1\%$. The content of arsenic, m_x, in the samples is calculated by

$$G(\cdot) = m_x = m_1(a_1 - a_2)/a_2$$

Because this expression is not in the form of Eq. 10, Eq. 13 cannot be used. Assuming that the quantities m_1, a_1 and a_2 are not correlated, results obtained by three methods of the Propagation-of-Errors program are identical (Table 1).

Table 1
Analysis of indirect measurements in isotope dilution

	Taylor series expansion	Two points estimation	Monte Carlo simulation
$\bar{y}$ (g)	7.1122×10^{-5}	7.1124×10^{-5}	7.1142×10^{-5}
$s(y)(\%)$	1.0130×10^{-6}	1.0132×10^{-6}	1.0433×10^{-6}
$\delta(y)(\%)$	1.42	1.42	1.47

4.2. Sample 2: error in indirect viscosity measurements

The viscosity of glycerol is calculated by the Stokes method from the following experimental data: the radius of the ball $r = 0.0112 \mp 0.0001$ cm; the density of the ball $d_0 = 1335$ kg m^{-3}, the density of glycerol $d = 1280$ kg m^{-3}, the trajectory $l_t = 31.23 \mp 0.05$ cm, the time $t = 62.1 \mp 0.2$ s, and the acceleration due to gravity $g = 9.801$ m s^{-1}. Viscosity, η, determined by the Stokes method is calculated from the expression

$$G(\cdot) = \eta = 2gr^2(d_0 - d)t/(9l_t)$$

Because this relation is not of the Eq. 10 type, the relative error cannot be calculated with the use of a simple relationship. Results obtained from three methods of the Propagation-of-Errors program are in good agreement (Table 2).

4.3. Sample 3: correlated errors in solution concentration

A mass (m) of 0.1 g zinc was dissolved in hydrochloric acid and diluted in a standard flask with a volume, V, of 1000 ml. A volume, V_1, of 100 ml of this solution was diluted to a volume, V_2, of 1000 ml. The sample for analysis was prepared by taking $V_3 = 5$ ml and diluting into $V_4 = 25$ ml. The concentration of the resulting sample and its relative error is calculated when the standard deviation of weighing, $s(m)$, is 0.3 mg and for the standard flasks $s(V) = s(V_2) = 0.2$ ml, $s(V_1) = 0.05$ ml, $s(V_3) = 0.005$ ml and $s(V_4) = 0.025$ ml. The concentration c is calculated from

$$G(\cdot) = c = mV_1V_3/(VV_2V_4)$$

Table 2
Analysis of indirect viscosity measurements

	Taylor series expansion	Two points estimation	Monte Carlo simulation
$\bar{y}$ (Pa s)	2.988×10^{-4}	2.988×10^{-4}	2.986×10^{-4}
$s(y)$ (Pa s)	5.443×10^{-6}	5.443×10^{-6}	5.304×10^{-6}
$\delta(y)$ (%)	1.82	1.82	1.78

Table 3
Analysis of indirect measurements in solution concentration

	Taylor series expansion	Two points estimation	Monte Carlo simulation
$\bar{y}$ (g dm^{-3})	2.00×10^{-3}	2.000×10^{-3}	2.000×10^{-3}
$s(y)$ (g dm^{-3})	6.732×10^{-6}	6.732×10^{-6}	6.853×10^{-6}
$\delta(y)$ (%)	0.34	0.34	0.34

Errors in volumes V_2 and V_4 are strongly correlated with errors of volumes V_1 and V_3.

The ideal case when correlation coefficients $r(V_1V_2) = r(V_3V_4) = 1$ is considered first, while other variables are uncorrelated. From Eq. 13 it is

$$\begin{aligned}\delta^2(c) \simeq {} & [s(m)/m]^2 + [s(V)/V]^2 \\ & + [s(V_1)/V_1]^2 + [s(V_2)/V_2]^2 \\ & + [s(V_3)/V_3]^2 + [s(V_4)/V_4]^2 \\ & - 2[s(V_1)/V_1][s(V_2)/V_2] \\ & - 2[s(V_3)/V_3][s(V_4)/V_4]\end{aligned}$$

and numerically $\delta(c) = 0.302\%$.

Then, consider that the correlations between V_1 and V_2,and between V_3 and V_4 are negligible, so that $r(V_1V_2) = r(V_3V_4) = 0$ and then $\delta(c) = 0.336\%$.

Eq. 5 allows the mean concentration $\bar{c}$ to be estimated

$$\begin{aligned}\bar{c} = {} & mV_1V_3/(VV_2V_4) + mV_1V_3[s^2(V)/(V^3V_2V_4) \\ & + s^2(V_2)/(V_2VV_4) + s^2(V_4)/(V_4VV_2)] \\ & - mV_3s(V_1)s(V_2)/(VV_2^2V_4) \\ & - mV_1s(V_3)s(V_4)/(VV_2V_4^2)\end{aligned}$$

where the first term is equal to 2×10^{-6} g cm^{-3}, the second 2.16×10^{-12} g cm^{-3} and the third is 2.2×10^{-12} g cm^{-3}. If the two smaller terms are neglected the mean concentration will be $\bar{c} = 2\times10^{-6}$ g cm^{-3} or 2×10^{-3} g dm^{-3}. Results obtained from the Propagation-of-Errors method for a case $r(V_1V_2) = r(V_3V_4) = 0$ are presented in Table 3. Correlation between volumes V_1 and V_3 and also between V_2 and V_4 diminishes the relative error of the resulting sample concentration.

5. Conclusion

The Propagation-of-Errors program in CHEMSTAT applies three different approaches to analysis of indirect measurements. All three methods calculate the mean $\bar{y}$, standard deviation $s(y)$ and variation coefficient $\delta(y)$ and lead practically to the same results. Application of the algorithm is simple, easy and quite convenient for analytical chemists but also physicists and biologists.

References

[1] M. Meloun, J. Militký and M. Forina, Chemometrics for Analytical Chemistry, Part 1, PC-Aided Statistical Data Analysis, Ellis Horwood, Chichester, 1992.
[2] L.M. Schwartz, Anal. Chem., 47 (1975) 963.
[3] B.F.J. Manly, Biomed. J., 28 (1986) 949.

ELSEVIER

Analytica Chimica Acta 293 (1994) 191–203

ANALYTICA CHIMICA ACTA

Numeric genetic algorithm
Part I. Theory, algorithm and simulated experiments

Peisheng Cong, Tonghua Li *

Department of Chemistry, Tongji University, Shanghai 200092, China

(Received 14th May 1993; revised manuscript received 16th December 1993)

Abstract

A numeric genetic algorithm (NGA) that optimizes value parameters, is described. The most attractive feature of NGA is that it is suitable for the optimization of a wide variety of problems in chemometrics, such as calibration, parameter estimation, non-linear model building and multi-dimensional data resolution. The representation of individuals and genetic operators such as crossover and mutation is designed to deal with value parameters. A new genetic operator, memory, is also developed to speed up and improve the evolution process. Two architectures of NGA are constructed and discussed in detail. One realizes bit operation of floating point and the other is numerical operation. The genetic parameters in NGA are also discussed in detail. These new algorithms are applied to find the global optima of some simulated mathematical functions and to optimize the parameters in a non-linear parameter estimation problem. The results show that for those mathematical functions NGA succeeds in converging to the global optima very fast and efficiently even when the optimization interval is enlarged and can always converge to the global optimum for these parameter estimation problems.

Key words: Optimization methods; Chemometrics; Genetic algorithm; Value parameters

1. Introduction

Genetic Algorithms were proposed by Holland [1] in the early 1960s for broad optimization problems. It is based on the simulation of natural genetics and evolutions. By encoding various complex structures with bit strings called chromosomes, Holland showed that these chromosomes could be rapidly improved in structure under some evolution rules like those for natural living beings. The application of GAs can be found in various fields [2]. GAs have been introduced into chemometrics in the past few years. Pioneering work was done by Lucasius and co-workers [3,4]. The optimum selection of the wavelength in multi-component analysis with GAs is a good example. Li et al. [5] proposed a new idea for modifying the GAs, which he named "the dynamic genetic algorithm" and applied to the optimization of a subset of the calibration data sets. Recently, GAs were introduced into the field of constitutional similarity [6].

In all of these applications, the information carried by chromosomes was selected from a large information table or discrete values of optimiza-

* Corresponding author.

SSDI 0003-2670(94)00079-2

tion. However, in chemometrics, a major problem may be considered to be the optimization of value parameters and it is difficult to handle them with the GAs mentioned above.

Although numerous optimization methods exist, each has its own limitations. Least-squares, non-linear least-squares and simplex methods are the most commonly used. Their limitation is that they may become useless for complex optimization problems when there is local optimum in the optimization interval. Simulated annealing (SA) is the most efficient optimization method so far in searching the global optima [7]. The weakness of SA is that the parameters cannot be easily controlled and usually SA could only converge to near the global optimum owing to its own intrinsic features.

Recently, a specialized genetic algorithm (SGA) was proposed for numerical optimization [8] and applied to optimize one-dimensional linear–quadratic models.

In this paper, a genetic algorithm which is also suitable for value parameter optimization, called the numeric genetic algorithm (NGA), is described and introduced into chemometrics. We use float point representation in NGA, which is similar to SGA. However, the implementations of genetic operators of NGA and SGA are different. Two architectures of NGA are constructed and discussed in detail. One realizes bit operation of floating point, which is not relevant in SGA, and is based on the principle of GAs. The other is numerical operation in which the way to determine the increment is different from that in SGA. In addition, a new genetic operator, memory, is developed to speed up and improve the evolution process.

2. Theory and algorithm

2.1. Genetic algorithms

Before discussing NGA, the principle of GAs is briefly described; interested readers can acquire more details in the literature mentioned above. The main idea of genetic algorithms is the survival of the fittest. At every moment during the genetic evolution process, GAs keep a population composed of a fixed number of individuals which fit the environment best. Each individual contains one chromosome, each chromosome being represented as a bit string with a fixed length. New individuals can be generated through genetic operations and are able to survive in the population only if they fit the environment better than the worst in the population. The worst dies and is left out of the population in order to keep the size of the population fixed. This loop continues and GAs will generate more and more competing individuals and make the population evolve and finally the solution of the problem is obtained.

GAs have two chief genetic operators, crossover and mutation. The individuals can generate their genes to the offspring by crossover, and the population can obtain new genes and new chromosomes by mutation. Usually the probability of crossover is high (say 80% of the total genetic operations) and the probability of mutation is low.

2.2. Numeric genetic algorithm

There are three issues that must be considered when a numeric genetic algorithm is constructed to optimize reals: (a) to carry out genetic operation on reals; (b) to search a more accurate global optimum; (c) to find the optimum quickly.

For the first issue, the representation and genetic operation of genetic algorithm will be redefined without losing the feature of parallel searching, and they are considered in detail in this section. For the second issue, it means that a near global optimum would not be satisfactory or, in other words, the refinement of a solution must be very efficient. This can be well done by controlling the parameters of NGA. For the last issue, usually it is difficult for genetic algorithms; however, for NGA it will be greatly improved by changing the data structures. We shall discuss this in the next paper in this series.

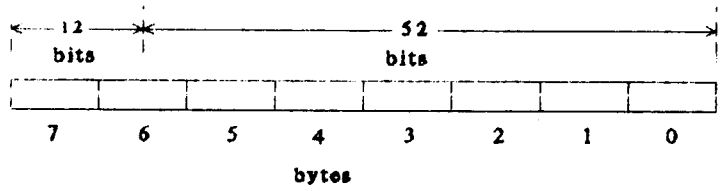

Fig. 1. Expression of a double (64 bits) in computer memory. The left part (12 bits) contains the exponent and the sign. The right part (52 bits) is the mantissa. The right-most byte is the zeroth byte.

Representation of individuals and chromosomes

NGA has a population with a fixed size like GAs. Each individual in a population is a solution of the optimization problem. However, as different parameters in a optimization problem may have different meanings or units and different amplitudes in most cases, it is unsuitable to put different parameters together in one chromosome. In NGA, each individual is defined to be a multi-chromosome individual, and each chromosome is a real number. Suppose there are n parameters to be optimized in a problem, then each individual is composed of n chromosomes. In computer programming, each individual is an array or vector whose elements are real numbers.

Genetic operators in NGA architecture I

For NGA architecture I, crossover and mutation are very similar to those of GAs. Suppose a float point (double precision) is expressed as a 64-bit (8 bytes, see Fig. 1) string in a microcomputer, then crossover and mutation operations directly handle the bits of the float point (interested readers should consult the Appendix to see how this is achieved by using C or Pascal).

Crossover. Crossover operator happens between the chromosomes at the same position in two different individuals in a population. It can be achieved as follows. First, randomly select two individuals as parents from the population and randomly decide which chromosomes are to be crossovered, then another random number between 0 and 7 (or 1 and 8) indicates which bytes in the selected chromosomes are to be exchanged. Fig. 2 shows a sketch of the crossover in architecture I. It is assumed that the second byte (in an individual) of the second chromosome is selected. In practice, more than one chromosome

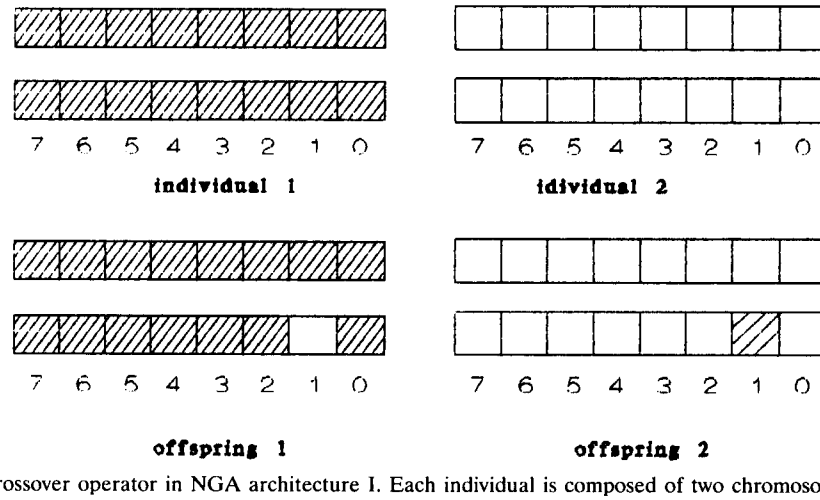

Fig. 2. Sketch of crossover operator in NGA architecture I. Each individual is composed of two chromosomes. The numbers 0–7 represent the bytes in a double number. Two offsprings are generated by exchanging the second byte in the second chromosome of the two selected individuals.

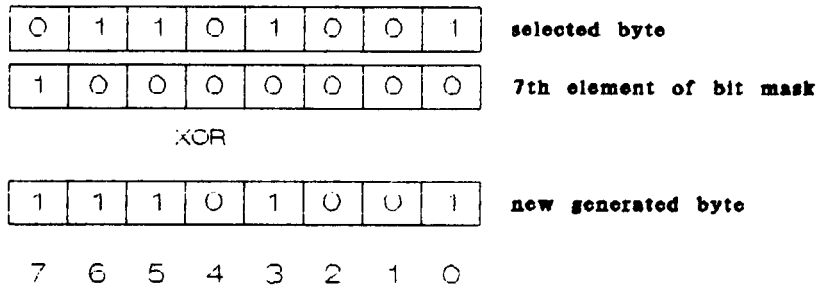

Fig. 3. Mutation operator through XOR logic. The numbers 0–7 represent the bits in a selected byte. The 7th bit is mutated from 0 to 1 by XOR with the 7th element of bit mask.

(or byte) can be selected in a single crossover operation.

Mutation. Mutation operation is achieved as follows. Randomly select an individual from a population and also select a chromosomes from this individual; again another random number is needed to indicate which byte of the chromosome is to be mutated. Usually only one bit of the selected byte (8 bits) is mutated. In practice, in order to achieve this operation more easily, a vector named "bit mask" which contains 8 elements (1, 2, 4, 8, 16, 32, 64, 128) is constructed, then the ith bit (the right-most bit is zeroth bit) in the byte is mutated from 1 to 0 or 0 to 1 by an XOR logic operator of the selected byte with the ith element in the bit mask. For example, the XOR operator of the byte with the 7th element of the bit mask results in the mutation of the 7th bit, as shown in Fig. 3.

NGA architecture I has the advantage of parallel searching in a very broad interval. Its genetic parameters are only the probability of crossover and mutation and can be controlled very easily. Hence it is very suitable for the optimization of poorly understood systems. The other advantage is that architecture I can prevent degeneration of the population (degeneration means all of the individuals in the population become equal or nearly equal). However, because this parallel searching occurs in a very broad interval, it is of low efficiency and is time consuming.

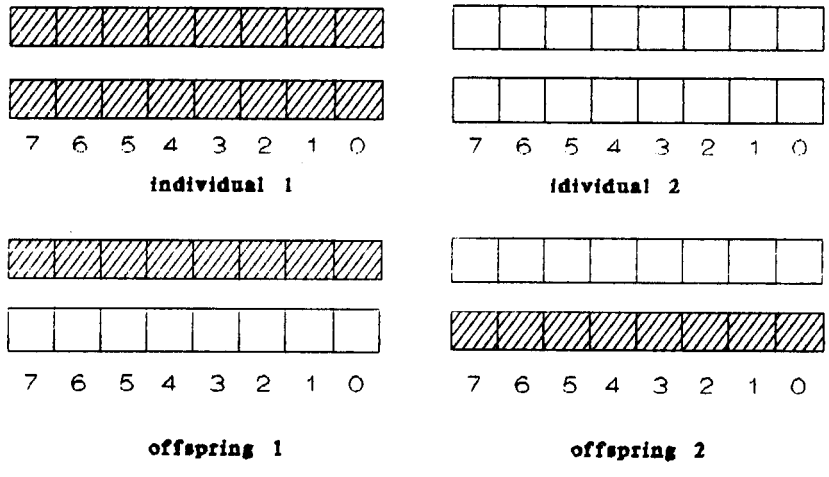

Fig. 4. Sketch of crossover operator in NGA architecture II. Each individual is composed of two chromosomes. The numbers 0–7 represent the bytes in a double number. Two offsprings are generated by exchanging the second chromosome of two selected individuals.

Genetic operations in NGA architecture II

In NGA, the chromosomes represent real numbers and the change in chromosomes is the change in the value of the corresponding parameters. Hence it is obvious that genetic operations can be achieved directly by numerical operations.

Crossover. In architecture II, two offsprings are generated by exchanging the chromosomes at the same position in two selected parents. In computer programming, it is realized by exchanging two real numbers in two different vectors. The number of chromosomes to be exchanged in one crossover operation is randomly determined. When the number is more than one, then these chromosomes are randomly selected. Fig. 4 illustrates how the two selected parents generate their offsprings. Two chromosomes at position 2 in two selected individuals are exchanged. (The chromosomes are written out in a computer bit string of a real number.)

Mutation. Mutation operator plays a very important role in NGA architecture II since now crossover operator does not generate a new value of any parameter which does not exist in the population. The mutation operator in architecture II can be expressed as

$$P_{new} = P_{old} + \text{increment} \quad (1)$$

where P_{old} is the value of the selected chromosome before mutation and P_{new} is its value after mutation. According to different cases, Eq. 1 can be rewritten in the following three forms. In practice, mutation operator can be composed of one or two or all of these three forms.

Mutation form 1 (MU1). This kind of mutation operator is defined as

$$P_{new} = P_{old} + P_{old} \times \text{scale1} \times \alpha$$
$$= P_{old}(1 + \text{scale1} \times \alpha) \quad (2)$$

where α is a random value between -1 and 1, scale1 is a positive value, usually $\leqslant 1$. This means that the value of the parameter after mutation equals its previous value plus a random number proportional to itself. Fig. 5 demonstrates how this form of mutation works and what task it completes. Suppose parameter P, at present, is 211 or 11010011 in binary, the increment equals 6 or 00000110. Then after mutation it equals 217 = 11011001, i.e. bits 1 and 3 have been mutated. The position of the bit to be mutated can be controlled by adjusting the value of scale1. A larger value of scale1 obtains the bits at the left part of the chromosome to mutate and thus the parameter varies greater in value, whereas a smaller value of scale1 obtains the bits at the right part of the chromosome to mutate.

MU1 is very suitable for poorly understood system; because it can adaptively adjust the increment. If scale1 is larger, the adjustment is larger and MU1 will be efficient in exploration. If scale1 is smaller, MU1 will be efficient in exploitation and it can make NGA converge to the optimum rapidly. Since usually $|\text{scale1}| <= 1$, MU1 can-

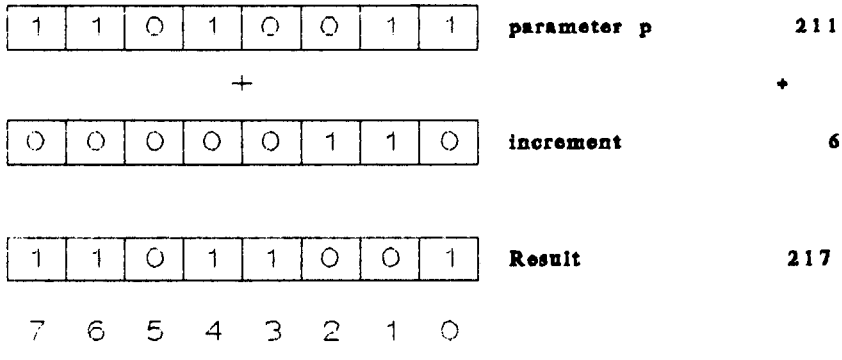

Fig. 5. Sketch of MU1 operator. Parameter P is assumed to be a one byte integer. Bits 1 and 3 are mutated after MU1 operation.

not change the sign of a parameter and may be invalid when P_{old} is zero or nearly zero.

Mutation form 2 (MU2). The second form of mutation is designed for the case when the optimization interval $[b, e]$ of each parameter is known. It is expressed by the equation

$$P_{new} = P_{old} + \alpha \times \text{scale2} \quad (3)$$

where scale2 is a positive value. Each parameter has its own corresponding scale2. These scale2s are set to be $(e-b)/2$ at the beginning of NGA and are adjusted during the NGA process to control the bits to be mutated in the selected chromosomes.

MU2 behaves in a very similar way to MU1. However, as the value of scale2 is independent of P_{old} and may be much more greater than P_{old}, MU2 operation is able to generate a completely new value. Unlike MU1, it will not be handicapped by a zero point. Usually MU2 operation is very efficient if some prior knowledge about the optimization problem is available, e.g., if the optimization interval is known for each parameter.

The functions of these two kinds of mutation operation are demonstrated in Fig. 6a. Suppose parameter P is now at point $x1$; if the value of scale1 and scale2 are smaller, then NGA tends to converge to point $x2$; however, if they are larger, NGA can pass over the nearby potential barrier $x3$ and converge to the global optimum $x4$ through mutation operation. If local optimum $x1$ was near the original point and NGA first converged to this point, as in Fig. 6b, MU1 would be invalid in converging to the global optimum but MU2 is still able to find $x4$.

Mutation form 3 (MU3). Even though MU1 and MU2 are able to pass over the potential barrier which is near the present solution, there still exist in practice some special cases where NGA cannot jump into the global optimum distinction through MU1 and MU2 operation (see Fig. 7). The third form of mutation operator is designed for this situation and is defined as a random sample from the optimization interval $[b,e]$ of the parameter, as described by the equation

$$P_{new} = (e-b)R(RS)/RS + b \quad (4)$$

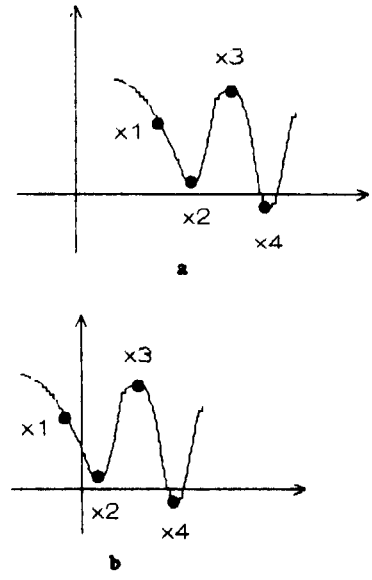

Fig. 6. Function of MU1 and MU2 operators. (a) The local optimum $x2$ is far from the original point; both MU1 and MU2 are able to find the global optimum $x4$ (b) The local optimum $x2$ is near zero; this may cause the failure of MU1.

where RS is a positive integer and $R(RS)$ is a function which generates random integers between 0 and RS-1. Hence MU3 set RS-1 sampling points in the optimization interval. It provides NGA with a fast searching strategy for optimization problems and is very efficient in space exploration.

The greater the value of RS the finer will the optimization interval be separated. The probability of NGA falling in a local optimum will be lower, but the costs of NGA rises too since MU3 is a grid search.

In Fig. 7, suppose NGA converges to local optimum $x2$ at present and all scales become small. If RS equals 3, thereby setting two sampling points in the optimization interval, then NGA will fail in finding the global optimum $x1$. In practice, RS is set to be a small integer at first and may be increased during the NGA process.

From the above discussions we can conclude the following: as it is possible to control scale1 or scale2 at different steps during the NGA process, NGA architecture II will be more efficient than architecture I. On the other hand, it is easily

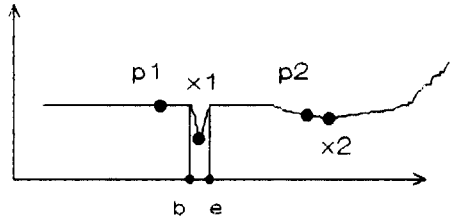

Fig. 7. The role of *RS*. It is assumed that NGA first converges to point $x2$ and all scales become nearly zero. $RS = 3$, thus setting two sampling points p1, p2 in the optimization interval. In this case, NGA will fail in converging to point $x1$ since no sampling point fall in the global optimal interval $[b, c]$.

understood and programmed because its genetic operations are only arithmetic operations. The disadvantage of architecture II, in comparison with architecture I, is that it has more parameters to be controlled during the optimization process.

Memory operator

This is a completely new operator and suitable for both architecture I and II. The idea of developing this operation is to use earlier progress in the population as prior knowledge to accelerate and improve later development of the population. The progress in the population is classified into two types. One is associated with a single genetic operator and is called a local progress. Suppose a new offspring is generated through a genetic operation such as crossover or mutation and survives in the population; if it is also better than its parent then a local progress is defined as the difference between this new offspring and its parent. The other type of progress, called global progress, is the accumulation of a lot of local progresses. It is defined as the difference between two most competing individuals at two moments t and $t+1$. The number of genetic operations between t and $t+1$ is defined as the size of a block. In a multi-dimensional space each individual is a vector. Suppose that the two individuals used to describe the progress are r_{new} and r_{old} (for local progress the offspring is r_{new},and for global progress the best-so-far at moment $t+1$ is r_{new}), then the progress can be expressed as

$$\delta r = r_{new} - r_{old} \tag{5}$$

This is used as prior knowledge and the memory operation is defined as the following three steps: (1) let $r_{old} = r_{new}$; (2) recalculate r_{new}, $r_{new} = r_{old} + \beta\delta r$; (3) evaluate r_{new}; if it is better than r_{old} then go to step 1, else terminate this memory operation. Here β is a positive number (in our experiments, for local progress, it is 1–2 and for global progress it is 0.001–0.2). The memory operation is limited to be a self-evolution, namely if memory operation succeeds then the parent dies and its child survives. This limitation guarantees that the population does not degenerate very quickly.

The combination of the local progress with the memory operation will make NGA very efficient in converging to an optimum even when the optimum is located in a very large monotonous interval. Also, the combination of the global progress with memory operation will make NGA very efficient for multi-variable optimization problems. When the variables in a multi-variable optimization problem correlate with each other, the memory operator would be expected to speed up and improve the genetic process powerfully.

Genetic parameters in NGA

Genetic parameters include the size of population, the probability of crossover, mutation, etc. In NGA, there are several other parameters that cannot be ignored which do not appear in GAs, such as scale1 and scale2s, the number of genetic operations included in one genetic block. In NGA, the number of individuals included in a population is usually about 50–100. The number of genetic operations included in one block should be controlled as it is used to evaluate statistically the success rate of mutation and controls the memory operation. The probability of crossover and mutation in architecture I can be controlled at the same level as in GAs or raise the probability of mutation and lower the probability of crossover properly. In architecture II, however, as crossover operation does not change the value of any parameter in individuals which survive in the population, so mutation operation becomes the chief factor and its probability should be raised. It is recommended here that it should be at least 50% and even higher. Also, the probability of

crossover decreases because a higher probability of crossover will quickly degenerate the population. The success rate of mutation is controlled between 20 and 40% by adjusting scale1 and scale2s. It should not be controlled at a very high level because this makes NGA tend to converge to a local optimum, and also note at a very low level as this lowers the efficiency of NGA. The last parameter, the probability of MU1, MU2, MU3 in total mutation operation, is also very important during the NGA process. The probability of MU3 should be at a very low level as MU3 is only a grid search. The probability of MU1 and MU2 can be equal.

The values of scale1 and scale2s are very important in practice. If they are larger, then NGA performs efficiently in space exploration. If they are smaller, then NGA is efficient in local exploration. In practice, scale1 and scale2 are set to be larger values at the very beginning of NGA and are adjusted according to the success rate of mutation. That is, keep scale1 and scale2s unchanged, take a number of genetic operations (a block) and evaluate statistically the success rate of MU1 and MU2 together. If the success rate is higher than a given threshold, then the values of the scales rise; if the success rate is lower than this threshold, on the other hand, then they are made smaller. It is known from the random sampling theory that the success rate of mutation is 50% at the maximum (see Eqs. 2 and 3). According to our knowledge from experiment, it is appropriate to keep this success rate between 20 and 40%. In applications in this paper, scale1 and scale2 are adjusted according to the following two equations:

$$\text{scale} = \text{scale} \times 10 \quad \text{if the success rate is greater than 40\%} \tag{6}$$

$$\text{scale} = \text{scale}/10 \quad \text{if the success rate is lower than 20\%} \tag{7}$$

Initial diversity of population

The convergence speed of NGA will be greatly increased when prior knowledge is put into the initial population. This is often possible since the parameters to be optimized in real problems usually have physical meanings. In this case, mutation composed of MU2 and MU3 is recommended. If we know nothing about the problem, each parameter in the initial population is usually set a random number between -1 and 1. MU1 is a better selection than MU2 and scale1 is set to be 1 initially.

3. Application and discussion

3.1. Simulated experiments

Several simulated mathematical functions that had been optimized with the modified simplex method and generalized simulated annealing (GSA) in ref. [7] are employed here to test NGA. They are listed in Table 1. In all of these mathematical examples, prior knowledge, i.e., the optimization interval $[b_i, e_i]$, is put into the initial population and mutation operation is composed of MU2 and MU3 in architecture II. The value of *RS* in Eq. 4 is 20 for the following NGA process. We shall see below that even more exciting results are obtained when compared with GSA.

The first function, named GSA1, has many stepped local optima and one global optimum at (0, 0). It has a one-dimensional form along the x-axis when $y = 0$ as shown in Fig. 8, and has a similar form along the y-axis when $x = 0$. Table 2 lists the optimization results of NGA in eight runs. In all eight runs, the initial population are initialized according to

$$P_i = (e_i - b_i)\gamma + b_i$$

Table 1
Mathematical functions optimized

Name	Expression	Optimization
GSA1	$1x^2 + 2y^2 - 0.3\cos(3\pi x) - 0.4\cos(4\pi y) + 0.7$	Minimization
3DPOLY	$9 - 8x - 6y - 4z + 2x^2 + 2y^2 + z^2 + 2xy + 2xz$	Minimization
SIN2	$1 + \sin^2(x) + \sin^2(y) - 0.1\exp(-x^2 - y^2)$	Minimization

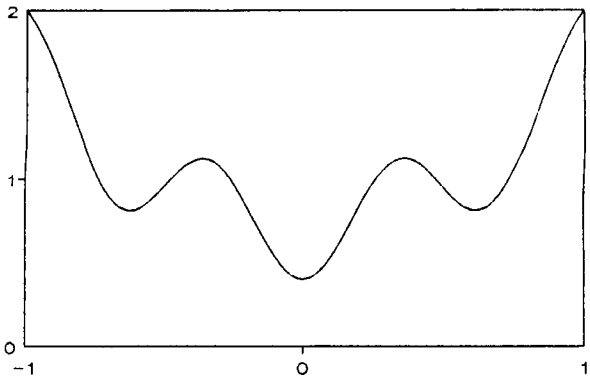

Fig. 8. One-dimensional plot of GSA1 function.

where P_i is the ith parameter and γ is a random number between 0 and 1. That means prior knowledge is put into the initial population. The optimization intervals are the same as in [9] in the first five runs. In the next three runs the populations are initialized by keeping the seed of the random number generator fixed while enlarging the optimization interval. Genetic parameters are kept the same for all eight runs and they are as follows. The probabilities of crossover and mutation are both 50%. MU3 is 25% of all mutation operations. Scale2s are set to be half of the optimization interval of the relevant parameter at first. The number of genetic operations included in one block is 100, namely 50 times crossover and 50 times mutation. Scale2s are adjusted by evaluating statistically the success rate of MU2 in one block according to Eqs. 5 and 6. Under these conditions, NGA converges to the global optimum rapidly through a relatively small number of operations in all eight runs. The number of genetic operations needed in the NGA optimization process increases when the optimization interval is enlarged. The success rate of crossover is very high when the success rate of MU2 is controlled between 20 and 40%. The success rate of MU3 is very low in most instances. This shows that the probability of MU3 should be low in order to save costs. GSA also converged to the global optimum in the range $-1 < x, y < 1$. The difference between them is that NGA always con-

Table 2
NGA optimization result of GSA1 function

Run	Rand seed	Success rate (%)			Total operations	Optimization interval [a]	Optimum response	Optimum coordinate	
		Crossover	MU3	MU2					
1	11	100.0	8.0	24.0	200	−1, 1	0.000	−0.001	0.001
2	3001	100.0	13.3	32.0	300	−1, 1	0.000	−0.002	−0.001
3	10001	100.0	2.6	22.2	300	−1, 1	0.000	−0.003	−0.002
4	11	96.4	9.6	21.3	500	−10, 10	0.000	0.000	0.000
5	11	98.0	6.7	25.8	600	−100, 100	0.000	−0.004	−0.001
6	11	92.0	5.7	26.3	700	−500, 500	0.000	0.001	−0.000

[a] The interval is the same for x and y.

Table 3
NGA optimization result of 3DPOLY function

Run	Rand seed	Success rate (%)			Total operations	Optimization interval [a]	Optimum response	Optimum coordinate		
		Crossover	MU3	MU2						
1	11	94.2	5.0	32.2	1100	0, 3	0.000	0.970	1.017	1.035
2	3001	97.0	13.0	25.8	300	0, 3	0.000	0.999	0.992	0.982
3	10001	87.3	8.0	25.8	300	0, 3	0.000	0.990	0.994	1.032
4	11	71.8	4.0	34.7	800	−10, 10	0.000	0.982	1.002	1.018
5	11	90.1	2.2	34.1	2200	−50, 50	0.000	1.020	0.985	0.966
6	11	85.7	2.5	38.1	3100	−100, 100	0.000	1.024	0.982	0.972

[a] The interval is the same for x, y and z for runs 4, 5 and 6. For the first three runs, the interval is [0, 3] for x, y and [0, 1.5] for z.

verged to the exact global optimum whereas GSA converged to near the global optimum.

The second function, named 3DPOLY, has a global optimum at (0, 0, 0). Also a total eight runs of NGA are taken and they were arranged in the same way as the GSA1 function except that the limitation of $x+y+z<=3.0$ is ignored. The optimization results are given in Table 3. They are very similar to those discussed in the function GSA1. The only difference is that the number of genetic operations needed in 3DPOLY is greater because there are three parameters to be optimized.

The third mathematical function, SIN2, has a global optimum 0.900 at (0, 0) and many equal local optima 1 in full domain. This function, as pointed out by Kalivas [7] presents the greatest challenge to all optimization methods. When $y=0$ the plot of this function along the x-axis is shown in Fig. 9 and it has a similar form along the y-axis when $x=0$. NGA tends to converge to one of the local optima very easily. When this happens NGA is able to jump out this local optimum if and only if one offspring is generated in the range of $-0.31<x,\ y<0.31$ because the basic idea of GAs is survival of the fittest. In this case, the optimization interval of two parameters is $-10<x,\ y<10$ and the global optimum (0, 0) is its centre. According to Eq. 3, NGA has the probability of sampling at (0, 0), which lies between $-0.31<x,\ y<0.31$, when RS is any even number. Hence NGA is able to find the global optimum very easily. This, as a special case, has been proved by our experiments. Therefore, the SIN2 function is changed to

$$1+\sin^2(x-\pi)+\sin^2(y-2\pi)-0.1\exp\left[-(x-\pi)^2-(y-2\pi)^2\right]$$

i.e., the global optimum has been moved to $(\pi, 2\pi)$ from (0, 0) and it is more difficult to search. The genetic parameters are equal to those in GSA1 except for the probability of MU3 in mutation and the value of RS. The optimization results are given in Table 4. When $RS=20$ and the probability of MU3 is 25% of total mutation operation, NGA succeeds in converging to the global optimum only when the seed of the random number generator is 10001. When RS is increased to 40, the probability of MU3 is still 25%, NGA succeeds in finding the global optimum in all five runs. When the probability of MU3 is increased to 75% while keeping $RS=40$, the costs decrease sharply. However, when the probability of MU3 is kept unchanged, the optimization intervals are separated even more finely, say into 640 equal parts, and the cost of NGA rises again (one exception is because of the random sampling feature of MU3). These experiments show that the optimization interval should not be separated too large or too finely. It is appropriate to separate the interval finely enough to ensure that at least one sampling point falls

Table 4
NGA optimization result of SIN2 function

Run	Rand seed	Success rate (%)			Total operations	Optimum response	Optimum coordinate		Sample points	Rate of MU3 in mutation (%)
		Crossover	MU3	MU2						
1	11	30.0	1.2	5.3	5200	0.900	3.140	6.280	40	25
2	3001	32.3	1.3	6.9	3800	0.900	3.141	6.289	40	25
3	10001	95.5	4.0	22.0	400	0.900	3.137	6.281	40	25
4	11	100.0	12.4	26.7	300	0.900	3.126	6.268	40	75
5	3001	52.6	1.6	19.2	2500	0.900	3.141	6.280	40	75
6	10001	92.0	8.6	26.0	400	0.900	3.127	6.280	40	75
7	11	83.4	7.2	38.9	700	0.900	3.141	6.286	640	75
8	3001	28.2	0.6	10.0	5700	0.900	3.120	6.280	640	75
9	10001	82.0	7.6	40.0	600	0.900	3.140	6.284	640	75

The optimization interval is -10, 10 for all nine runs.

Table 5
Experimental data in the parameter estimation problem

Sample	y	s	z
1	6.08	10.0	5.0
2	2.42	20.0	5.0
3	2.10	30.0	5.0
4	7.31	10.0	5.5
5	3.00	20.0	5.5
6	3.13	30.0	5.5
7	7.06	10.0	6.0
8	3.72	20.0	6.0
9	3.37	30.0	6.0

into the global optimization interval. The probability of MU3 rises to a very high level since the global optimization area ($-0.31 < x, y < 0.31$) is only a small part of the total optimization interval. In most cases, the success rate of crossover and mutation is very low for the SIN2 function when compared with GSA1 and 3DPOLY. This is because NGA converges to one of the local optima and does not jump out immediately through several blocks of genetic operations.

3.2. Parameter estimation

In the last example, NGA is applied to a real parameter estimation problem [10]. The experimental data are given in Table 5. This is a non-linear parameter estimation problem and the non-linear model is

$$y = ax^2 + bz^2 + cxz + dx + ez + f.$$

The parameters a–f had been optimized by the simplex method [10], GSA [8], and non-linear least squares [11]. The results are all given in Table 6. The results of NGA is also given for comparison. The best-fit criterion is the same as that used in [11] (designated by OC). During the NGA process, the population is initially set to be random numbers between -1 and 1 because no prior knowledge about these parameters is available. Genetic parameters are initially set as follows: mutation operation is composed of MU1 and MU3, the probability of MU3 is 10% of total mutation operations and MU3 is allowed to sample in the range between -100 and 100, which is separated into 20 equal parts. The probability of

Table 6
Optimization results with different methods

Method	a	b	c	d	e	f	OC
Simplex	0.0179	−1.4202	0.0145	−0.9951	16.159	−33.4635	35.84
GSA	−0.0022	−0.0041	−0.0209	0.0020	2.3226	−5.1236	9.444
NLS	0.018	−1.42	0.014	−0.995	16.5	−33.4	0.2305
NGA	0.01795	−1.4213	0.01447	−0.99517	16.5288	−33.449	0.2305

Table 7
Optimization process of NGA

Run	Time (min)	a	b	c	d	e	f	OC
1	0	0.1201	−0.5087	−0.3551	0.0928	0.8253	−0.8432	6471.42
	10	0.0180	−1.1670	0.0151	−1.0018	13.7117	−25.7116	0.2387
	23	0.0180	−1.4213	0.0145	−0.9951	16.5288	−33.4990	0.2305
2	0	−0.1099	−0.2117	0.6491	0.3229	0.4942	−0.5022	3519.65
	10	0.0182	−0.9317	0.0181	−1.0256	11.0709	−18.2836	0.2630
	20	0.0179	−1.0864	0.0152	−0.9984	12.8287	−23.3448	0.2445
	30	0.0180	−1.1709	0.0162	−1.0256	13.7346	−25.7383	0.2386
	40	0.0179	−1.2029	0.0152	−0.9982	14.1058	−26.8298	0.2365
	60	0.0179	−1.3958	0.0144	−0.9947	16.2486	−32.7356	0.23058
	70	0.0180	−1.4016	0.0144	−0.9952	16.3118	−32.9061	0.23055
	80	0.0179	−1.4200	0.0145	−0.9952	16.5134	−33.4555	0.2305

crossover and mutation is 30% and 70%, respectively. The number of genetic operations included in one block is 200. Scale1 is set to be 1 at first. After several runs had been made, it was found that NGA always converges to the global optimum 0.2305, the same as NLS. However, the cost of different runs differed greatly. Two typical optimization processes are listed in Table 7. The random seed of run1 is the default value set by the computer system, and it is 19 in run2. Under the same conditions, run1 takes about 20 min whereas run2 takes about 80 min on an IBM PC 8088 with an 8087 mathematical coprocessor. The OC value decreases sharply from several thousand to below 0.3 in the first 10 min in both cases. Thereafter, the convergence speed becomes relatively slow. For example, in run2 it takes about 50 min to make OC decrease from 0.2386 to 0.2306. Although this is not always the case, it does happen very often in our experiments. However, when the data are preprocessed, for example mean centred or normalized, NGA is able to find the optimum 0.2305 with 2 min. This means that the data structure has a strong effect on the convergence speed of NGA. This will be discussed in detail in the next paper in this series.

4. Conclusion

NGA is designed to be a global value parameter optimization method. It retains the parallel searching, large-scale optimization features of GAs. It enlarges the application field of GAs. It is able to find the global optimum among many local optima in a broad range. In this regard, it is very similar to SA. However, unlike SA, NGA is able to converge to the exact optimum. The theory of NGA is very simple and thus NGA has the advantage of easy programming. The genetic parameters can also be easily controlled. All these points make it very suitable for the optimization of large-scale and poorly understood systems. Areas that may benefit greatly from using NGA in the chemometrics field are, for example, curve resolution, calibration, parameter estimation, non-linear model building and multi-dimensional data resolution. In subsequent papers in this series, non-linear model building and multi-dimensional data resolution will be discussed in detail.

Acknowledgement

The authors are grateful to the National Natural Science Foundation of China for supporting this research.

Appendix

6.1. Application of C or Pascal language in handling bits of a double

Suppose a real number (double precision) is expressed as a 64-bit (8-byte) string in a microcomputer, then the data structure UNION in C or VARIANT RECORD in Pascal can be employed for handling different part of this 64-bit string. For example, one may define such a UNION in C

```
union chromosome{
    double parameter;
    char para-in-byte [8];
}
and such a VARIANT RECORD in Pascal,
TYPE
  op=(in-real,in-byte);
  chromosome=record
    case op of
    in-real:(parameter:double);
    in-byte:(para-in-byte:array [1..8] of
byte);
  end;
```

then the double parameter and the array of para-in-byte occupy the same memory in a computer, and the bytes in array para-in-byte are the different parts of a 64-bit string of a parameter. The change in the ith element of para-in-byte results in a change in the ith byte of the double. In a microcomputer, this 64-bit string is arranged as in Fig. 1. The para-in-byte [0] is the last 8-bit of 52-bit mantissa in the 64-bit of a double and para-in-byte [7] is a part of the exponent and the sign of a double. Hence genetic operations can be realized easily as in GAs. The operation probabil-

ity of different parts should be different in different steps of the NGA process in order to make NGA more efficient. For example, the operation probability of the part which represents the exponent of the parameter should be higher at the beginning of NGA and should be very low during the refinement of parameters. In our experiment, only the first seven bytes take part in the genetic operations since the 7th byte represents the highest part of the exponent and may easily cause an overflow error in the next numeric calculations.

References

[1] J.H. Holland, Adaptation in Natural and Artificial Systems, University of Michigan Press, Ann Arbor, MI, 1975.

[2] L. Davis and M. Steenstrup, Genetic Algorithms and Simulated Annealing, Pitman, London, 1987, pp. 1–11.

[3] C.B. Lucasius and G. Kateman, Trends Anal. Chem., 8 (1991) 254.

[4] C.B. Lucasius, M.J.J. Blommers, L.M.C. Buydens and G. Kateman, in L. Davis (Ed.), A Genetic Algorithm for Conformational Analysis of DNA, Handbook of Genetic Algorithms, Van Nostrand Reinhold, New York, 1991, Chap. 18, p. 251.

[5] T.-H. Li, C.B. Lucasius and G. Kateman, Anal. Chim. Acta, 268 (1992) 123.

[6] E. Fontain, J. Chem. Inf. Comput. Sci., 32 (1992) 748.

[7] J.H. Kalivas, N. Roberts and M. Sutter, Anal. Chem., 61 (1989) 2024.

[8] C.Z. Janikow and Z. Michalewicz, in Proceedings of the 2nd International IEEE Conference on Tools for Artificial Intelligence, 1990, p. 798.

[9] J.M. Sutter and J.H. Kalivas, Anal. Chem., 63 (1991) 2383.

[10] J. Zupan and F.X. Rius, Anal. Chim. Acta, 239 (1990) 311.

[11] E.E. Tucker, J.H. Kalivas and J.M. Sutter, Anal. Chem., 64 (1992) 1199.

ELSEVIER

Analytica Chimica Acta 293 (1994) 205–210

ANALYTICA CHIMICA ACTA

Computational method for evaluating and optimizing response surface curves based on mixture designs

Domingo González-Arjona *,[a], A. Gustavo González [b]

[a] Department of Physical Chemistry, and [b] Department of Analytical Chemistry, University of Seville, E-41012 Seville, Spain

(Received 16th December 1993)

Abstract

A straightforward algorithm for the evaluation of the coefficients of the response-surface curve emerging from a mixture design is described. When the form of the response function in the factor space is known, its maximum was calculated by using a modified simplex procedure. A program called MIXOP was employed in the computations. The method was checked by using several examples taken from the literature.

Key words: Optimization methods; Mixture design

1. Introduction

Knowledge of mixture designs is needed when studying the properties of a q-component mixture, depending on the component ratio only. In this case, a constraint is easily derived thereof:

$$\sum_{i=1}^{q} x_i = 1;\ \forall x_i \geqslant 0 \qquad (1)$$

where x_i is the fraction of the component and q is the number of components. Mixture designs are well known and consequently they have been revisited by several authors [1–4]. The representation of response-surface curves of these systems in a hyperplane is not possible. The response curve may be depicted however when the factor space is a regular simplex design of a q vertex. Therefore, mixture designs are also referred to as simplex-lattice designs. This term is unfortunate because it creates confusion between the simplex method for direct search optimization (described below in this paper) and the mixture designs considered: a completely different technique [5]. In order to avoid further confusion, we shall use the term Scheffe centroid [6] designs.

While designing experiments for attacking mixture problems involving composition-properties diagrams (such as the well-known Rozebum's triangle for a three component mixture), the studied property is assumed to be expanded in a polynomial series. This obviates the need for a spatial representation of complex surfaces, as the properties that are searched for can be derived from equations, while the possibility for interpreting the results graphically is retained. Scheffe centroid designs [6] contain 2^{q-1} points, q of which fall on pure components, $C_{q,2}$ ($C_{q,r}$ refers to

* Corresponding author.

SSDI 0003-2670(94)00080-6

combinations of q items taken r at a time) on binary mixtures, $C_{q,3}$ for ternary mixtures until $C_{q,q} = 1$ for a q-component mixture. Scheffe centroid designs consist of the points whose coordinates are $(1,0,0\ldots0)$, $(1/2,1/2,0,\ldots,0)$, ..., $(1/q,1/q,1/q,\ldots,1/q)$ as well as the points that can be obtained from these by permutation of coordinates. This design contains a point at the centroid of the simplex, $(1/q,1/q,\ldots,1/q)$. To describe the response-surface curves adequately with these designs, Gorman and Hinman [4] suggested the use of *reduced polynomials*. These polynomials have the general form:

$$\hat{y} = \sum_{i=1}^{q} \beta_i x_i + \sum_{q}^{j>i} \beta_{ij} x_i x_j + \sum_{k>j>i}^{q} \beta_{ijk} x_i x_j x_k + \ldots + \beta_{12\ldots q} x_1 x_2 \ldots x_q \quad (2)$$

where $\hat{y}$ is the response function and the β's are the coefficients of the polynomial. Remembering Eq. 1, the factor levels or variables x_i cannot be varied independently. The two, three and higher degree terms in Eq. 2 are therefore not called interaction terms, but non-linear blending terms.

Mixture designs have been extensively used in liquid chromatography (LC) [7–10], pharmaceutical formulation designs [11–14], liquid–liquid extraction of drugs from biological matrices [15] and chemical engineering designs [6].

The aim of the present paper is to provide the analyst (as well as any scientific worker) concerned for experimental designs and optimization, with a computational procedure which evaluates the response function from the experimental points and performs an optimization *via simplex* for attaining the coordinates of the point corresponding to the maximal response within the experimental range.

2. Outline of the method

Scheffe centroid designs are *saturated*, which means that the number of observations and the number of coefficients to be determined in the response function are exactly the same. Therefore, the determination procedure is based on the resolution of a non-linear system of equations, as Berridge [16] has done for LC optimizations. However, a general expression for evaluating the β coefficients has been proposed by Scheffe [6]:

$$\beta_{ij\ldots} = r \sum_{t=1}^{r} (-1)^{r-t} t^{r-1} S_t \quad (3)$$

where r is the number of indices of the β coefficient; S_t is the sum of experimental results, y, for all the t-component mixtures taken in equal proportions $(1/t)$. For example, in a 7-component mixture, for the β_{1357} coefficient we have $r = 4$ (four indices 1, 3, 5 and 7) and four sums:

$$S_1 = y_1 + y_3 + y_5 + y_7 \quad (t = 1)$$

$$S_2 = y_{13} + y_{15} + y_{17} + y_{35} + y_{37} + y_{57} \quad (t = 2)$$

$$S_3 = y_{135} + y_{137} + y_{357} \quad (t = 3)$$

$$S_4 = y_{1357} \quad (t = 4)$$

the response y_{137}, for instance, represents the experimental result corresponding to a 1/3:1/3:1/3 mixture of the components 1, 3 and 7.

Consequently, once the β coefficients have been evaluated, the form of the response-surface function is known and our effort was then focused on seeking the optimal conditions. It is desirable to attain the coordinates of the point on the component space which corresponds to the maximum response. A procedure for seeking the maximum involves the Lagrange multiplier technique due to the existence of constraints, whose performance leads to intricate computational schedules with substantial need of programming expertise. In order to avoid this, we have performed an optimization using the simplex direct search method [17,18]. A routine published in Numerical Recipes [19] was conveniently modified by us and produced excellent results.

3. Computational details

The proposed procedure was implemented in QuickBasic for an IBM compatible PC (XT or AT). In order to avoid slow computations it is advisable to use at least an 80286 processor. A program called MIXOP was divided into blocks for the sake of a better understanding of its structure. MIXOP consists of the following principal procedures:

INDICES: From the number of components involved in the mixture design, this procedure generates an ordered string array containing the subindices of the β coefficients to be further evaluated from the Scheffe algorithm (implemented in the procedure BETACOEF).

INITX: This procedure creates the input coordinate matrix of the mixture design. The rows of the matrix are the different mixtures studied and the columns contain the values of each fractional component. Each matrix element X(row,col) represents the fractional component value X_{col} of the mixture *row*.

The experimental response corresponding to each mixture *row* is entered using the keyboard via the **DATAIN** procedure or alternatively it may be read from an ASCII file previously generated.

BETACOEF: This procedure calculates the values of the β coefficients by using the algorithm derived from Eq. 3.

Once this coefficients have been evaluated and therefore the form of the response function in our factor space is known, the optimization step begins.

First, the procedure **SORT** creates an ordered sequence of the experimental response values for selecting the higher $q+1$ values which correspond to the simplex guess need to start the optimization process.

MODSIMPLEX: This performs a direct search for the maximum of the response function by using a modified simplex method. This procedure calls to **RESPONSE** for computing the response value in any design point by applying Eq. 2. MODSIMPLEX also avoid any possible boundary violation as stated in Eq. 1. The user indicates the tolerance of response and the maximum number of iterations. A tolerance 10^{-K} indicates the number, K, of stable digits of the response. If J is the place corresponding to the last significant figure of the response data, then $K = J + 1$ should be selected.

4. Examples

In order to show how the program works and for the sake of illustration we have selected three examples from literature.

Example 1. The data for this example were taken from Bolton [14]. It deals with the design of pharmaceutical formulations. The experiment was prompted by problems with tablet hardness for a large volume of marketed product. The problems were caused by three components of the tablets (ingredients A, B and C). Together these components consisted of 25% of the original formulation or 75 mg of the total tablet weight of 300 mg. A careful evaluation of the product ingredients indicated that the three components had to be present in an amount equal to at least 10 mg of each in order to satisfactorily compress the tablet. Thus the recommended Scheffe centroid design consisted of varying the three components with the constraint so that the sum of the components was 75 mg, and that each component was present in an amount equal to at least 10 mg. Accordingly, the minimum amount was 10 mg and the maximum 55 mg. In order to apply the Scheffe centroid design in a suitable manner, the actual amounts used must be transformed into fractions so that the minimum corresponds to 0 and the maximum to 1. This was easily accomplished by coding the amount of the ingredient used in the following way: actual fraction = (amount used − minimum)/(maximum − minimum). The fractions x_1, x_2 and x_3 refer to ingredients A, B and C, respectively. The three component simplex design is given in Table 1. The response is the hardness average of 20 tablets drawn at random from experimental batches.

By using MIXTOP, the third degree polynomial fit is represented by

$$y = 6.1x_1 + 7.5x_2 + 5.3x_3 - 0.8x_1x_2 + 2.8x_1x_3 + 2.0x_2x_3 + 15.0x_1x_2x_3 \quad (4)$$

Table 1
Mixture design for example 1

Component fractions			Average hardness
x_1	x_2	x_3	y
1	0	0	6.1
0	1	0	7.5
0	0	1	5.3
0.5	0.5	0	6.6
0.5	0	0.5	6.4
0	0.5	0.5	6.9
0.333	0.333	0.333	7.3

Bolton [14] found for the last term of Eq. 4 the value of 15.24 instead of 15.0. González [5] found the same value based on a linear regression without degrees of freedom. The only reason for this difference in the term containing the contributions of the three factors is due to the use of the coordinates (0.333, 0.333, 0.333) for the ternary mixture instead of the exact values (1/3, 1/3, 1/3). Our program calculated the coefficients from the Scheffe algorithm and consequently always gave unbiased results. Bolton published a check point of coordinates (0.5, 0.25, 0.25) which yielded a response of 7.2. The response value predicted by Eq. 4 is 7.29, which is in excellent agreement with the experimental value. In order to obtain the best response we optimized the response surface by the simplex procedure using a tolerance in the response of 0.01, which gave a final simplex whose coordinates and responses are:

(0.00, 1.00, 0.00) 7.50

(0.04, 0.85, 0.11) 7.43

(0.03, 0.86, 0.11) 7.43

(0.01, 0.85, 0.14) 7.43

The best vertex corresponds to the coordinates (0.00, 1.00, 0.00), one of the points of the Scheffe centroid design, and consequently, the best blend corresponds to 10 mg of A, 55 mg of B and 10 mg of C.

Example 2. This example has been taken from the paper of Fisher and Mikheeva cited in [6]. We tried to determine how the activity of a platinum catalyst supported by a non-porous metal carrier depends on the catalyst composition at 350°C. The total mass of components was maintained constant from experiment to experiment. The x_1 component is a ground, dead reforming Pt/Al_2O_3 catalyst. Components x_2 and x_3 are inorganic oxides of metals belonging to groups II and III of the Periodic Table.

The data corresponding to the Scheffe centroid design are depicted in Table 2. The corresponding polynomial fit from MIXOP is:

$$y = 97.4x_1 + 3.0x_2 + 4.7x_3 + 79.2x_1x_2 + 59.8x_1x_3 + 11.8x_2x_3 + 1177.5x_1x_2x_3 \quad (5)$$

As in the previous example, the last term of Eq. 5 differs from the one presented in Ref. 6, which is 1175.35 due to imprecisions in the regression procedure. In order to calculate the optimum response we selected a tolerance of 0.01 which lead to a final simplex whose vertex coordinates and associated response are shown below:

(0.51, 0.25, 0.24) 105.7

(0.52, 0.24, 0.24) 105.8

(0.56, 0.24, 0.20) 105.7

(0.56, 0.21, 0.23) 105.8

These results agree well with the true maximum evaluated by applying the Lagrange multiplier technique to Eq. 5 which yields:

(0.58, 0.22, 0.20) 105.7

Maximization/minimization of polynomials like those in Eq. 2 by using the Lagrange Multiplier technique lead to a set of non-linear equations which after successive substitutions produced a higher degree equation in one variable (a fourth degree equation for three components).

Table 2
Mixture design for example 2

Component fractions			Catalyst activity
x_1	x_2	x_3	y
1	0	0	97.4
0	1	0	3.0
0	0	1	4.7
0.5	0.5	0	70.0
0.5	0	0.5	66.0
0	0.5	0.5	6.8
0.333	0.333	0.333	95.4

All these calculations involving derivations, substitutions, rearrangements and iterative resolution of the high degree final equation are cumbersome and awkward to handle, and evidently, the simplex approach gave good results in a more straightforward way.

Example 3. Mobile phase LC optimizations using mixture designs is a common task in analytical practice and sometimes the procedure is referred as the 'Sentinel Method' [20]. A mixture of nine substituted naphthalenes was chosen by Glajch et al. [21] for the optimization technique. The first step consisted of adjusting the solvent strength of a modifier in water to produce a range of capacity factors k' of about 1–10 for all solutes. Once the necessary composition, for instance for methanol and water, were experimentally evaluated, isoeluotropic aqueous mixtures of acetonitrile and tetrahydrofuran were calculated [22,23]. For the cited solutes, the isoeluotropic mixtures were: methanol–water (63:37), acetonitrile–water (52:48) and tetrahydrofuran–water (39:61), labelled as A, B and C, respectively. The response-surface is the so-called chromatographic optimization function (COF) defined in this case as follows:

$$\mathrm{COF} = \sum_{i=1}^{n} \ln\left(\frac{R_i}{R_d}\right) \qquad (6)$$

where R_i is the resolution of the adjacent peak pairs i and $i+1$. R_d is the desired resolution for every pair and n is the number of peak pairs of interest. In order to obtain meaningful results and for comparing the effect of the optimum locator, Glajch et al. [21] selected three values of R_d: 1.2, 1.8 and 2.4. The resulting COF values for seven chromatograms according to a mixture design utilizing the isoeluotropic solvents A, B and C are collected in Table 3. The authors experimentally reported that for $R_d = 1.8$ and 2.4 the blend (0.00, 0.69, 0.31) gives the best COF value, close to the target value of COF = 0.

After applying MIXOP to the data of Table 3, we have obtained the fitted polynomial:

$$\mathrm{COF} = -3.79A - 2.38B - 6.53C - 0.38AB + 3.56AC + 16.62BC + 36.81ABC \qquad (7)$$

for the best case corresponding to $R_d = 2.4$. For

Table 3
Mixture design for example 3

Component fractions			COF values		
A	B	C	$R_d = 1.2$	$R_d = 1.8$	$R_d = 2.4$
1	0	0	−2.48	−3.21	−3.79
0	1	0	−0.99	−1.80	−2.38
0	0	1	−4.97	−5.78	−6.53
0.5	0.5	0	−2.48	−2.89	−3.18
0.5	0	0.5	−2.48	−3.41	−4.27
0	0.5	0.5	0.00	−0.02	−0.30
0.333	0.333	0.333	0.00	−0.38	−0.67

calculating the optimum response we choose a tolerance of 0.001 which leads to a final simplex whose vertex coordinates and associated response are shown below

(0.08, 0.56, 0.36) 0.043

(0.08, 0.56, 0.36) 0.043

(0.08, 0.56, 0.36) 0.043

(0.08, 0.56, 0.36) 0.043

The COF response is also very close to the target value 0.00. This optimum relatively agrees with the one obtained by Glajch et al. [21]. However, these authors found the optimum solvent composition using a graphical examination of the contour COF diagram. Therefore, the blend (0.00, 0.69, 0.31) is said to be a *useful optimum* instead of a true optimum. In order to obtain a more convenient approach these authors developed the so-called overlapping resolution maps (ORM) method [21] which leads to a solvent blend region where all the chromatographic peaks are well resolved. This region encompasses a number of *optimum solvent mixtures* leading to a COF value near 0.00 in all cases. It is remarkable that both optimum blend values (0.00, 0.69, 0.31) and (0.08, 0.56, 0.36) fall in this region.

5. Conclusion

The proposed program performs adequately the optimization of experimental mixture designs and can be useful in a number of stages on the searching planning of a number of experimental sciences.

Acknowledgements

Financial support from the Dirección General de Investigación Científica y Técnica de España through Project PB 87-0932 is gratefully acknowledged.

References

[1] J.A. Cornell, Technometrics, 21 (1979) 95.
[2] H. Scheffe, J. Roy. Stat. Soc. Ser. B, 20 (1958) 344.
[3] R.D. Snee, CHEMTECH, 9 (1979) 702.
[4] J.W. Gorman and J.E. Hinman, Technometrics, 4 (1962) 463.
[5] A.G. González, Int. J. Pharm., 97 (1993) 149
[6] S. Akhnazarova and V. Kafarov, Experiment Optimization in Chemistry and Chemical Engineering, MIR, Moscow, 1982.
[7] R. Leher, Ind. Res. Dev., 25 (1983) 116.
[8] D.T. Harvey, S. Byerly, A. Bowman and J. Tomlin, J. Chem. Educ., 68 (1991) 162.
[9] R.G. Brereton, Anal. Proc., 28 (1991) 145
[10] J. Wieling, H. Dijkstra, C.K. Mensink, J.H.G. Jonkman, P.M.J. Coenegracht, C.A.A. Duineveld and D.A. Doornbos, J. Chromatogr., 629 (1993) 181.
[11] K. Takayama, H. Imaizumi, N. Nambu and T. Nagai, Chem. Pharm. Bull., 33 (1985) 292.
[12] R. Huisman, H.V. van Kamp, J.W. Weyland, D.A. Doornbos, G.K. Bolhuis and C.F. Lerk, Pharm. Weekbl. Sci. Ed., 6 (1984) 185.
[13] T. Hamoir, B. Bourguignon and D.L. Massart, J. Chromatogr., 633 (1993) 43.
[14] S. Bolton, Pharmaceutical Statistics. Practical and Clinical Applications, Marcel Dekker, New York, 1984.
[15] J. Wieling, P.M. Hempenius, P.M.J. Coenegracht, J.H.G. Jonkman, C.K. Mensink and D.A. Doornbos, Pharm. Weekbl. Sci. Ed., 11 (1989) N11.
[16] J.C. Berridge, Techniques for the Automated Optimization of HPLC Separations, Wiley, Chichester, 1985.
[17] E. Morgan and K.W. Burton, Chem. Int. Lab. Syst., 7 (1990) 209.
[18] E. Morgan and K.W. Burton, Chem. Int. Lab. Syst., 8 (1990) 97.
[19] W.H. Press, B.P. Flannery, S.A. Teukolsky and W.T. Vetterling, Numerical Recipes in C., Cambridge University Press, 1990.
[20] P.J. Schoenmakers, Optimization of Chromatographic Selectivity. A Guide to Method Development, Elsevier, 1988.
[21] J.L. Glajch, J.J. Kirkland and K.A. Squire, J. Chromatogr., 199 (1980) 57.
[22] L.R. Snyder and J.J. Kirkland, Introduction to Modern Liquid Chromatography, Wiley, New York, 2nd edn., 1979.
[23] A.G. González and A.G. Asuero, Int. J. Pharm., 93 (1993) 183.

ELSEVIER

Analytica Chimica Acta 293 (1994) 211–218

ANALYTICA CHIMICA ACTA

Simultaneous determination of arsenic(V) and arsenic(III) in water by inductively coupled plasma atomic emission spectrometry using reduction of arsenic(V) by L-cysteine and a small co-centric hydride generator without a gas–liquid separator

Yong-lai Feng *, Jian-ping Cao

Physical and Chemical Test Centre of Jiangsu Province, Nanjing 210002, China

(Received 5th October 1993; revised manuscript received 10th January 1994)

Abstract

A small co-centric hydride generator can be used to determine arsenic by inductively coupled plasma atomic emission spectrometry with a minitorch of 0.65 kW power. Because the reaction of arsenic(V) with L-cysteine is linearly dependent on time up to 9 min, the determination of arsenic(V) based on reduction kinetics is possible. Interferences from transition elements are low. The detection limit for arsenic(V) is 3.4 ng ml^{-1} and for arsenic(III) 0.7 ng ml^{-1}. The relative standard deviation for ten determinations of solutions containing 100 ng ml^{-1} As(V) was 1.45% and for a solution containing 100 ng ml^{-1} As(III) it is 1.21%. A major advantage of this system is the simultaneous determination of arsenic(V) and arsenic(III) under conditions of low acid and low power using a normal spray chamber.

Key words: Atomic emission spectrometry; Inductively coupled plasma; Arsenic; Hydride generation; Waters;

1. Introduction

Hydride generation combined with atomic spectrometry has been widely used for the determination of arsenic in various samples during the past 20 years [1–8]. In the previous work, the hydride generators used can be classified into three types, i.e., a hydride generator with and without a gas–liquid separator and with a combined separator [9–15]. A conventional gas–liquid separator for generation of hydrides from concentrated acid media, as first described by Thompson et al. [16,17], can keep the plasma stable when high power is used, but memory effects originate from large generator volumes and delay hydride reactions in the drain. Moreover, the large amount of hydrogen that is generated by the reaction between tetrahydroborate(III) and concentrated acid may result in extinction of the plasma discharge when high power is not used.

To improve the analytical performance and to reduce these drawbacks, different types of gas–

* Corresponding author.

SSDI 0003-2670(94)00069-X

liquid separators such as a packed U-tube [18], porous PTFE membrane [19,20] and microporous PTFE tubing [21–23] were designed. Brindle and co-workers [24,25] reported that the combined generator–separator for continuous generation can be used in media of low acidity and that lower detection limits were obtained, but that it is difficult to use in a plasma system of low power. A continuous-flow hydride generator without a gas–liquid separator which was used to determine arsenic, antimony, bismuth, selenium and tin was reported by Schramel and Xu [26], but the same drawback occurred.

As in the arsenic hydride generation process trivalent arsenic can react more easily than pentavalent arsenic with tetrahydroborate(III), arsenic(V) was usually determined by a method involving prereducing it to arsenic(III) with a reductant. The critical points are the selection of the reductant and the complete prereduction of arsenic(V) to arsenic(III). The most popular reductant is potassium iodide, which has usually been employed in combination with ascorbic acid in strongly acidic media, but it takes a long time to complete the prereduction reaction at room temperature. Some other reductants, such as sodium thiosulphate [27,28] and titanium(III) chloride [29], have also been reported for the prereduction of arsenic(V) in solvent extraction techniques. To reduce the acidity of the media, Chen et al. [30] used L-cysteine as a prereductant and achieved the determination of general arsenic in media of lower acidity. However, all these methods have serious a drawback, i.e., the prereduction of arsenic(V) to arsenic(III) must be fully completed. It is difficult to determine arsenic(V) and arsenic(III) simultaneously under the conditions prevailing in solution, and the several hours required for prereduction are too long for practical analyses for arsenic(V).

In this work, a small co-centric hydride generator without a gas–liquid separator was employed with inductively coupled plasma atomic emission spectrometry (ICP-AES) with a minitorch of 0.65 kW power, and the reduction kinetics of arsenic(V) to arsenic(III) by L-cysteine were investigated. The generator can be directly and easily used with a normal spray chamber instead of a nebulizer. Arsenic(V) and arsenic(III) can be simultaneously determined by this method. From these studies a prereduction time of 8 min, 0.08 mol l^{-1} hydrochloric acid medium and other conditions were chosen and arsenic(V) in a mixed solution of arsenic(V) and arsenic(III) was determined. The detection limit of this method is 3.4 ng ml^{-1} for arsenic(V).

2. Theory

Arsenic(V) can be reduced to arsenic(III) by L-cysteine as follows:

$$R\text{–}S\text{–}S\text{–}R + As(V) \xrightarrow{\text{slow}} 2R\text{–}SH + As(III) \quad (1)$$

where $R = -CH_2CH(NH_2)CO_2H$;

$$d[As(III)]/dt = k[R\text{–}S\text{–}S\text{–}R][As(V)] \quad (2)$$

Eq. 2 can be simply integrated, which yields

$$[As(III)] = k[R\text{–}S\text{–}S\text{–}R][As(V)]t + b \quad (3)$$

During the initial stage, the changes in the concentration of L-cysteine ([R–S–S–R]) and the concentration of arsenic(V) {[As(V)]} are so small that they can be neglected. If the concentration of L-cysteine ([R–S–S–R]) is constant and the concentration of arsenic(V) {[As(V)]} is C, the equation can be expressed as

$$[As(III)] = k_1Ct + b \quad (4)$$

From above equation, if t is constant then the graph of concentration of arsenic(III) {[As(III)]} versus concentration of arsenic(V) (C) is a straight line. If [As(III)] is measured at two times, t_1 and t_2, the following equation holds:

$$\{[As(III)]_2 - [As(III)]_1\}/(t_2 - t_1) = k_1C \quad (5)$$

Eqs. 4 and 5 are the basis for the determination of arsenic(V) and arsenic(III) in this paper.

3. Experimental

3.1. Apparatus

For ICP-AES, an ARL Model 3410 sequential scanning spectrometer equipped with a PS/2

computer that controls instrument operations, data conversions and storage (Applied Research Laboratory, Valencia, CA) was used. The torch is a minitorch. Fig. 1 shows a schematic diagram of the hydride generator and the experimental facility. The two peristaltic pumps used were a Cole-Palmer 1-100 RPM five-channel peristaltic pump and a single-channel peristaltic pump (Gilson Minipuls 1). The operating conditions of the system are given in Table 1. Off-peak spectral background correction was applied based on the spectral profiling.

Table 1
Operating parameters of the ICP-AES instrument

Coolant (argon) flow-rate	7.5 l min^{-1}
Plasma (argon) flow-rate	0.8 l min^{-1}
Carrier gas (argon) flow-rate	0.45 l min^{-1}
Wavelength	228.81 nm
Incident power	0.65 kW
Observation height	9.0 mm
Integration time	30 s
Sample flow-rate	2.3 ml min^{-1}
$NaBH_4$ flow-rate	0.8 ml min^{-1}
Torch	Minitorch

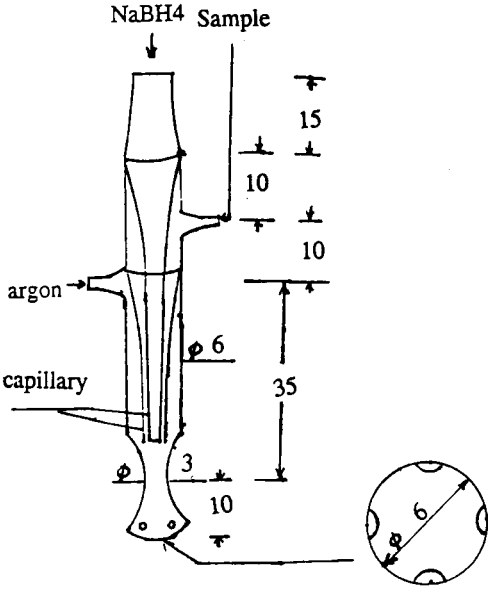

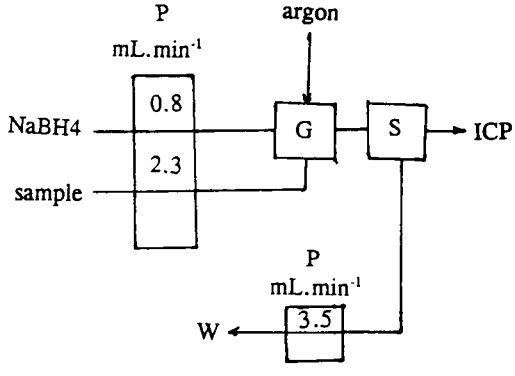

Fig. 1. Manifold for small co-centric hydride generator (all dimensions in mm) P = peristaltic pump; S = normal spray chamber; G = hydride generator; W = waste.

3.2. Reagents

Arsenic(III) standard solution (1.0 mg ml^{-1}) was prepared from As_2O_3 (Thorn Smith, Beulah, MI). Arsenic(V) standard solution was prepared from AnalaR-grade $Na_2HAsO_4 \cdot 7H_2O$ (BDH, Toronto, Ontario) and sodium tetrahydroborate (III) (Merck–Schuchardt, Darmstadt) solution (0.5–40 mg ml^{-1}) was prepared in 0.05 mol l^{-1} sodium hydroxide solution. L-Cysteine was obtained from Sigma. All other reagents were of analytical-reagent grade or better.

3.3. Hydride generation conditions

The acidified analyte solution which contains 1–120 mg ml^{-1} L-cysteine and 0.5–40 mg ml^{-1} tetrahydroborate(III) solution containing 2 mg ml^{-1} sodium hydroxide were continuously pumped into the co-centric hydride generator via a multichannel peristaltic pump. The hydride was introduced directly into the plasma and the signal intensity was recorded via the computer.

3.4. Kinetic aspects

A 15-ml aliquot of water, 62.5 or 125 mg of L-cysteine and 2.5 ml of 1.0 mol l^{-1} hydrochloric acid were placed in a 25-ml volumetric flask, then the solution was diluted to ca. 20 mL. Arsenic(V) solution was added to the flask and the solution was immediately diluted to the mark and the time

was recorded. The concentration of arsenic(III) as a function of time was determined. From this relationship the kinetics for the reduction reaction of arsenic(V) to arsenic(III) can be obtained. When time is fixed, a plot of concentration of arsenic(III) versus concentration of arsenic(V) can be obtained with this procedure.

3.5. Analytical procedure

First, a graph of concentration of arsenic(III) versus concentration of arsenic(V) must be plotted (see Fig. 7, line I). Then the concentrations of arsenic(III) in a standard solution of arsenic(V) with L-cysteine were determined separately at the 2nd and 8th minutes, the differences in these two concentrations were obtained and the ratio of the difference in the two concentrations to the difference in the two times, i.e., $\{[As(III)]_8 - [As(III)]_2\}/(8-2)$, was plotted against concentration of arsenic(V), resulting in line II in Fig. 7. From line I [when the original concentration of arsenic (III) is zero] or line II, the concentration of arsenic(V) in samples can be calculated. As the reaction of arsenic(III) with tetrahydroborate(III) is not affected by time when L-cysteine is present in the solution, the original concentration of arsenic(III) in the sample solution does not change with time. For this reason, when the concentration of arsenic(V) is calculated from line II we can calculate the concentration arsenic(III) converted from arsenic(V) at the 8th minute from line I, and finally the original concentration of arsenic(III) in the sample solution is obtained by subtracting the concentration of arsenic(III) which is converted from arsenic(V) at the 8th minute from the concentration of arsenic(III) which is determined at the 8th minute.

4. Results and discussion

4.1. Hydride generator

The small co-centric hydride generator, shown in Fig. 1, is significantly smaller and simpler than the continuous hydride generator for a 1-kW inductively coupled plasma [31]. Unlike the conventional hydride generator, this technique has been successfully employed in a 0.65-kW ICP-AES system with a minitorch. In this system the acidified sample solution, tetrahydroborate(III) solution and argon were mixed at the top of the hydride generator through three co-centric tubes; this arrangement can reduce the memory effects. Optimization of the hydride generator and plasma conditions were obtained in this study.

4.2. Influence of HCl, L-cysteine and $NaBH_4$ concentrations and carrier gas (argon) flow-rate

The effect of hydrochloric acid concentration in the sample solution on the net intensity of arsenic(III) is shown in Fig. 2. It can be seen that the net intensity of arsenic(III) increases with increase in hydrochloric acid concentration and reaches a maximum at about 0.09 mol l^{-1} and then decrease from 0.10 mol l^{-1}. This behaviour is similar to that reported by Chen et al. [30].

Fig. 3 shows the influence of L-cysteine concentration on the net intensity of arsenic(III). It can be seen that the graph reaches a plateau above 5 mg ml^{-1}.

Fig. 4 shows that the net intensity of arsenic(III) increases markedly with increase in sodium

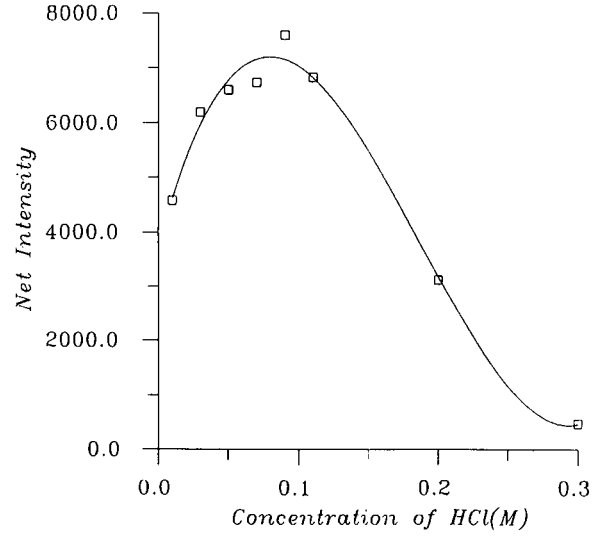

Fig. 2. Effect of hydrocholoric acid concentration on net intensity. 100 ng ml^{-1} As(III) with 5 mg ml^{-1} L-cysteine, 1% (w/v) $NaBH_4$ (0.05 M NaOH) solution.

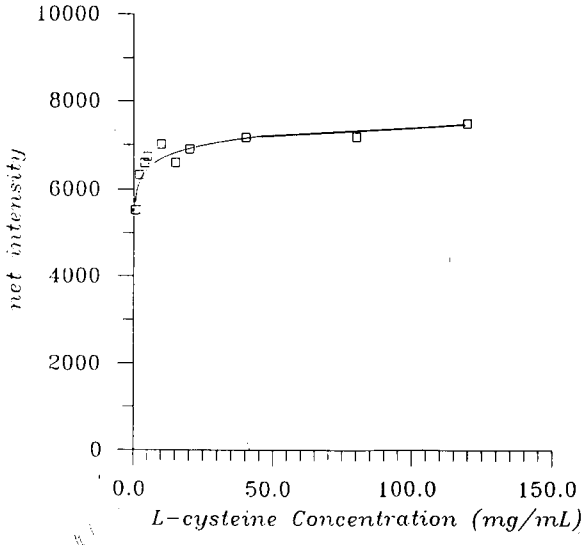

Fig. 3. Effect of L-cysteine concentration on arsenic(III) net intensity. 100 ng ml^{-1} As(III) in 0.08 M HCl with 1% (w/v) $NaBH_4$ (0.05 M NaOH) solution.

tetrahydroborate(III) concentration from 0.5 to 5.0 mg ml^{-1} and reaches a plateau at concentrations above 10 mg ml^{-1}.

The effect of the carrier gas (argon) flow-rate is shown in Fig. 5. There is a peak at 0.45 l min^{-1}.

Based on the above results, concentrations of

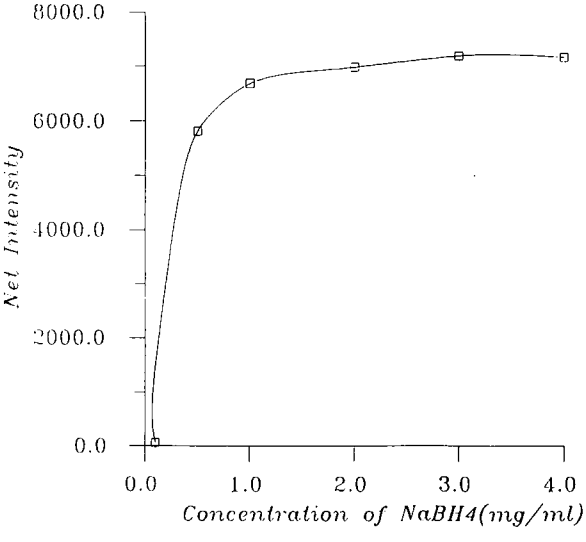

Fig. 4. Effect of sodium tetrahydroborate(III) concentration on arsenic(III) net intensity. 100 ng ml^{-1} As(III) in 0.08 M HCl in the presence of 5 mg ml^{-1} L-cysteine. NaOH concentration for $NaBH_4$ solution 0.05 M.

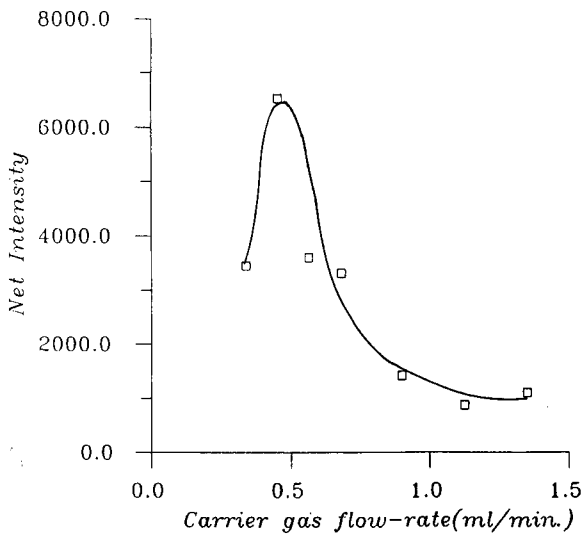

Fig. 5. Effect of carrier gas (argon) flow-rate on arsenic(III) net intensity. 100 ng ml^{-1} As(III) in 0.08 M HCl with 5 mg ml^{-1} L-cysteine, 1% (w/v) $NaBH_4$.

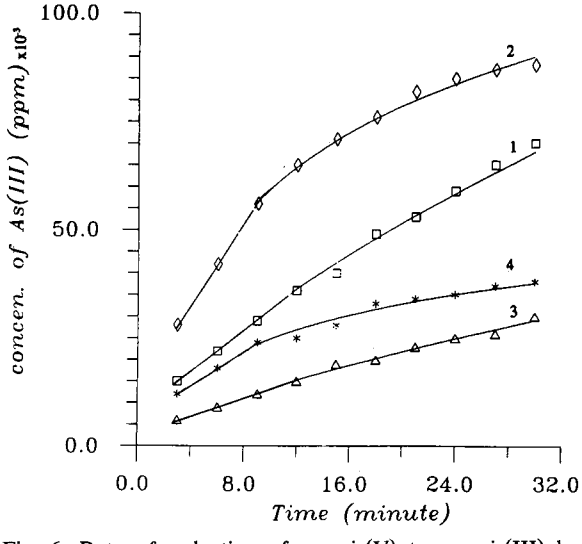

Fig. 6. Rate of reduction of arsenic(V) to arsenic(III) by L-cysteine. (1) 100 ng ml^{-1} As(V) in 0.08 M HCl with 2.5 mg ml^{-1} L-cysteine, 1% (w/v) $NaBH_4$; (2) 100 ng ml^{-1} As(V) in 0.08 M HCl with 5.0 mg ml^{-1} L-cysteine, 1% (w/v) $NaBH_4$; (3) 50 ng ml^{-1} As(V) in 0.08 M HCl with 2.5 mg ml^{-1} L-cysteine, 1% (w/v) $NaBH_4$; (4) 50 ng ml^{-1} As(V) in 0.08 M HCl with 5.0 mg ml^{-1} L-cysteine, 1% (w/v) $NaBH_4$.

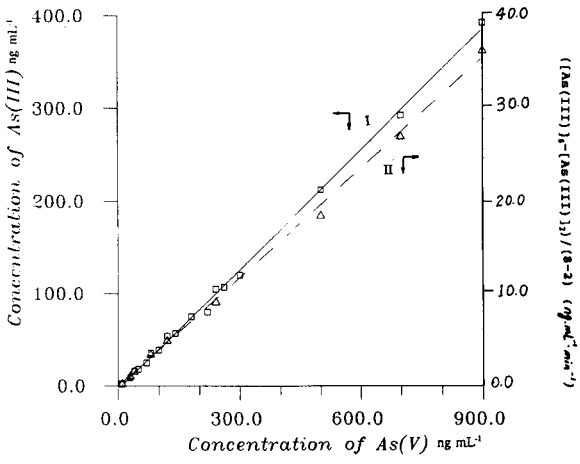

Fig. 7. Calibration. (I) Concentration of As(V) versus concentration of As(III) at 8th minute {[As(V)] = 5–900 ng ml^{-1}}; (II) [As(V)] versus $([As(III)]_8 - [As(III)]_2)/(8-2)$ {[As(V) = 5–900 ng ml^{-1}}. [HCl] 0.08 M, [L-cysteine] = 5 mg ml^{-1}, $[NaBH_4]$ = 1% ([NaOH] = 0.05 M).

0.08 mol l^{-1} hydrochloric acid, 5 mg ml^{-1} L-cysteine and 10 mg ml^{-1} sodium tetrahydroborate-(III) and a carrier gas (argon) flow-rate of 0.45 l min^{-1} were used in subsequent experiments.

4.3. Rate of reduction of arsenic(V) to arsenic(III) by L-cysteine

When the rate of reduction of arsenic(V) was studied, it was found that for the first 9 min the graph of concentration of arsenic(III) determined by the above method versus time is a straight line (Fig. 6), and for longer times the graph is no longer linear.

4.4. Calibration

Following the above analytical procedure, the concentrations of arsenic(III) in a series of standard solutions of arsenic(V) (5–900 ng ml^{-1}) with L-cysteine (5 mg ml^{-1}) were determined separately at the 2nd and 8th minutes, then line I for $[As(III)]_8$ as a function of [As(V)] (C) (Eq. 4) and line II for $\{[As(III)]_8 - [As(III)]_2\}/(8-2)$ as a function of [As(V)] (C) (Eq. 5) were obtained (Fig. 7) and both were straight lines. The linear regression equation for these two calibration graphs for concentrations of arsenic(V) from 5 to 900 ng ml^{-1} were found to be

$$y = -0.002827 + 0.0004302x$$

and

$$y = 0.0001452 + 0.00003839x$$

Table 2
Interferences from transition elements

Ion	Concentration (mg kg^{-1})	Recovery (%) (with 5 mg ml^{-1} L-cysteine)
Hg(II)	20	96
	200	100
Co(II)	20	95
	200	63
Cd(II)	20	122
	200	600
Cr(VI)	20	97
	200	63
Al(III)	20	98
	200	98
Cu(II)	20	98
	200	96
Zn(II)	20	97
	200	97
Ni(II)	2	103
	20	60
Fe(III)	20	108
	200	104
Fe(II)	20	108
	200	110

Table 3
Determination of arsenic(V) and arsenic(III) in standard reference metals

Sample	Found [Mean ± S.D. (n = 3)] (mg kg^{-1})			certified value (mg kg^{-1})
	As(V)	As(III)	As(V) + As(III)	
Low Alloy Steel 362	868.71 ± 9.98	2.07 + 3.6	870.78 ± 11.57	900
Low Alloy Steel 363	82.33 ± 4.06	16.39 + 2.37	98.76 ± 1.68	100
Low Alloy Steel 364	459.02 ± 22.32	9.07 + 9.34	468.09 ± 14.07	500
Cast Iron CKD 229	91.57 ± 1.25	5.69 + 0.41	97.26 ± 0.84	100

respectively. The correlation coefficients were 0.9994 and 0.9991, respectively. These two graphs are the basis for sample analysis.

4.5. Interferences

A 1-ml volume of interfering ion solution (concentration 0.05, 0.5 or 5.0 mg ml^{-1}) was added 100 ng ml^{-1} arsenic(V) and 5 mg ml^{-1} L-cysteine in a 25-ml volummetric flask, then time recording was started and the solution was immediately diluted to the mark. Following the above analytical procedure, the solution was introduced into the generator at the 2nd and 8th minutes, and based on Eqs. 4 and 5 and Fig. 7 the concentration of arsenic(V) was calculated and the recovery of arsenic(V) was obtained (Table 2). The results in Table 2 show that the interference of ten ions at concentrations between 2.0 and 200 mg l^{-1} was acceptably small except for nickel(II) and cadmium(II).

4.6. Limit of detection

The limit of detection, defined as three times the standard deviation of the blank, was 3.4 ng ml^{-1} for arsenic(V) and 0.7 ng ml^{-1} for arsenic(III). The R.S.D. for a solution containing 100 ng ml^{-1} of arsenic(V) or arsenic(III) was 1.45 or 1.21% respectively (ten replicates).

4.7. Sample analysis

The results of application of the method for the determination of arsenic(V) and arsenic(III) in certified samples from the National Institute of Standards and Technology (NIST), i.e. Cast Iron CKD 229 and Low Alloy Steels 362, 363 and 364, are given in Table 3. The total arsenic content in Table 3 obtained by combination of arsenic(V) and arsenic(III) shows acceptable agreement with the certified values.

5. Conclusion

This study has shown that the small co-centric hydride generator combined with reduction kinetics of arsenic(V) by L-cysteine can be used to determine arsenic(V) and arsenic(III) simultaneously by ICP-AES with a minitorch of 0.65-kW power. The linear analytical range is between 5 to 900 ng ml^{-1} for arsenic(V). The interferences from transition elements can be significantly decreased which makes this system of potential value in a wide range of applications. Finally, the determination of arsenic(V) and arsenic(III) in metals was achieved with satisfactory results were obtained.

Acknowledgement

The authors thank Professor Li-Ching Tian of Nanjing University for checking the paper.

References

[1] P.D. Goulden, D.H.J. Anthony and K.D.D. Austen, Anal. Chem., 53 (1981) 2027.
[2] C. Baluja-Santos and A. Gonzalez-Portal, Talanta, 39 (1992) 329.
[3] X. Wang and Ramon M. Barnes, Spectrochim. Acta, Part B, 42 (1987) 139.
[4] D.D. Nygaard and J.H. Lowry, Anal. Chem., 54 (1982) 803.
[5] H. Narasaki and M. Ikeda, Anal. Chem., 56 (1984) 2059.
[6] M. Yamamoto, M. Yasuda and Y.K. Yamamoto, Anal. Chem., 57 (1985) 1382.
[7] K. Matsumoto, T. Ishiwatari and K. Fuwa, Anal. Chem., 56 (1984) 1545.
[8] A.P. D'silva, G.W. Rice and V.A. Fassel, Appl. Spectrosc., 34 (1980) 578.
[9] B. Huang, Z. Zhang and X. Zeng, Spectrochim. Acta, Part B, 42 (1987) 129.
[10] L. Zhang, S. McIntosh, G.R. Carnrick and W. Slavin, Spectrochim. Acta, Part B, 47 (1992) 701.
[11] G. Vujicie and I. Steffan, Mikrochim. Acta, III (1989) 267.
[12] R.C. Fry, M.B. Denton, D.L. Windsor and S.J. Northway, Appl. Spectrosc., 33 (1979) 399.
[13] L. Halicz and G.M. Russell, Analyst, 111 (1986) 15.
[14] S. Stieg and A. Dennis, Anal. Chem., 54 (1982) 605.
[15] R.C. Hutton and B. Preston, Analyst, 108 (1983) 1409.
[16] M. Thompson, B. Pahlavanpour, S.J. Walton and G.F. Kirkbright, Analyst, 103 (1978) 568.
[17] M. Thompson, B. Pahlavanpour, S.J. Walton and G.F. Kirkbright, Analyst, 103 (1978) 705.
[18] F.D. Pierce, T.C. Lamoreaux and K.S. Fraser, Appl. Spectrosc., 30 (1976) 38.

[19] M. Yamamoto, Anal. Chem., 59 (1987) 2446.
[20] X. Wang and R.-M. Barnes, J. Anal. At. Spectrom., 3 (1988) 1091.
[21] G.E. Pacey, Anal. Chem., 58 (1986) 502.
[22] F. Nakata, H. Sunahara, H. Fujimoto, M. Yamamoto and T. Kumamaru, J. Anal. At. Spectrom., 3 (1988) 579.
[23] R.M. Barnes and X. Wang, J. Anal. At. Spectrom., 3 (1988) 1083.
[24] I.D. Brindle, H. Alarabi, S. Karshman, X. Le, S. Zheng and H. Chen, Analyst, 117 (1992) 407.
[25] H. Chen, I.D. Brindle and S. Zeng, Analyst, 117 (1992) 1603.
[26] P. Schramel and L. Xu, Fresenius' J. Anal. Chem., 340 (1991) 41.
[27] K.S. Subramanian and J.C. Meranger, Anal. Chim. Acta, 124 (1981) 131.
[28] D. Chakrabotlb, W. De Jonghe and F. Adam, Anal. Chim. Acta, 120 (1980) 121.
[29] C. Chung, E. Iwamoto, M. Yamamoto and Y. Yamamoto, Spectrochim. Acta, Part B, 39 (1984) 459.
[30] H. Chen, I.D. Brindle and X. Le, Anal. Chem., 64 (1992) 667.
[31] J.D. Hwang, G.D. Guenther and J.P. Diomiguardi, Anal. Chem., 61 (1989) 285.

PUBLICATION SCHEDULE FOR 1994

	J	F	M	A	M	J	J	A	S	O	N	D
Anal. Chim. Acta	284/3 285/1–2 285/3	286/1 286/2 286/3	287/1–2 287/3 288/1–2	288/3 289/1 289/2	289/3 290/1–2 290/3	291/1–2 291/3 292/1–2	292/3 293/1–2 293/3	294/1 294/2 294/3	295/1 295/2 295/3	296/1–2 296/3 297/1–2	297/3 298/1 298/2–3	299/1 299/2–3 300/1
Vib. Spec.	6/2		6/3		7/1		7/2		7/3		8/1	

INFORMATION FOR AUTHORS

Detailed "Instructions to Authors" for *Analytica Chimica Acta* was published in Volume 289, No. 3, pp. 381–384. Free reprints of the "Instructions to Authors" of *Analytica Chimica Acta* and *Vibrational Spectroscopy* are available from the Editors or from: Elsevier Science B.V., P.O. Box 330, 1000 AH Amsterdam, The Netherlands. Telefax: (+31-20) 5862459.

Manuscripts. The language of the journal is English. English linguistic improvement is provided as part of the normal editorial processing. Authors should submit three copies of the manuscript in clear double-spaced typing on one side of the paper only. *Vibrational Spectroscopy* also accepts papers in English only.

Rapid publication letters. *Letters* are short papers that describe innovative research. Criteria for letters are novelty, quality, significance, urgency and brevity. Submission data: max. of 2 printed pages (incl. Figs., Tables, Abstr., Refs.); short abstract (e.g., 3 lines); *no* proofs will be sent to the authors; submission on floppy disc; *no* revision will be possible.

Abstract. All papers and reviews begin with an Abstract (50–250 words) which should comprise a factual account of the contents of the paper, with emphasis on new information.

Figures. Figures should be prepared in black waterproof drawing ink on drawing or tracing paper of the same size as that on which the manuscript is typed. One original (or sharp glossy print) and two photostat (or other) copies are required. Attention should be given to line thickness, lettering (which should be kept to a minimum) and spacing on axes of graphs, to ensure suitability for reduction in size on printing. Axes of a graph should be clearly labelled, along the axes, outside the graph itself. All figures should be numbered with Arabic numerals, and require descriptive legends which should be typed on a separate sheet of paper. Simple straight-line graphs are not acceptable, because they can readily be described in the text by means of an equation or a sentence. Claims of linearity should be supported by regression data that include slope, intercept, standard deviations of the slope and intercept, standard error and the number of data points; correlation coefficients are optional.

Photographs should be glossy prints and be as rich in contrast as possible; colour photographs cannot be accepted. Line diagrams are generally preferred to photographs of equipment. Computer outputs for reproduction as figures must be good quality on blank paper, and should preferably be submitted as glossy prints.

Nomenclature, abbreviations and symbols. In general, the recommendations of IUPAC should be followed, and attention should be given to the recommendations of the Analytical Chemistry Division in the journal *Pure and Applied Chemistry* (see also *IUPAC Compendium of Analytical Nomenclature, Definitive Rules*, 1987).

References. The references should be collected at the end of the paper, numbered in the order of their appearance in the text (*not* alphabetically) and typed on a separate sheet.

Reprints. Fifty reprints will be supplied free of charge. Additional reprints (minimum 100) can be ordered. An order form containing price quotations will be sent to the authors together with the proofs of their article.

Papers dealing with vibrational spectroscopy should be sent to: Dr J.G. Grasselli, 150 Greentree Road, Chagrin Falls, OH 44022, U.S.A. Telefax: (+1-216) 2473360 (Americas, Canada, Australia and New Zealand) or Dr J.H. van der Maas, Department of Analytical Molecular Spectrometry, Faculty of Chemistry, University of Utrecht, P.O. Box 80083, 3508 TB Utrecht, The Netherlands. Telefax: (+31-30) 518219 (all other countries).

0003-2670/94/$07.00

0003-2670(19940720)293:1/2;1-8